

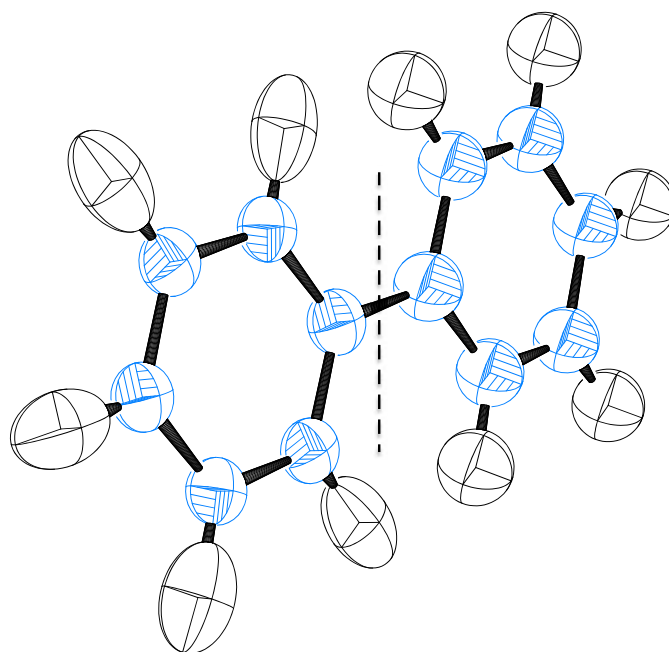


TOR VERGATA
UNIVERSITÀ DEGLI STUDI DI ROMA

A novel γ -sensitive detector apparatus for eV neutron spectroscopy applied to hydrogen-bonded systems

Pierfrancesco Ulpiani

Dissertation for the degree of philosophiae doctor
in
“Materials for Health, Environment and Energy”



Supervisors: Prof. C. Andreani and Prof. R. Senesi

PhD Coordinator: Prof. E. Di Bartolomeo

The material in this publication is protected by copyright law.

Academic Year: 2019/2020

Title: A novel γ -sensitive detector apparatus for eV neutron spectroscopy
applied to hydrogen-bonded systems

Author: Pierfrancesco Ulpiani

*O me! O life! of the questions of these recurring,
Of the endless trains of the faithless, of cities fill'd with the foolish,
Of myself forever reproaching myself,
(for who more foolish than I, and who more faithless?)
Of eyes that vainly crave the light of the objects mean, of the struggle ever renew'd,
Of the poor results of all, of the plodding and sordid crowds I see around me,
Of the empty and useless years of the rest, with the rest me intertwined,
The question, O me! so sad, recurring - What good amid these, O me O life?*

*Answer
That you are here - that life exists and identity,
That the powerful play goes on, and you may contribute a verse.
— Walter Whitman*

Abstract

The work presented in this thesis collects the activities I addressed during the three-year PhD project in *Materials for Health, Environment and Energy*. The objective of my PhD project is the development of a novel detector apparatus, named γ DA, and methodology for eV neutron spectroscopy applied to the characterization of hydrogen-bonded systems.

Neutrons, being uncharged particles, are the probe of choice to study the nuclear dynamics in condensed-matter systems. The nuclear dynamics is an increasingly requested feature in material characterization as it has a central role in many open questions in Physics and Chemistry. The nuclear dynamics is studied with neutrons of energy in the eV range, in a technique called Deep Inelastic Neutron Scattering. I used this technique at high momentum, \mathbf{Q} , and energy transfers, $\hbar\omega$, to study the single-particle dynamics in hydrogen-bonded systems with the above mentioned device that will broaden the capability of Deep Inelastic Neutron Scattering. The work is a prosecution of the e.Verdi project where the cornerstones of the detection technology development of neutrons at the eV were established. The γ DA is thought to operate on the VESUVIO spectrometer at the ISIS pulsed neutron and muon source.

In the first part of the thesis I described the basic theory of neutron scattering and the facility where neutrons are produced, with a particular attention on VESUVIO and the detection strategy used at present. The second part of the thesis is devoted to the configurations tested for the apparatus, with a detailed description of the preliminary tests performed on a polyethylene sample, used as a neutron spectroscopy standard, together with the calibration and the response simulation, performed within the FLUKA environment, of the detector. Once the optimal configuration was found I investigated the nuclear dynamics in biphenyl that is generally used as a model compound to emulate the lignin decomposition in monocyclic hydrocarbons in the biofuel-production research. The measurements demonstrated a detection count-rate increase of five times and a signal-background ratio improvement of 50%. This means faster and cleaner measurements. The biphenyl dynamics was also simulated with ab-initio calculations performed within the Quantum Espresso and CASTEP environments and compared with the experimental results accessed by neutron scattering techniques. The simulations allowed us to determine the reason why structures with a considerable number of internal vibrations show an isotropic dynamics, *i.e.*, same kinetic energy in all the Cartesian directions. In fact, if the number of nuclei is big enough the Central Limit Theorem can be applied as I have shown with the simulation of saturated hydrocarbons from methane to decane where a decreasing trend in the anisotropy was observed from the simulation as a function of the nuclei present in the molecule. In the last part of the thesis, after a brief introduction to the physics of ice, I described the neutron scattering experiments, in collaboration with the University College London, performed at ISIS, used to demonstrate the unusual stability of ice II. In fact, ice II is the only hydro-

gen ordered phase that does not have any disordered counterpart and it is stable up to high temperatures. The stability of the phase is motivated by the very low kinetic energy of hydrogens, probed by eV neutron scattering, and by the high displacement, probed by quasi elastic neutron scattering. In particular, as the stability is given by the Gibbs free energy, at lower energy and higher entropy it corresponds a more stable phase. The beauty and the reason why this study was so fascinating is that the hydrogen displacement brings an additional term to the entropy, a *dynamic disorder* that makes, together with the low energy, the ice II very stable. Hence ice II is *ordered by the disorder*, a wonderful joke of Nature.

Contents

1	Introduction	1
2	Neutron-scattering techniques	5
2.1	Basic properties of neutrons	5
2.2	Elastic Scattering	12
2.2.1	Debye-Waller factor	13
2.3	Inelastic Neutron Scattering	14
2.4	Deep Inelastic Neutron Scattering	14
2.4.1	Mean Force	17
2.5	The Anisotropic case	17
2.6	Other neutron interactions	19
3	Sources and Instrumentation	23
3.1	Neutron Sources and Facilities	23
3.2	Time of Flight technique	24
3.3	The VESUVIO spectrometer	27
3.3.1	Detectors	29
3.3.2	Resonance Detector technique	31
3.3.3	Data reduction and analysis	35
3.4	The IRIS spectrometer	36
4	γDA development	39
4.1	Calibration and FLUKA simulations	39
4.2	Polyethylene preliminary results	43
4.2.1	Counting error and noise reduction	44
4.2.2	Line-shape analysis with optimized set-up	46
4.2.3	Mean-force analysis with optimized set-up	49
4.2.4	Bi-parametric spectra	50
4.3	Biphenyl	52
4.3.1	Configurations for the γ DA	53
4.3.2	Transfer Function Optimization	53
4.3.3	Energy Threshold Optimization	55
4.3.4	DINS	59
5	Ab-initio Simulations	65
5.1	Adiabatic Approximation	65
5.2	Density Functional Theory	66

5.2.1	Electronic Calculation	66
5.2.2	Crystal and Molecule Structure and Vibrations	67
5.2.3	Relation between DINS, INS, QENS and Simulation	69
5.3	Biphenyl Simulation	72
5.4	Approach to the Central Limit Distribution	76
6	Ice Experiments	83
6.1	The fascinating world of Water and Ice	83
6.1.1	Order and ice rules	84
6.1.2	Ice II, a unique phase	85
6.1.3	Sample Preparation	86
6.2	Stability induced by Energy	87
6.2.1	Sample Container Optimization	89
6.2.2	Visual Evidence	90
6.2.3	Fit on the NCPs	90
6.2.4	Mean Force	92
6.3	Stability induced by Entropy	92
6.3.1	Experimental Detail	96
6.3.2	Data Reduction and Analysis	96
6.4	Inelastic scattering	99
6.4.1	Dynamics simulation	103
7	Conclusion	107
8	Outlook and future perspectives	109
9	Publications and Activities	111
9.1	Published papers	111
9.2	Communications	112
9.3	Prizes	112
9.4	Experiments	113
9.5	Other Activities	113
9.5.1	“Percorso Formativo 24 CFU”	113
9.5.2	Part-time Employment	114
9.5.3	Seminars	114
A	Quantum Espresso Input	115
A.1	Structure and Nuclear Potential Calculation	115
A.2	Vibrations and Eigenvectors	117
B	Bi-parametric analysis script	119
C	Mean Force calculation script	127
D	Ice $\overline{F}(y, Q)$	131
	Bibliography	135

Acknowledgements

149

List of Abbreviations and Symbols

AF	Analyser Foil
CCR	Closed Circuit Refrigerator
CE	Compton Edge
CLT	Central Limit Theorem
CRI	Count-Rate Increase
DINS	Deep Inelastic Neutron Scattering
ER	Error Reduction
FCT	Foil Cycling Technique
FEP	Full Energy Peak
FF	Filter Foil
FoR	Frame of Reference
INS	Inelastic Neutron Scattering
LLDT	Low Level Discrimination Threshold
MF	Mean Force
MSD	Mean Square Displacement
NCP	Neutron Compton Profile
NMD	Nuclear Momentum Distribution
NQE	Nuclear Quantum Effect
NRCA	Neutron Resonance Capture Analysis
PGAA	Prompt Gamma Activation Analysis
QE	Quantum Espresso
QENS	Quasi Elastic Neutron Scattering
RD	Resonance Detector
RF	Resonance Filter
TDHO	Three Dimensional Harmonic Oscillator
ToF	Time of Flight

T-PGAA	Time-resolved Prompt Gamma Activation Analysis
VDoS	Vibrational Density of States
YAP	Yttrium Aluminium Perovskite
γ DA	γ -sensitive Detector Apparatus
$E_i, E_f, k_i, k_f,$ v_i, v_f	Energy, wave vector and velocity of neutron before and after the scattering
m, M	neutron and nuclear mass
k_B	Boltzmann constant
\hbar	reduced Planck's constant
Q	momentum transfer
σ_b, σ_f	total bound and free scattering cross section
$\frac{d^2\sigma}{\hbar d\omega d\Omega}$	partial differential cross section
N	number of nuclei in the scattering system
$S(\mathbf{Q}, \omega)$	scattering function
\tilde{V}	crystal volume
$\langle A \rangle$	thermal average of operator A

Chapter 1

Introduction

The theme of dynamics has always attracted a great interest in the history of philosophy and science. According to Heraclitus, even what is apparently static is in truth in continuous movement and in his most famous aphorism, *panta rei*, we can glimpse life itself in the dynamics and death in its opposite. The myth of dynamics then evolved influencing the most disparate forms of art such as the Futurist movement. Fig. 1.1 is an example of that where the portrait by Giacomo Balla tries to represent the frantic movement of a small dog.



Figure 1.1: *Dinamismo di un cane al guinzaglio* by Giacomo Balla.

The techniques described in this thesis go in the same direction where the main actors of the dynamics are not animals or people but molecules and atoms; in this sense I will describe the way of painting the nuclear dynamics.

Condensed-matter physics is becoming a fundamental field in the natural sciences as it is attracting more and more interests both within academic and R&D industrial framework. In this context, a great effort is required in material characterizations. Depending on what property it is of interest, the most suitable probe is chosen. The non invasive and highly penetrating nature of neutrons makes them ideal to study non destructively the structure and dynamics of matter with an atomic scale resolution. In particular, inelastic neutron scattering at eV energies is an experimental technique for the measurement of nuclear momentum distributions, and as such is capable to obtain information on the nuclear quantum dynamics in materials [1, 2, 3].

The aim of my PhD project is the development of neutron techniques with applications for materials of interest in the applied condensed-matter physics. The PhD research activities took place partly at the University of Rome “Tor Vergata” and partly at the ISIS pulsed neutron and muon source where experiments on the VESUVIO and IRIS spectrometer have been performed. During the PhD, I took part to experimental campaigns where I developed a novel γ -sensitive Detector Apparatus, hereafter named γ DA, for eV neutron spectroscopy. The γ DA was then installed on the forward scattering detector bank of the VESUVIO spectrometer and used to measure samples for both fundamental physics and green energy production application. In the first two chapters of the thesis the principles of the neutron scattering techniques are described. In particular, in Chapter 2 the theory of the neutron scattering needed for the comprehension of the phenomena analysed in the thesis is reported while in Chapter 3 the neutron spectrometer and instrumentation improved during the project are described. In a second part of the thesis, Chapter 4, the instrumentation development of the γ DA, its potentiality and impact are explained. In fact, the characterization of the microscopic state and comparison with theoretical model goes hand in hand with the quality of the experimental data in terms of statistical errors and noise. The best sensitivity at present on VESUVIO is of the order of $40 \mu\text{mol}/\text{cm}^2$ [4] but there are applications such as the hydrogen content in fusion materials [5] or the study of the structures and operation of the catalyst at the molecular level for catalysis reactions [6] or parametric study as temperature or pressure scans that need faster and higher sensitivity measurements. For these reasons it is important to find experimental methods finalised to improve the quality of the data acquired increasing the counting statistics of signal and reducing noise and background. The applications of the γ DA start from Sec. 4.3 where the improvement of the technique is applied to a biphenyl sample, a model compound for lignin decomposition in monomers. Lignin, particularly abundant in the cell walls of plants and bark [7] is the main component of the second-generation biomass used to produce fuel. To avoid its disposal as a by-product of the process, effort is directed into the thermochemical conversion of lignin to higher-value products [8, 9, 10, 11, 12]. To better understand the catalysed decomposition of lignin, it is common to use model compounds containing the most significant linkages present in lignin and show similar characteristics to the natural biopolymer [13, 14, 15]. Biphenyl linkages represent the second most abundant linkage type in softwood [16] and are often used as a model compound to tackle the conversion of lignin into monocyclic hydrocarbons [17]. Because of the complexity in the process of dissociation of lignin and its compounds, modeling and computer simulations, such as phonon

calculations based on Density Functional Theory, are often employed. In fact, first principles calculations are frequently used as complementary tool for material characterization for large scale screening of potentially interesting materials, Ref. [18] can be taken as an example where the effect of anharmonicity and Nuclear Quantum Effects (NQE) on the structural and thermal properties of Metal Organic Framework is modelled and quantified while Ref. [19] emphasise the importance of NQEs on the biphenyl equilibrium structure. In Chapter 5 the experimental mean kinetic energy, degree of harmonicity and isotropy of the hydrogen local potential in biphenyl, probed with the γ DA on VESUVIO, is compared with phonon calculations based on ab-initio simulations.

The work on the instrumentation development is further motivated when nuclear dynamics experiments are performed in order to study the differences between similar structures. As water in its liquid and solid forms is ubiquitous in nature, being one of the most abundant molecules in the universe, and it is thought to be a prerequisite to sustain life in our solar system and beyond [20, 21], the allotropic forms of ice were chosen as samples for my PhD project in Health, Environment and Energy. In fact, while the water molecule is small, it has a surprising amount of complexity that makes it an intriguing target for basic studies of molecules and deriving properties of quantum mechanics [22, 23]. Water has a number of properties that make it quite unique among many common substances even if many ice characteristics were then found in other materials such as the stacking disorder in diamond [24, 25]. In Chapter 6 small, yet important, differences in the hydrogen dynamics of five ice phases are an example of how much important are the steps forward made in this work. The description and data analysis of eV and quasi-elastic neutron spectroscopy measurements are reported to motivate the stability of the ice II phase in the phenomenology of the water phase diagram.

In the work reported in this thesis the competition between the experiment, which represents the observable, and the simulation which provides the opportunity to predict the trend of the observable, is condensed and emerges from many points of view. The competition is mediated by the instrument optimization for more precise results that, on the one hand, allows more accurate comparisons between the experiment and the simulation but, on the other hand, allows to set limits to the simulations so that they are increasingly performing and fit better the physics involved. In the case studied in this thesis, the theory provides a prediction of the trend of the degree of anisotropy of the nuclear potential which tends to zero for systems with a considerable number of atoms. However the experiment, that emerges distinctly from the calculation thanks to the instrumentation development, shows that a lower number of atoms are required in order to have an isotropic potential because multiple degrees of freedom such as structural disorder and molecular-vibration couplings are involved. The nuclear and molecular environments that have been studied are, in the case of biphenyl, developed to provide support to the biomass production community (Energy) while, in the case of ice, for a deeper knowledge of the molecule thanks to which life exists on Earth (Health and Environment).

The experiments were designed and performed by me during the three-year PhD project, the details of the activities, published papers and talks are reported in Chapter 9.

Chapter 2

Neutron-scattering techniques

2.1 Basic properties of neutrons

With the advent of nuclear reactors, neutrons have become an important tool for investigating many features of matter such as the non-destructive detection and quantification of hydrogen in bulk media or to probe the nuclear dynamics even for valuable specimens, *e.g.*, historical artifacts for Cultural Heritage [26]. The basic physical properties of neutrons are:

- mass $m = 1.67510^{-27} kg$
- Charge $q = 0$
- spin $1/2$
- magnetic dipole moment $\mu_n = -1.913 \mu_N$.

The energy E of a neutron with a wave vector \mathbf{k} is

$$E = \frac{\hbar^2 k^2}{2m}. \quad (2.1)$$

In neutron spectroscopy, the energies are often given in units of meV ; using $m = 1.0087 u$ and $\hbar = 2.044\sqrt{u \cdot meV} \text{ \AA}$ we have

$$\frac{\hbar^2}{2m} = 2.08 meV \text{ \AA}^2.$$

From this expression we can see that a neutron with a wave vector $k \sim 1 \text{ \AA}^{-1}$ has an energy $E \sim 2 meV$. This energy is characteristic of the one carried by lattice vibrations. Using the de Broglie relation

$$\lambda = \frac{h}{mv} \quad (2.2)$$

we can see that neutrons with energy $E \sim meV$ have a wavelength λ comparable with atomic spacing in condensed matter. As a consequence the diffraction of neutrons from condensed matter can display interference effects.

Slow-neutron beams (under 20 MeV) are often described as being cold, thermal, hot or epithermal. There is no standard definition of these terms but one convention is shown in Table 2.1.

	E (meV)
Cold	0.1-10 meV
Thermal	10-100 meV
Hot	100-500 meV
Epithermal	>500 meV

Table 2.1: Nomenclature for neutron energies.

In neutron scattering experiments the key variables are the change in the neutron energy and in the wave vector. Calling the incident and scattered neutron energy and wave vector E_i, k_i and E_f, k_f we can define the energy transferred as

$$\hbar\omega = E_i - E_f = \frac{\hbar^2(k_i^2 - k_f^2)}{2m} \quad (2.3)$$

and the scattering wave vector

$$\mathbf{Q} = \mathbf{k}_i - \mathbf{k}_f. \quad (2.4)$$

The motion of atoms and their spatial correlations are revealed in a neutron scattering experiment when $\hbar\omega$ and $Q = |\mathbf{Q}|$ match the corresponding energies and wave vectors involved. It is evident from Eq. 2.3 that ω and Q are related; this relation imposes kinematic constraints on the scattering experiments. For example, in order to gain access to the domain of large ω and small Q it is necessary to use incident neutrons with high energy and small scattering angles; not all of (Q, ω) space is generally accessible in a single neutron scattering experiment and it means that the neutron source and spectrometer configuration limit the range of experiments that can be performed.

The penetration depth of neutrons in matter is extremely large with respect to the other particles, mainly because they do not have charge so there is no Coulomb interaction to overcome, in Fig. 2.1 the penetration depth of thermal neutrons, X-rays and electrons is represented as a function of the atomic number. It can be noticed the logarithmic scale on the y-axis in order to represent the lengths associated with both electrons (ca. 10 μm), photons (ca. 100 μm) and neutrons (ca. cm). Neutrons are thus scattered by nuclear forces and the scattering process is well suited to the study of bulk properties. The scattering provides information on the physical and chemical properties of the target sample which remains mostly unaffected after the interaction with the experimental probe, being neutron studies non destructive.

As opposed to X-ray interaction, where the intensity is a monotonic function of Z , the neutron cross section doesn't show any simple dependence upon Z (atomic number) or A (mass number) values, see Fig. 2.1. This feature of the scattering can be very valuable, enabling studies using isotopes substitutions. An example could be the contrast between hydrogen and deuterium where the scattering from hydrogen exceeds the deuterium one by an order of magnitude.

We can conclude that the most important properties of neutron characterization are:

- sensitivity to different isotopes (*i.e.*, separation between hydrogen and deuterium)
- deep penetration into the target

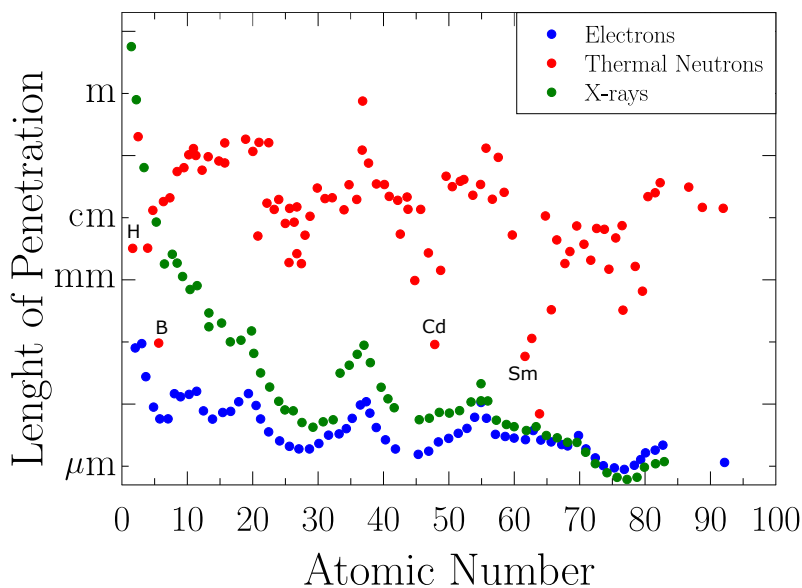


Figure 2.1: Penetration depth of thermal neutrons, X-rays and electrons as a function of the atomic number.

- not-destructive probe
- energy of thermal neutrons are of the same order of many lattice and molecular excitations
- de Broglie wavelength of thermal neutrons is of the order of interatomic distances

The geometry of a scattering experiment is shown in Fig. 2.2

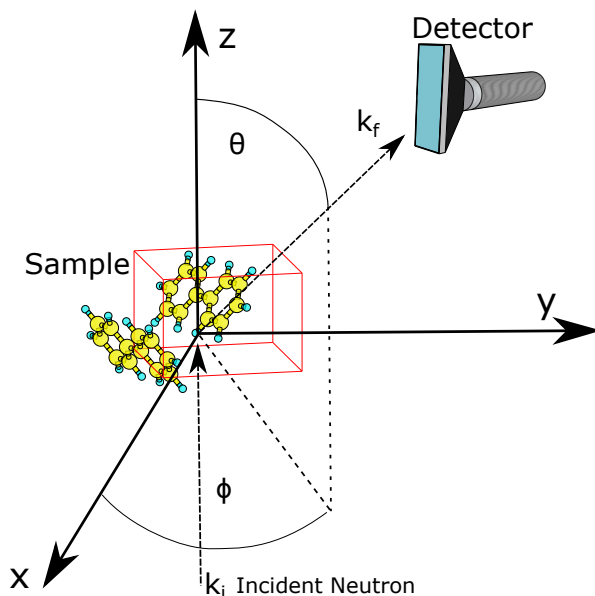


Figure 2.2: Scheme of a neutron scattering experiment.

A neutron in the scattering experiment with wave vector \mathbf{k}_i is scattered into a state with wave vector \mathbf{k}_f and \mathbf{Q} is the momentum transferred. If $|\mathbf{k}_i| \neq |\mathbf{k}_f|$ the scattering process will be called inelastic, otherwise it will be called elastic. This nomenclature is different from the

high-energy physics field where the elastic scattering is associated with the conservation of both the energy and momentum. For this reason our inelastic scattering where the momentum and energy are conserved but $|\mathbf{k}_i| \neq |\mathbf{k}_f|$ is called elastic in other fields of application.

If we consider a mono-energetic neutron beam and a solid-type sample as a scattering system various types of measurement can be performed after the interaction. The scattering process can always be described with a quantity named partial differential cross-section, $\frac{d^2\sigma(E_i)}{d\Omega dE_f}$ that describes the number of neutrons scattered in a solid angle $d\Omega$ with a final energy within E_f and $E_f + dE_f$.

The response of the system to the perturbation is described by the dynamical structure factor, $S(\mathbf{Q}, \hbar\omega)$. Depending on the energy exchanged in the scattering, $S(\mathbf{Q}, \hbar\omega)$ is described within a different regime. In Fig. 2.3 a representative $S(\mathbf{Q}, \hbar\omega)$ is reported in the Quasi Elastic Neutron Scattering (QENS) [27], Inelastic Neutron Scattering (INS) [28] and Deep inelastic Neutron Scattering (DINS) [3] regime, used in this work for sample characterization.

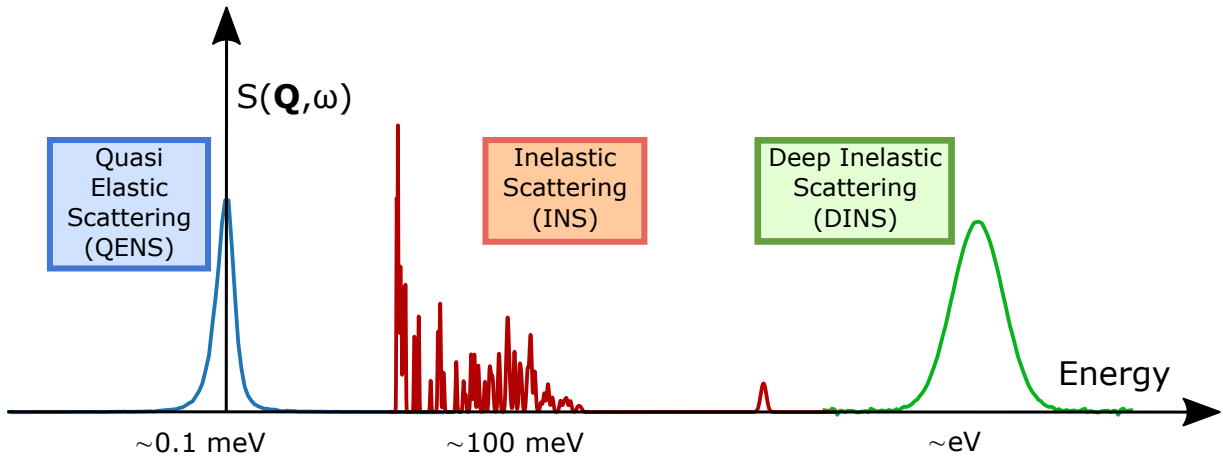


Figure 2.3: Dynamical structure factor, $S(\mathbf{Q}, \hbar\omega)$, as a function of the exchanged energy in the scattering process.

The nuclear dynamics can be hence probed by different neutron energies which give information strictly correlated. The differential cross section has the dimension of area/energy per solid angle. The only satisfactory way to derive an expression for the cross-section, to be related with $S(\mathbf{Q}, \hbar\omega)$, is to use the formal scattering theory. We will describe the scattering process for a general neutron scattering with no resonances or absorption and then focus on the specific scattering regime.

In general we can assume that the initial state of neutron $|k_i\rangle$ is described by a plane wave

$$|k_i\rangle \sim \frac{1}{\sqrt{\tilde{V}}} e^{i\mathbf{k}_i \cdot \mathbf{R}}. \quad (2.5)$$

Even the final state can be described by a plane wave under the assumption that we are far away from the sample (scattering point), it is called Born approximation

$$|k_f\rangle \sim \frac{1}{\sqrt{\tilde{V}}} e^{i\mathbf{k}_f \cdot \mathbf{R}'}. \quad (2.6)$$

In scattering experiments, the detectors measure the number of neutrons scattered per unit time that depends on the differential cross section. In order to describe the counts of the detectors we can write

$$\frac{d^3 N}{\hbar d\omega d\Omega dt} = \frac{d^2 \sigma}{\hbar d\omega d\Omega} \frac{d^2 N}{d\sigma dt}, \quad (2.7)$$

where N is the number of neutrons. The term on the left side of the equation is the number of scattered neutrons in a solid angle $d\Omega$ around a general direction with an energy exchange in the process $\hbar\omega = E_i - E_f$ in a $d\omega$ interval for unit time ($\hbar\omega$ comes from any combination of suitable \mathbf{k}_i and \mathbf{k}_f). The first term on the right side of the equation is the double differential cross-section to scatter neutrons in a solid angle $d\Omega$ with energy exchange $\hbar\omega$ in $\hbar d\omega$ interval; the second term is the number of incident neutrons for unit area and time that is equal to $\frac{N}{\tilde{V}} v_i$ (\tilde{V} = volume and $v_i = \frac{k_i}{m}$ velocity of the incident neutron) obtaining

$$\frac{d^3 N}{\hbar d\omega d\Omega dt} = \frac{N}{\tilde{V}} \frac{k_i}{m} \frac{d^2 \sigma}{\hbar d\omega d\Omega}. \quad (2.8)$$

The left side term of the equation represents the number of neutrons that pass from $|k_i\rangle$ to $|k_f\rangle$ with $\hbar\omega$ corresponding to the energy exchange. Dividing this term by N we get the probability of transition from i to f state for one particle

$$W_{fi} = \frac{d^3 N}{\hbar d\omega d\Omega dt} \frac{1}{N}. \quad (2.9)$$

This probability can be calculated using the Fermi's golden rule [29] (time-dependent perturbation theory). In this case, we can describe our system composed by the neutron and scattering centre with the Hamiltonian

$$H = H_0 + V(t), \quad (2.10)$$

where H_0 is the unperturbed Hamiltonian and $V(t)$ is the interaction potential probe-target that is turned on when they interact.

$$V(t) = \begin{cases} 0 & t \leq 0 \\ V & t > 0 \end{cases}$$

The interaction takes place when the neutron feels the nuclear field of atoms which compose the sample. The interaction time is $\sim 10^{-18} s$, being associated with the residual strong interaction. With this preliminaries using the Fermi's golden rule

$$W_{fi} = \frac{2\pi}{\hbar} |\langle \psi_f | V | \psi_i \rangle|^2 \delta(\hbar\omega - \hbar\omega_{fi}), \quad (2.11)$$

where $\hbar\omega_{fi}$ is the energy exchanged in the process, $|\psi_i\rangle$ and $|\psi_f\rangle$ are the asymptotic state of the total system (sample-probe) that can be decoupled in the product of the sample and probe state

$$\begin{aligned} |\psi_i\rangle &= |i, k_i\rangle = |i\rangle |k_i\rangle \\ |\psi_f\rangle &= |f, k_f\rangle = |f\rangle |k_f\rangle. \end{aligned}$$

In order to obtain an expression for W_{fi} , Fermi assumed that the interaction potential was not dependent upon the scattering angle and strictly localized. Fermi introduced a pseudopotential of the form

$$V = \sum_j v(\mathbf{R} - \mathbf{R}_j) = \frac{2\pi\hbar^2}{m} b \sum_j \delta(\mathbf{R} - \mathbf{R}_j), \quad (2.12)$$

where j runs over the j -nucleus, b is the scattering length (the dimension of the nucleus seen by the neutron), m is the neutron mass, the delta function express the localization of the target and $R_j(t) = R_j + u_j(t)$ the position of the nucleus at the time t displaced from the equilibrium position R_j by a quantity $u_j(t)$. Using Eq. 2.8 and Eq. 2.9 we get

$$W_{fi} \frac{m\tilde{V}}{k_i} = \frac{d^2\sigma}{\hbar d\omega d\Omega}. \quad (2.13)$$

In this expression we can substitute W_{fi} in Eq. 2.11 with the Fermi's pseudopotential and asymptotic states obtaining

$$\begin{aligned} W_{fi} &= \frac{2\pi}{\hbar} |\langle f, k_f | V | i, k_i \rangle|^2 \delta(\hbar\omega - \hbar\omega_{fi}) = \\ & \frac{2\pi}{\hbar} \left| \frac{2\pi\hbar^2}{m} \frac{b}{\tilde{V}} \langle f | \sum_j \int d\mathbf{R} \delta(\mathbf{R} - \mathbf{R}_j) e^{i\mathbf{k}_i \cdot \mathbf{R}} e^{-i\mathbf{k}_f \cdot \mathbf{R}} | i \rangle \right|^2 \delta(\hbar\omega - \hbar\omega_{fi}) = \\ & = \frac{2\pi}{\hbar} \left| \frac{2\pi\hbar^2}{m} \frac{b}{\tilde{V}} \langle f | \sum_j e^{i\mathbf{Q} \cdot \mathbf{R}_j} | i \rangle \right|^2 \delta(\hbar\omega - \hbar\omega_{fi}). \end{aligned} \quad (2.14)$$

To get the complete expression, for each k_i , we have to consider all the possible final states of neutron and sample after the scattering and all the possible initial states of the sample. First we can consider the density of states of neutrons after the scattering process as the ratio between the d^3k_f volume and the smallest k_f^3 change $\frac{\tilde{V}}{(2\pi)^3}$ (as in the case of a particle in a box)

$$dn = \frac{\tilde{V}}{(2\pi)^3} d^3k_f = \frac{\tilde{V}}{(2\pi)^3} k_f^2 dk_f d\Omega. \quad (2.15)$$

Because of the relation

$$\hbar\omega_f = \frac{\hbar^2 k_f^2}{2m} \rightarrow \hbar d\omega_f = \frac{\hbar^2 k_f}{m} dk_f$$

we get

$$dn = \frac{\tilde{V}}{(2\pi)^3} \frac{m}{\hbar} k_f d\omega_f d\Omega \rightarrow \frac{d^2n}{\hbar d\omega_f d\Omega} = \frac{\tilde{V}}{(2\pi)^3} \frac{k_f}{\hbar^2} m. \quad (2.16)$$

Multiplying Eq. 2.14 with 2.16, summing on the final states of sample and averaging on the initial state of sample and using Eq. 2.13 we obtain an expression for the double differential cross section called master equation for neutron scattering

$$\frac{d^2\sigma}{\hbar d\omega d\Omega} = \hbar \frac{k_f}{k_i} b^2 \sum_{|i\rangle} \hat{P}_{|i\rangle} \sum_{\langle f|} |\langle f | \rho_Q | i \rangle|^2 \delta(\hbar\omega - \hbar\omega_{fi}), \quad (2.17)$$

where $\rho_Q = \sum_{j=1}^N e^{i\mathbf{Q} \cdot \mathbf{R}_j}$ is the density operator $\hat{P}_{|i\rangle}$ is the probability of the sample to be in a initial state i . Now we can use the integral expression for the delta function

$$\delta(\hbar\omega) = \frac{1}{2\pi\hbar} \int_{-\infty}^{\infty} dt e^{i\omega t}$$

obtaining

$$\frac{d^2\sigma}{\hbar d\omega d\Omega} = \frac{k_f}{k_i} \frac{b^2}{2\pi} \sum_{|i\rangle} \hat{P}_{|i\rangle} \sum_{\langle f|} \int_{-\infty}^{\infty} dt e^{i\omega t} e^{-i(\omega_i - \omega_f)t} |\langle f | \rho_Q | i \rangle|^2. \quad (2.18)$$

For the energy conservation

$$E_0 + \hbar\omega_i = E_1 + \hbar\omega_f \rightarrow \hbar(\omega_i - \omega_f) = E_1 - E_0,$$

where E_0 and E_1 are the initial and final energies of the sample described by the Hamiltonian H_{target} with

$$\begin{aligned} H_{target} |i\rangle &= E_0 |i\rangle \\ H_{target} |f\rangle &= E_1 |f\rangle. \end{aligned}$$

Using these relations we can rewrite

$$e^{\frac{i}{\hbar}(E_0 - E_1)t} |\langle f | \rho_Q | i \rangle|^2 = \langle i | \rho_{-Q} | f \rangle \langle f | e^{\frac{i}{\hbar} H_{target} t} \rho_Q e^{-\frac{i}{\hbar} H_{target} t} | i \rangle = \langle i | \rho_{-Q}(0) | f \rangle \langle f | \rho_Q(t) | i \rangle \quad (2.19)$$

where we have used the Heisenberg representation for the density operator in the last step. In this way the Eq. 2.18 become

$$\frac{d^2\sigma}{\hbar d\omega d\Omega} = \frac{k_f}{k_i} \frac{b^2}{2\pi} \int_{-\infty}^{\infty} dt \sum_{|i\rangle} \hat{P}_{|i\rangle} \langle i | \rho_{-Q}(0) \rho_Q(t) | i \rangle e^{i\omega t}. \quad (2.20)$$

This expression can be written introducing the dynamical structure factor $S(\mathbf{Q}, \omega)$

$$\frac{d^2\sigma}{\hbar d\omega d\Omega} = \frac{k_f}{k_i} b^2 S(\mathbf{Q}, \omega). \quad (2.21)$$

Hereafter, we will take into account the dynamical structure factor keeping in mind the relation with the cross section. Up to now we have considered b , the scattering length, as constant in the sample but it is not the most general case; when the scattering length is different for different scattering centre (different element, spin or isotopes) we obtain for $S(\mathbf{Q}, \omega)$

$$S(\mathbf{Q}, \omega) = \langle b^2 \rangle S_S(\mathbf{Q}, \omega) + \langle b \rangle^2 S_D(\mathbf{Q}, \omega), \quad (2.22)$$

where the first term gives the contribution due to the self correlation of a nucleus at time 0 and t and the second term gives the contribution of the correlation between one nucleus at time 0 with another nucleus at time t . Rewriting Eq. 2.22 introducing S_{S+D} we get

$$S(\mathbf{Q}, \omega) = \langle b \rangle^2 S(\mathbf{Q}, \omega)_{S+D} + [\langle b^2 \rangle - \langle b \rangle^2] S(\mathbf{Q}, \omega)_S, \quad (2.23)$$

where $S(\mathbf{Q}, \omega)_{S+D}$ is the coherent term from self and distinct correlation and $S(\mathbf{Q}, \omega)_S$ is the incoherent term only from self correlation.

We can see from Eq. 2.23 that in general for a certain \mathbf{Q} one has a coherent and incoherent scattering which are profoundly different. In the coherent scattering there is an interference between the waves scattered. In the incoherent scattering there is no interference at all. Physically we can think of the coherent and incoherent scattering as follows: because the scattering length varies from one isotope to another, the neutron is not affected by a uniform scattering potential but the scattering varies from one point to the next. It is only the average scattering potential that can give interference effect; this average scattering potential is proportional to $\langle b \rangle$ and hence the coherent scattering cross-section is proportional to $\langle b \rangle^2$. The deviations from the average potential are randomly distributed and therefore

cannot give interference effects; they therefore give incoherent scattering proportional to the mean square deviation (deviation from the average $\langle b \rangle$, i.e. to $\langle (b - \langle b \rangle)^2 \rangle = [\langle b^2 \rangle - \langle b \rangle^2]$). These correlations describe atomic motions that are a function of the interatomic forces present in the material structure.

Introducing the coherent and incoherent cross sections, σ_{coh} and σ_{incoh} Eq. 2.23 can be written as [30]:

$$\frac{d^2\sigma}{\hbar d\omega d\Omega} = \frac{1}{4\pi} \frac{k_f}{k_i} [\sigma_{coh} S_{S+D}(\mathbf{Q}, \omega) + \sigma_{incoh} S_S(\mathbf{Q}, \omega)]. \quad (2.24)$$

For hydrogenous materials the contribution of S_D to the integrated scattering cross section is negligible. Applying this approximation ($S_D = 0$), we can rewrite $S(\mathbf{Q}, \omega) \simeq S_S(\mathbf{Q}, \omega)$. The absence of interference in incoherent scattering and the neglect of interference in coherent inelastic scattering allows us to construct the *incoherent approximation*, and it allows Eq. 2.24 to be rewritten as

$$\frac{d^2\sigma}{\hbar d\omega d\Omega} = \frac{1}{4\pi} \frac{k_f}{k_i} [\sigma_{coh} S_S(\mathbf{Q}, \omega) + \sigma_{incoh} S_S(\mathbf{Q}, \omega)] \quad (2.25)$$

$$= \frac{\sigma_b}{4\pi} \frac{k_f}{k_i} S_S(\mathbf{Q}, \omega), \quad (2.26)$$

$$(2.27)$$

where the bound cross section is given by

$$\sigma_b = (\sigma_{coh} + \sigma_{inc}). \quad (2.28)$$

2.2 Elastic Scattering

As $S(\mathbf{Q}, \omega)$ describes the response to the neutron interaction we can divide the interaction into elastic and inelastic. The elastic interaction is characterised by an energy exchange equal to zero and hence a peak in the $S(\mathbf{Q}, \omega)$ centred at $\hbar\omega = 0$. The elastic line is then broadened by the nuclear motion. The motion of nuclei inside a crystal or a molecule can be described by the vibrational density of states $g(\omega)$ which gives the probability of finding a nucleus vibrating with a frequency ω . As an example a molecule with N nuclei has a $N_v = 3N$ degrees of freedom composed by 3 translations, 3 rotations, and $3N-6$ internal vibrations; in the case of water a symmetric stretching, an asymmetric stretching and a bending modes [31]. If we consider a discrete oscillator for each j -nucleus

$$g_j(\omega) = \sum_v \delta(\omega - \omega_v) |\vec{e}_{v,j}|^2 \quad (2.29)$$

where $|\vec{e}_{v,j}|^2$ quantifies the contribution from the j nucleus to the v vibration. For each vibration

$$\sum_j |\vec{e}_{v,j}|^2 = 1 \quad (2.30)$$

and

$$\int_0^\infty g(\omega) d\omega = N_v. \quad (2.31)$$

To find the expression of the elastic incoherent cross section we can rewrite Eq. 2.20 as

$$\frac{d^2\sigma}{\hbar d\omega d\Omega} = \frac{k_f}{k_i} \frac{b^2}{2\pi\hbar} \int_{-\infty}^{\infty} dt I(\mathbf{Q}, t) e^{i\omega t} = \frac{k_f}{k_i} \frac{b^2}{2\pi} \int_{-\infty}^{\infty} dt \langle e^U e^V \rangle e^{i\omega t} \quad (2.32)$$

where $I(\mathbf{Q}, t)$ is the intermediate scattering function, *i.e.* the Fourier transform of $S(\mathbf{Q}, \omega)$, the $\langle \dots \rangle$ is average over the state of the sample and

$$U = -i\mathbf{Q} \cdot \mathbf{u}(0) \quad (2.33)$$

$$V = i\mathbf{Q} \cdot \mathbf{u}(t) \quad (2.34)$$

It can be show that [32] Eq. 2.32 becomes

$$\frac{d^2\sigma}{\hbar d\omega d\Omega} = \frac{k_f}{k_i} \frac{b^2}{2\pi} e^{\langle U^2 \rangle} \int_{-\infty}^{\infty} dt e^{\langle UV \rangle} e^{i\omega t}. \quad (2.35)$$

The term $e^{\langle UV \rangle}$ can be expanded with the so-called phonon expansion as

$$e^{\langle UV \rangle} = 1 + \langle UV \rangle + \frac{1}{2!} \langle UV \rangle^2 + \dots \quad (2.36)$$

The first term gives the elastic cross-section, the second term when one phonon is exited and so on.

2.2.1 Debye-Waller factor

The contribution to the elastic cross section from the nuclear vibrations is associated to the Debye-Waller factor that is the $\langle U^2 \rangle$ in the first term of the phonon expansion, Eq. 2.36. In harmonic crystals, where the displacements are small compared to atomic distances, it can be expressed as

$$2W_j = -\langle U^2 \rangle = \frac{\hbar}{2M_j} \sum_v \frac{(\mathbf{Q} \cdot \vec{e}_{v,j})^2}{\omega_v} \langle 2n_v + 1 \rangle, \quad (2.37)$$

where the subscript v stands for the vibration, n_v is the occupation operator, ω_v is the frequency of mode v , $\vec{e}_{v,j}$ is its polarisation vector and M_j is the nuclear mass. In a cubic Bravais crystal if, for the same polarisation branch, ω_v remains the same in the three directions for each v , and the mean value of $(\mathbf{Q} \cdot \vec{e}_{v,j})^2$ is $\frac{1}{3}Q^2$. Using also that $\langle 2n_v + 1 \rangle = \coth\left(\frac{\hbar\omega_v}{2k_B T}\right)$, the Eq. 2.37 can be simplified as

$$2W_j = \frac{\hbar}{2M_j} \frac{Q^2}{3} \sum_v \frac{1}{\omega_v} \coth\left(\frac{\hbar\omega_v}{2k_B T}\right). \quad (2.38)$$

Since, for a cubic crystal, the Debye-Waller factor depends only on the frequencies of the normal modes, it can be expressed in terms of the vibrational density of states $g(\omega)$ Therefore

$$2W_j = \frac{\hbar}{2M_j} \frac{Q^2}{3} \sum_v \frac{1}{\omega_v} \coth\left(\frac{\hbar\omega_v}{2k_B T}\right) = \frac{\hbar}{2M_j} \frac{Q^2}{3} \int_0^{\omega_{max}} \frac{g_j(\omega)}{\omega} \coth\left(\frac{\hbar\omega}{2k_B T}\right) \quad (2.39)$$

$$= \frac{\hbar Q^2}{6M_j} \int_0^{\omega_{max}} \frac{g_j(\omega)}{\omega} \coth\left(\frac{\hbar\omega}{2k_B T}\right) d\omega. \quad (2.40)$$

In the Eq. 2.40 we can identify the term

$$\langle u^2 \rangle_j = \frac{\hbar}{2M_j} \int_0^{\omega_{max}} \frac{g_j(\omega)}{\omega} \coth \left(\frac{\hbar\omega}{2k_B T} \right) d\omega \quad (2.41)$$

that is the Mean Square Displacement (MSD) of the j -nucleus around the equilibrium position. In case of an isotropic system $g_j(\omega)$ is three times the projection on the α -Cartesian axes. In this work a measurement of the MSD has been performed on the IRIS spectrometer [33] at ISIS with a QENS experiment on four ice phases, ice II, VI, IX and stacking disordered (sd). The QENS spectra are composed by the measurement of the elastic peak and how it is broadened. In experiment where crystal are put inside the beam just the Debye-Waller factor broadens the elastic peak but when liquids are measured the elastic peak is broadened even more as the diffusion of the molecules becomes important.

2.3 Inelastic Neutron Scattering

The second term of the phonon expansion of Eq. 2.36 describes the inelastic scattering processes where one phonon is excited. If we consider the nuclei all connected with springs in a harmonic approximation, this processes brings the nucleus from an energetic level n to $n + 1$. The expression of the differential cross-section becomes

$$\left(\frac{d^2\sigma}{\hbar d\omega d\Omega} \right) = \frac{\sigma_b k_f Q^2}{4\pi k_i 4M} e^{-2W} \frac{g_j(\omega)}{\omega} \left[\coth \left(\frac{\hbar\omega}{2k_B T} \right) + 1 \right], \quad (2.42)$$

proportional to the first order contribution to the INS spectra. The INS experiments analysed in this work, data take from literature, are performed at the TOSCA spectrometer [34] at ISIS where a wide range of energy transfer $\hbar\omega$ is available. The INS can be considered as a resonant technique as the incident neutron excite a phonon of a certain energy, in fact, the spectra are composed of a collection of peaks centred at the molecule/crystal vibration. The frequency, ω_v can be seen as the eigenvalues of the dynamics and $|\vec{e}_j|^2$ the contribution of each atom. The INS scattering will be fundamental in this work for the interpretation of the QENS experiments on Ice and will be extremely important to relate the results with DINS experiments.

2.4 Deep Inelastic Neutron Scattering

We can consider now a particular case of the neutron scattering, the Deep Inelastic Neutron Scattering (DINS). It is similar to the Compton effect, observed for X-rays, but using neutrons. In fact in the Compton effect a photon with high energy impinges on a bound electron; the energy of the photon is so high that after the scattering the electron has a free recoil. This event is sensitive to the momentum of the electron before the scattering. We can imagine to do the same thing using neutrons instead of photons and nuclei instead of electrons. The recoil energy is

$$\hbar\omega_r = \frac{\hbar^2 Q^2}{2M} \quad (2.43)$$

where M is the mass of the struck atom. It is obvious that for smaller masses (hydrogen for example) the recoil energy is higher.

We can now specialize Eq. 2.21 for the DINS case. In fact, when the energy of the incident neutron is higher than any characteristic energy of excitations in the sample, we can apply the Impulse Approximation (IA) [35] and think that all the terms of the phonon expansion are taken into account [36]. This implies that the force exerted on the nuclei can be neglected and its position vector can be approximated by

$$\mathbf{R}(t) \sim \mathbf{R}(0) + \frac{t}{M}\mathbf{p} \quad (2.44)$$

with \mathbf{p} is the nuclear momentum before the scattering process. This approximation is motivated by the fact that energetic neutrons spend a little time in the sample and the nucleus can move freely without any interaction with its neighbours. In this case we are studying the vibration of atoms at the bottom of the interatomic potential, with a very small characteristic length ($< \text{\AA}$). In this way we get an expression for the dynamical structure factor considering only one nuclear mass [36, 3]

$$S(\mathbf{Q}, \omega)_{IA} = \hbar \int_{-\infty}^{\infty} d\mathbf{p} n(\mathbf{p}) \delta(\hbar\omega - \frac{\hbar^2 Q^2}{2M} - \frac{\hbar}{M} \mathbf{Q} \cdot \mathbf{p}) \quad (2.45)$$

where $n(\mathbf{p})$ is the momentum distribution function of nuclei in the sample. In fact the most important DINS application is the measurement of the probability distribution of the nuclear momentum.

The momentum distribution is weighting $S(\mathbf{Q}, \omega)$ obtaining a peak centred at the recoil energy but broadened by the momentum distribution which is one of the most straightforward observable in DINS experiments. A consequence is that our measurement should be precise not only to for the peak position but also for its line shape.

The information obtained has a very important physical meaning as DINS [1, 3] is a direct experimental technique to probe the local nuclear dynamics of atoms in materials [2] and can be directly compared to state-of-the-art computer simulations assessing the importance of nuclear quantum effects (*e.g.*, Refs. [37, 38, 39]) and phenomenological modelling (*e.g.*, Refs. [40, 41]). In fact, as the nuclear momentum is measured, we can calculate the mean kinetic energy as:

$$\langle E_k \rangle = \frac{3}{2M} \int p^2 n(p) dp, \quad (2.46)$$

in case of an isotropic nuclear potential where the nuclear kinetic energy is the same in all the directions. In other words DINS experiments can be seen as a moving billiard game (see Fig. 2.4). In fact, we can think that the white ball is the neutron and the moving coloured balls are the nuclei: studying the scattering between the white ball and the moving coloured balls we can have information of the momentum distribution of the coloured balls before the scattering; in the same way studying the scattering between neutron and nuclei we can go back to the nuclear momentum distribution.

In the IA, the scattering variables, \mathbf{Q} and E are coupled by introducing the *West-scaling* variable [42], which is a measure of the atomic momentum component along the direction of \mathbf{Q}

$$y = \frac{1}{\hbar} \mathbf{p} \cdot \hat{\mathbf{Q}}. \quad (2.47)$$

The new variable y is the momentum \mathbf{p} of the nucleus in the initial state projected onto the scattering vector \mathbf{Q} and $\hat{\mathbf{Q}}$ is a unit vector in the direction of the momentum transfer.

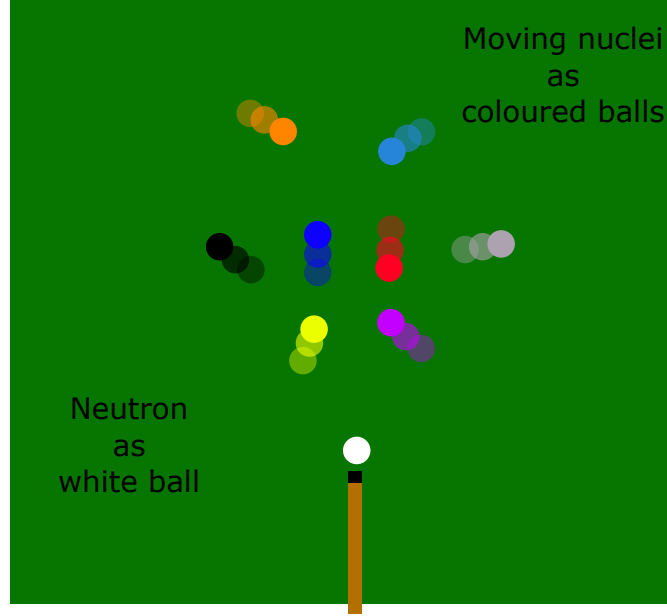


Figure 2.4: DINS as a billiard game.

Therefore, the dynamic structure factor can be rewritten in terms of the new variable via

$$S_{IA}(\mathbf{Q}, \omega) = \frac{M}{\hbar Q} J_{IA}(y, \hat{\mathbf{Q}}), \quad (2.48)$$

the function $J_{IA}(y, \hat{\mathbf{Q}})$ is called Neutron Compton Profile (NCP)

$$J_{IA}(y, \hat{\mathbf{Q}}) = \hbar \int d\mathbf{p} n(\mathbf{p}) \delta(\hbar y - \mathbf{p} \cdot \hat{\mathbf{Q}}). \quad (2.49)$$

It gives the probability that an atom has a momentum of magnitude between $\hbar y$ and $\hbar(y + dy)$ related to the mean kinetic energy as

$$\langle E_k \rangle = \frac{3\hbar^2}{2M} \int y^2 J(y) dy = \frac{3\hbar^2 \sigma^2}{2M}, \quad (2.50)$$

where σ^2 is the NCP second moment. The NCP connects momentum and energy exchanged in the process; in this way we have obtained a quantity independent on the magnitude of \mathbf{Q} which gives information on the nuclear momentum distribution centred in $y = 0$ for any \mathbf{Q} exchanged; it is important because we will be able to sum spectra were different \mathbf{Q} value are involved.

The deviations from the IA is a consequence of the residual force that the nucleus feels after the interaction, those effects are called Final State Effects (FSEs) [1]. The FSEs make the NCP dependent on the \mathbf{Q} not just the $\hat{\mathbf{Q}}$. The effect of the deviation from the IA can be explicated with a power series of $1/Q$, in the isotropic case [43]

$$J(y, Q) = J(y) - \frac{A_3}{Q} \frac{d^3}{dy^3} J(y) + \frac{A_4}{Q^2} \frac{d^4}{dy^4} J(y). \quad (2.51)$$

The VESUVIO spectrometer is the flagship instrument for DINS measurements and it will be described in detail in Sec. 3.3. The experimental NCP, $F(y, Q)$, is affected by the

instrument resolution as well as the FSEs. If we focus on a specific scattering angle $F(y, Q)$ can be expressed as:

$$F(y, Q) = [J(y) + \Delta J(y, Q)] \star R(y, Q), \quad (2.52)$$

where $\Delta J(y, Q)$ is the deviation from the IA, and $\star R(y, Q)$ is the convolution with the instrument resolution function at a fixed angle. When all the scattering angles are taken into account we can refer to $\overline{F}(y, Q)$ as the average over all the scattering angles and hence over all the Q . The scattering-angle average is performed as most of the time the experiments are performed with powder samples and, moreover, the results from the detectors, placed at different scattering angles, are summed.

2.4.1 Mean Force

Recently, the Mean Force (MF) approach has been used to analyse DINS data [44, 45, 46] as it provides a model-independent and non-parametric tool to highlight differences in systems with various degrees of anharmonicity and anisotropy. The experimental MF function is defined for amorphous or polycrystalline samples as

$$f(x_{\parallel}) = -\frac{Mx_{\parallel}}{\beta^2\hbar^2} + \frac{1}{\beta} \frac{\int_0^{\infty} y \sin(x_{\parallel}y) \overline{F}(y) dy}{\int_0^{\infty} \cos(x_{\parallel}y) \overline{F}(y) dy}, \quad (2.53)$$

where $\overline{F}(y)$ for brevity stands for $\overline{F}(y, Q)$, x_{\parallel} is the projection of the spatial coordinate (displacement) along the direction of the momentum transfer, $\beta = 1/k_B T$, T is the thermodynamic temperature, k_B the Boltzmann's constant [45].

The MF is an extension of the Hooke's law applied to atomic displacements in the sub-nanometer scale, representing the force exerted on an atom in a molecular system, as a function of the displacement from the equilibrium position, and averaged along the Cartesian directions. In fact, a linear relation between the force and the displacement holds for harmonic and isotropic potentials for which one can write $f(x_{\parallel}) = (-\frac{1}{\beta} + \frac{2\langle E_k \rangle}{3}) \frac{M}{\beta\hbar^2} x_{\parallel}$. The DINS technique allows an experimental determination of the mean force and, in the present case, deviations from linearity between displacement and force provide quantitative information on the anisotropy of the effective local potential exerted on hydrogen atoms. Furthermore, in the isotropic case, the MF slope is proportional to the mean kinetic energy.

2.5 The Anisotropic case

For a system where an isotropic and harmonic potential is exerted on the nucleus the general form of the NCP is a simple Gaussian:

$$J(y) = \frac{1}{\sqrt{2\pi}\sigma} e^{-\frac{y^2}{2\sigma^2}}. \quad (2.54)$$

When the hydrogen local potential is not isotropic [44, 47, 48, 49, 50, 51], as well as for heavier elements [52, 53, 54, 55], for each of the α -Cartesian direction the nuclear energy is different, hence $J(y)$ is a multivariate Gaussian function and Eq. 2.50 becomes [56, 57, 58, 59]

$$\langle E_k \rangle_{j,\alpha} = \frac{\hbar^2 \sigma_{j,\alpha}^2}{2M_j}, \quad (2.55)$$

with $\sigma_{j,\alpha}^2$ the NCP second momentum in $p_{j,\alpha}$ and $\langle E_k \rangle_\alpha$ the average over the nuclei in the molecule. In this case the total mean kinetic energy is:

$$\langle E_k \rangle = \langle E_k \rangle_x + \langle E_k \rangle_y + \langle E_k \rangle_z. \quad (2.56)$$

Furthermore, in the case of powder samples, used in this work, $J(y)$ is spherically averaged and information about $\hat{\mathbf{Q}}$ is lost. All the deviations from a Gaussian of the NCP, and hence to a purely isotropic potential, can be taken into account with a Gauss-Hermite expansion [43]:

$$J(y) = \frac{1}{\sqrt{2\pi}\sigma} e^{-\frac{y^2}{2\sigma^2}} \sum_n \frac{c_{2n}}{2^{2n}n!} H_{2n}\left(\frac{y}{\sqrt{2}\sigma}\right), \quad (2.57)$$

where $\sigma^2 = \frac{\sigma_x^2 + \sigma_y^2 + \sigma_z^2}{3}$. The leading Gaussian term in Eq. 2.57 represents the NCP in a harmonic and isotropic local potential while the coefficients c_{2n} and the Hermite polynomials H_{2n} represent correction terms due to the anisotropy and anharmonicity of the system where the first and second term are $c_0 = 1$ and $c_2 = 0$ to reproduce the $J(y)$ normalization to unity, being a density probability function, and to reproduce the second moment as the standard deviation of the distribution [60]. In this work the anharmonicity will not be taken into account and the most general case will be a Three-Dimensional (anisotropic) Harmonic Oscillator (TDHO). In this case $J(y)$ is a spherically averaged Gaussian function that, once compared with Eq. 2.57, gives the most important term c_4 and c_6 as

$$c_4 = \frac{2}{5} \left(3 \frac{\sum_\alpha \langle E_k \rangle_\alpha^2}{\langle E_k \rangle^2} - 1 \right) \quad (2.58)$$

$$c_6 = \frac{8}{35} \left(3 \frac{\sum_\alpha \langle E_k \rangle_\alpha^3 + 6 \prod_\alpha \langle E_k \rangle_\alpha}{\langle E_k \rangle^3} - 1 \right), \quad (2.59)$$

where $\frac{\sum_\alpha \langle E_k \rangle_\alpha^2}{\langle E_k \rangle^2}$ is the kurtosis of the distribution and hence the deviation from a Gaussian is a symmetric oscillation around $y = 0$.

In the case of anisotropic distribution Eq. 2.29 2.30 2.31 becomes:

$$g_{j,\alpha}(\omega) = \sum_v \delta(\omega - \omega_v) |\hat{\alpha} \cdot \vec{e}_{v,j}|^2 \quad (2.60)$$

where $|\hat{\alpha} \cdot \vec{e}_{v,j}|^2$ quantifies the contribution from the j nucleus to the v vibration along the α direction. For each vibration

$$\sum_{j\alpha} |\hat{\alpha} \cdot \vec{e}_{v,j}|^2 = 1. \quad (2.61)$$

For anisotropic environment the MSD in each direction α can be calculated with the proper $g_{j\alpha}$, from Eq. 2.41

$$\langle u^2 \rangle_{j,\alpha} = \frac{\hbar}{2M_j} \int_0^{\omega_{max}} \frac{g_{j,\alpha}(\omega)}{\omega} \coth\left(\frac{\hbar\omega}{2k_B T}\right) d\omega \quad (2.62)$$

with $\langle u^2 \rangle = \langle u^2 \rangle_x + \langle u^2 \rangle_y + \langle u^2 \rangle_z$ where the j -index is dropped when the average over the nuclei in the molecule is performed.

2.6 Other neutron interactions

There are other physical phenomena other than the scattering which will be important to explain experimental techniques in the next chapters. In fact, the interactions of the neutron with materials can be classified as scattering or absorption reactions. Related to the scattering we can have Elastic or Inelastic scattering as described in Sec. 2.2, 2.3 and 2.4. In scattering processes change in energy and direction of the incident neutron can occur, but the nucleus is left with the same number of protons and neutrons. On the contrary, for the absorption we have a nuclear reaction which leads to the disappearance of free neutrons and a wide range of radiations emitted or fission can be induced. The different types of interactions are summarized in Fig. 2.5.

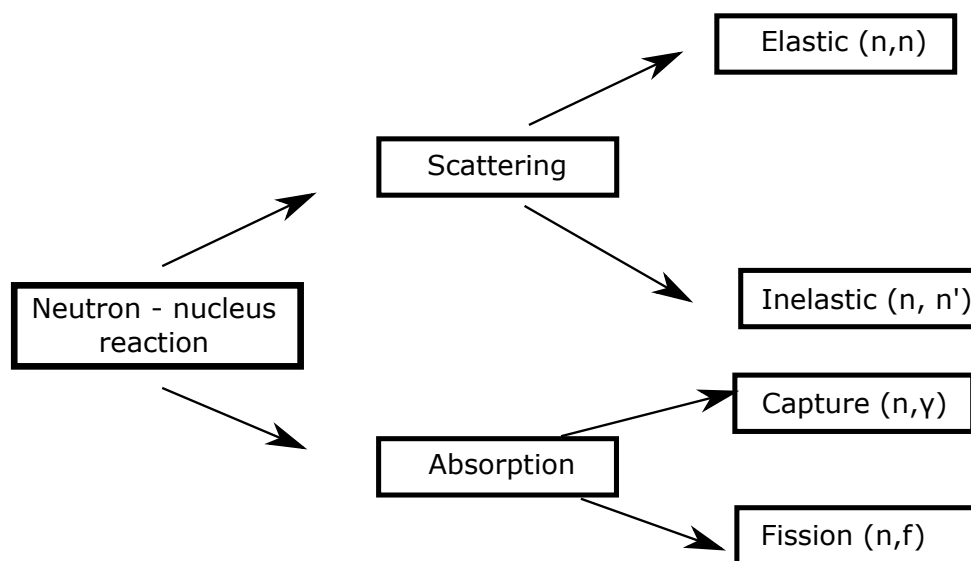
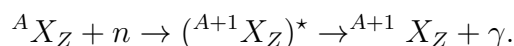


Figure 2.5: Types of interaction between neutron and nucleus.

In particular we are interested in the radiative neutron capture (n, γ) . The absorption of the neutron by a nucleus which ends with an emission of gamma rays within a very short time ($\sim 10^{-14}s$) is called *radiative capture*. The capture reaction can be modelled as the formation and decay of a compound nucleus following the reaction



There are three different regions in the radiative capture cross section showed in Fig. 2.6. For low energy neutrons, before the first capture resonance, the neutron absorption cross section, σ_γ , is approximately $1/v$ where v is the velocity of the neutron. After this region we can find isolated resonances and the radiative cross section assumes the shape of the typical Breit-Wigner resonance [62]. This region of isolated resonances begins in the keV region in medium weighted nuclei, in the MeV region in light nuclei and in the eV region for very heavy non-magnetic nuclei [61]. Finally at higher energies ($\sim MeV$) the resonances start to overlap and it becomes impossible to distinguish them. Moreover, other reactions begin to intervene in competition with the radiative capture for their share of the compound nucleus cross section. The result of this behaviour is a decrease of σ_γ to very low values at high energies.

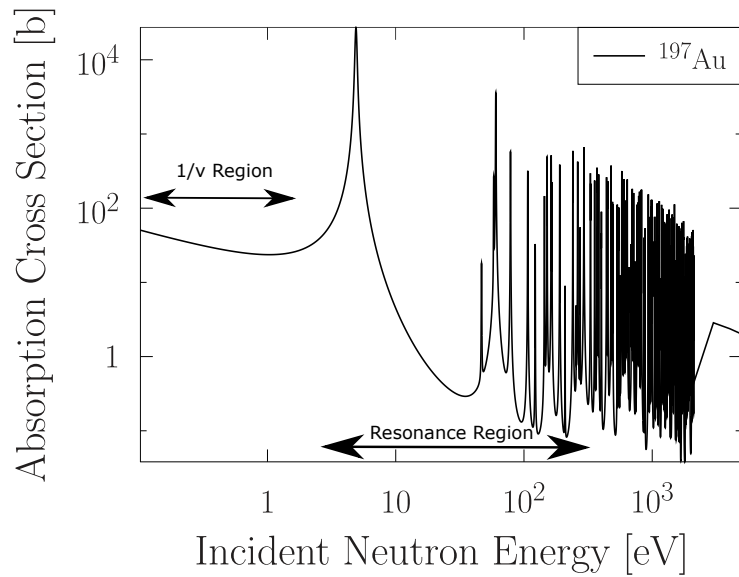


Figure 2.6: Radiative capture cross section of Au as a function of neutron incident energy, data taken from Ref. [61].

After the emission of prompt γ rays the $(A+1)$ isotope is, in most of cases, β unstable; it means an emission of e^- or e^+ with a consequent γ emission if the new element is in an excited configuration (see Fig. 2.7 and 2.8). This delayed emission is completely random in time for the stochastic nature of the process.

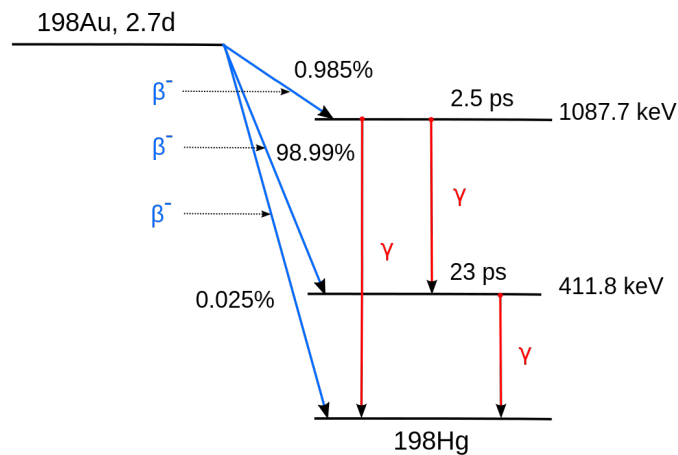


Figure 2.7: Decay scheme of ^{198}Au after the radiative capture of ^{197}Au .

For our instrumentation development purposes it will be used, as we will see, the radiative neutron capture of a gold (^{197}Au) foil which has a large absorption neutron resonance at $4.91 \pm 0.15\text{eV}$.

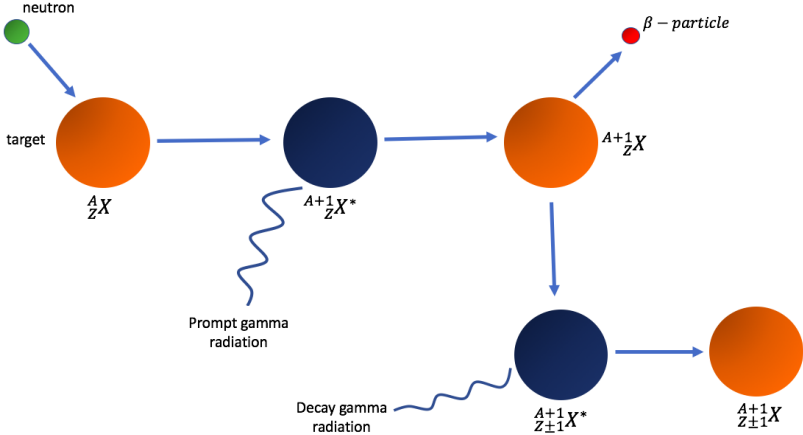


Figure 2.8: Scheme a radiative neutron capture reaction.

Chapter 3

Sources and Instrumentation

3.1 Neutron Sources and Facilities

One might think it is not necessary to have any detailed knowledge of the neutron source in order to use the techniques of neutron scattering. However, the distribution of neutrons from the source in terms of energy and time, and the distribution of “background” (fast neutrons, delayed neutrons, gammas, ...), has a direct effect on the design of neutron scattering instruments and their performance, on how measured “raw” data must be corrected to make them scientifically meaningful, and on the types of measurements that can be undertaken. Even if the average user does not design the instrument, the user needs to choose the source/instrument to be used for a particular experiment or measurement, so some knowledge of the different types of sources is advisable. There are two kinds of neutron sources for neutron scattering :

- reactor sources
- large accelerator-based neutron sources

Nuclear reactors use the fission process to produce neutrons. Most of the current reactor sources for scattering applications were built in the 1960s and 1970s and were primarily designed for materials testing for the nuclear industry, providing medium flux. The best reactor source, optimized for neutron scattering applications, is still the High-Flux Reactor (HFR) at the Institut Laue-Langevin (ILL), built in 1972 in Grenoble, France. Neutrons can also be produced by the spallation process, in which high-energy protons strike a solid target. The development of proton accelerator technology, driven by other applications such as particle physics, helped to increase the potential power and hence the neutron flux of spallation sources. The pulsed nature of most accelerator-based neutron sources can offer a significant advantage in experiments using the Time of Flight (ToF) technique [63, 64], in which the speed of the neutron is measured by timing its flight from the source to the detector. One of the most important pulsed proton-driven neutron sources is the ISIS facility [65], near Oxford, UK. Both fission and spallation produce neutrons in the megaelectron volt energy range. However, neutron scattering and most neutron imaging applications require neutrons at electron volt or lower energies. Moderators are used to slow the neutrons to these energies. The technologies for accelerator-driven sources offer many more parameters that can be varied to optimize the source for different purposes. The neutron experiments, described in the next chapters, were all performed at the Target

Station 1 of the ISIS pulsed neutron and muon source schematically shown in Fig. 3.3. In the pulsed neutron sources a *white* beam is generated and, in order to catch information on the neutron energy before the scattering process, the ToF is used and detailed in the following section.

3.2 Time of Flight technique

The total neutron ToF t is the time that a neutron takes to travel from the moderator to the detector. It can be written as:

$$t = t_0 + \frac{L_0}{v_i} + \frac{L_1}{v_f} \quad (3.1)$$

where t_0 is a fixed electronic time delay, L_0 and L_1 are the incident and scattering flight paths of the instrument, while v_i and v_f are the velocities associated to the initial and final neutron energy, respectively. Figure 3.1 represents a schematic drawing of an instrument that exploits the ToF technique. ToF technique requires the knowledge of L_0 , L_1 and of the initial or the final neutron energy (E_i or E_f) to reconstruct the kinematic of the scattering process.

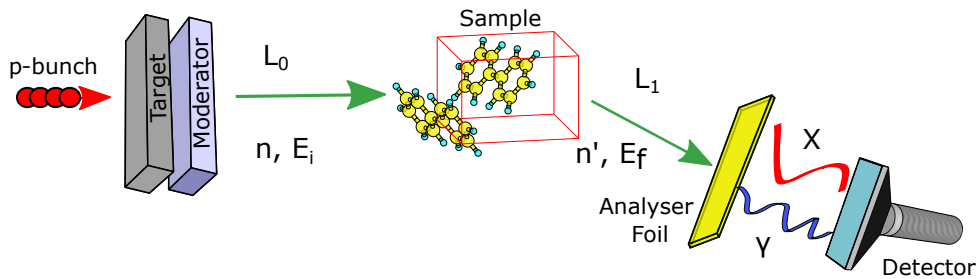


Figure 3.1: Scheme of a ToF spectrometer: L_0 is the primary flight path (moderator-sample distance), L_1 is the secondary flight path (sample-detector distance). The t_{start} and, t_{stop} are provided by the proton beam monitor and the detector, respectively.

By knowing the initial (final) energy, the measurement of the total neutron ToF allows for the measurement of the final (initial) energy. The ToF acquisition chain can briefly be described as follows: before the proton bunch impinges on the heavy metal spallation target, a proton beam monitor, placed close to the target, triggers the opening of a time gate ($t = t_{start}$) of fixed duration $\delta t = 20ms$. During δt the acquisition electronics of the instrument is enabled to process the electric signals provided by the detection system. Every event is stored in a time slot that corresponds to the time difference between the initial time of the gate t_{start} (approximately corresponding to the instant the neutron leaves the moderator) and the detection instant (t_{stop}). A fixed time delay t_0 (see Eq. 3.1) of about $5\mu s$ is electronically provided, a small electronic delay in the reference time signal from the ISIS synchrotron.

A typical DINS-ToF spectrum acquired on VESUVIO is showed in Fig. 3.2, in the specific case there are two recoil peaks (Biphenyl sample $C_{12}H_{10}$) associated with hydrogen (lower ToF) and carbon (higher ToF); the hydrogen peak is at lower ToF because hydrogen is

lighter than carbon and it is more intense because the bound cross section of carbon is smaller than the hydrogen one.

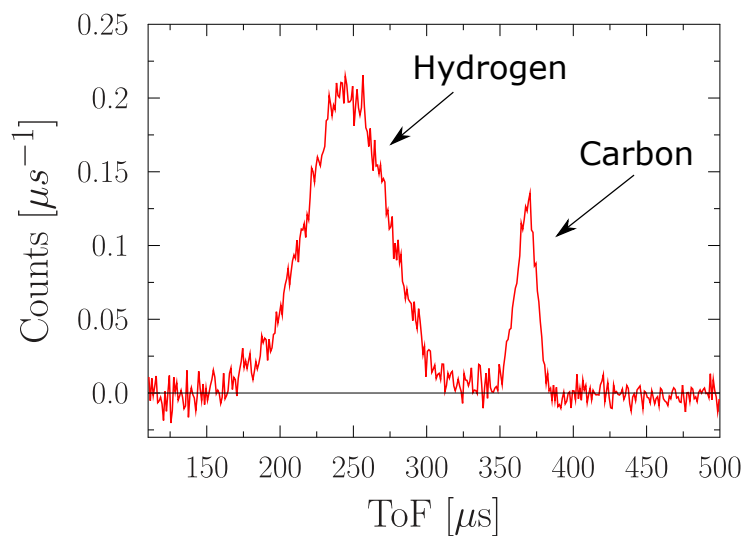


Figure 3.2: Example of ToF spectrum in a DINS experiment for a biphenyl sample.

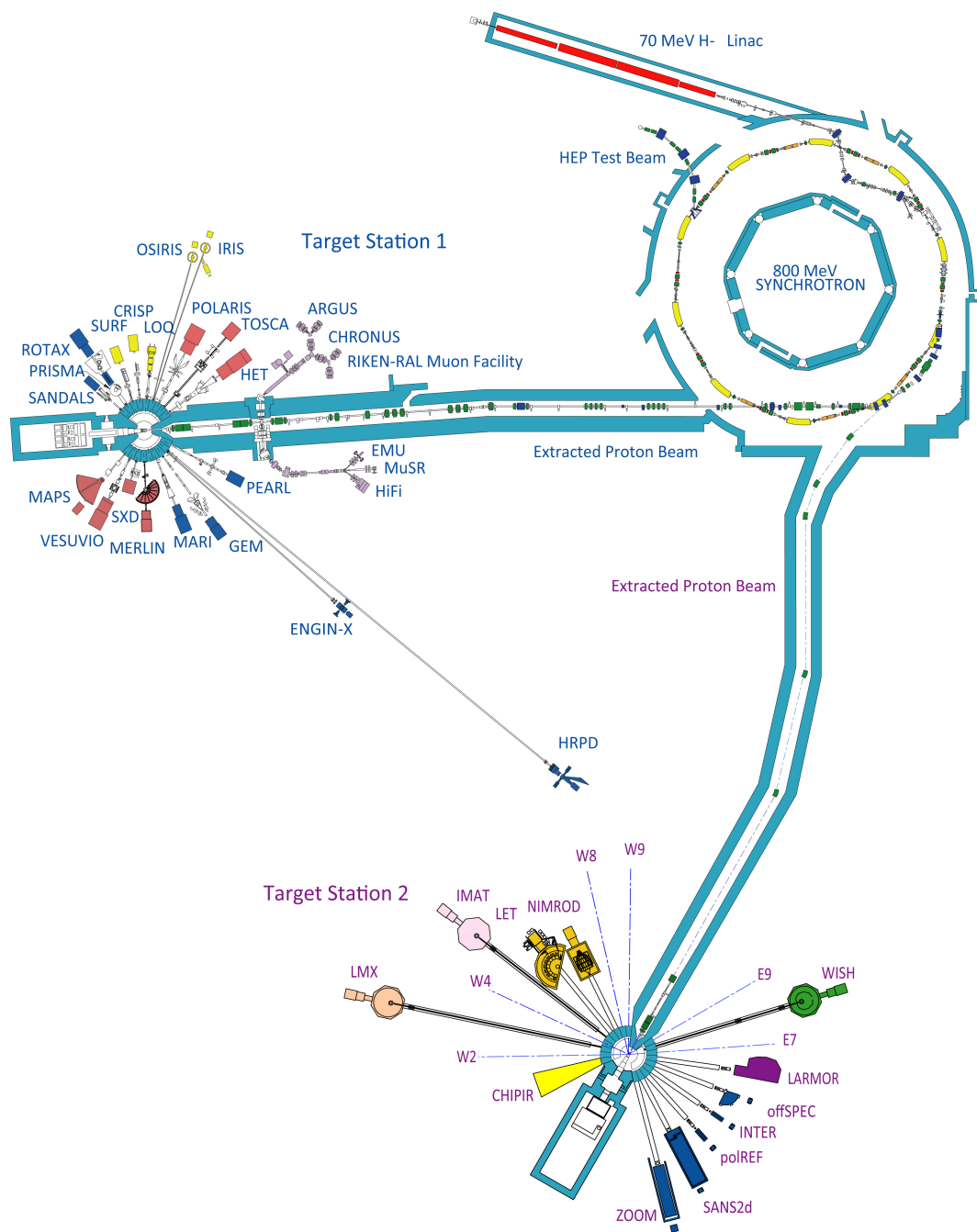


Figure 3.3: Scheme of ISIS target stations, Ref. [65].

3.3 The VESUVIO spectrometer

The novel γ DA, is intended to be installed and operate on the VESUVIO spectrometer. VESUVIO is an inverse geometry neutron spectrometer operating at ISIS spallation source since 2002. VESUVIO makes use of a polychromatic incident neutron beam, resulting from the use of a water moderator at 295 K, characterized by an energy spectrum peaked at about 0.03 eV and with an $E_i^{-0.9}$ tail in the epithermal region shown in Fig. 3.4. With VESUVIO we have access to a region of $(\mathbf{Q}, \hbar\omega)$ kinematic space characterised by high energy ($\hbar\omega \geq 1\text{eV}$) and high wave vector ($Q \geq 30 \text{ \AA}$). To reconstruct the kinematics the initial and final neutron energies have to be calculated. The wave vector, Q , and energy transfer, $\hbar\omega$, can be then obtained by imposing momentum and energy conservation:

$$\mathbf{Q} = \mathbf{k}_i - \mathbf{k}_f, \quad (3.2)$$

$$\hbar\omega = \frac{\hbar^2(k_i^2 - k_f^2)}{2m} = E_i - E_f, \quad (3.3)$$

k_i and k_f being the initial and final neutron wave vectors, and m the neutron mass, respectively. The conservation laws apply rather stringent limitations to the values of \mathbf{Q} and $\hbar\omega$ which may be observed. The relation linking \mathbf{Q} and ω can be found starting from the relation:

$$Q^2 = k_i^2 + k_f^2 - 2k_i k_f \cos\theta \quad (3.4)$$

or in energy units:

$$\frac{\hbar^2 Q^2}{2m} = E_i + E_f - 2\sqrt{E_i E_f} \cos\theta \quad (3.5)$$

In the direct geometry configuration E_i is selected while for an inverse geometry instrument, as VESUVIO, E_f is fixed using monochromators or analysers.

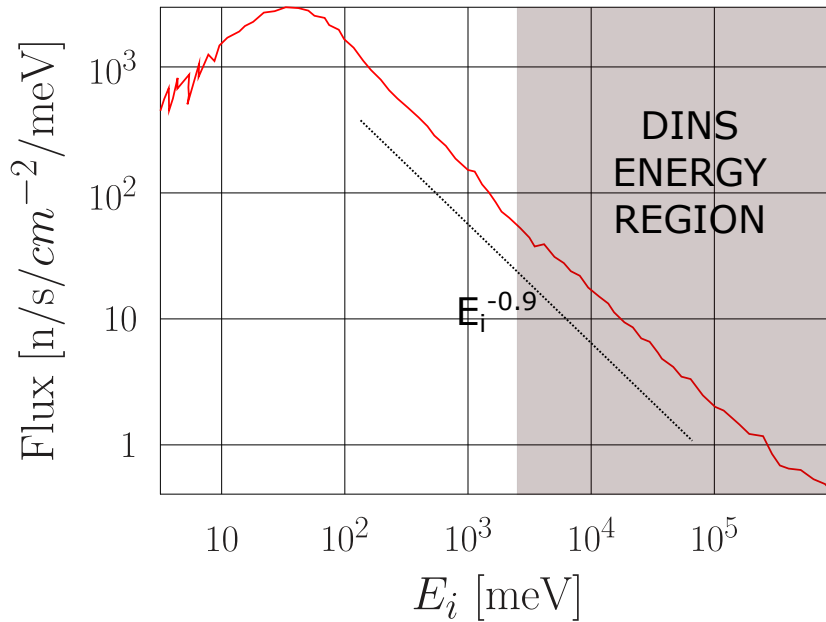


Figure 3.4: Incident neutron flux at the sample position on VESUVIO (red line). The black dashed line is proportional to $E^{-0.9}$ and the shadowed region represents the energy range used in DINS. Data digitalised from Ref. [66].

Geometry configuration	Inverse
Energy analysis method	Nuclear resonance
Neutron detectors	^6Li -glass Cerium activated
γ detectors	YAP Cerium activated
L_0	$\sim 11m$
L_1	$\sim 0.7m$
Forward angular range	30° - 70°
Backward angular range	120° - 170°

Table 3.1: General characteristics of the VESUVIO spectrometer.

The main instrumental parameters of the spectrometer are listed in Table 3.1, while Figure 3.5 represents a schematic drawings of VESUVIO from a top and side views.

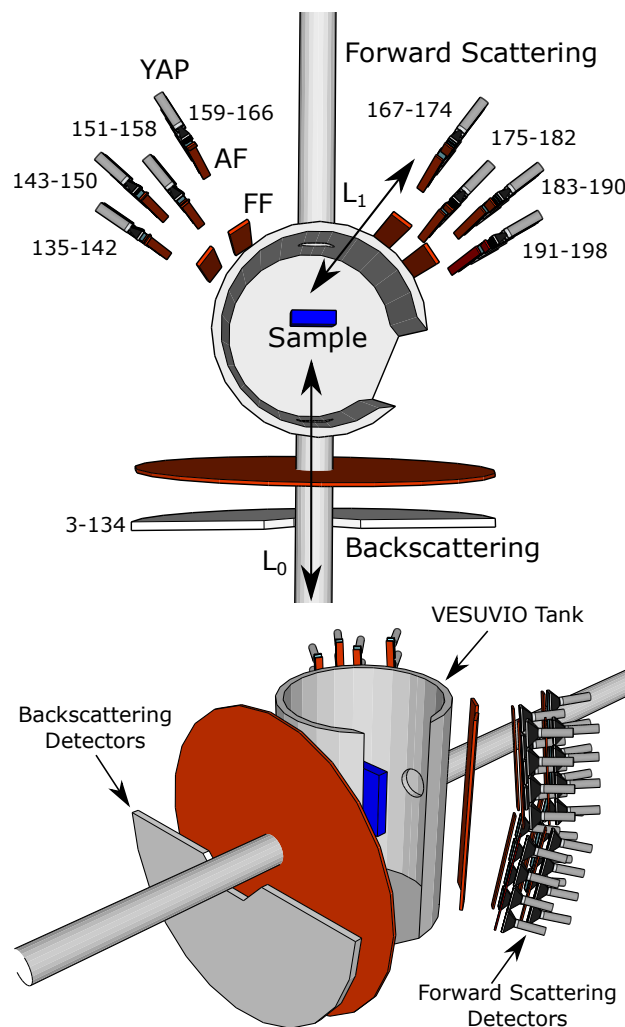


Figure 3.5: Top and side schematic representation of the VESUVIO spectrometer.

Incident neutrons with initial energy E_i travel over a primary flight path L_0 from the moderator to the sample. The sample under study can be taken under controlled temperature with a Closed Cycle Refrigerator (CCR). The CCR has a big temperature working range

from 5 K to 600 K. After the scattering process happens, at certain angle, neutrons with final energy E_f travel over a secondary flight path L_1 to the detector and finally they are counted using different methods. In fact the energy selection and neutron detection on VESUVIO operates in two modes:

- Resonance-Filter (RF) backward detection with ^6Li -glass from 3 to 134 in Fig. 3.5
- Resonance-Detector (RD) forward detection with YAP(Ce) Scintillators from 135 to 198 in Fig. 3.5

As the γ DA will operate in the forward-scattering direction just the RD detection method will be described in detail in Sec. 3.3.1 and 3.3.2.

3.3.1 Detectors

YAP(Ce)

An X-ray or gamma-ray photon interacts with electrons of the material ionising them through photoelectric or Compton effect that transfers all or part of the photon energy to the absorbing material. The fast electrons created in gamma-ray interactions have a maximum energy equal to the energy of the incident gamma-ray photon and will slow down and lose their energy through ionization and excitation of atoms within the absorber material.

Beginning in the late 1980s, it was realized that the cerium activator could be incorporated into new categories of crystals, resulting in scintillators with reasonably good light yield [67]. The scintillation light is generated when the energy deposited in the crystal is transferred to cerium activator sites, where they undergo a transition from the 5d to 4f states. The principal decay time of the cerium luminescence ranges from about 20 to 80 ns, depending on the host crystal. Thus the timing characteristics of these scintillators occupy an intermediate position between the organics with a few nanosecond decay time and the older inorganics in which it is several hundred nanoseconds. After about two decades of development, it has become evident that both rare earth halides and a range of rare earth oxides are the best scintillator host crystals for cerium activation. The rare earth aluminium perovskites YAlO_3 (or YAP) have shown very good scintillation characteristics. In general, the aluminium perovskites have higher densities, higher indices of refraction, shorter decay times and shorter peak emission wavelengths. YAP displays excellent physical properties of hardness, strength, and inertness that facilitate fabrication and handling. For example, in contrast with many other scintillation materials that are either hygroscopic or fragile, YAP can be cut into thin elements for assembly into arrays for use as a position-sensing scintillator. Small-size crystals show excellent energy resolution for example, 4.4% at 662 keV and at the same time offering outstanding timing resolution as low as 160 ps. Finally another important characteristic of YAP detectors the absence, in the active medium, of isotopes possessing neutron resonances in the 1-100 eV. These resonances produce a correlated background with the consequent worsening of the signal to background ratio. In Table 3.2 the main physical characteristics of YAP(Ce) scintillator are shown.

Effective atomic number	36
Density ($\frac{g}{cm^3}$)	5.55
Maximum emission λ (nm)	350
Refractive index at λ_{max}	1.94
Light yield ($\frac{photons}{MeV}$)	$18 \cdot 10^4$
Decay time (ns)	27
Hygroscopic	no

Table 3.2: General characteristics of the YAP scintillator.

Pulse processing

The fundamental output of all the pulse-type radiation detectors, as the scintillators, is a burst of charge liberated by the radiation in the detector. The charge is proportional to the energy deposited and is delivered as a transient current $I(t)$, where the charge is the time integral of the current pulse. With a continued exposure the input to the pulse processing system is a series of transient current pulses while the output is either a count rate or an energy spectrum. The basic component in a typical signal processing chain are shown in Fig. 3.6.

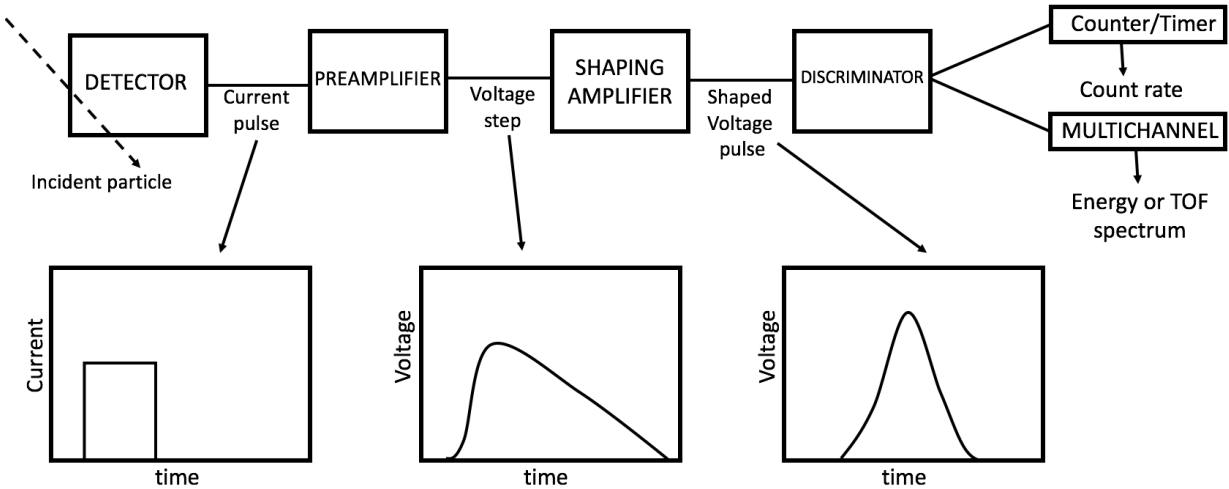


Figure 3.6: Scheme of the acquisition chain.

The radiation interacts with the detector depositing energy that is converted into a current pulse. The total charge is usually too small to be sensed directly, in fact the current is sent to a preamplifier that produces a voltage step ΔV proportional to the deposited charge. Then the shaping amplifier converts the preamplifier output signal into a form suitable for measurements producing an output voltage pulse with pulse height V_{peak} . The output of the shaping amplifier should return rapidly to zero (or baseline) to prevent pulses from overlapping and a resulting distortion of measurements. The amplifier is characterized by a time shaping constant that should be as small as possible to minimize overlap or pulse pile-up. The shaped pulse is sent to circuits that select pulses for further processing, selecting only certain type of signals. The discriminator used on VESUVIO selects all pulses

with pulse height (therefore energy) above a certain Low Level Discrimination Threshold (LLDT) and consists of a device that produces a logic output pulse only if the input pulse amplitude exceeds a set discrimination level. The discrimination level is normally set just above the system noise and is used, as in our case, to enhance the signal-background ratio because the background may be limited to relatively low pulse amplitudes. On VESUVIO the LLDT is set, at present, at 600 keV in order to discard part of the environmental gamma-background. The background is composed mainly by the boron gamma-emission at 478 keV. As a final step the signal is processed in a counting system, multichannel in our case, that accumulates the logic pulses recorded during the time of measurements.

3.3.2 Resonance Detector technique

The Resonance Detector detection method, used in forward scattering on VESUVIO, performs the scattered-neutron-energy analysis exploiting the nuclear resonances of Analyser Foils (AF). The signal acquired in this configuration is given by the photon-YAP detectors which reveal the prompt γ - ray cascade [68] produced, via (n, γ) reactions, by scattered neutron absorbed by the AF placed on the face of the detector. The RD counting procedure relies upon two main steps: in the first step, the scattered neutron beam impinges onto the AF which provides the energy analysis by means of (n, γ) resonant absorption at a given resonance energy E_r . In the second step, the prompt gamma rays are detected and provide the total ToF of the absorbed neutron. The neutron absorption cross sections of isotopes such as ^{238}U and ^{197}Au are characterised by the presence of intense and narrow resonances of radiative neutron capture in the electron Volt energy region. Figures 2.6 and 3.7 show the absorption cross section of ^{197}Au and ^{238}U which are commonly used as energy analysers.

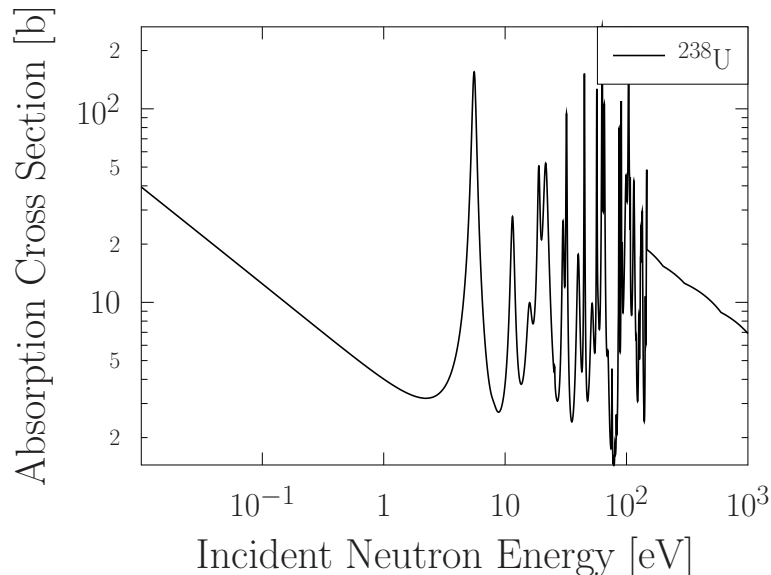


Figure 3.7: Neutron absorption cross section of ^{238}U , data taken from Ref. [61].

It has to be emphasized that, at present on VESUVIO, the gamma detectors are used as counters: they provide a trigger to the counting electronics if the signal is above the LLDT, set electronically, and then the ToF is stored in the multichannel.

The AF has to fulfil some important requirements:

- the radiative capture cross section has to show isolated and intense resonances in the energy region of interest
- these resonances should have small widths
- the emitted γ -ray spectrum should contain lines with appreciable relative intensities

The first two requirements are important in order to properly select the scattered neutron energy and to ensure a low contribution to the energy component of the resolution function of the spectrometer, respectively. The third requirement allows for selecting gamma rays that provide the best signal to background (S/B) ratio.

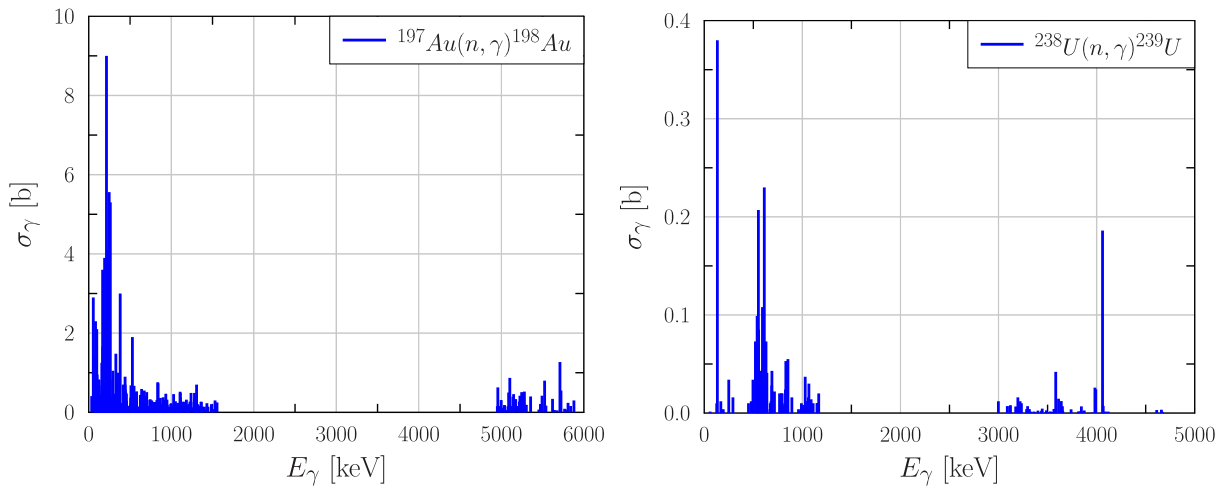


Figure 3.8: Phonon emission spectrum for gold and uranium as reported in Ref. [69]. The most intense part of the γ emission shown in the figure of gold is below 600 keV, threshold used at present on VESUVIO.

The gamma emission lines of ^{197}Au and ^{238}U , the two most widely used isotopes, are shown in Figure 3.8. The preferred isotope depends for example on the momentum transfer that is assessed, the energy resolution that is required and the data collection time that is allocated for the experiment. The width of the ^{238}U resonances are narrower than the ^{197}Au resonance, giving a better energy resolution, but this narrower width results in less neutrons being absorbed in the AF. For relatively short allocated data collection times, the limited counting statistics with a ^{238}U foil might give less-accurate lineshape functions than with a ^{197}Au AF. Furthermore the numerous and close peaks in the ^{238}U radiative neutron capture absorption shown in Fig. 3.7 could give superposition effects in the ToF spectra that are not present for the ^{197}Au case (see Fig. 2.6). For these reasons, and for the handling issues of ^{238}U , now at VESUVIO ^{197}Au is used. A neutron having an energy within the width of the resonance is strongly absorbed while an off-resonance neutron interacts with less probability. The γ emission detected by the YAPs produces a voltage signal which is processed by a fast electronic chain, providing the stop signal for the acquisition electronics. To be competitive with instruments that operate continuous user-programmes, a couple of issues have to be addressed: energy resolution improvement and gamma background reduction. Both the energy resolution and gamma background drawbacks of RD technique

can be effectively solved by using the Foil Cycling Technique (FCT) [70, 71, 72]. The FCT enhance the overall resolution of the spectrometer and obtain a good subtraction of the gamma background [73, 74, 75, 76, 77]. This allows a more reliable lineshape analysis of the recoil peaks. In this technique an additional foil is used, called Filter Foil (FF), between the sample and detector, that can be cycled in and out of the flight path of the neutrons, see Figure 3.9.

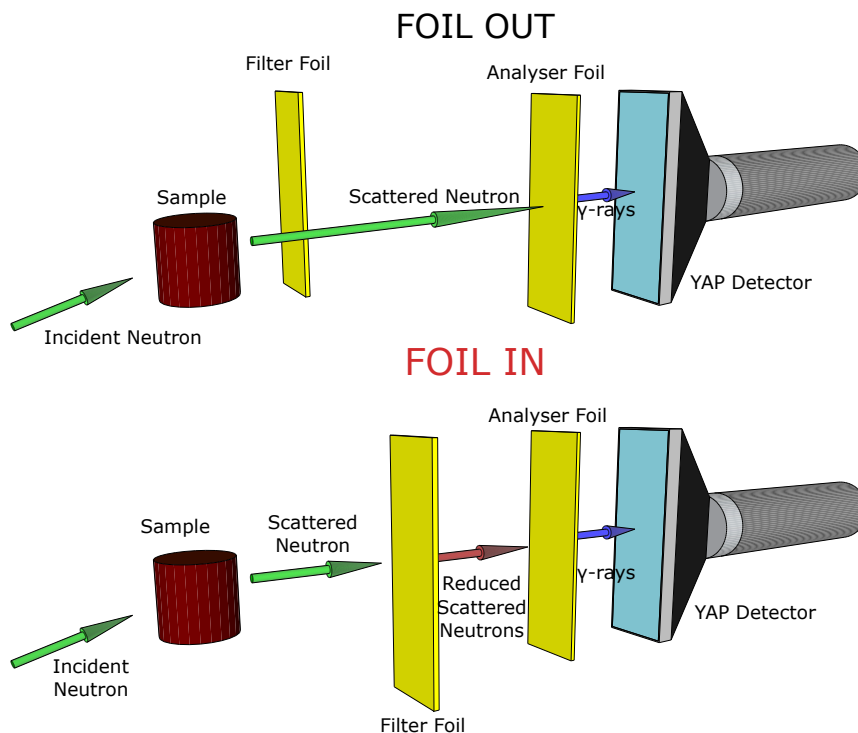


Figure 3.9: Schematic representation of the set-up used in the foil cycling technique.

The background reduction is obtained by subtracting the signal recorded in the foil-out position with the signal recorded in the foil-in position. In the foil-in position the FF is placed between the sample and the detector while in the foil-out configuration the FF is outside the sample-detector direction. In the foil-out configuration the photons detected are background photons from the environment (neutron interaction between neutrons and the block-house) and signal photons from the gold foil (radiative neutron capture at 4.9 eV); in the foil-in configuration the photons detected are in the same number for the background but are less for signal. The FF reduces neutrons that impinge on the gold AF in front of the detector, in this way we obtain a less intense peak characterised by the Lorentzian tails of the resonance that were present also in the foil-out measurement. Making the difference between the in and out spectra we get an isolation of signal and a better energy resolution with respect to the standard RD. The signal isolation obtained with the FCT is shown in Fig. 3.10 for a biphenyl sample, where the black spectrum is acquired in foil-out configuration, the red one in foil-in configuration and finally the blue spectrum is the difference between foil-in and foil-out.

RD does not require the use of gamma detectors with a good energy resolution. Scintillator detectors are therefore attractive because of their high density and relatively low cost per unit area. The detectors are used as counters and do not require a significant amount of

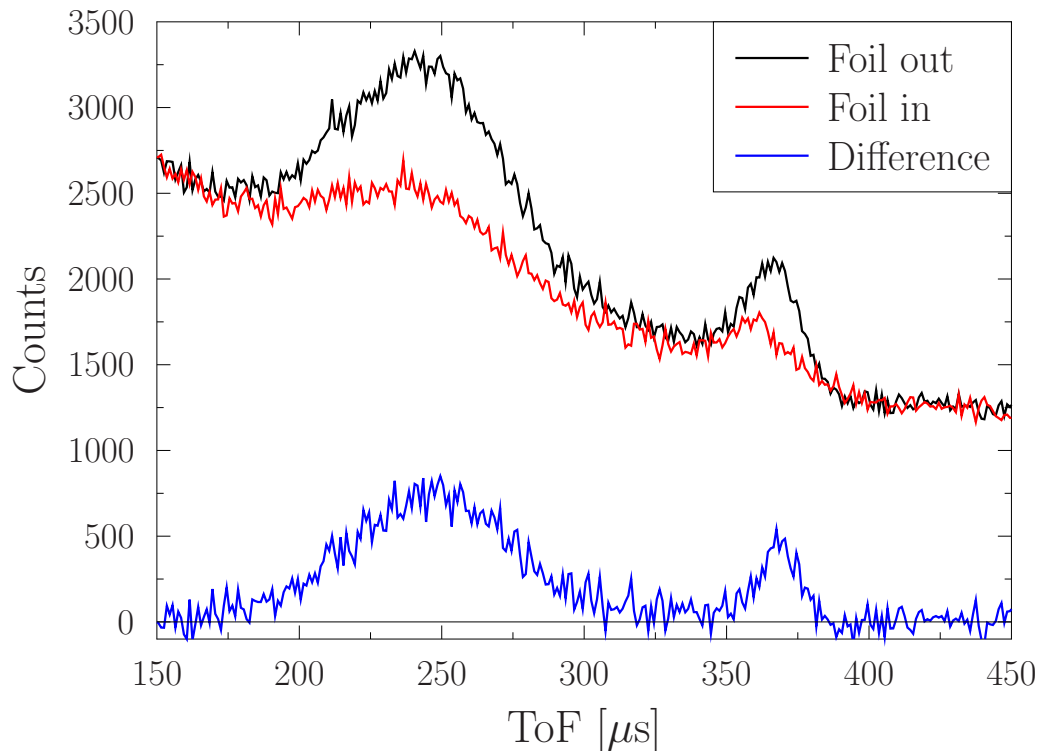


Figure 3.10: Measurement of a biphenyl sample using FCT with gold foils and YAP(Ce) detectors. The black spectrum is acquired in foil-out configuration, the red one in foil-in configuration and the blue spectrum is the difference between foil-out and foil-in.

gamma to be absorbed by the photoelectric effect, allowing the use of scintillators with a relatively low atomic number (Z). YAP(Ce) is therefore an attractive scintillator material because it has no neutron absorption resonances in the energy range of interest and has favourable scintillation properties.

It was found [76, 78] that using a discrimination threshold above 600 keV, it was possible to maximise the S/B and count rate. This can be explained by the suppression of the 480 keV gammas coming from neutron capture on Boron, used as absorbing material in the walls surrounding the spectrometer as well as in the beam dump. From 2007 the ^{238}U analyser foils were substituted by gold foils but studies on the new best threshold are still missing and it was left to 600 keV even if the most intense γ peak after radiative neutron capture are concentrated at energy smaller than 600 keV. In fact, in Ref. [69] the tabulated gold-line gamma emission whose the most intense of them is at 215 keV as represented in Fig. 3.8. There is another “prompt” gamma contribution which is attributed to the *internal conversion*. This emission is due to the de-excitation of $^{198}\text{Au}^*$ nucleus that produces a gamma ray that doesn’t emerge from the atom but interact with an electron that leaves the atom. Now the unstable configuration turns in the stable state emitting a prompt gamma ray at low energy (under 300 keV) characteristic of the electronic configuration. The process is sketched in Fig. 3.11.

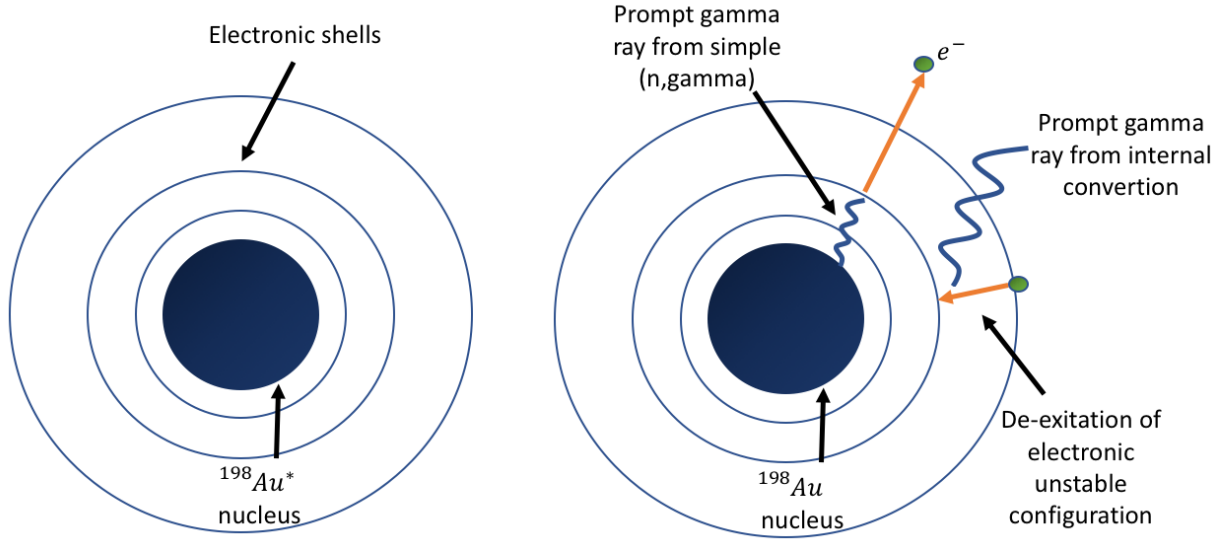


Figure 3.11: Scheme of the internal conversion emission.

3.3.3 Data reduction and analysis

The reduction of the VESUVIO spectra is generally performed in the ToF domain. After the application of the FCT a mass-resolved spectrum is obtained where each peak is centred in correspondence of the recoil energy $E_{recoil} = \frac{\hbar^2 Q^2}{2M}$ at a ToF

$$t = \sqrt{\frac{m}{2E_1}} \left(\sqrt{\frac{E_1}{E_1 + E_{recoil}}} + L_1 \right). \quad (3.6)$$

As the recoil energy is inversely dependent upon the nuclear mass, lighter the elements lower the ToF peak centre while the heavier masses populate higher ToF until the infinite mass limit where $t_\infty = \sqrt{\frac{m}{2E_1}}(L_1 + L_0) \sim 390\mu s$ on VESUVIO. The raw spectra acquired are corrected by a residual γ background from the FCT and by the multiple scattering effects. These corrections need some parameters of the NCP such as a first estimate of the kinetic energy and intensity of the ToF peak, I_M . For this reason a preliminary ToF fit is performed constrained by the stoichiometry of the system; as an example for a hydrogenated molecule with N_H and N_C the number of hydrogen and carbon respectively

$$I_H = \frac{N_H \sigma_{bH}}{N_C \sigma_{bC}} I_C. \quad (3.7)$$

The ToF fit together with the gamma and multiple scattering corrections are showed in Fig. 3.12 for biphenyl. The gamma-background correction [79] is an oscillation under each NCP mass while the multiple scattering effect is originated by the thickness of the sample and the consequent probability to interact more times [80] that is related to the neutron transmission as:

$$T(E_i > 1eV) = 1 - e^{-n\sigma_f d}, \quad (3.8)$$

where n is the numerical nuclear density, d is the sample thickness and σ_f is the free scattering neutron cross section defined as

$$\sigma_f = \sum_M N_M \frac{\sigma_{bM}^2}{\left(1 + \frac{m}{M}\right)^2}. \quad (3.9)$$

The quantity $n\sigma_f d$ is called scattering power, generally chosen so as to have a transmission of 90% for epithermal neutrons in order to have a considerable DINS signal and low multiple scattering that is estimated with a Monte Carlo simulation [81].

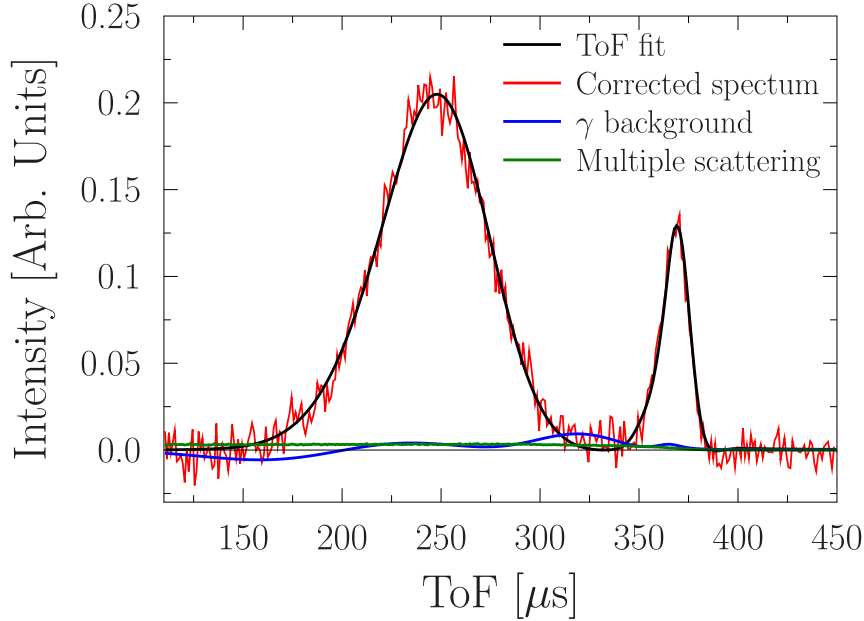


Figure 3.12: Biphenyl spectrum acquired on VESUVIO after the multiple scattering and gamma-background corrections (red line). In blue and green the gamma and the multiple scattering contributions while in black the ToF fit.

After the implementation of the corrections an additional ToF fit is performed in order to isolate the signal from each mass and in order to perform the final fit in the y -space with a Gauss-Hermite expansion, as described in Sec. 2.5.

The PhD work is focussed on the development of a new detector apparatus the γ DA and a new methodology for the acquisition of DINS spectra. The result will be quantified in terms of signal to background ratio and signal gain. The configuration introduced will then be applied first to standard sample such as polyethylene and then to materials of interest in the material science such as biphenyl and ice.

3.4 The IRIS spectrometer

The IRIS [82] spectrometer is a quasi-elastic inverted-geometry neutron spectrometer with high resolution and high diffraction capabilities. The instrument will be used in Chapter 6 in order to characterise the displacement of the hydrogen nuclei, around the equilibrium position, in a set of ice phases and motivate the stability of ice II. In fact, the energetic stability induced by a low nuclear kinetic energy, probed on VESUVIO, will be enforced by the large nuclear entropy, given by the hydrogen MSD, probed on IRIS. In this case the expression for The Nuclear Momentum Distribution can be generalised in order to include the Nuclear Displacement Distribution (NDD) of a nucleus j within a 3D harmonic system as

$$n(x_j) = \left\langle \prod_{\alpha} \frac{1}{\sqrt{2\pi}d_{j\alpha}} \exp\left(-\frac{x_{j\alpha}^2}{2d_{j\alpha}^2}\right) \right\rangle_{\Omega} \quad (3.10)$$

where $\langle \dots \rangle_\Omega$ is the spherical average, $x_{j\alpha}$ is the component along the Cartesian direction α of either the momentum, $\vec{x} = \vec{p}$, in wave vector units, or displacement, $\vec{x} = \vec{u}$. Moreover, $d_{j\alpha}^2$ is the standard deviation of the resulting multivariate distribution along α , corresponding to either the mean square momentum, $\sigma_{j\alpha}^2$, or mean square displacement, $\langle u^2 \rangle_{j\alpha}$ respectively.

The neutrons scattered by the sample on IRIS are energy-analysed by means of Bragg scattering [83] from a crystal-analyser array and the ToF technique, see Sec. 3.2, is used. The instrument is placed at the N6 beam line at ISIS with a liquid nitrogen moderator at 25 K that allows the presence of low-energy cold neutrons. IRIS can be divided in two part: the incident neutron path and a *scattering chamber*. The incident neutron path is composed by neutron guides designed to maximise the incident neutron flux with an energy spectrum, extended up to ca. 18 Å, showed in Fig. 3.13 measured with the Incident Beam Monitor (IBM). In this first part a system of two choppers, made by neutron absorbing material, is used to define the incident neutron energy range. They are located at 6.3 m and 10 m from the moderator respectively, and operating at either 50, 25, 16.6 or 10 Hz leave an aperture through which neutrons may pass. The lower and upper limits of the incident wavelength band are therefore defined by adjusting the chopper phases, and hence opening times of each aperture, with respect to t_0 (the moment at which neutrons are produced in the target). Wavelength-band selection effectively defines the energy-transfer range (inelastic) or d-spacing range (elastic) covered during an experiment.

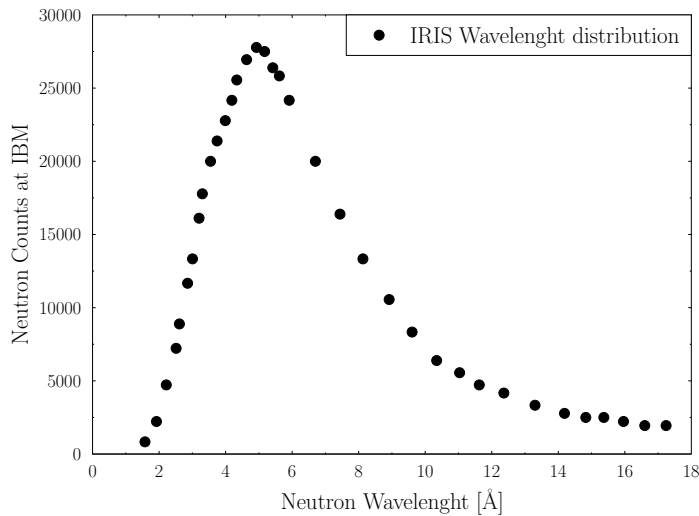


Figure 3.13: Wavelength distribution as measured on IRIS with the IBM for each μAh , taken from Ref. [83].

The second part of the spectrometer consists of a 2 m diameter vacuum vessel containing two crystal analyser arrays (pyrolytic graphite and mica), two 51 element ZnS scintillator detector banks and a diffraction detector bank that covers 170° containing ten ^3He gas-tubes. Incident and transmitted beam monitors are also located before and after the sample position respectively. In our experiment of quasi-elastic neutron scattering, the final neutron energy is fixed by means of Bragg-scattering from a large array of single crystals (Pyrolytic Graphite or Mica). Only neutrons with the appropriate wavelength/energy to satisfy the

Bragg condition are directed towards the detector bank. By recording the time of arrival of each analysed neutron in a detector relative to the ISIS synchrotron pulse t_0 , the neutron energy gain/loss occurred within the sample is investigated. There are many pre-setted options for the neutron incident-energy range and energy resolution that may be chosen according to the type of experiment that it is of interest. There are two type of cell available at IRIS: flat and cylindrical cell. For our purposes we chose the flat can in order to have quick temperature changes and fine control at the expenses of a reduced scattering signal in the plane of the sample container. In this case it is very important to choose carefully the can orientation in order to maximise the scattering signal at low or high Q.

Chapter 4

γ DA development

In this chapter a novel photon sensitive detector, referred to γ DA, for epithermal neutron spectroscopy to be installed on the VESUVIO spectrometer is described. The response of the γ DA in terms of efficiency and resolution as a function of the incident photon energy is simulated and reported in Sec. 4.1, then preliminary tests of the acquisition chain on a polyethylene sample, considered as a standard for neutron spectroscopy, are described in Sec. 4.2. Finally, in Sec. 4.3, nuclear dynamics in biphenyl, chosen as a model compound for the decomposition of lignin in monomers in the biofuel production, was probed in the optimised configuration.

On VESUVIO, the YAP detectors count the prompt radiation following the resonant capture of the neutron, together with the additional background radiation arising from the neutron interaction with blockhouse elements [84]. Fig. 4.1 shows the photon spectrum as recently measured with a high-purity germanium detector on the INES beamline [85] from a gold sample in correspondence of the resonance at ca. 4.9 eV, in red, and outside the resonance, in black. The insert indicates the presence of the main gamma lines from gold after the background correction of the red plot. The use of gold foils was preferred to the previous ^{238}U because of safety reasons. Moreover, ^{238}U has less-separated neutron-induced resonances, leading to inconvenient overlap effects on the measured ToF spectra. In the current photon-sensitive detector configuration, the LLDT is set at ca. 600 keV [77], as pictorially shown in Fig. 4.1, so as to exclude background photons from boron, present in the instrument blockhouse, (peak A at ca. 480 keV) and annihilation (peak B at ca. 511 keV) [86]. Preliminary results presented in Ref. [87] suggest that the instrument sensitivity can be improved by setting the LLDT to a lower value, so as to detect intense photon peaks in the energy region from 70 keV to 300 keV, as evidenced in the insert of the same figure.

4.1 Calibration and FLUKA simulations

The detectors used were calibrated with standard radioactive sources of ^{22}Na (emission at $E_\gamma=511$ and 1274 keV), ^{133}Ba (emission at $E_\gamma=356$ keV), and ^{137}Cs (emission at $E_\gamma=662$ and 32 keV) available at ISIS. The spectra were also modelled with FLUKA [88] Monte Carlo simulations to calculate the efficiency and energy resolution of the detectors, assuming a crystal density $\rho = 5.37$ g/cm³, and dimensions $a = 0.66$ cm (thickness), $b = 2.5$ cm (width) and $c = 8.0$ cm (length) shown in Fig. 4.2. The FLUKA results showed a good

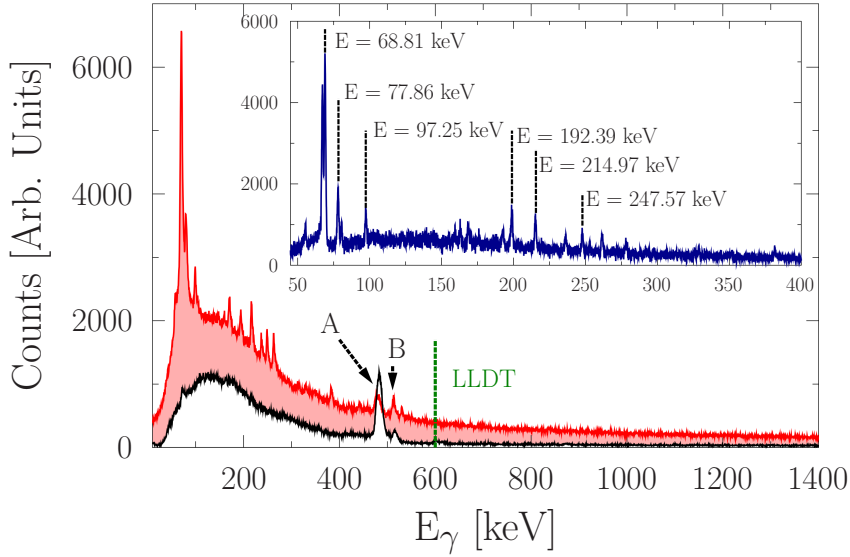


Figure 4.1: Photons from gold in correspondence of the resonance at ca. 4.9 eV, in red, and outside the resonance, in black, measured on the INES beamline, using a high-purity germanium detector. The insert indicates the presence of the main gamma lines from gold after the background correction of the red plot.

agreement with experimental data both in the shape of the Full Energy Peak (FEP) and of the Compton Edge [89](CE), as shown in Fig. 4.3. The FLUKA spectra were obtained with a mono-energetic photon beam at the energy radioactive sources and the resolution was taken into account with a Gaussian energy spread that reproduce the experimental spectra. The energy resolution $R = \frac{\Delta E}{E}$ of the detector, where ΔE is the full width at half maximum (FWHM), spans from 94% to 17% for photon energies from 32 keV to 1.3 MeV, respectively as shown in Fig. 4.4. The experimental ΔE are extrapolated with a FEP fit while FLUKA ΔE are imposed by the comparison of the experimental and simulated FEP.

The aim of the simulation is to use the radioactive sources as a benchmark in order to model the detector response for the γ -lines emitted by the gold AF.

As reported in the literature [90], the resolution follows the trend $R \sim \frac{1}{\sqrt{E}}$, used as a fit in Fig. 4.4, from which we obtain a value of $R = 44\%$ for an Au-photon of 215 keV, the most intense line from Au in the E_γ energy range of interest (as shown in Fig. 4.1). Once the resolution was characterised, the efficiency of the detector has been simulated as the ratio between the number of counts in the FEP corresponding to energy E_γ , and the number of photons with energy E_γ emitted by the source (primaries generated in the simulation) is the detector FEP efficiency. This number varies from 95% to 2% for the ^{137}Cs photons from 32 keV to 662 keV, respectively, as shown in Fig. 4.5. All simulations were performed with the source position on the detector surface. For a photon of 215 keV the simulated FEP efficiency value is 27%. The blue squares indicate the ratio between the incident gamma-rays that are actually detected, therefore the total number of counts in the spectrum, and the number of primary photons with energy E generated in the simulation, namely detector Total Efficiency.

Below 100 keV the photoelectric interaction is the dominant process for energy deposi-

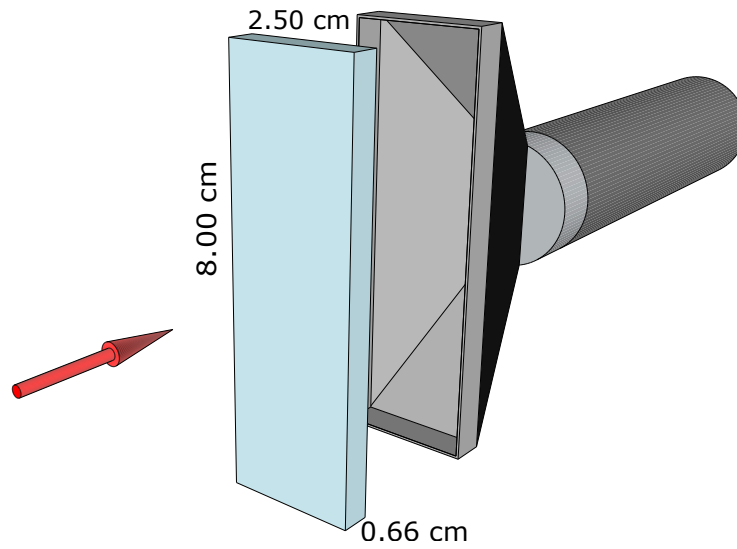


Figure 4.2: Geometry of the current YAP(Ce) configuration installed on VESUVIO beam-line [85].

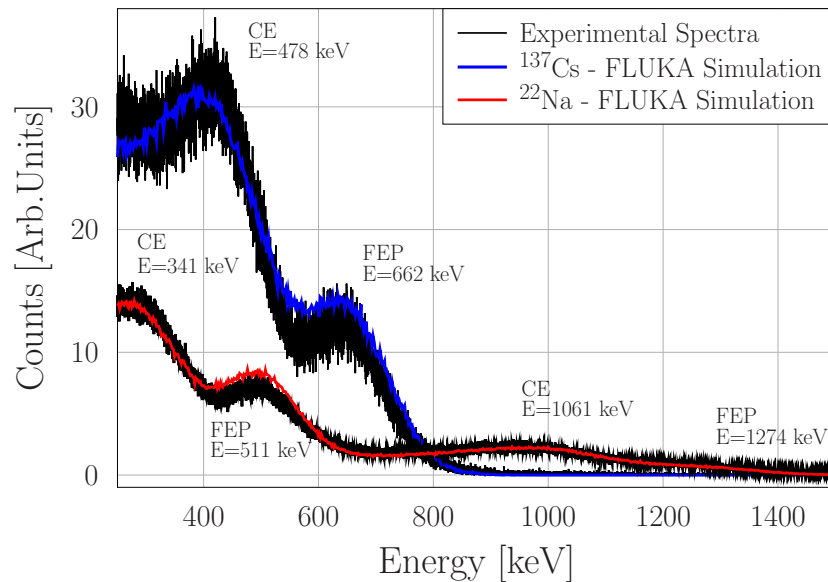


Figure 4.3: Comparison of the experimental spectra (black lines) and the simulated results for ^{22}Na (red line) and ^{137}Cs (blue line) [85].

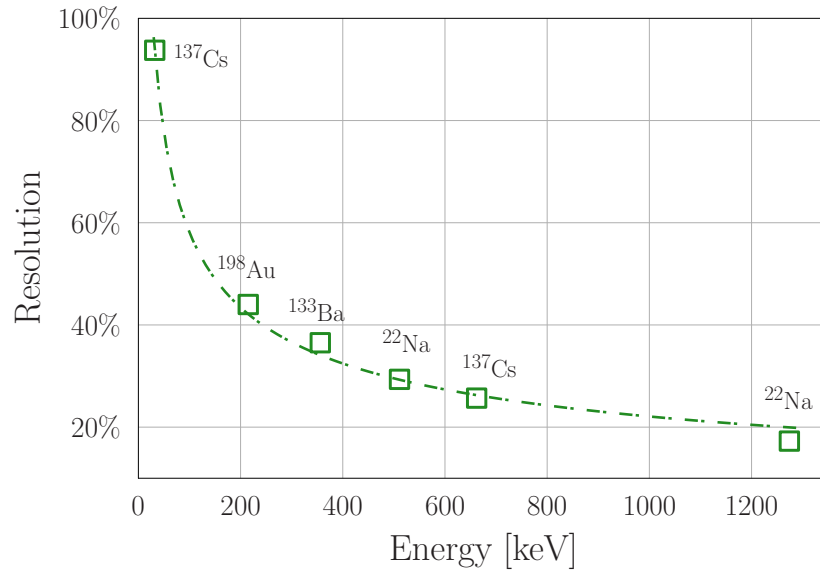


Figure 4.4: Energy resolution $\Delta E/E_\gamma$ of the YAP(Ce) detectors as a function of the photons energy E_γ for the fitted experimental data (green squares) and the fit of the simulated results (green dashed line) [85].

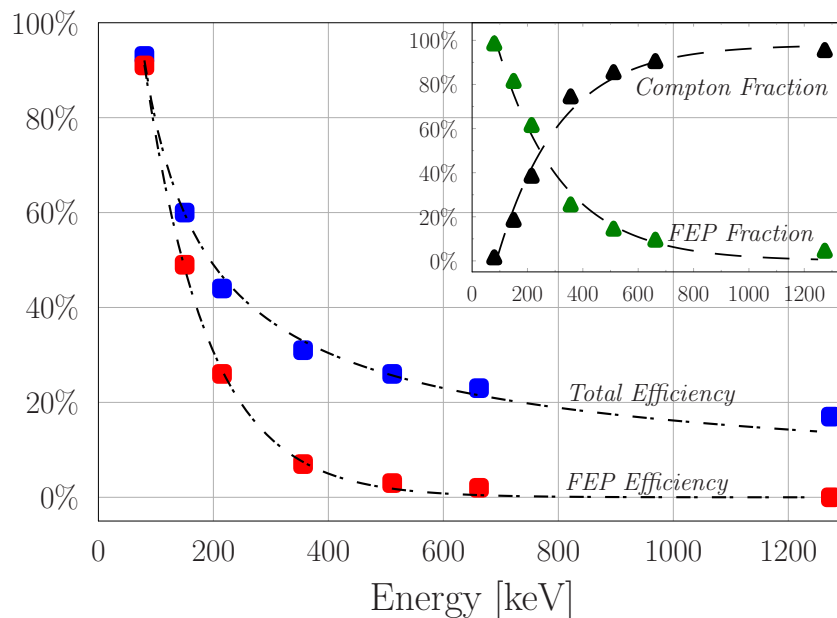


Figure 4.5: Simulated FEP Efficiency (red squares) and total efficiency (blue squares) as functions of the photon energy E_γ . In the insert, the FEP (green triangles) and Compton (black triangles) fractions of the simulated spectra. Black dashed lines represent fits to the simulation results [85].

tion in the crystal and guarantees 100% total absorption probability. For a photon energy of 600 keV the absorption probability is 25% while for 200 keV is ca. 45%. In the insert of Fig. 4.5, with the black triangles, the contribution of the Compton process to the whole spectrum is calculated, as a function of the incident energy. As expected, above 250 keV the Compton interaction becomes the dominant mechanism for energy deposition in the crystal [91]. It increases with the photon energy and saturates at 100% for 1.3 MeV. Fi-

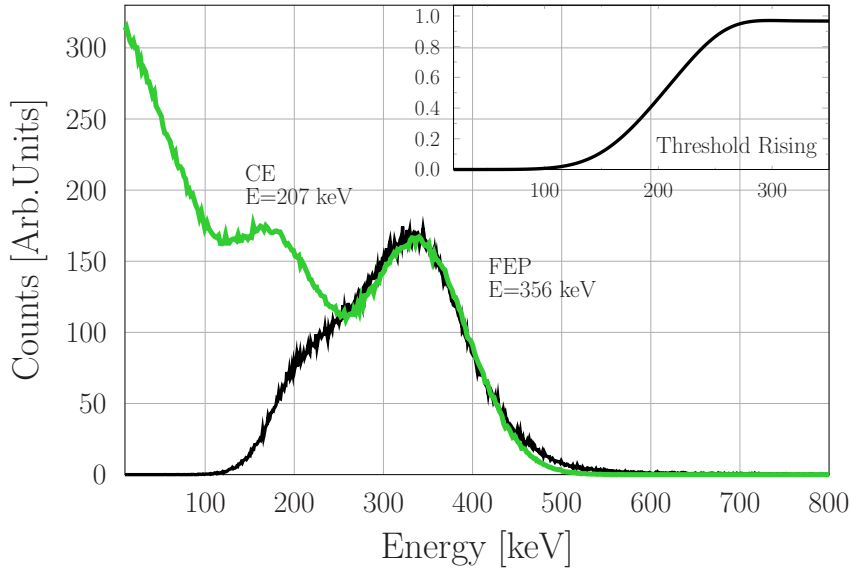


Figure 4.6: Simulated spectrum (green line) and experimental spectrum (black line) of the ^{133}Ba source when the LLDT was set to 180 keV. In the insert, the ratio between the two spectra represented in figure.

nally, in order to characterise the effect of the threshold on the spectra, we set the LLDT for one of the detectors to 180 keV during the exposure of the YAP to the ^{133}Ba source, and we compared (see Fig. 4.6) the acquired spectrum with the one simulated with the same source without any energy cut-off. The ratio between the two spectra, in the insert of Fig. 4.6, shows that the threshold is not a sharp step function, with the ratio smoothly changing from 0 to 1 over an 80-keV energy region. The FLUKA simulations [85] tell us that the low photon-energy region is to be preferred not only for the greater amount of gold-photons but even for the higher efficiency and resolution of the detector response.

4.2 Polyethylene preliminary results

Here we report measurements on polyethylene and gold reference samples on the VESUVIO spectrometer, using five values of LLDT, showing the improvement of counting statistics and noise reduction on DINS data. Moreover, in section 4.2.2 and 4.2.3 we report estimates on the improvement in the analysis of Nuclear Momentum Dynamics (NMD) and Mean Force (MF) [45] for model systems with anisotropic local potentials.

4.2.1 Counting error and noise reduction

Five YAP detectors, labelled from A to E were used to test the improved detection method of a polyethylene sample with five values of LLDT lower than 600 keV as suggested by the detector simulation and gamma emission of gold. The detectors were calibrated with radioactive sources of ^{22}Na , ^{137}Cs , ^{133}Ba and ^{241}Am available at the ISIS facility; the detector position and LLDT configuration are listed in Table 4.1. Fig. 4.7 shows an example of ToF spectra for detector A with scattering angle $\theta \simeq 52^\circ$, in the case of the original LLDT (green squares), and for the lowest value of the LLDT (red circles) used, 60 keV. In the top Figure, both the original and changed configurations are normalised to the proton charge accumulated in the synchrotron, so as to show the increase in the count rate of a factor ca. 3. The green spectrum in the bottom and the red one in the middle panel are, instead, unit-area normalised so as to stress the Error Reduction (ER) of ca. 40% when the LLDT is lowered [87], and prompt-gamma rays from the gold resonance in the range between 60 and 600 keV are also included. Smaller Count-Rate Increases (CRI) were observed for the other detectors with modified LLDTs, as reported in Table 4.1. In order to quantify the reduction of the noise level in DINS spectra, two ToF ranges were studied where the DINS signal is expected to be vanishing. The ranges chosen are to the right of the carbon peak, range 1 ($390 \mu\text{s} < \text{ToF} < 450 \mu\text{s}$), and to the left of the hydrogen peak, range 2 ($100 \mu\text{s} < \text{ToF} < 160 \mu\text{s}$).

Table 4.1: The set-up parameters for the detectors A – E : the value of the LLDT; their position with respect to the sample in polar coordinates r , θ , and ϕ ; the average count rate increase; the drop of noise and error-bar with respect to the values for the original LLDT.

Det.	LLDT[keV]	r [m]	θ [deg]	ϕ [deg]	CRI	ER	noise (1)	noise (2)
A	~ 60	0.51	52	131	+200%	-40%	-32%	-35%
B	~ 170	0.50	47	140	+150%	-22%	+4%	-18%
C	~ 280	0.50	44	151	+100%	-12%	-23%	-8%
D	~ 380	0.51	41	163	+20%	-13%	-24%	-6%
E	~ 490	0.52	52	-132	+0%	-18%	-20%	-18%

The standard deviation, Δc , of the distribution of counts in these ranges was calculated for the original and changed LLDTs, and it was used to give a measure of the noise and scatter of the data. The noise in the ToF spectra is related to the difference of two count rates in the foil-in and foil-out configurations [71], thus being sensitive to the LLDT value. The standard deviation Δc is calculated using

$$\Delta c^2 = \frac{1}{N-1} \sum_i^N (c(t_i) - \bar{c})^2, \quad (4.1)$$

where i runs over the N bins in the ToF range $\{t_i\}$, $c(t_i)$ is the count rate in the time interval between t_i and t_{i+1} , and \bar{c} is the average count rate over the range considered. The values of $\bar{c} \pm \Delta c$ are shown in Fig. 4.7 for detector A for both ToF ranges considered.

Detector A shows the largest noise reduction of about 35% on both ToF ranges. On the other hand, detectors B – D show different reductions on the two ranges as listed in Table 4.1.

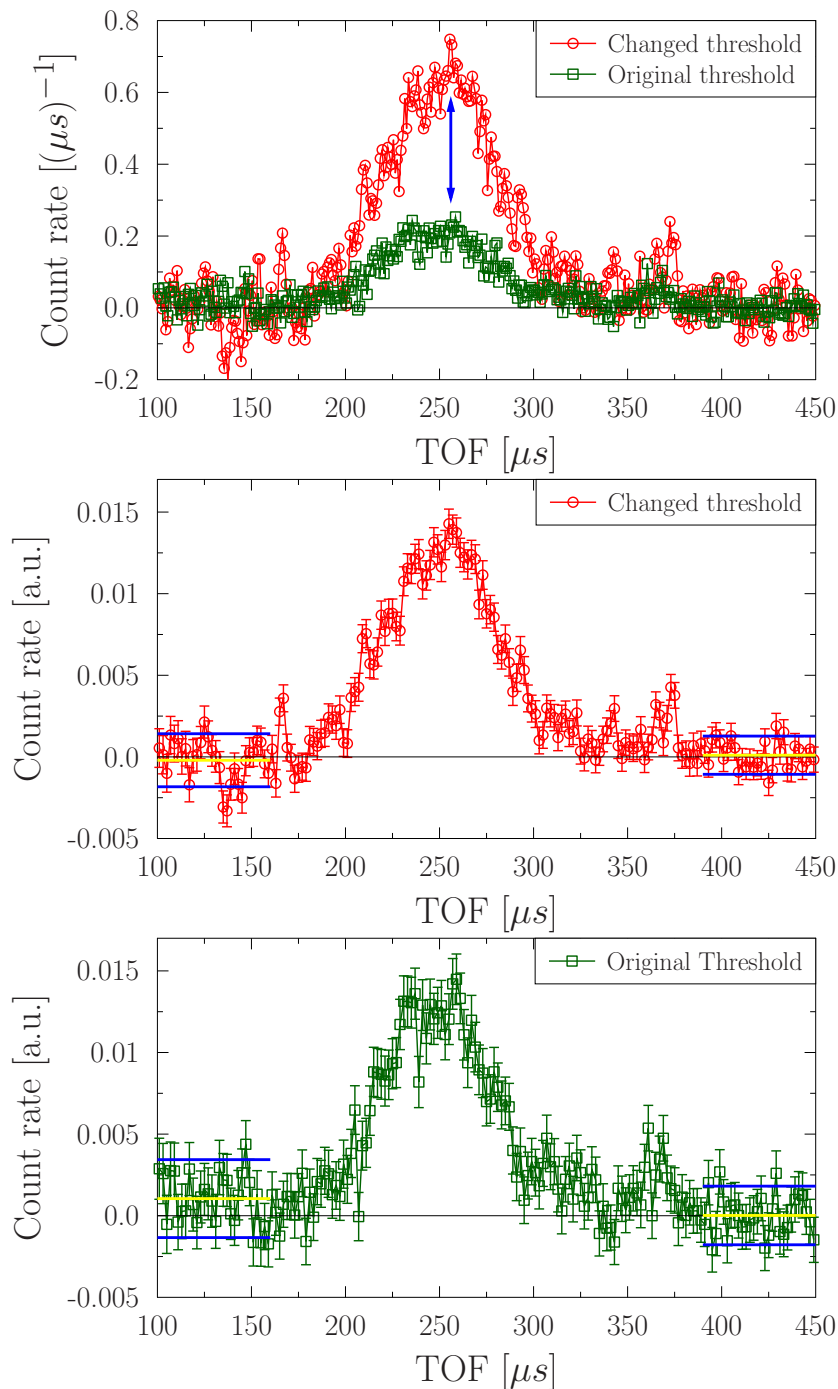


Figure 4.7: Spectra from detector *A* for a polyethylene sample, hydrogen and carbon DINS peaks are evident at lower and higher ToF respectively. In the top Figure, spectra in both the configurations normalized to the proton charge accumulated in the synchrotron; the blue arrow indicates the increase in the counting statistics of a factor ca. 3. Unit-area normalised spectra from detector *A* recorded with the original (bottom) and modified (middle) LLDT; here for the ToF ranges 1 and 2 the noise levels have been evaluated and indicated as blue lines, and the average count rate in the range as a yellow line.

Such behaviour can be linked, in first approximation, to the photons emitted by ^{113}Cd in the LLDT energy range investigated, of which the most intense is at 558 keV [86]. Indeed, at the time of the experiment, the forward-scattering VESUVIO detectors were equipped with 1-mm-thick cadmium foils for calibration purposes. In addition to the $E^{-1/2}$ -dependent absorption cross section, ^{113}Cd has neutron-induced capture resonances in the neutron-energy range between 10 and 70 eV, which roughly corresponds to the ToF values in range 1 for scattered epithermal neutrons. These photons provide counts from the background only, and the present study suggests that the calibration-related cadmium foils should be generally removed during experiments, and for any value of the LLDT as we will do for the biphenyl experiment in Sec 4.3.

4.2.2 Line-shape analysis with optimized set-up

The reduction of noise level and error bars are crucial factors in the analysis of NCPs. Indeed, a more precise line-shape analysis of Compton profiles allows for a more detailed determination of the local potential affecting nuclei in a given system. In fact, the optimization is reflected on the physical parameters obtained by DINS. The NCP found for hydrogen in polyethylene is isotropic, in Table 4.2 the mean kinetic energies measured with the standard and optimised set-up are reported. As we can see the error bar is decreased by the 50%.

Table 4.2: Mean kinetic energy measured by DINS in the standard and optimised configurations.

	Standard configuration	Optimised Configuration [meV]
$\langle E_k \rangle$	148 ± 11	145 ± 6

The extent of the benefits from an optimisation of the LLDT is discussed below, taking as an example the case of hydrogen in a molecular system with local potential and NMD similar to that of the condensed phases of water. To this aim, we have calculated two hydrogen experimental NCPs for isotropic and anisotropic harmonic potentials, $\bar{F}(y, Q)$, shown in Fig. 4.8, both of which would result in the same mean kinetic energy. The two $\bar{F}(y, Q)$, for brevity called $\bar{F}(y)$, functions are calculated using Eq. 2.57 shaping $J(y)$ with Eq. 2.52 into a spherically-averaged multivariate Gaussian function. In particular, the isotropic function is characterized by the mean kinetic energy $\langle E_k \rangle = 143.1$ meV, while the multivariate function corresponds to $\langle E_k \rangle_x = 8.3$ meV, $\langle E_k \rangle_y = 33.2$ meV, and $\langle E_k \rangle_z = 101.6$ meV. Both isotropic and anisotropic NCPs are reported in Fig. 4.8, together with their difference. The aim of this calculation is to relate the optimisation of the LLDT values to an improved experimental sensitivity able to distinguish two NCP line shapes with the same variance, *i.e.*, the same second moment, but with different fourth and sixth moments [60, 1].

The anisotropic profile in Fig. 4.8 is transformed into simulated experimental data by adding typical experimental error bars from VESUVIO measurements [92, 59], and numerically-generated random noise. The simulated data are reported in Fig. 4.9(a-b). The difference between the calculated isotropic and anisotropic systems (Fig. 4.8) is also

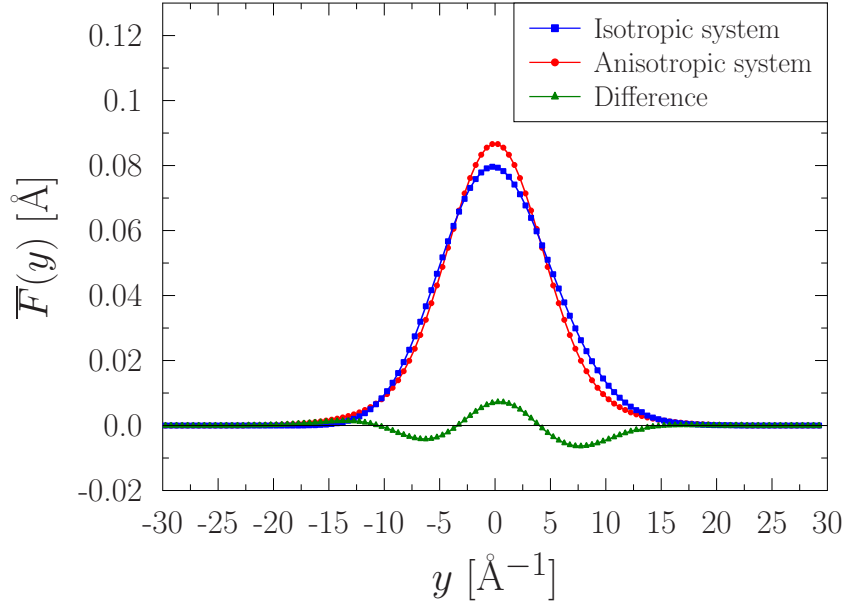


Figure 4.8: Calculated isotropic (blue) and anisotropic (red) NCPs as defined in the text, together with their difference (green).

shown for comparison. The right panel of Fig. 4.9 shows an enlarged view of the NCP differences between the simulated anisotropic data and the calculated isotropic model. The error bars and noise in Fig. 4.9a are representative of a VESUVIO measurement from a 10% scattering-power sample measured for ca. 3600 μAh of integrated ISIS proton current and acquired with the original LLDT at 600 keV. For the same sample, Fig. 4.9b corresponds to the same acquisition time (3600 μAh), but with the error bars and noise as if all detectors had the same modified LLDT as detector *A*. In particular, the error bars and noise of Fig. 4.9a are reduced by 40% and 35% respectively as indicated by the results shown in Table 4.1. The random noise is generated using a ROOT script that exploits the TRandom3 function that produces a random number in a given range [93].

The single-detector simulated experimental spectra, whose detector average is reported in Fig. 4.9 in red, were thus fitted using a global fitting procedure using a multivariate Gaussian profile to model the anisotropic momentum distribution as described in Ref. [49] and Chapter 2. The results are compared to the input parameters for $\langle E_k \rangle_\alpha$ in the calculated anisotropic profile, and are reported for the two cases in Table 4.3. Results from Fig. 4.9a (case 1) are consistent with the input values, and the associated error bars are of the same order as those reported in recent investigations [92, 59]. The fitted parameters from Fig. 4.9b (case 2), corresponding to the configuration proposed in the present work, are associated with error bars about half of those in the previous case. Such level of accuracy in the determination of the directional contributions to the mean kinetic energy would represent a valuable benchmark, for example, for computer simulations tackling competing quantum effects from subtle changes in the hydrogen-bonding network in water and ice [49, 39].

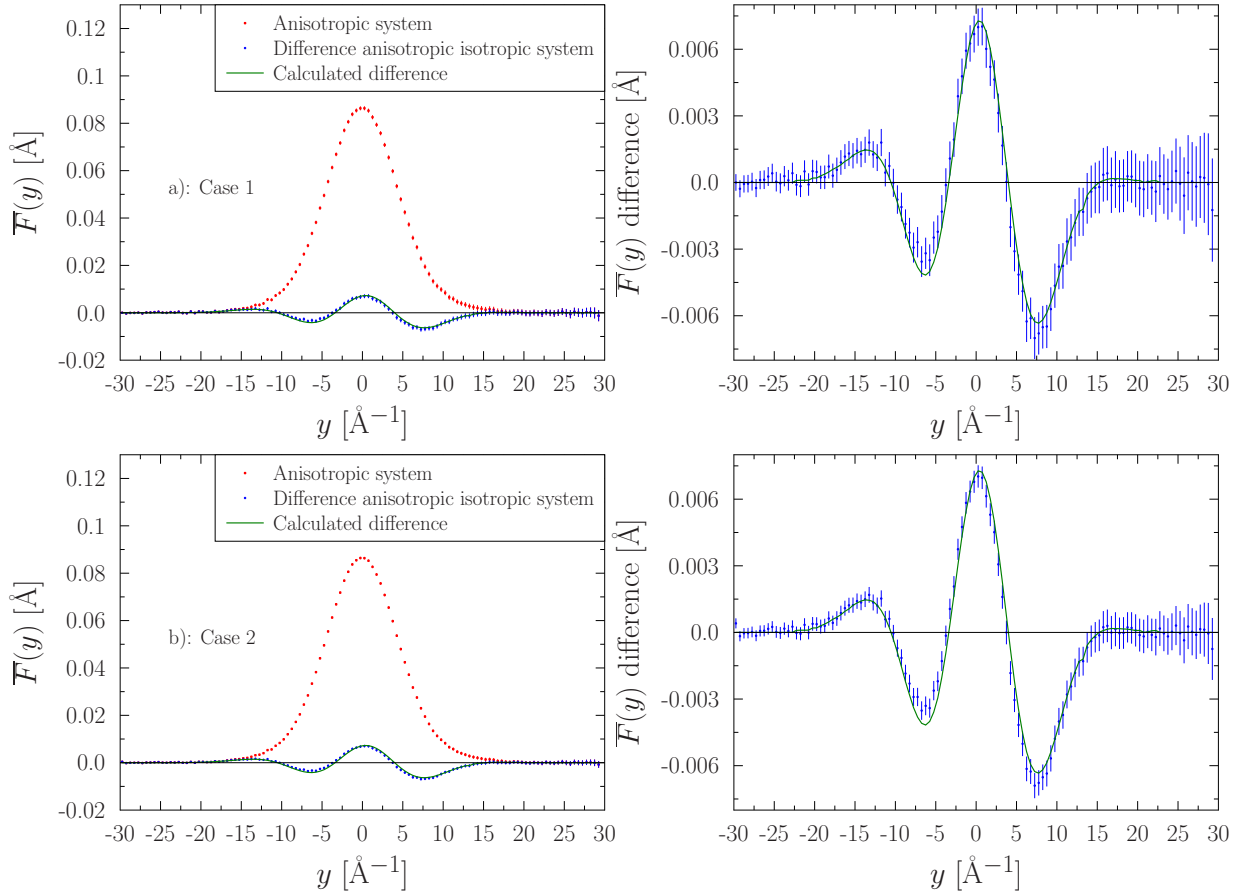


Figure 4.9: (a–b) Simulated experimental anisotropic $\bar{F}(y)$ profile with error bars and noise in red, in blue the difference with the calculated isotropic $\bar{F}(y)$ and in green the difference reported in Fig. 4.8. On the right of each profile an enlarged view of the Compton profile differences between the simulated anisotropic data and the calculated isotropic model. Case 1 is representative of a VESUVIO measurement from a 10% scattering-power sample measured for ca. 3600 μAh of integrated ISIS proton current and acquired with the original LLDT at 600 keV while case 2 corresponds to the same acquisition time but with the error bars and noise as if all detectors had the same modified LLDT as detector A.

Table 4.3: $\langle E_k \rangle_\alpha$ values of the calculated anisotropic $\bar{F}(y)$ and of the simulated experimental $\bar{F}(y)$ in the two cases obtained from the fitting procedure.

$\langle E_k \rangle_\alpha$	Input parameters [meV]	case 1 [meV]	case 2 [meV]
$\langle E_k \rangle_x$	8.3	7.9 ± 2.4	8.1 ± 1.5
$\langle E_k \rangle_y$	33.2	35.7 ± 4.3	34.7 ± 2.7
$\langle E_k \rangle_z$	101.6	98.4 ± 4.9	99.7 ± 2.9
$\langle E_k \rangle_{tot}$	143.1	142.0 ± 6.9	142.5 ± 4.2

4.2.3 Mean-force analysis with optimized set-up

The MF was calculated using the script reported in Appendix C and following the derivation reported in Sec. 2.4.1 and in Ref. [46, 47, 45]. The MF determined from the simulated experimental NCPs in Figs. 4.9(a–b) after the correction of the FSEs, are shown in Fig. 4.10(a–b), together with the MF from the isotropic and harmonic system reported in blue in Fig. 4.8. The anisotropic behaviour, *i.e.*, the deviation from linearity, is clearly identified for case 1, where noise and error bars are comparable to the present performance of VESUVIO, for $x_{\parallel} > 0.18 \text{ \AA}$, while in case 2, the optimized configuration proposed in this work, the discrimination is already possible for $x_{\parallel} > 0.14 \text{ \AA}$. In this case the optimization

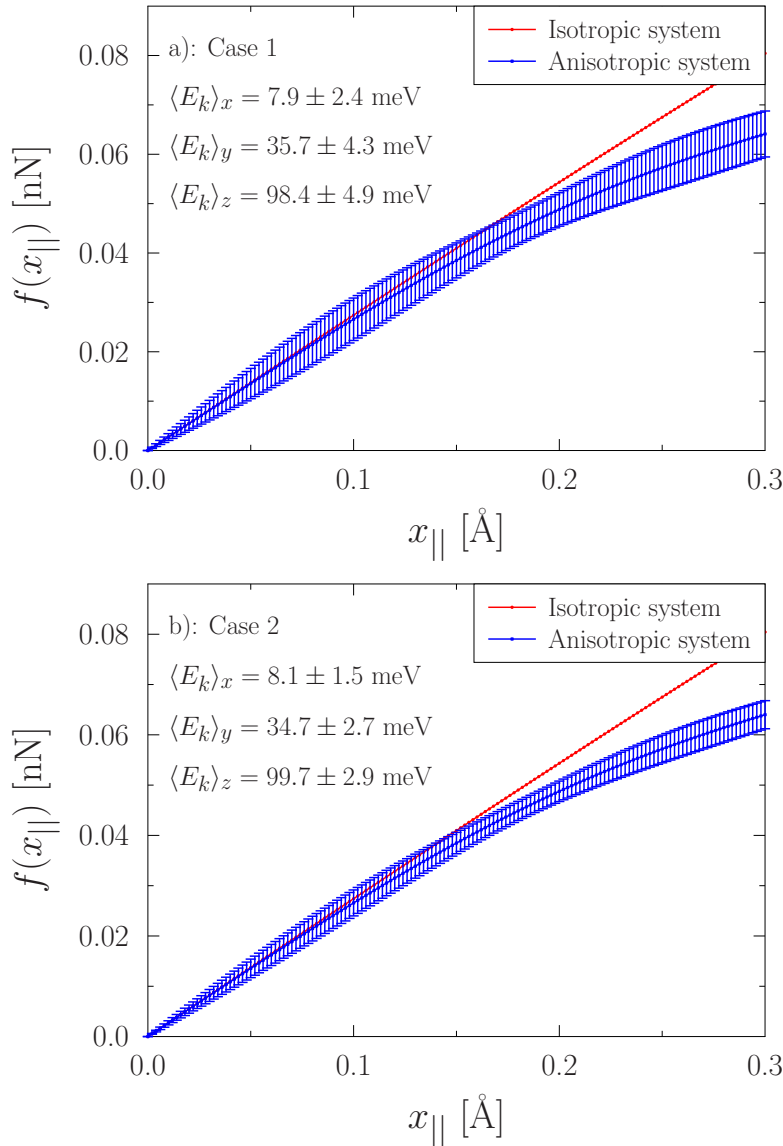


Figure 4.10: (a–b) MF for calculated isotropic and harmonic system in red and MF for simulated experimental NCPs of Figs. 4.9(a–b) in blue. The results from the fitting procedure are also reported for the two cases. The red line is reported without error bars as it is a calculation used to determine when the simulated experimental results start to show an anisotropic behaviour.

proposed is clearly to be preferred as allows the identification of the anisotropy, *i.e.* the

deviation from the isotropic line, of the potential for lower x_{\parallel} . Furthermore the lower error bars allow measurements more accurate or, equivalently, faster.

4.2.4 Bi-parametric spectra

In this section I will describe a technique implemented on the γ DA, called bi-parametric or T-PGAA acquisition, that allows an off-line selection of the LLDT in contrast to what performed in the polyethylene experiment where the LLDT change was achieved with hardware tune of the discrimination module.

This technique is the composition of:

- Neutron Resonance Capture Analysis (NRCA)
- Prompt Gamma Activation Analysis (PGAA)

In the NRCA it is exploited the (n, γ) radiative neutron capture to study the photons emitted by a sample [94]. In this technique the neutron ToF is measured (the travel time of photons is negligible) obtaining the energy value of the radiative absorption which is characteristic of an isotope with the relation:

$$ToF = \frac{L_0}{v_i} = \frac{\sqrt{m}}{2} \frac{L_0}{\sqrt{E_i}} \quad (4.2)$$

where L_0 , v_i and E_i are the incident flight path, neutron velocity, and energy respectively. In the PGAA the (n, γ) reaction process is used to study the energy of photons emitted by a sample [95] after the neutron absorption. In fact, each isotope has a characteristic emission spectrum of (n, γ) , in other words after the neutron absorption there is a photon emission of energy value described by the associated cross section.

The bi-parametric acquisition is obtained merging the PGAA and NRCA technique [96]. In this way we get the Time-resolved Prompt-Gamma Activation Analysis (T-PGAA) with a bi-parametric map which gives information about the energy spectrum of photon emitted at a certain ToF. In our experiments the (n, γ) emission of the AF builds up the DINS signal where the recoil peaks are situated at a certain ToF value and information about the photon energy of photons who build the peak is lost. Sometime it is useful to study the energy distribution of the photons emitted by the analyser due to the neutrons scattered by the sample. Using the tabulated (or measured) energy distribution of photon emitted by (n, γ) analyser reaction we are able to distinguish the signal from the background simply because background photons have a different energy distribution. For these reasons we performed a first test with a bi-parametric acquisition of a gold sample on the VESUVIO spectrometer, with an additional YAP detector placed within the blockhouse, at ca. 90 cm from the sample position. The scintillator dimensions were 1 inch in thickness and 1 inch in diameter. The detector was shielded with a 5-cm-thick wall of Pb bricks towards the beam stop, and we noticed that such facility, not available at present for the other YAP detectors, reduced significantly the background radiation from low-energy photons. An 8-channel CAEN digitiser DT5730 was used to acquire the signal from the YAP as well as the time stamp of the ISIS synchrotron, t_0 . The time stamp is taken as the moment the neutrons are generated within the source. For each photon detected by the YAP, the area of the peak, proportional to the photon energy, E_{γ} , and the detection time, t_{γ} , were recorded.

For each event, the ToF is calculated by taking the difference between the detection time and the time stamp, $ToF = t_\gamma - t_0$. The result is an intensity contour map as a function of the photon energy and ToF. The digitiser stores the event in a binary format to compress the amount of the data. The output is analysed in order to extrapolate the ToF, E_γ and intensity with a python script reported in Appendix B that will be implemented in Mantid [97, 98, 99, 100, 101, 102], the software used at ISIS for data analysis.

The tests on the biparametric acquisition were performed on a gold foil where the neutron resonance at 4.9 eV corresponds to ca. 360 μ s as obtained from Eq. 4.2. Fig. 4.11 represents a biparametric acquisition of a gold foil where the most important contribution to the resonance, and hence to the VESUVIO signal, is concentrated at low energy where the detector is more efficient and the gold emission is predominant as shown in Fig. 4.1.

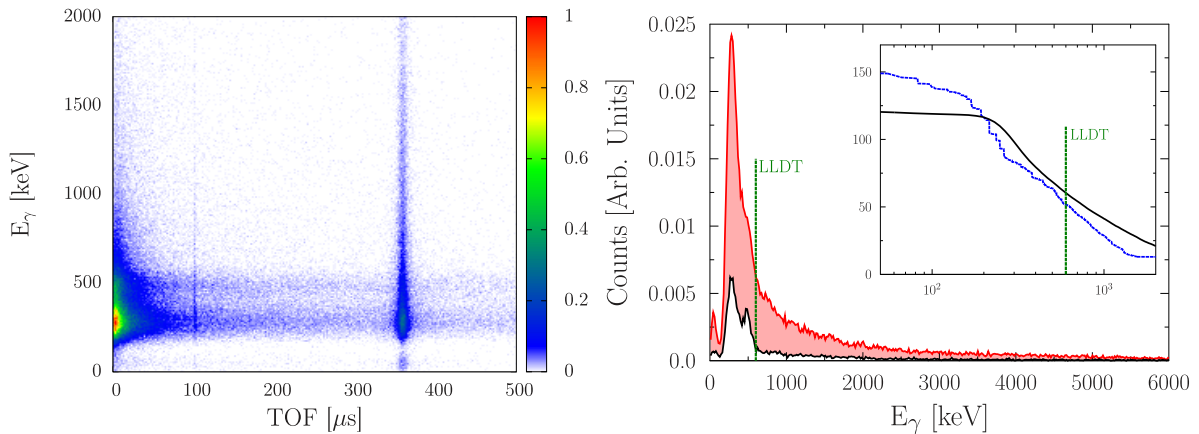


Figure 4.11: (Left) Bi-parametric data from ^{197}Au measured on the VESUVIO spectrometer, as function of the neutron ToF and photon energy. The colour map shows the counts in arbitrary units. (Right) The projection on the photon-energy axis of the above data integrated between 340 μ s and 380 μ s (red line), and 240 μ s and 280 μ s (black line), corresponding to the on- and off-resonance signal from the gold resonance at ca. 4.9 eV, respectively. In the insert, the integration of the on-resonance signal as a function of the lower limit of integration [keV] (black line), compared to the prediction from Ref. [86] in arbitrary units (blue-dashed line).

Fig. 4.11 (left) shows the biparametric spectrum from the Au sample in the ToF range typical of DINS measurements on VESUVIO, and for photon energies below 2 MeV. Vertical lines correspond to neutron-induced resonances at ca. 4.9 eV and 61 eV. The horizontal line at ca. 480 keV represents the main component to the gamma background from the prompt photons emitted by boron in several instrument components. At lower photon energies the detector efficiency and the background increase, corresponding to a step increase in the count rate, with an apparent maximum at the detection threshold of 200 keV. In Fig. 4.11 (right), the black line corresponds to the bi-parametric spectrum projected onto the photon-energy axis by integration between 240 μ s and 280 μ s (off resonance), and one can recognise the boron peak at ca. 480 keV. In the same Figure, the red line is the result of a similar procedure as before with the ToF integration between 340 μ s and 380 μ s, *i.e.*, corresponding to the prompt cascade from the resonance at 4.9 eV (on resonance). One can notice a huge increase in the signal with respect to the off-resonance background. This increase is mainly due to the many intense peaks in the photon emission spectrum of Au

between 200 keV and 300 keV, already showed in the insert of Fig. 4.1. On VESUVIO, the DINS signal is proportional to the integral of the on-resonance spectrum integrated between a fixed upper limit (around 6 MeV for gold [86]), and the lower limit at the value of the LLDT. The blue dashed line in the insert of Fig. 4.11 (right) corresponds to such numerical integration of the tabulated Au resonance from Ref. [86], and it is compared to the numerical integration of our on-resonance experimental signal (black line). The shape of the step-like prediction curve compares very favourably with the experimental one, considering that the latter i) was obtained with a low-resolution YAP detector not enabling the discrimination of neighbour peaks; and ii) the measured intensity is partially redistributed between photon peaks and Compton edges. Both curves suggest that the measured signal from Au can increase up to 2-3 times when the LLDT is lowered between 60 keV and 200 keV. One should notice that the LLDT used at present was established when DINS spectra on VESUVIO were collected using a ^{238}U foil. Uranium has less intense photon peaks below 600 keV, and mainly centred around the background peaks from boron and annihilation, thus explaining the decision to set the LLDT at 600 keV in the first place [77].

4.3 Biphenyl

Lignin, particularly abundant in the cell walls of plants and bark [7], is the main component of the second-generation biomass used to produce fuel. To avoid its disposal as a by-product of the process, effort is directed into the thermochemical conversion of lignin to higher-value products [8, 9, 10, 11, 12]. To better understand the catalysed decomposition of lignin, it is common to use model compounds containing the most significant linkages present in lignin and show similar characteristics to the natural biopolymer [13, 14, 15]. Biphenyl linkages represent the second most abundant linkage type in softwood lignin [16] and are often used as a model compound to tackle the conversion of lignin into monocyclic hydrocarbons [17].

Because of the complexity of the process of dissociation of lignin and its compounds, modelling and computer simulations, such as Density Functional Theory (DFT), often rely on the harmonic approximation of the nuclear dynamics (*e.g.*, see Refs. [14, 15]). This is taken as a safe approximation most of the times, although it is seldom benchmarked.

We present an experimental investigation of the hydrogen momentum distribution in biphenyl using deep inelastic neutron scattering. DINS measurements were performed at the VESUVIO [103, 66] spectrometer on a 0.5-mm-thick biphenyl powder sample ($\text{C}_{12}\text{H}_{10}$) commercially available [104] enclosed in an Al container and placed within the evacuated instrument tank at room temperature.

Our experimental results suggest that the local potential affecting hydrogen is both harmonic and isotropic within experimental uncertainties. This feature is interpreted in the framework of the central limit theorem, whereby the three-dimensional momentum distribution is expected to become a purely Gaussian function as the number of vibrational modes in a system increases. We also performed Ab-Initio phonon calculations on biphenyl and other saturated hydrocarbons, from methane to decane as will be reported in Sec. 5.4. The γ DA is used to increase the count-rate and signal-to-background ratio.

4.3.1 Configurations for the γ DA

The values of the AF and FF thickness $d_{AF} = d_{FF} = 12.5 \mu\text{m}$ used at present was obtained from the analysis of a figure of merit optimizing both the count rate and the width of the FCT transfer function T_{FCT} [71]. However, the resolution function of the instrument is dominated, in forward scattering, by the uncertainty on the scattering angle [105, 106, 107], thus representing a mismatch to the other resolution components. Inspection of Fig. 4.13 (right) suggests that, by doubling the thickness of both the AF and the FF (full-diamond marker), one can increase the count rate by ca. 26%. However, thicker cycling foils are also expected to increase the sample-dependent background. In this experiment I have tested subsets of detectors with different thickness of the two foils, as well as with and without additional shielding, so as to suppress the increased FCT background and find the optimal γ DA configuration. The resulting set-up of the VESUVIO forward-scattering detectors was as follows:

- detectors 135 – 182 in the standard geometry, with $d_{FF} = d_{AF} = 12.5 \mu\text{m}$. This configuration is referred to as C(1,1);
- detectors 184 – 186 with $d_{FF} = 25 \mu\text{m}$ and $d_{AF} = 12.5 \mu\text{m}$, referred to as C(2,1);
- detectors 189 – 190 with $d_{FF} = 25 \mu\text{m}$ and $d_{AF} = 25 \mu\text{m}$, referred to as C(2,2);
- detectors 187 – 188 with $d_{FF} = 25 \mu\text{m}$ and $d_{AF} = 25 \mu\text{m}$, and with 1.25 mm of lead shielding in front of the analyser foil, referred to as C(2,2,Pb).

The detectors are labelled as in Ref. [3] and Fig. 3.5, in Fig. 4.12 the configurations tested are represented. In yellow the gold foil already present and in orange the second foil added of the same thickness. Acquisition C(2,1), C(2,2) and C(2,2, Pb) were collected in foil-in and out configuration for ca. 720 μAh while C(1,1) for ca. 12500 μAh of the ISIS synchrotron proton charge. The change in the thickness of the gold foils is performed in order to verify the improvement described in Section 4.3.2 while the lead foil is used in order to suppress the gamma background coming from the blockhouse elements and the FCT technique. In fact, lead has a high photon absorption probability, for a 1.25 mm foil the absorption is ca 40% at 300 keV and increases up to 1 for lower energies while it has a low neutron cross section. For this reason the lead foil in front of the AF will stop the background photons from the blockhouse but lets the neutron pass and produce the (n, γ) neutron conversion with the AF.

Moreover, the ToF spectra from detectors 184–190 were acquired using the biparametric acquisition T-PGAA. The T-PGAA acquisition was used in order to obtain DINS spectra for a series of LLDT values, between 30 keV and 600 keV, so as to characterise the instrument response in the aforementioned configurations of detectors 184–190.

4.3.2 Transfer Function Optimization

In the Foil Cycling Technique (FCT) [71] currently used on VESUVIO, two gold foils are used to largely suppress the environmental gamma-background from the blockhouse elements and to reduce the width of the resolution function as described in Sec. 3.3.2. When the FF is in the foil-in configuration, only neutrons with energy E_r that are not absorbed by the FF are detected by the YAP detectors while the photon produced by the

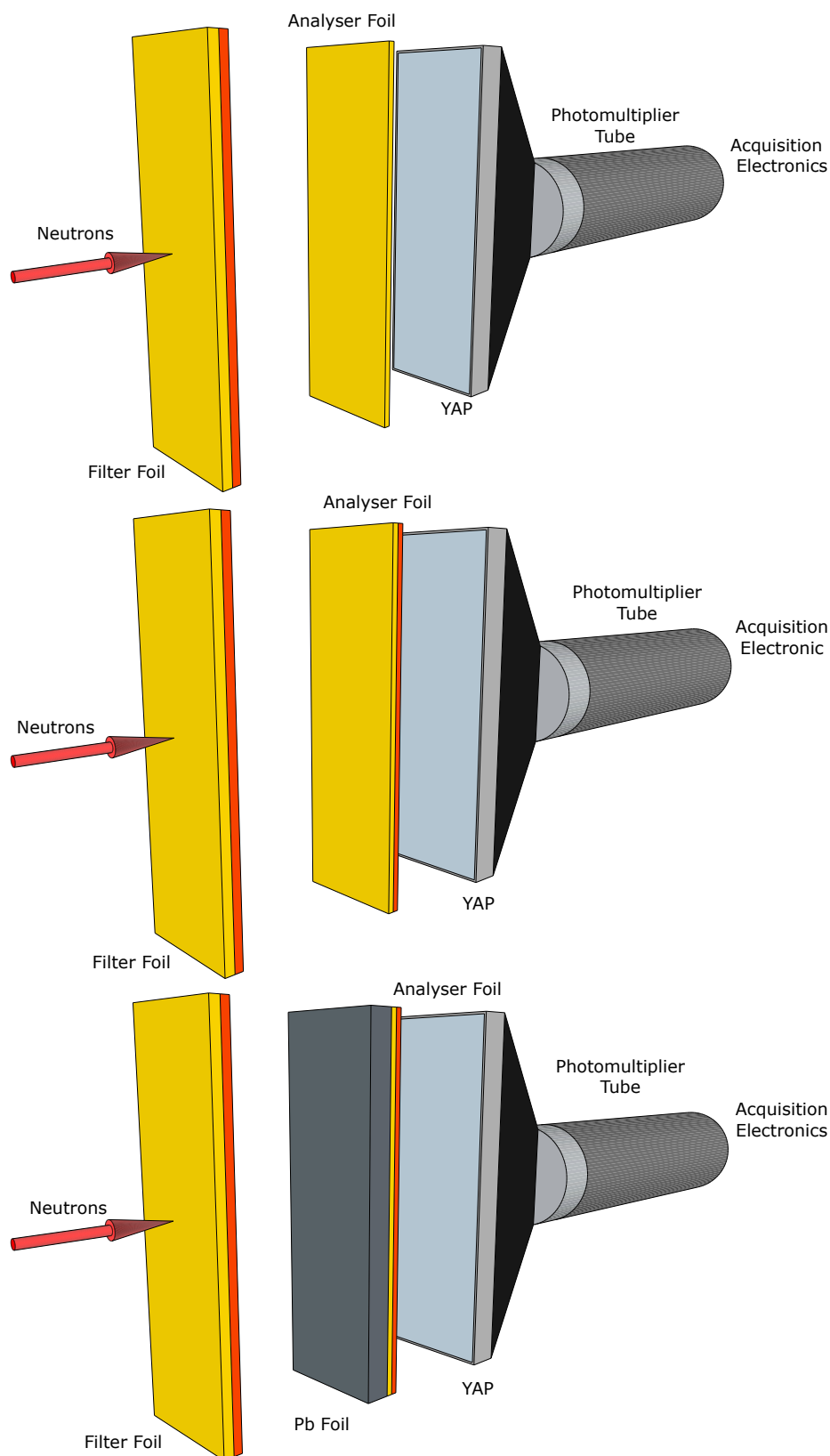


Figure 4.12: The three optimised γ DA set-ups tested. The gold foils currently used on VESUVIO are represented in yellow as opposed to those used in the new configurations, represented in orange. Finally the lead shielding is in dark grey in the bottom figure.

cyclers are much less detected due to the lower solid angle of the detector and make up the cycling gamma background [103]. The improvement of the transfer function can be explained considering the foil-in and out configurations where an AF of thickness d_{AF} and a FF of thickness d_{FF} are used. In the foil-out position the transfer function T_{out} takes the form

$$T_{out} = 1 - e^{-n\sigma_\gamma(E)d_{AF}}, \quad (4.3)$$

where n is the number of gold nuclei for unit volume and $\sigma_\gamma(E)$ is the energy-dependent resonant gamma-emission cross section. The transfer function of the cyclers is T_c

$$T_c = e^{-n\sigma_T(E)d_{FF}}, \quad (4.4)$$

where σ_T is the total absorption neutron cross section accounting for all the physical processes. In the foil-in configuration T_{in} is the the product of T_{out} and T_c

$$T_{in} = T_{out} \cdot T_c = e^{-n\sigma_T(E)d_{FF}}[1 - e^{-n\sigma_\gamma(E)d_{AF}}]. \quad (4.5)$$

The FCT transfer function, T_{FCT} , is obtained as the difference of the foil-out and in configurations improving the VESUVIO resolution with the subtraction of the Lorentzian tails of the neutron absorption. As in correspondence of the resonance $\sigma_T \sim \sigma_\gamma$ the T_{FCT} becomes

$$T_{FCT} = T_{out} - T_{in} = [1 - e^{-n\sigma_\gamma(E)d_{AF}}][1 - e^{-n\sigma_\gamma(E)d_{FF}}], \quad (4.6)$$

that is symmetric upon the change of the cyclers and analyser foil thickness. The transfer function is improved when its peak value at E_r is approximately 1 without affecting the resolution function that is in forward scattering, analysed in this paper, mainly affected by the angular resolution rather than the energetic one. In Fig. 4.13 (left) T_{FCT} for three thickness configuration is represented as a function of the neutron energy (right and upper axis): the current 12.5 – 12.5 μm , 7 – 7 μm and C(2, 2). Together with T_{FCT} an intensity contour map of the T_{FCT} peak values is also represented as a function of the cyclers and analyser thickness (left and bottom axis). The map and the transfer function show how the T_{FCT} peaks increase with the foil thickness going from yellow to green. In the right panel of Fig. 4.13 three paths on the contour map are reported where one of the two foil has a fixed thickness of 25 μm , 12.5 μm and when both of them have the same thickness. The expected improvement from the current configuration to the proposed one is ca. 26% as shown in the right panel of Fig. 4.13.

4.3.3 Energy Threshold Optimization

Data reduction

The raw data in configuration C(1,1) were analysed with a procedure available within the VESUVIO routines described in Ref. [103, 108] and in Sec. 3.3.3. Raw biparametric data in configuration C(2,1), C(2,2) and C(2,2,Pb) are acquired in the VESUVIO foil-in and -out position. Then the two spectra are normalised to the acquisition time and to the same area for a ToF greater than 420 μs , outside the kinematic of the DINS domain, before the subtraction. In order to obtain the ToF VESUVIO measurements the biparametric spectra are projected on the ToF axis for each chosen LLDT as shown in Fig. 4.14. Here each LLDT of the right panel indicates the sum of the signal for energy greater than the LLDT,

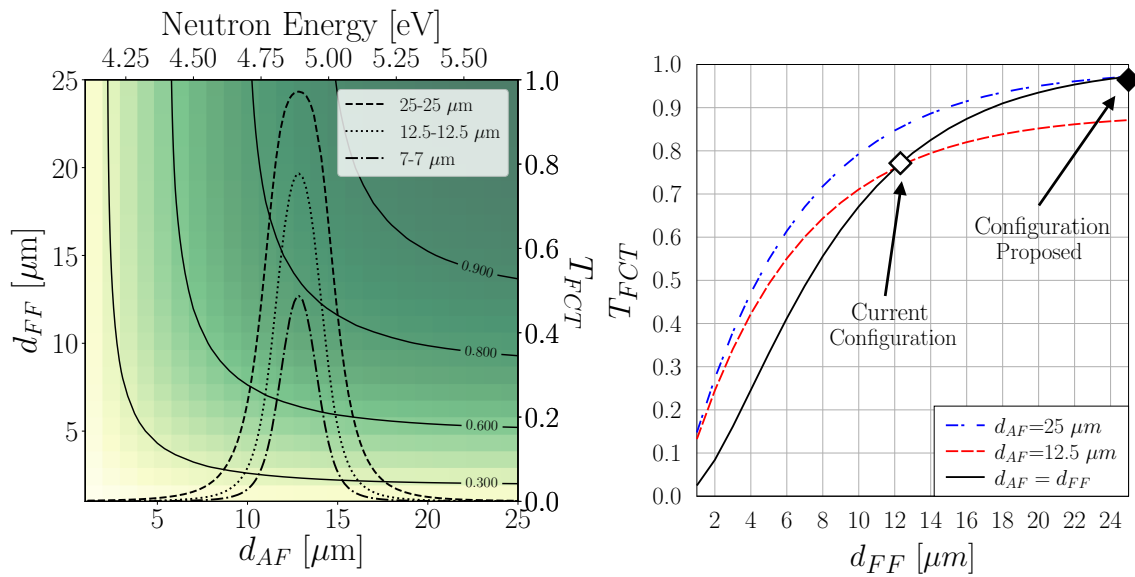


Figure 4.13: (Left) Transfer function of the original 12.5 – 12.5 μm , proposed 25 – 25 μm and 7 – 7 μm configuration are represented (right-top axes); a contour map for the calculated neutron transfer peak as a function of the cycling and fixed foil thickness is also present on the background (left and bottom axes). (Right) Three paths on the intensity contour map are represented where the two foils have the same thickness and when one of them is 25 or 12.5 μm -thick.

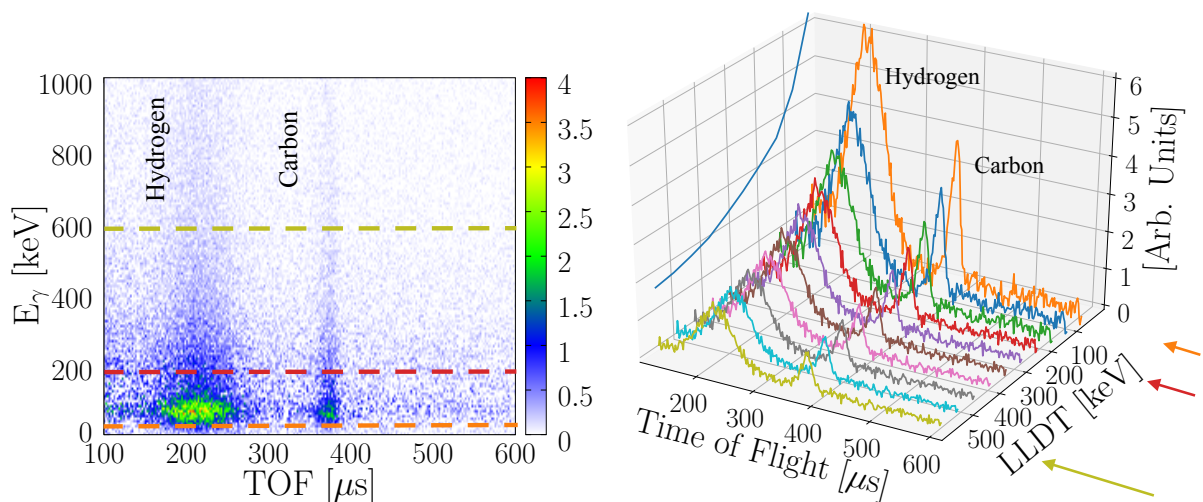


Figure 4.14: (Left) Biparametric acquisition of DINS measurement after the foil cycling subtraction. (Right) ToF spectra obtained projecting the biparametric measurements on the ToF axis with an increasing values of the LLDT. The arrows indicates the LLDTs associated with the dotted line of the left panel: the ToF signal of the right panel comes from the sum of the energies greater than the dotted line on the contour map.

on the left panel, projected on the ToF axis. The right panel shows how the count rate increases as a function of the energy threshold quantified in detail in this Section. After the ToF projection the data analysis is performed within the Mantid environment [97]. The obtained spectra are affected by an acquisition background that has the same shape of the foil in/out spectra for low ToF. The background is subtracted with an exponential decay fit that resembles the foil in/out spectra before the subtraction procedure as shown in Fig. 4.15.

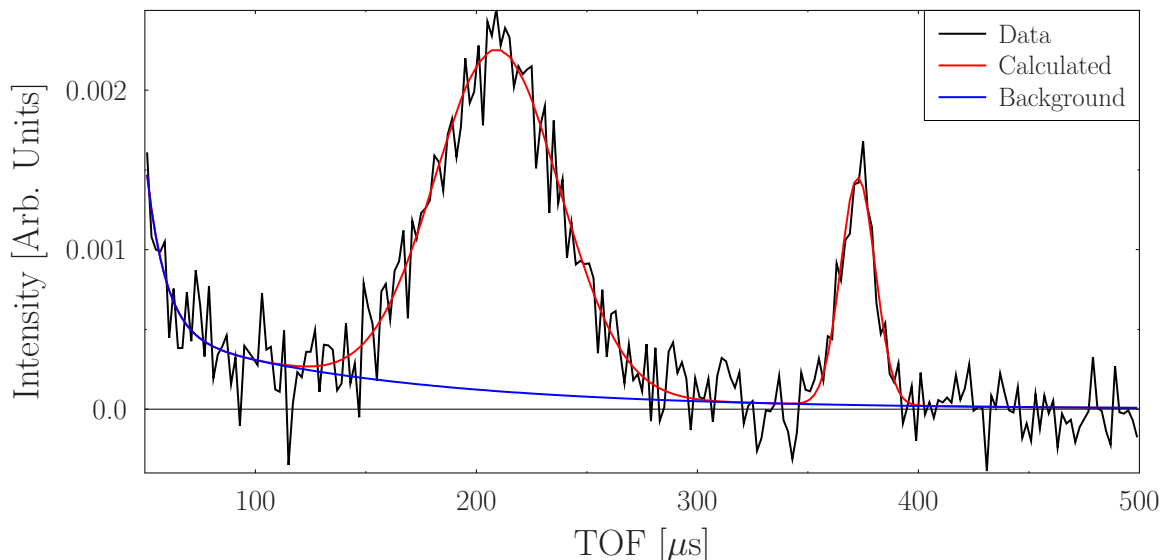


Figure 4.15: ToF spectrum of detector 184 after the FCT (black line). At low ToF there is a background subtracted with an exponential decay fit (blue line) with the same shape of the foil in/out measurement.

As the contribution to the multiple scattering has been taken into account with the previous fitting procedure and as the sample scattering power is less than 10%, no further multiple scattering correction is applied. Finally the gamma background from the FCT is calculated and subtracted as explained in Ref. [103].

Count rate increase and signal to background ratio optimization

In this section the effect of the configurations C(2,1), C(2,2) and C(2,2,Pb) is discussed in terms of count rate increase and signal to background ratio improvement [87, 109, 84, 85] on the ToF spectra once the energy range of the biparametric acquisition is selected. The optimization is taken with respect to the original configuration for each detector, *i.e.* 600 keV and $(d_{AF}, d_{FF}) = (12.5, 12.5) \mu m$, on the hydrogen peak. The signal is calculated by integrating the biphenyl hydrogen peak in a range of 100 μs around the peak position and the background value is obtained by integrating the foil-in configuration in the same ToF range. In Fig. 4.16 the count rate increase is represented for the three configurations, in the insert the signal to background ratio is referred to the standard configuration at 600 keV. The line style is associated with the configuration of the detection set-up (original with dashed line) while the colour is associated with the detector used. The signal gain decreases as the LLDT is increased until it reaches one for the original configuration

at 600 keV (the normalization value). For each LLDT the difference between the original and modified configuration gain is associated with the set-up, *i.e.*, Pb shielding and foil-thickness optimization. Both for the original and modified configuration the signal to background ratio decreases as the LLDT decreases. For C(2,1) the gain in the modified configuration is about 1.5 times, for each LLDT, the original one and the gain increases until 5. For this configuration there isn't a significant difference between the original and modified configuration for the S/B ratio as a function of the LLDT.

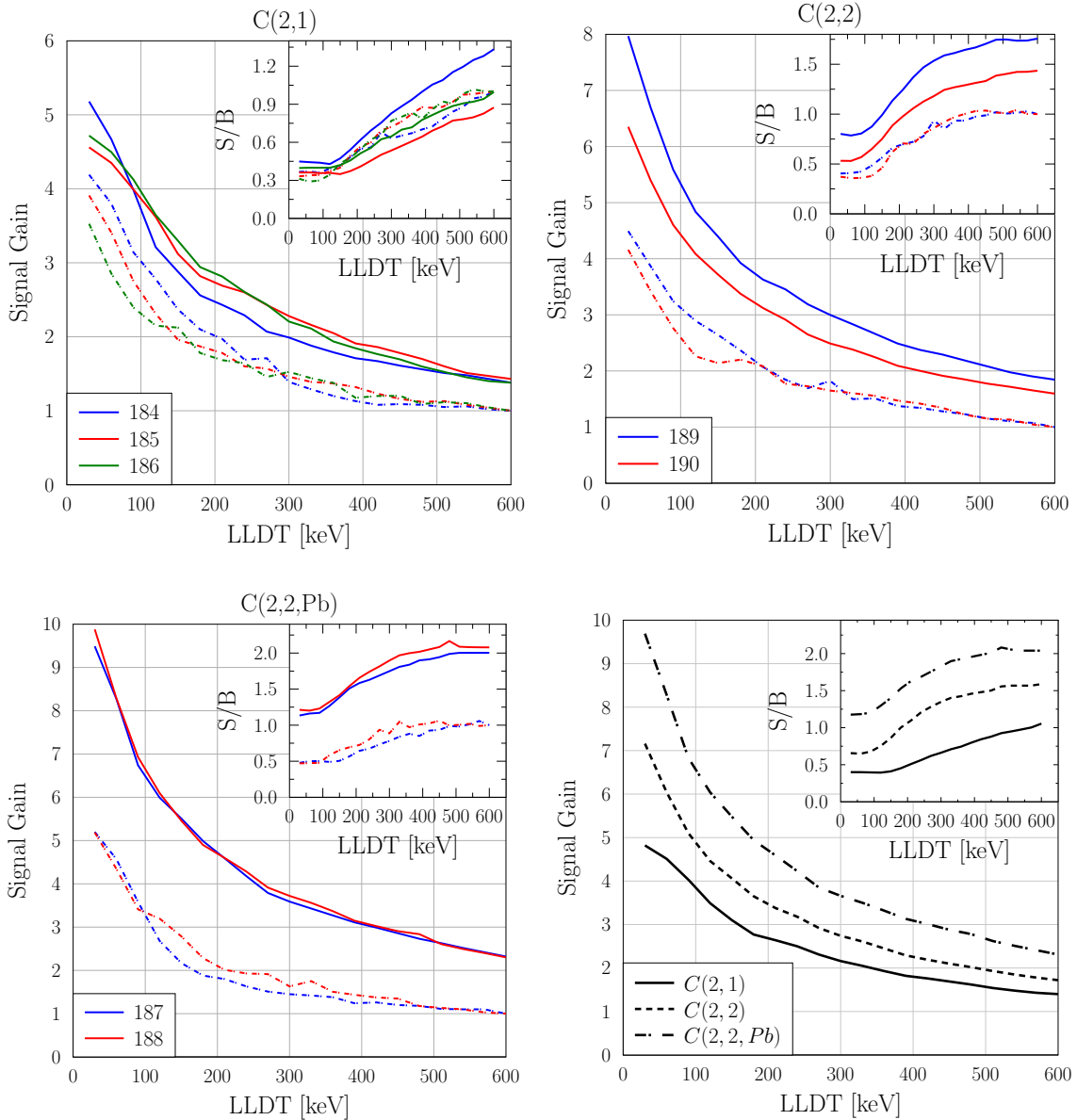


Figure 4.16: Signal gain of the γ DA configurations tested with respect to the standard configuration at 600 keV (represented with dashed lines) acquired with the same detector. In the insert the signal to background ratio normalized as the signal gain. At the bottom right panel the average over the detector used for each configuration is reported.

For C(2,2,Pb) the modified configuration is about 2.5 times the original one for each LLDT and the gain ranges from 2.5 to 10 times the original configuration. The signal to background ratio is improved by a factor 2 with respect to the original configuration and

it decreases of about 4% at 200 keV. Finally for C(2,2) the gain is about 1.7 times the original configuration and the gain increases in modified set-up up to a factor 8. For this configuration the S/B ratio is increased by a factor 1.5. In the same panel the detector average for each configuration is also represented. The most promising configuration is the C(2,2,Pb), in fact, taking as an example 200 keV as the final LLDT for the γ DA, there is a count rate increase of ca. 5 times and a signal to background optimization of ca. 50%. In Fig. 4.16 it can be seen the difference between the detector efficiency, in fact even if the overall behaviour is the same for all the detectors the absolute values changes for the different elements.

4.3.4 DINS

The West-scaling variable [42], y , was used to fit the average of the experimental $n(p)$. In this space the detector-averaged NMD is called $\bar{F}(y)$ and it is reported in Fig. 4.17 together with its fit and resolution function for the C(1,1) and C(2,2) configuration. The resolutions represented in the Figure shows how the contribution to the resolution broadening of the transfer function is negligible; in fact, the angular uncertainty dominates in the forward scattering detection. This result was obtained following the standard reduction of the

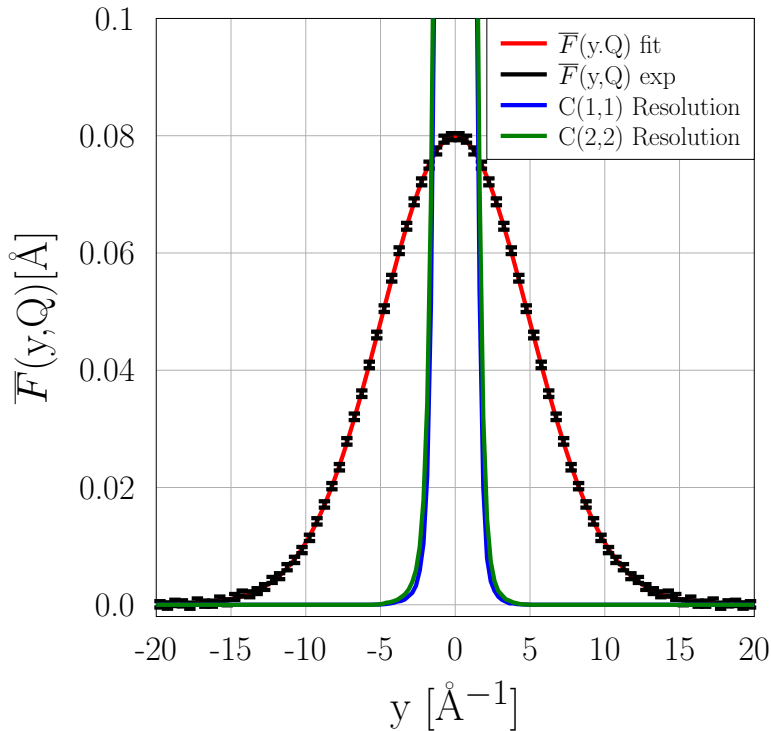


Figure 4.17: Symmetrised experimental and fitted $\bar{F}(y, Q)$ with resolution function in the C(1,1) and C(2,2) configuration.

data [108, 81], and symmetrizing the corrected NCP so as to remove the Q -dependent final state effects [110]. The transmission of the sample for epithermal neutrons was measured concurrently [111] and found to be 0.926, corresponding to a minute multiple-scattering

contribution. Moreover, intensity constraints were applied to the fit of hydrogen and carbon NCPs, keeping them proportional to their total bound scattering cross sections [108, 112] and molecular stoichiometry. The experimental NCP was fitted via a numerical convolution of the Gauss-Hermite expansion (Eq. 2.57) with the instrument resolution function [81], $\bar{F}(y, Q) = \bar{J}(y) \star \bar{R}(y, Q)$. The result of the fitting procedure is also reported in the same figure, showing a satisfactory agreement with the experimental data. As the result of the fit, we found $\langle E_k \rangle_H = 145.7 \pm 1.4$ meV. The first Hermite coefficient was found to be $c_4 = -0.008 \pm 0.012$. Therefore, we set $c_4 \equiv 0$ in the final fit. The possibility to reproduce the experimental NCP with a simple Gaussian function brings to the conclusion that the effects of anharmonicity and anisotropy are approximately negligible in the ground-state potential affecting hydrogen, a point that we interpret in the framework of the Central Limit Theorem [113, 114], as we discuss in detail in Sec. 5.4. This result was also obtained for other samples where C-H bonding is present as in polyethylene as reported in 4.2 and in Ref. [109, 108]. The accuracy of the measurement follows by the fact that detector 135-182 measured the hydrogen dynamics with a good statistics (12500 μAh) and they were all summed in the y space for the experimental NCP fit.

The other configurations are less accurate as they acquired less statistics with few detectors (two or three). For each detector and threshold the spectrum was converted in the y space and fitted after the symmetrization of the experimental NCP. In order to consider the γ DA configurations proposed as eligible candidates for a new VESUVIO acquisition, it was checked that we did not introduce a configuration-related effect on the NCP. In the following, the fitted $\langle E_k \rangle$ are compared for all the configurations. In Fig. 4.18 all the fitted $\langle E_k \rangle$ values are represented with the average and standard deviation of the distribution for each configuration used. Each point of configuration C(1,1) is associated with one detector while for C(2,1), C(2,2) and C(2,2,Pb) with one LLDT. The spread applied to the point is used to make the representation clearer.

The $\langle E_k \rangle$ distributions of all the configurations are the same within one standard deviation. The values of averages and standard deviations of the distributions are reported in Table 4.4. The average of the distribution of configuration C(2,2,Pb) and C(2,2) looks lower than the C(1,1) because the detector used would populate the lowest part of the C(1,1) distribution.

Table 4.4: Average and standard deviations for the $\langle E_k \rangle$ distribution in the configurations tested.

Configuration	Average [meV]
C(1,1)	143 ± 8
C(2,1)	143 ± 11
C(2,2,Pb)	130 ± 5
C(2,2)	135 ± 5

The last check that can be performed is the correlation study between the value of the fit results and the LLDT (for configuration C(2,1), C(2,2) and C(2,2,Pb)) or the detector used (for configuration C(1,1)). In Fig. 4.19 the $\langle E_k \rangle$ values are represented as a function of the LLDT and detector number (configuration C(1,1)), the shadow area and the red line represent the standard deviation of the distributions and average respectively. The LLDTs

and detectors do not affect the measurement if the $\langle E_k \rangle$ distribution is flat as a function of the LLDT/detector as evidenced in the scatter plot of Fig. 4.19.

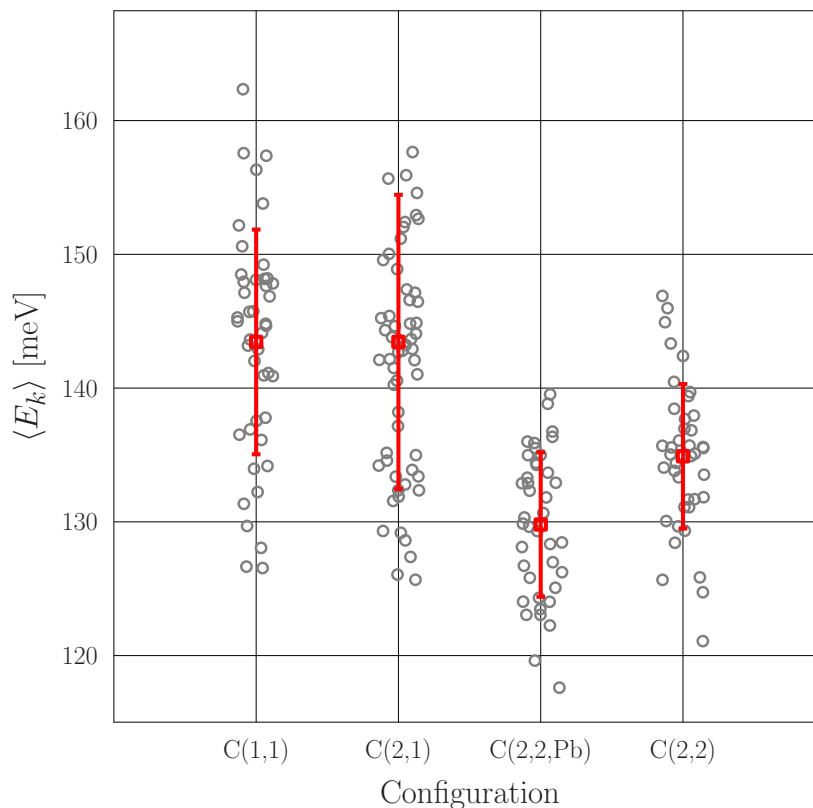


Figure 4.18: Fitted $\langle E_k \rangle$ distribution with average and standard deviation for each configuration used. In configuration C(1,1) each point stands for a detector and for a LLDT in configuration C(2,1), C(2,2) and C(2,2,Pb).

In Figure 4.20 the configuration-averaged $\langle E_k \rangle$ and $\Delta\langle E_k \rangle$ values, *i.e.*, the variation with respect to the average of the distribution, are represented as a function of the LLDT. The distribution of the $\langle E_k \rangle$ does not show a dependence upon the LLDT, in fact, the $\Delta\langle E_k \rangle$ for each set-up at different LLDTs are all within $\pm 8\%$.

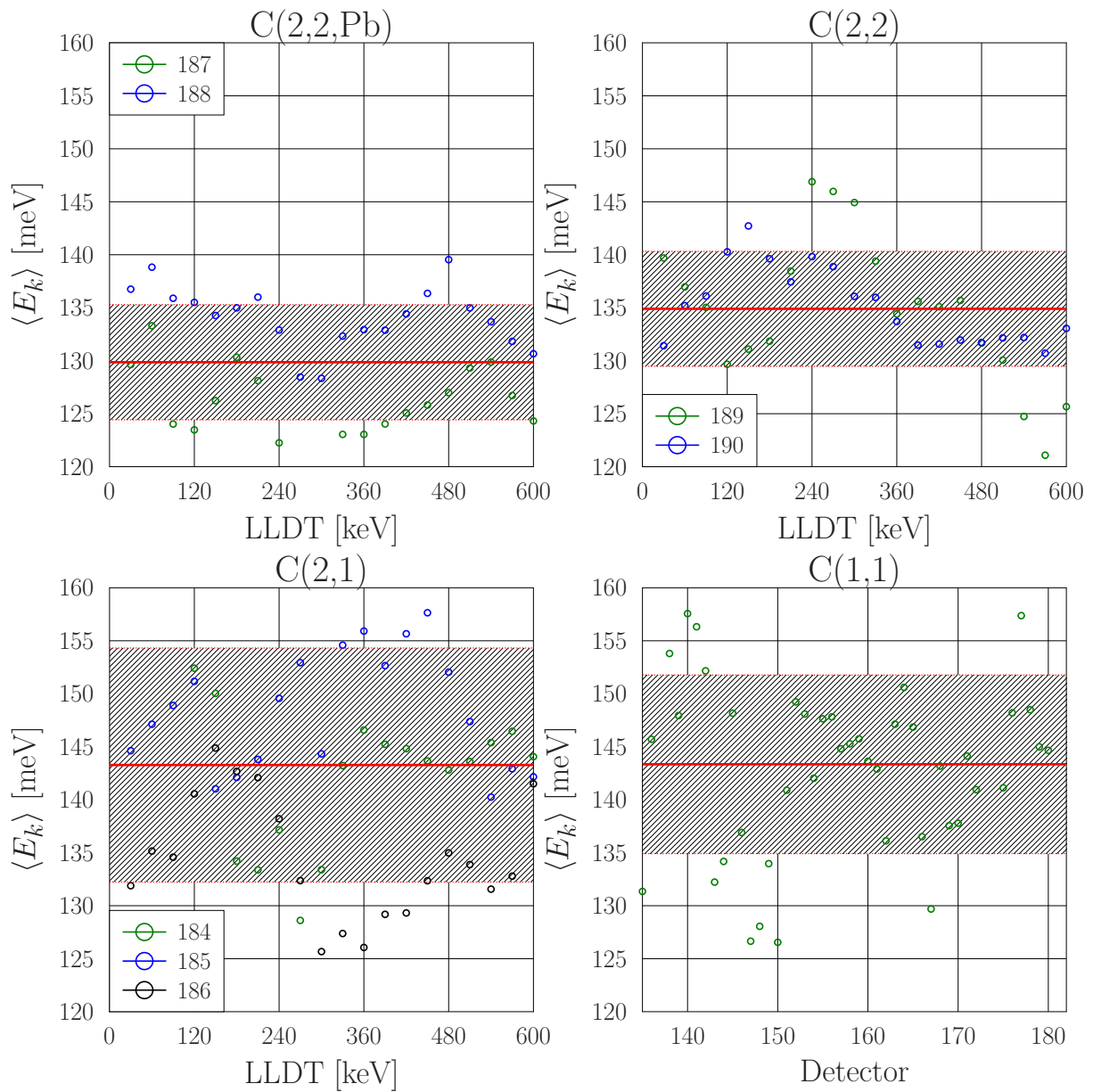
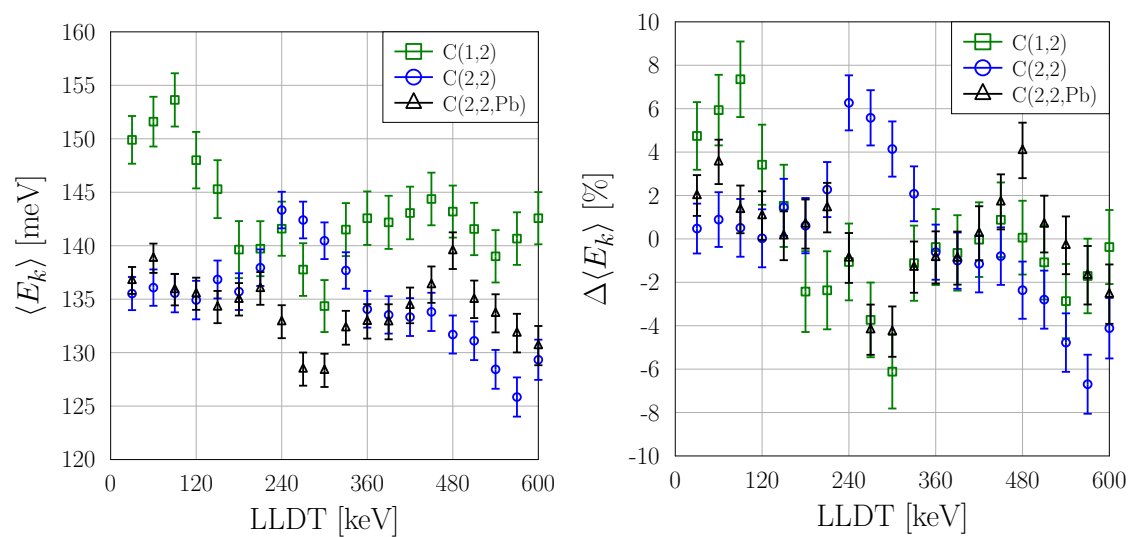


Figure 4.19: Fitted $\langle E_k \rangle$ as a function of the LLDT and detector (conf. C(1,1)); the flat correlation motivate the independence from LLDT/detector.

Figure 4.20: Configuration averaged $\langle E_k \rangle$ and $\Delta \langle E_k \rangle$.

Chapter 5

Ab-initio Simulations

The results of DINS experiments are reported in Sec. 4.3, in this section we will compare the experiment with Ab-Initio simulations and interpret the result in the framework of the Central Limit Theorem (CLT).

5.1 Adiabatic Approximation

A crystal sample is made by a large number of interacting particle so as a theoretical approach cannot avoid some approximations. The Hamiltonian for a crystal in the non-relativistic limit and considering just the Coulomb interaction is

$$H_c = T_N + T_e + V_{ee} + V_{eN} + V_{NN} = - \sum_i \frac{\hbar^2}{2M_i} \nabla_i^2 - \sum_I \frac{\hbar^2}{2m_e I} \nabla_I^2 + \quad (5.1)$$
$$+ \frac{1}{2} \sum_{I \neq J} \frac{e^2}{|\mathbf{r}_I - \mathbf{r}_J|} - \frac{1}{2} \sum_{i,I} \frac{Z_i e^2}{|\mathbf{r}_I - \mathbf{R}_i|} + \frac{1}{2} \sum_{i \neq j} \frac{Z_i Z_j e^2}{|\mathbf{R}_i - \mathbf{R}_j|},$$

\mathbf{R} runs over the nuclear coordinates of a nucleus with atomic number Z and mass M while \mathbf{r} runs over the electron coordinates with mass m_e . Where T_N is the nuclear kinetic energy, T_e the electron kinetic energy, V_{ee} the electron-electron interaction, V_{eN} the electron-nucleus interaction and V_{NN} the nucleus-nucleus interaction. The most simple approximation is to notice the difference in the nuclear and electron mass that allows the decoupling of the nuclear and electron motion. This decoupling is called *Adiabatic approximation* or *Born-Oppenheimer approximation*. This approximation is used to fix the nuclear positions while computing the electronic eigenvalues. The eigenvalues obtained as a function of the nuclear position \mathbf{R} describe a potential surface where the nuclei move. The step that follows is the study of the nuclear dynamics. In fact, the resulting Schroedinger equation is

$$[T_N(\mathbf{R}) + T_e(\mathbf{r}) + V(\mathbf{r}, \mathbf{R})] \Psi(\mathbf{r}, \mathbf{R}) = W \Psi(\mathbf{r}, \mathbf{R}) \quad (5.2)$$

with $H_e(\mathbf{r}, \mathbf{R}) = T_e + V_{ee} + V_{eN} + V_{NN} = T_e(\mathbf{r}) + V(\mathbf{r}, \mathbf{R})$ the electronic Hamiltonian. Taking $\Psi(\mathbf{r}, \mathbf{R})$, the crystal wave function, as

$$\Psi(\mathbf{r}, \mathbf{R}) = \sum_m \chi_m(\mathbf{R}) \Psi_m(\mathbf{r}, \mathbf{R}) \quad \text{with} \quad H_e \Psi_m = E_m(\mathbf{R}) \Psi_m \quad (5.3)$$

where Ψ_m is a base for $\Psi(\mathbf{r}, \mathbf{R})$ with $\chi_m(\mathbf{R})$ as coefficients. From this Ansatz follows, within the Adiabatic approximation

$$(T_N + E_n(\mathbf{R}))\chi_n(\mathbf{R}) = W\chi_n(\mathbf{R}), \quad (5.4)$$

where the nuclei are moving inside a potential $E_n(\mathbf{R})$ given by the electronic Hamiltonian. The electronic and nuclear motion are now decoupled and we need to solve as a first step

$$H_e(\mathbf{r}, \mathbf{R})\Psi(\mathbf{r}, \mathbf{R}) = E(\mathbf{R})\Psi(\mathbf{r}, \mathbf{R}) \quad (5.5)$$

and then Eq. 5.4.

5.2 Density Functional Theory

The description of many-particle systems covers much of physics and chemistry. In computational nanoscience we focus on atoms, molecules, and solids, on their structural and cohesive properties, and on how they interact with each other. In the following sections I will describe the electron and the nuclear dynamic calculation and how they relate to the neutron scattering techniques.

5.2.1 Electronic Calculation

The Density Functional Theory (DFT) is used to determine the fundamental-state properties of interacting electrons, Eq. 5.5, reducing the many-body problem to a one-body system. In fact if we perform a 10-time sampling on each electronic and nuclear wave function on the three Cartesian direction we have $(10^3)^{n_{el}+N_{nuclei}}$, a numerical exponential complexity called *Exponential wall*. DFT is based upon the Hohenberg and Kohn theorem and the Kohn and Sham equation, where a single particle electron-density was introduced. In fact, Hohenberg and Kohn [115] showed that ground state properties, in particular the total energy, of a system of interacting particles could be related to the density distribution, $n(r)$. For a ground state of a system of electrons in the presence of a scalar field, they showed that the density uniquely determines the potential. Its application to the total energy of the interacting system is the determination of the energy of the ground state by the solution of a single-particle equations [116]. We can derive with a heuristic approach an expression of the Kohn-Sham equation. First we could try to ignore all the interactions between electrons solving all the single electron Hamiltonian H_0 ; with this poor approximation we have just $n_{ele} \cdot 10^3$ samples to perform. We can then add a potential term V_H which takes into consideration an average interaction between electrons by placing the electron in the V_H mean field called Hartree potential. The third step is to add a V_{xc} potential where all the exchange and correlation of the electrons are considered; we can think about this term as we were in a room full of people and if one person raise one hand all the other people feel the presence of the hand raised. In practice, total energy calculations require approximations to be made for an exchange-correlation energy term V_{xc} . The most common approximation used is the Local Density Approximation (LDA) where the V_{xc} term is taken for an homogeneous electron gas Ref. [117]. Finally, as the Coulomb potential has a singularity, the effect of the core-electrons is considered with a pseudopotential, in fact, it would take a very large number of plane waves to expand the wave functions of core

electrons because they are highly oscillatory near nuclei and, with a good approximation, only valence electrons participate to the chemical bonding [118].

5.2.2 Crystal and Molecule Structure and Vibrations

Until now we discussed the ground state of a system of electrons under the assumption that the nuclear coordinates are fixed. In particular, we have seen how to calculate the total energy, E for such a system using DFT. When the nuclear coordinates are not available from experiment or the information about nuclear position is incomplete it is important to be able to predict the equilibrium structure of a material starting from the first principles for molecules and solids. We could almost say that, while the electron behaves like a wave, the nucleus behaves like a point particle. We can formalize this observation by making the assumption that quantum mechanics is not necessary for describing the dynamics of nuclei, and we can revert to classical mechanics as a first approximation. When the classical Hamiltonian for a set of particles is known, it is possible to use Hamilton's equations of motion in order to derive Newton's equations

$$F_j = \frac{\partial E_j}{\partial \mathbf{R}_j} \quad (5.6)$$

establishes the link between the total energy of electrons and nuclei and the equilibrium structures of materials. In fact, this equation tells us that the equilibrium structures, is the configurations where the nuclei have no acceleration and therefore are immobile in an inertial reference frame. The potential $E_j(R)$ can be taken as a parabolic approximation around the equilibrium configuration, this approximation is referred to as the harmonic approximation where

$$E_j(\mathbf{R}) = E_j(0) + \frac{1}{2}k(d - d_0)^2 \quad (5.7)$$

where $E_j(0)$ is the potential at the bottom of the well and d is the displacement from the equilibrium position d_0 .

The time-dependent position of the j -nucleus can be expressed as

$$\mathbf{R}_j(t) = \mathbf{R}_j^0 + \mathbf{u}_j(t). \quad (5.8)$$

Making use of the adiabatic approximation and considering nuclei as classic particles the nuclear equation of motion 5.6 can be expressed as

$$M_j \ddot{\mathbf{u}}_j = -\frac{\partial E}{\partial \mathbf{u}_j}, \quad (5.9)$$

where the nuclear potential E is calculated by DFT solving Eq. 5.5 with the approximations made in Sec. 5.2.1. The potential can be expanded in a Taylor series around the equilibrium position where the forces on each nucleus vanishes

$$E = E_0 + \sum_{j,\alpha,i,\beta} F_{j\alpha,i\beta} u_{j\alpha} u_{i\beta}, \quad (5.10)$$

with α and β Cartesian directions, *i.e.*, $\hat{\mathbf{n}}_\alpha \cdot \mathbf{u}_j = u_{j\alpha}$, higher orders are neglected in the so-called harmonic approximation. The Newton's equation in this approximation is written as

$$M_j \ddot{u}_{j\alpha} = -\sum_{i,\beta} F_{j\alpha,i\beta} u_{i\beta}. \quad (5.11)$$

The formal solution of Eq. 5.11 is derived introducing the mass-weighted displacements

$$e_{j\alpha} = M_j^{\frac{1}{2}} u_{j\alpha}, \quad (5.12)$$

with this definition the previous equation becomes

$$\ddot{e}_{j\alpha} = - \sum_{i,\beta} \frac{F_{j\alpha,i\beta}}{(M_j M_i)^{\frac{1}{2}}} e_{i\beta}. \quad (5.13)$$

This equation describes the dynamics of $3N_{nuclei}$ springs connected by the $F_{j\alpha,j\beta}$ force constants, with N_{nuclei} the number nuclei in the molecule or in the unit crystal cell. The system is solved by the diagonalization of the $3N_{nuclei}$ by $3N_{nuclei}$ term $\frac{F_{j\alpha,i\beta}}{(M_j M_i)^{\frac{1}{2}}}$ called dynamical matrix, D . Each of the $3N$ eigenvalues of the dynamical matrix, ω_v , is a normal frequency of the vibration v while the associated eigenvector $e_{j\alpha v}$ is the mass-weighted normal mode of vibration of the j -nucleus in the α direction. \mathbf{e}_v gives information about how much the nucleus contributes to the v -vibration, while \mathbf{u}_v can be understood as proportional to a nuclear displacement. With the diagonalization we can write D in its diagonal form Ω and write Eq. 5.13 as

$$\ddot{\mathbf{w}} = -\Omega^2 \mathbf{w}. \quad (5.14)$$

with \mathbf{w} a vector that describe a collective displacement like the displacement of the centre of mass for the translations. As Ω is in its diagonal form we have divided the coupled linear system of Eq. 5.13 in $3N_{nuclei}$ independent simple harmonic oscillators with cosine and sine functions as solutions. Hence we started from a coupled nuclear motion and we ended with decoupled harmonic oscillators where all nuclei move with a frequency ω with a \mathbf{w} displacement proportional to $e_{j\alpha}$ with

$$e_{j\alpha} = \sum_v e_{j\alpha,v} [A_v \cos(\omega_v t) + B_v \sin(\omega_v t)] \quad (5.15)$$

with A_v and B_v determined by the initial conditions on the nuclear position and velocities. The calculation described is usually performed within environment already developed such as Quantum Espresso (QE) [119] and CASTEP [120]. Quantum Espresso (open Source Package for Research in Electronic Structure, Simulation, and Optimization) and CASTEP are a tools for electronic-structure calculations and materials modeling, based on density-functional theory, plane waves, and pseudopotentials. The script for electronic structure calculation is reported in Sec. A.1. In this step the potential where the nuclei can move is calculated with the solution of 5.5. It is important to stress that a single molecule calculation is performed with a single k-point simulation in the Brillouin zone with the molecule in a big unit cell to eliminate the intermolecular interactions. For a crystal calculation instead, more k-points should be used in order to reproduce accurately all the characteristics. In fact, with a $2 \times 2 \times 2$ k-points 8 unit cell will be simulated with the Born Von Karman boundary conditions [121], hence the 8 repeated cells will be our simulated crystal. In Sec. A.2 the script for the phonon calculation is reported where the nuclei are moved in the harmonic potential simulated. As a phonon calculation result, the eigenfrequencies ω_v with the \mathbf{e}_v eigenvectors normalised so as $\sum_{\alpha=1}^3 \sum_{j=1}^N |\hat{\mathbf{n}}_{\alpha} \cdot \vec{e}_{v,j}|^2 = 1$ being $e_{j\alpha v}^2$ the probability to find the j -nucleus in the $\alpha - v$ vibrational state.

5.2.3 Relation between DINS, INS, QENS and Simulation

The simulation of the nuclear dynamics is, in this section, used to derive a link between Quasi Elastic, Inelastic, and Deep Inelastic neutron scattering. In fact, in this section we will relate the kinetic energy measured on VESUVIO with the Mean Square Displacement measured with QENS through the vibrational density of state that can be simulated or deduced by INS experiments.

With the phonon calculation we have the eigenvectors and the eigenfrequencies. The first step is the reconstruction of the Vibrational Density of States (VDoS) $g(\omega)$. As the $|e_{j\alpha v}|^2$ can be seen as the probability to find the j -nucleus in the $\alpha - v$ vibrational state we can build the atom-projected VDoS for the j -nucleus along the direction α in a Cartesian Frame of Reference (FoR) as [122]

$$g_{j\alpha}(\omega) = \sum_{v=1}^{N_v} \delta(\omega - \omega_v) |\hat{\alpha} \cdot \vec{e}_{v,j}|^2, \quad (5.16)$$

where $|\hat{\alpha} \cdot \vec{e}_{v,j}|^2$ quantifies the contribution from the j -nucleus to the v -vibration along the direction α . Here, $\vec{e}_{v,j} = \sqrt{M_j} \vec{u}_{v,j}$ is the eigenvector of the dynamic matrix corresponding to the eigenvalue frequency ω_v , and $\vec{u}_{v,j}$ is the related atomic displacement, expressed as the difference of the time-dependent and mean nuclear positions, $\vec{u}_j(t) = \vec{R}_j(t) - \vec{R}_j^0$. By imposing that, for each vibration v , the sum of the energy uptakes over all atoms and directions is normalized to unity,

$$\sum_{\alpha=1}^3 \sum_{j=1}^N |\hat{\alpha} \cdot \vec{e}_{v,j}|^2 = 1, \quad (5.17)$$

the total VDoS is normalized to the number of vibrations,

$$\int_0^\infty g(\omega) d\omega = \sum_{j,\alpha} \int_0^\infty g_{j,\alpha}(\omega) d\omega = N_v. \quad (5.18)$$

In Fig. 5.1 the VDoS of biphenyl is represented where the carbon and hydrogen contribution to the total $g(\omega)$ is divided by colours; their sum is normalised to $3N_{nuclei}$. Both of the contributions can be split amongst N_{nuclei} to obtain the individual carbon/hydrogen nucleus contribution $g_j(\omega)$. Each individual contribution takes into account all the Cartesian directions and can be divided by three to get the $g_{j\alpha}$ in the isotropic case; generally for simulations we have access to all the direction without the necessity to use the isotropic approximation.

We can see how the hydrogen contribution to the total $g(\omega)$ increases at higher energies with the molecule stretching modes while carbon contributes more where the motion of the centre of mass is involved at lower energies. The kinetic energy is strictly correlated with the vibration: in the harmonic approximation each vibration brings $\frac{\hbar\omega}{4}$, this quantity should be multiplied by the probability that the nucleus vibrates at that frequency and by the thermal occupation number. Hence, for a finite temperature T , one can express the nuclear mean kinetic energy of atom j in the direction α as [56, 57, 58, 59]

$$\langle E_k \rangle_{j,\alpha} = \sum_{v=1}^{N_v} \frac{\hbar\omega_v}{4} |\hat{\alpha} \cdot \vec{e}_{v,j}|^2 \coth\left(\frac{\hbar\omega_v}{2k_B T}\right), \quad (5.19)$$

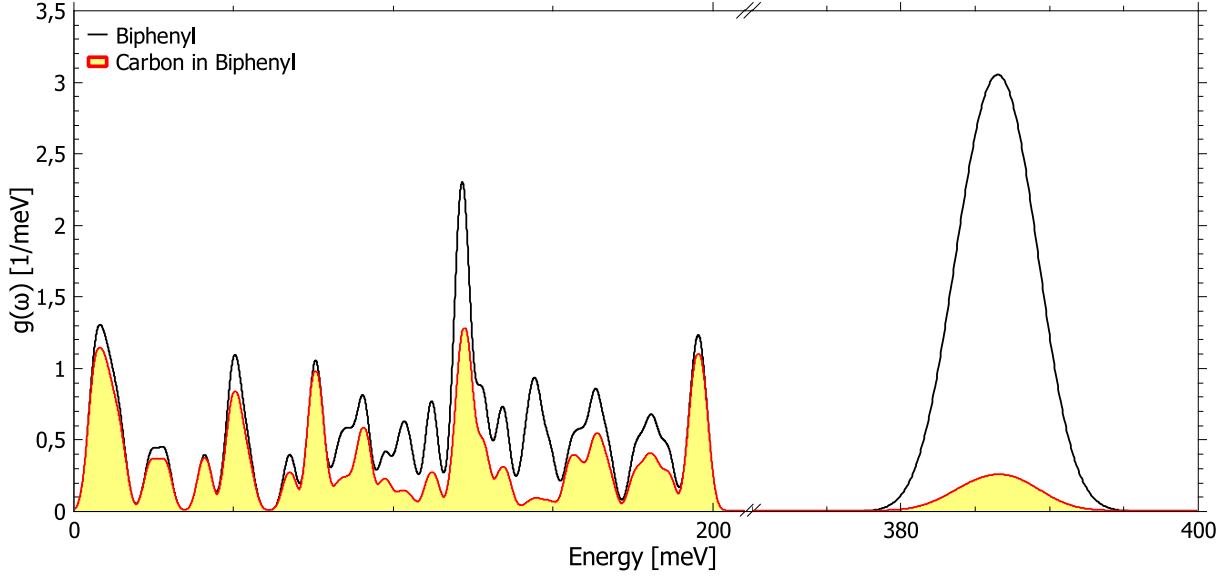


Figure 5.1: Total Biphennyl $g(\omega)$. In yellow the carbon contribution to the vibrations while the complementary is the hydrogen contribution.

where k_B is the Boltzmann's constant. The values $\langle E_k \rangle_{j,\alpha}$ from Eq. 5.19 depend on the orientation of the FoR. In a phonon calculation, the system can always be described with a TDHO. In this case, the values $\langle E_k \rangle_{j,\alpha}$ from Eq. 5.19 and those introduced in Sec. 2.5 are the same as long as the FoR and the axes of the TDHO have the same orientation. For a general orientation of the FoR, the values of $\langle E_k \rangle_{j,\alpha}$ along the axes of the TDHO correspond to the eigenvalues of the 3×3 kinetic ellipsoid tensor, defined as

$$\mathbf{K}_j = \sum_{v=1}^{N_v} \frac{\hbar\omega_v}{4} \vec{e}_{v,j} [\vec{e}_{v,j}]^T \coth \left(\frac{\hbar\omega_v}{2k_B T} \right). \quad (5.20)$$

The diagonal terms of tensor \mathbf{K}_j are equivalent to the values defined in Eq. 5.19. It is interesting to notice how $\langle E_k \rangle_j$ is independent upon the definition of the FoR, for the trace of a tensor is always equal to the sum of its eigenvalues. This is because even if the nuclear displacements are coupled their energy fractions are independent and just the Cartesian directions have to be decoupled. This can be easily seen by a 2-D picture with two vibrations, hence two eigenvectors $\mathbf{e}_1 = (0, a)$ and $\mathbf{e}_2 = (b, 0)$ and two eigenfrequencies ω_1 and ω_2 . In Fig. 5.2 on the left the vibrations are represented in a FoR where the Cartesian directions are independent, *i.e.*, if one of them increases the other is not affected, while on the right it is rotated by a θ angle in a FoR where they are mixed.

The energy calculated with Eq. 5.19 for the configurations of Fig. 5.2 is

$$\text{Left } E \sim a^2 + b^2 \quad (5.21)$$

$$\text{Right } E \sim a^2(\cos^2\theta + \sin^2\theta) + b^2(\cos^2\theta + \sin^2\theta) = a^2 + b^2. \quad (5.22)$$

Hence in terms of total energy both FoRs give the same result. The fact that the diagonalization corresponds to a rotation of the FoR in a way to make the energy fractions along the Cartesian directions independent can be seen by the diagonalization of \mathbf{K}_j for a single vibration $\mathbf{e}_1 = (a_1, a_2)$ in 2-D in a general FoR. The \mathbf{K}_j is

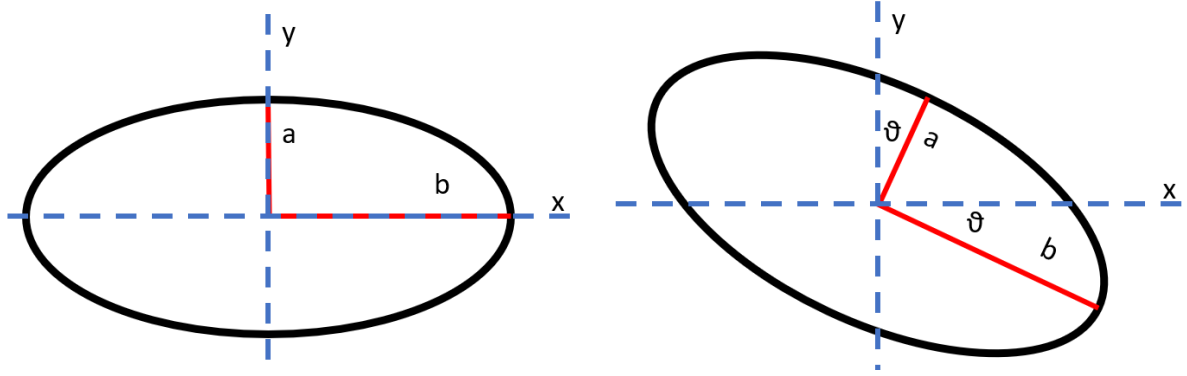


Figure 5.2: Two different reference of frame with two vibrations a and b . On the right the FoR is rotated by a θ angle.

$$\mathbf{K} = \begin{pmatrix} a_1^2 & a_1 a_2 \\ a_1 a_2 & a_2^2 \end{pmatrix} \xrightarrow{\text{Diagonalization}} \begin{pmatrix} a_1^2 + a_2^2 & 0 \\ 0 & 0 \end{pmatrix},$$

the non-diagonal terms of the matrix represent the correlation between the Cartesian directions that disappear with the diagonalization that is equivalent to a FoR rotation. While the total energy is FoR independent this does not apply to the values of $\langle E_k \rangle_{j,\alpha}$ and c_{2n} as defined in Eq. 2.58, Eq. 2.59, and Ref. [60]. It is also important to notice that Eqs. 2.58 and 2.59 can only be applied to calculate c_4 and c_6 when \mathbf{K}_j is in its diagonal form as they are derived in this environment. In all other cases, one would always underestimate them. In Fig. 5.3 the c_4 value as a function of the FoR rotation as in Fig. 5.2 is represented using Eq. 2.58 for a single vibration. The maximum value of c_4 is 0.8 obtained when θ is zero or a multiple of $\pi/2$, in fact with a rotation of $\pi/2$ just the axes are exchanged. For a generic θ , Fig. 5.2 right, c_4 has a lower value and Eq. 2.58 can't be used any more.

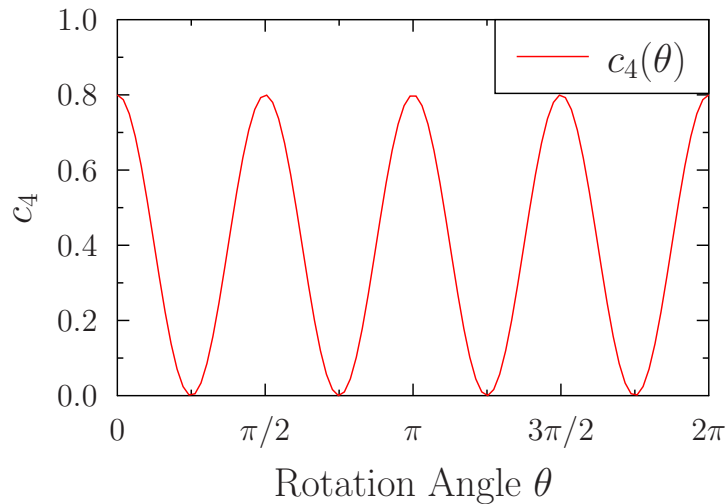


Figure 5.3: c_4 calculated with Eq. 2.58 for a single vibration as a function of a FoR rotation angle.

The eigenvectors can be used even to calculate the Mean Square Displacement (MSD) [123] in each Cartesian direction. In principle in classical physics the calculation of the MSD requires the initial position and velocity of the particle as shown in Eq. 5.15. In Quantum

Mechanics the particle, described by a wave function, is de localised and the position is obtained from the average of the position operator \mathbf{U} over the system state defined as

$$\sum_{\lambda} P_{\lambda} \langle \lambda | \mathbf{U}_j | \lambda \rangle \quad \text{where} \quad \mathbf{U}_j = \left(\frac{\hbar}{2M} \right)^{\frac{1}{2}} \sum_v \frac{\vec{e}_{v,j}}{\sqrt{\omega_v}} (\mathbf{a} + \mathbf{a}^+). \quad (5.23)$$

The MSD expression is given by the $\langle U^2 \rangle \sim \langle a a^+ + a^+ a \rangle = 2n_v + 1 = \coth \left(\frac{\hbar\omega}{2k_B T} \right)$ where a, a^+ are the annihilation and creation operators while n_v is the excitation number of the v oscillator. For these reason the MSD expression in each Cartesian direction is

$$\langle u^2 \rangle_{j\alpha} = \frac{\hbar}{2M_j} \sum_v \frac{|\hat{\mathbf{n}}_{\alpha} \cdot \vec{e}_{v,j}|^2 \coth \left(\frac{\hbar\omega_v}{2k_B T} \right)}{\omega_v}. \quad (5.24)$$

The MSDs are generally represented in literature with the so-called thermal ellipsoids and the same approach can be used for the kinetic energy represented in Figure 5.6. Full information of the MSD ellipsoids, dimension of the main axes and their orientation with respect the FoR considered, is contained in the matrix

$$\mathbf{B}_j = \frac{\hbar}{2M_j} \sum_v \frac{1}{\omega_v} \vec{e}_{v,j} [\vec{e}_{v,j}]^T \coth \left(\frac{\hbar\omega_v}{2k_B T} \right), \quad (5.25)$$

where the same diagonalization approach used for \mathbf{K} holds. The representation of \mathbf{K} is the equivalent of what Balla did in his portrait 1.1 but instead of representing dogs and people with colours he we have represented nuclei and molecules with neutrons. The \mathbf{B} and \mathbf{K} matrices can be visualised using the ORTEP tool [124].

5.3 Biphenyl Simulation

First-principles simulations of the vibrational dynamics of the biphenyl molecule were run using the CASTEP [120] and QE [119] codes, with a $6 \times 6 \times 6$ k-grid in the first Brillouin zone of the crystal structure using the script reported in Sec. A.1. Biphenyl has an equilibrium torsion angle of ca. 45° and shows both a planar, 0° , and a perpendicular, 90° , torsional activation energy. In fact, there is a competing effect between the stabilization of H-H bonding and the destabilization of the two joining carbons [125, 126]. The equilibrium between the two contributions is reached when the nuclear dynamics is taken into account as the entropy, induced by the molecular vibration, decreases when the value of the torsion angle goes to zero [19]. The input structure [127, 128] was geometry-optimized through a minimization of the atomic forces and represented in Fig. 5.4. The optimization was performed with a Perdew-Burke-Ernzerhof (PBE) exchange-correlation functional that reduces the input torsion angle; this could be avoided in future studies with the inclusion of non local long-range Van der Waals forces [129], as will be done for ices in Sec. 6.4.1. The unit cell, including two biphenyl molecules, is monoclinic (space group $P2_1/a$ [130]) with crystallographic constants: $a = 9.82 \text{ \AA}$, $b = 5.58 \text{ \AA}$, $c = 9.44 \text{ \AA}$, and $\alpha = 90^\circ$, $\beta = 94.6^\circ$, $\gamma = 90^\circ$. The pseudopotentials used were taken from Ref. [131] and Ref. [132] for CASTEP and QE simulations, respectively.

A phonon calculation was run on the optimized geometry, the output corresponded to a collection of eigenvalues of the molecular normal modes, ω_v , and eigenvectors representing

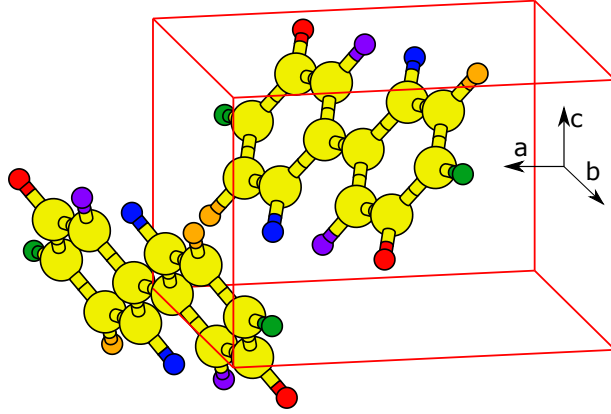


Figure 5.4: Biphenyl unit cell in the real space. Hydrogen atoms with the same $\langle E_k \rangle$ and c_4 have been represented with same colour. The structure is taken from Ref. [127, 128] and geometry optimised in order to perform the phonon calculation. The optimization reduces the torsion angle in order to minimize the forces acting on each atom.

each atomic motion for a given normal mode, $\vec{e}_{v,j}$. Given the $N = 44$ atoms in the unit cell, in the following discussion we considered $N_v = 3N - 3 = 129$ normal modes, where we neglected the three lowest-energy translational modes. In fact, as the phonon calculation has been performed at the gamma point, the rigid translations needs to be zero in order to satisfy the acoustic sum rule, furthermore the exclusion of those vibrations does not affect the energy computation as they give a negligible small contribution.

An Additional insight on the hydrogen dynamics, with respect to DINS experiment of Sec. 4.3, is obtained by the analysis of the simulated VDoS calculated with Eq. 5.16. Figure 5.5 shows the comparison of the hydrogen-projected VDoS from CASTEP and QE with the experimental spectrum from Ref. [17] collected at the TOSCA [133] spectrometer at ISIS. The simulated results were projected onto the scattering trajectories probed by the instrument using the AbINS [134] routine. The experimental spectra are interpreted within the incoherent approximation, whereby the hydrogen contribution to the measured signal dominates over the ones from other elements, owing to its high incoherent scattering cross section. The two simulations overlap almost completely, and reproduce satisfactorily the experimental spectra, despite a slight overestimation of the stretching frequencies. In general, the errors in the DFT-simulated frequencies are within ca. 5%, as reported in Ref. [117]. The vibrational spectrum can be divided in four energy ranges, the first between 370 and 400 meV with the stretching modes where the hydrogen nuclei move along the covalent bond direction. In the second energy range between 90 and 200 meV in-plane scissoring and rocking vibrations are included while in the third one, between 50 and 90 meV, there are the out-of-phenyl-ring-plane wagging and twisting hydrogen vibrations. Finally under 50 meV there are the ring vibrations such as the C-C stretching, torsions and librations.

The values of $\langle E_k \rangle$ and c_4 from the CASTEP and QE calculations, averaged over all the hydrogen atoms in the unit cell, are reported in Table 5.1 and compared with the measured results. As expected from the earlier comparison in Figure 5.5, the values of $\langle E_k \rangle$ from the two simulations are practically identical, while they overestimate the experimental value of about 7%. Such discrepancy, in line with what reported for liquid water at room temperature [49, 136, 137, 138], is likely a combination of several factors, including the

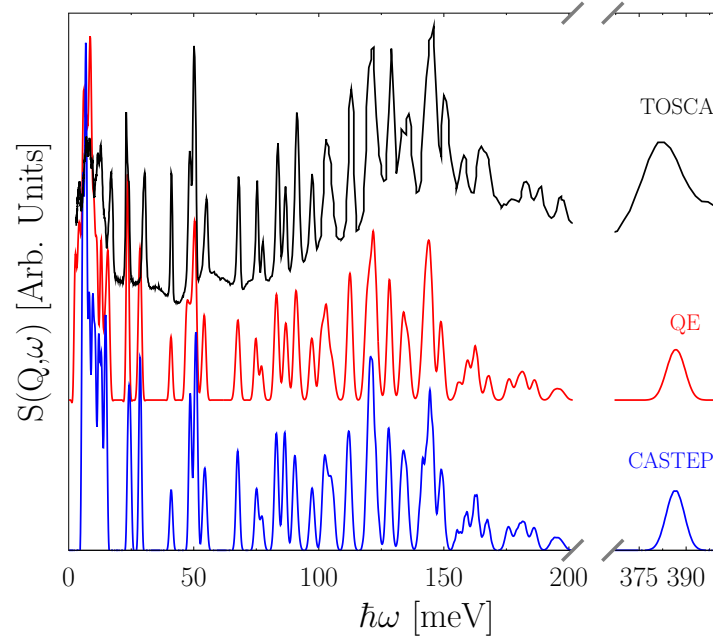


Figure 5.5: Simulated INS spectrum with CASTEP and QE, compared to the experimental measurement from Ref. [135, 17]. The measured spectra are vertically shifted for the sake of clarity.

Table 5.1: Hydrogen $\langle E_k \rangle$ and c_4 results obtained by integrating the simulated $g(\omega)$.

	$\langle E_k \rangle$ [meV]	c_4
DINS Experiment	145.7 ± 1.44	0.00 ± 0.01
CASTEP Simulation	152.85	0.127
QE Simulation	152.91	0.126

aforementioned overestimate of the vibrational frequencies [117]. The overestimate of the parameter c_4 in the simulation, compared to the vanishing experimental value, is more difficult to explain. The uncertainty on the measured value, including the effects of the instrument resolution and the statistics of the data, is clearly smaller than the discrepancy with the theory. The vanishing experimental value of c_4 is a result of the CLT [113], and that it can be obtained only when the number of normal modes is increasingly higher, that is, when the perfect single crystal of the simulation is replaced with a real, disordered powder sample, and coupling effects between intra and inter-molecular vibrations are included. Figure 5.6 shows a graphical representation of the kinetic ellipsoids of hydrogen and carbon calculated with Eq. 5.20, for one of the two equivalent phenyl rings of biphenyl, as obtained from the calculation (left side of dotted line) and from the experiment (right side of dotted line). We can see how in Fig. 5.6 the simulated result the kinetic ellipsoid is oriented along

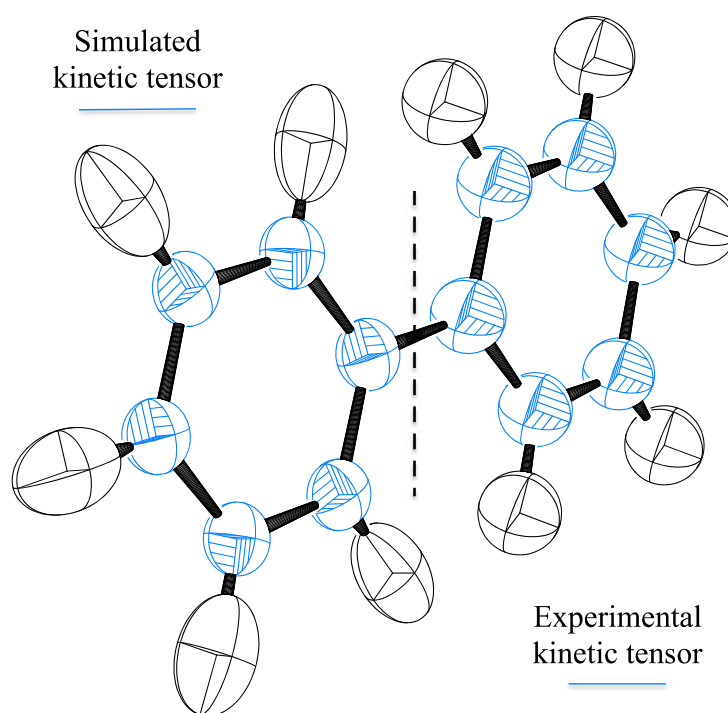


Figure 5.6: Graphical representation in real space of the simulated (left side of dotted line), calculated with Eq. 5.19, and experimental (right side of dotted line) kinetic tensor. The dotted line is used just to divide the result from experiment and simulation representing them in a single molecule.

the C-H bond, in fact, the most important contribution to the hydrogen energy comes from the stretching modes. With the simulation and Eq. 5.25 we have access even to the MSD of biphenyl represented in Fig. 5.7 with the so-called thermal or displacement ellipsoids, we can see how it is, in a first approximation, the conjugate with respect to the kinetic space as the main axis of the kinetic ellipsoid is along the covalent bond as opposed to the thermal that is orthogonal to that. The values of the MSD, averaged over all the biphenyl hydrogens, obtained with the simulation performed within this project and from literature are reported in the Table 5.2.

One should note how, in a number of recent investigations [140, 49, 141, 54] on the triatomic water molecule ($n_v = 6$), it was found $c_4 \simeq 0.10 - 0.15$, with variations due to

Table 5.2: Experimental and calculated result for the hydrogen MSD at 300 K, in bold the result from the present work.

	$\langle u^2 \rangle / \text{\AA}^2$
Experiment	0.145 [139]
Simulation	0.174 ; 0.185 [139]

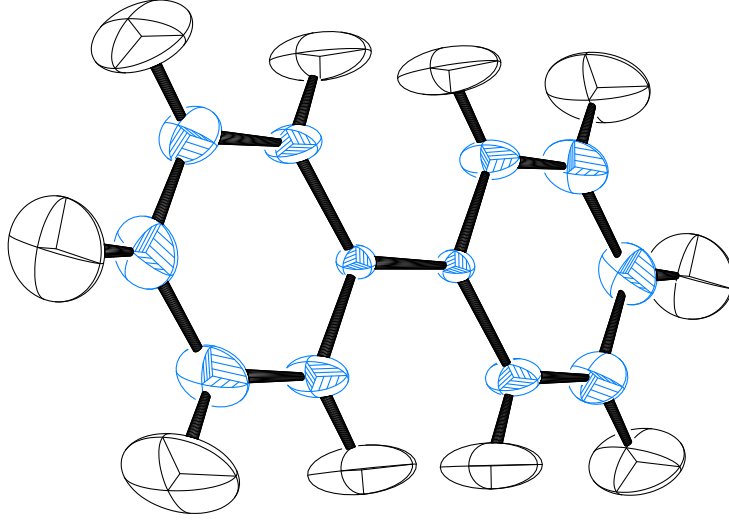


Figure 5.7: Graphical representation in real space of the simulated thermal or displacement ellipsoids calculated with Eq. 5.25.

different local environments. Moreover, for polyethylene, a standard polymer ($n_v \rightarrow \infty$) sample routinely used on VESUVIO, one has $c_4 \simeq 0$ as expected (*e.g.*, see Ref. [108, 109]).

5.4 Approach to the Central Limit Distribution

To investigate the relation between the value of c_4 , the CLT, and the number of vibrations, we first performed a *Gedankenexperiment* whereby we consider an increasing subset of n_v normal modes, and re-calculate the values of the hydrogen $\langle E_k \rangle_\alpha$ and c_4 over this subset using Eqs. 5.19 and 2.58. Figure 5.8 shows the results of this procedure, with the point at $n_v = 1$ resulting from the highest-frequency stretching mode only, $\hbar\omega_1 = 390$ meV, and the values for $n_v > 1$ calculated over the subset of normal modes in the range $[\hbar\omega_{n_v}, \hbar\omega_1]$. At low values of n_v , *i.e.*, considering only high-frequency modes, \bar{c}_4 and \bar{c}_6 (the $\bar{}$ stands for the average over all the hydrogen nuclei) display their maximum values. Such high-energy modes correspond to a large displacement of each H atom along the CH direction, in a very similar manner to what would happen in a diatomic molecule, where the local potential is expected to be highly anisotropic. As one includes more vibrations in the evaluation of c_4 , its value decreases stepwise to the one reported in Table 5.1 at $c_4 \simeq 0.13$. This decrease is related to the incoherent interference of an increasing number of independent vibrations. As each vibration causes a given H atom to move in a different direction, the incoherent sum of all these effects makes the resulting potential increasingly isotropic, *i.e.*, better approximated by a Gaussian NCP. The step-like behaviour in the decrease of c_4 can be explained with the grouping of all normal modes in smaller categories. For example, the

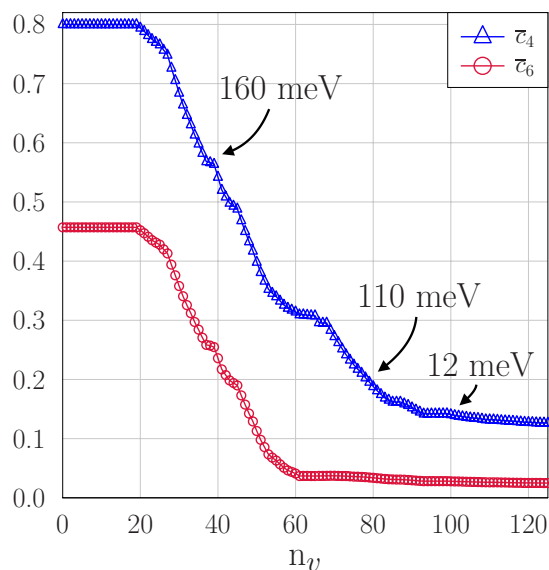


Figure 5.8: Calculated values of \bar{c}_4 and \bar{c}_6 , averaged over all H atoms in the biphenyl molecule, as a function of the number of vibrational modes considered. For example: when $n_v = 1$, only the normal mode at $\hbar\omega_1 \simeq 390$ meV is considered; when $n_v = 40$, all modes with energies between $\hbar\omega_1$ and $\hbar\omega_{40} \simeq 160$ meV are considered.

first 20 modes are localised stretching vibrations all contributing to the motion of a given H atom only in the CH direction. As these do not decrease the anisotropy of the motion, the value of c_4 in the range $n_v = 1 - 20$ stays practically constant.

The grouping of the normal modes can be understood even considering how the thermal and kinetic ellipsoids change as a function of the lower limit of the normal mode subset ($\hbar\omega_{n_v}$ or $\hbar\tilde{\omega}$). Looking at Figure 5.9 (over the dotted line) the kinetic ellipsoids change from a stick along the covalent bond, when $\hbar\tilde{\omega} = \hbar\omega_1$, with a maximum in the anisotropy (see Fig. 5.8) to a 2-D ellipsoid when the bending modes are included and finally to a 3-D ellipsoid when the out of plane twisting and wagging are considered. The anisotropy of the NMD shown in Fig. 5.8 has a monotonic decrease as all of these modes make the original stick smoother in the space. As the most important contribution to the kinetics is given by the high energy modes the direction of the main ellipsoid axes never changes as opposed to the thermal ellipsoid where low energies has the main effect on the orientation (see Eq. 5.25). In fact, one can appreciate that, in Figure 5.9 (under the dotted line) changing $\hbar\tilde{\omega}$ from the maximum value of 395 meV to the lower value of 125 meV, the shape of the MSD ellipsoids changes from a stick-like distribution, when only stretching modes are considered, to a disk-like distribution, when other planar vibrations are considered. The overall anisotropy of the MSD first decreases till the disk is a circle, then starts to increase again when the circle becomes an elliptic disc in the direction perpendicular to that of the original stick. When $\tilde{\omega}$ is further decreased, the bidimensional disk changes to an ellipsoid, thus decreasing the value of the anisotropy, as out-of-plane vibrations are finally included.

The decreasing trend of the c_4 coefficient as a function of the increasing number of degrees of freedom has also been confirmed by single-molecule DFT calculations, using QE, of saturated hydrocarbons in the gas phase, from methane (CH_4 , $N = 5$, $N_v = 12$) to decane ($\text{C}_{10}\text{H}_{22}$, $N = 32$, $N_v = 93$). The hydrogen values of \bar{c}_4 are reported in Fig. 5.10,

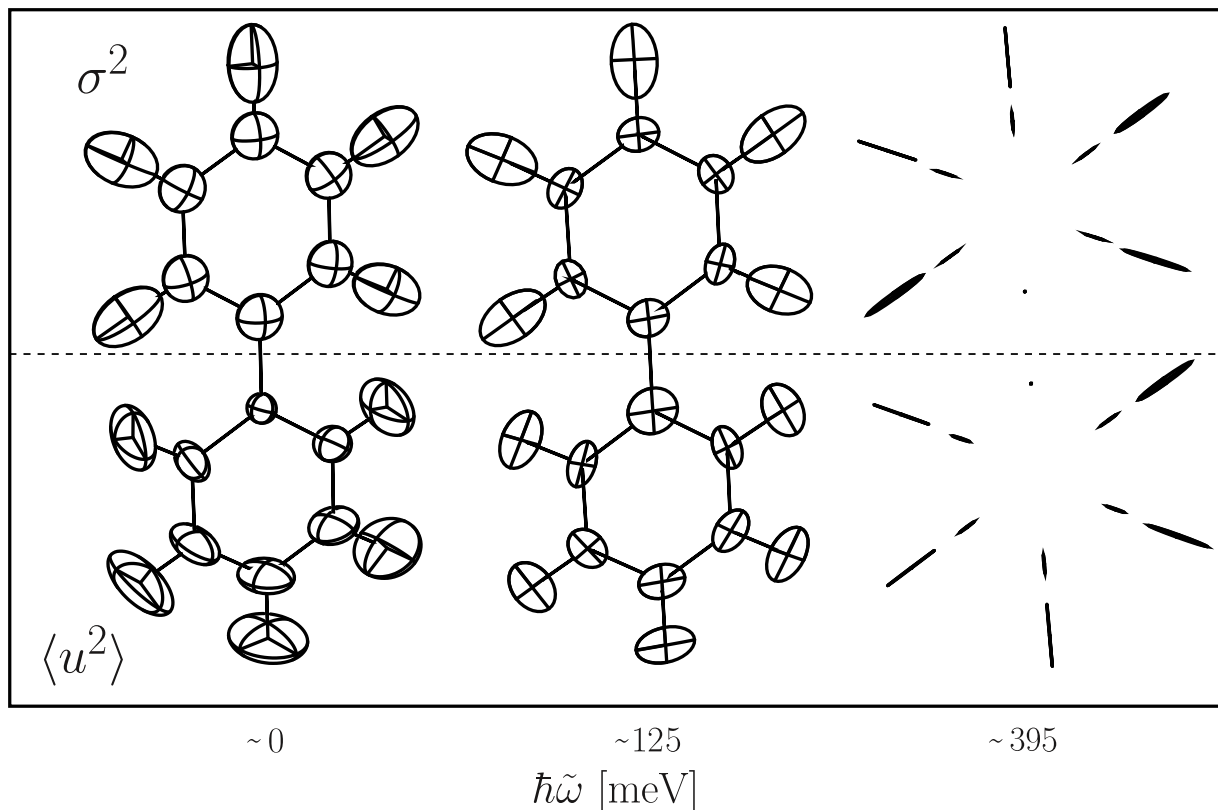


Figure 5.9: Thermal (under dotted line) and kinetic (over dotted line) ellipsoids as a function of $\tilde{\omega}$.

together with the maximum and minimum values of the $c_{4,j}$ for each molecule considered. When inspecting the trend of \bar{c}_4 , one can readily recognise its decrease for larger molecules, *i.e.*, for an increasing number of normal modes, from ca. 0.18 in methane to ca. 0.09 in decane that can be approximated by $1/\sqrt{N}$. As in the case of biphenyl, the values stay larger than zero, for the simulations are performed at the centre of the Brillouin zone, without any inter-molecular interactions and structural disorder in the corresponding condensed phases, and coupling of normal modes is not considered.

Figure 5.11 shows the anisotropic part of the NCPs of hydrogen in biphenyl and other hydrocarbons, *i.e.*, the terms proportional to c_4 and c_6 in Eq. 2.57. The curves appear as oscillatory functions symmetric around $y = 0$, each with vanishing integrated area and with 4 nodes, in the range $-20 \text{ \AA} < y < 20 \text{ \AA}$, for the dominating term is the fourth-order H_4 Hermite polynomial. As a first comment, one can notice how the amplitude of the oscillation becomes smaller (more isotropic) when going from methane to decane. In fact, the amplitude at $y = 0$, where the absolute deviation from the isotropic contribution is maximum, is proportional to $3/8 c_4 - 5/16 c_6$, and both c_4 and c_6 are found to decrease for larger molecules. In a DINS experiment, such oscillation is smoothed and flattened as a result of the convolution with the experimental resolution. Such effect, in the case of hydrogen, suppresses the oscillation at $y = 0$ of about 15%, not enough to prevent the data fitting from detecting the system anisotropy. The convolution of the model anisotropic contribution to the NMD with the experimental resolution for hydrogen is reported in Fig. 5.11 as black diamonds for biphenyl.

We can see how in Fig. 5.10 the $c_{4,j}$ minimum and maximum for methane is the same

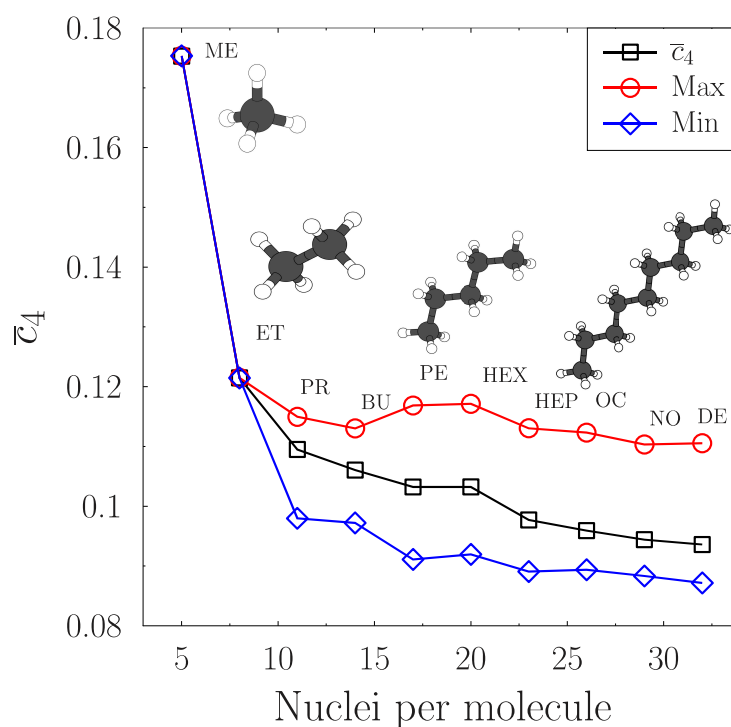


Figure 5.10: The maximum (red), minimum (blue), and average (black) values of c_{4j} for a series of hydrocarbons, ordered with the increasing number of atoms per molecule, N . In particular, methane (ME, $N=5$), ethane (ET, $N=8$), propane (PR, $N=11$), butane (BU, $N=14$), pentane (PE, $N=17$), hexane (HEX, $N=20$), heptane (HEP, $N=23$), octane (OC, $N=26$), nonane (NO, $N=29$) and decane (DE, $N=32$).

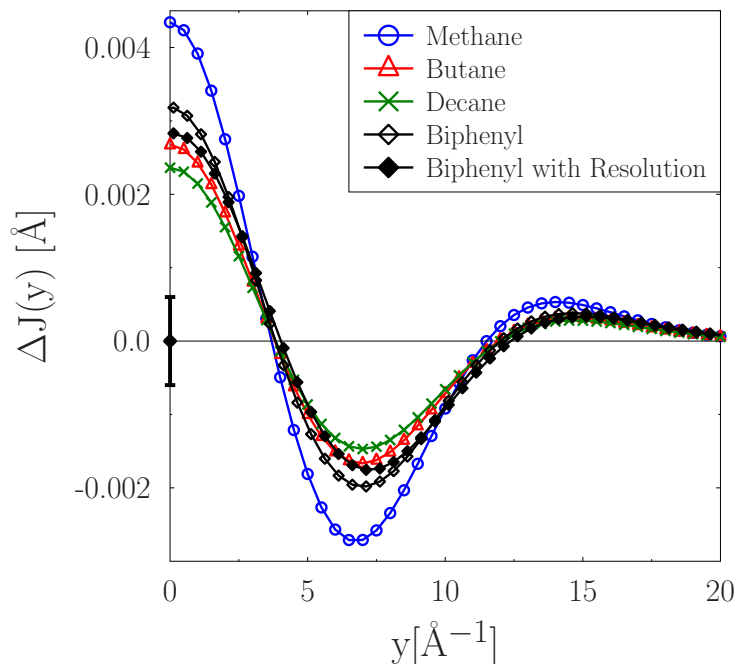


Figure 5.11: The theoretical anisotropic contribution to the hydrogen NCP (empty marks) for methane, butane, decane, and biphenyl, as functions of the y -scaling variable. In the case of biphenyl, the convolution of the model function with the experimental resolution is also reported (full diamonds). The error bar at the origin represents the experimental uncertainty on our data.

as all the hydrogen are equivalent. This is shown in Fig. 5.12 where the kinetic and displacement tensor are represented. As in biphenyle we can note how \mathbf{K} is aligned along the covalent bond while \mathbf{B} is perpendicular to that.

In Sec. 4.3, we demonstrated experimentally that the nuclear momentum distribution of hydrogen in biphenyl is a pure Gaussian function, both isotropic and harmonic. On the one hand, this proves that the harmonic approximation for the nuclear dynamics within the molecule, at the base of DFT-based phonon calculations, is valid. On the other hand as found in this section, when such simulations are run on a single molecule or on single crystal, the theory predicts some anisotropy that is not found in the experimental data. I related the experimental result to the application of the Central Limit Theorem *in practice*, *i.e.*, for the real (disordered) system, where the number of independent vibrations affecting the hydrogen dynamics is substantially higher than in a typical computer simulation and coupling effects of different normal modes are expected to reduce the level of anisotropy of the local potential. Hence, the theorem can be applied even on the simulation results just when more number of degree of freedom are included. These are important pieces of information for the community studying molecular spectroscopy, *e.g.*, as for the modelling of chemical processes to convert lignin into monocyclic hydrocarbons.

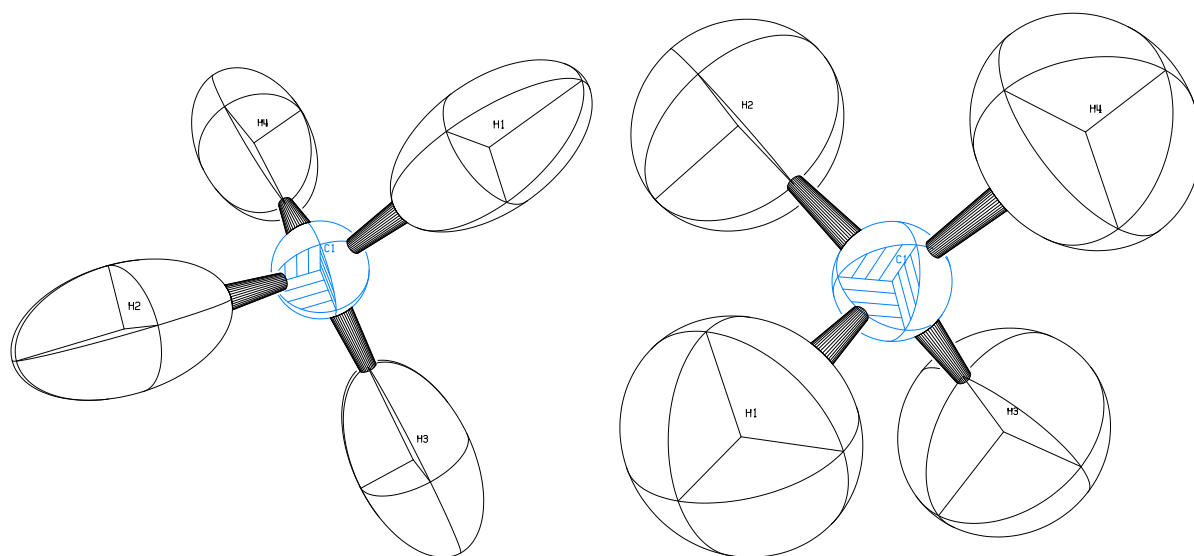


Figure 5.12: Kinetic and MSD tensor for a methane molecule.

Chapter 6

Ice Experiments

An experimental campaign of neutron scattering experiments performed by me on the VESUVIO and IRIS spectrometers is discussed in order to demonstrate the extraordinary stability of ice II with respect to the other phases of ice. The results will be then compared with INS data available in literature and Ab-Initio simulations. This experiment is a clear example of how the work described in the previous chapters about the instrumentation development can be applied so as to achieve higher accuracy on the measurements performed in order to discriminate the difference between the hydrogen dynamics in the ice phases.

6.1 The fascinating world of Water and Ice

As water in its liquid and solid forms is ubiquitous in nature, being one of the most abundant molecules in the universe, and it is thought to be a prerequisite to sustain life in our solar system and beyond [20, 21], it was chosen as a sample for my PhD project in Health, Environment and Energy. While the water molecule is small, it has a surprising amount of complexity that makes it an intriguing target for basic studies of molecules and deriving properties of quantum mechanics [22, 23]. Water has a number of properties that make it quite unique among many common substances even if many ice characteristics were then found in other materials such as the stacking disorder in diamond [24, 25].

The water molecule is composed of two hydrogen atoms and one oxygen atom. The hydrogen are covalently bound to the oxygen and, as oxygen is a highly electronegative elements, a dipole is formed where a δ^+ charge is placed on the hydrogen and a δ^- on the oxygen [142]. An additional interaction is present between oxygen and hydrogen atoms of surrounding molecules, the so-called *hydrogen bond*. In particular each hydrogen interacts with one oxygen via covalent bond and with another via hydrogen bond while oxygen is bound covalently with two hydrogens and two more via hydrogen bond. We generally refer to this rule as *Ice or Bernal-Fowler Rule*. The existence of the hydrogen bond is at the origin of many of the water properties and makes water a unique element [143] that allows the world and life to exist and grow. Water, when cooled below 0°C, becomes ice I_h . A characteristic of this phase is that it does not sink into the water as its density is lower, as a consequence of its open-channel crystallization, allowing fish to survive during winter.

Water exhibits a fascinating range of 18 experimentally known solid phases [144], and all of these are referred to as forms of ice. Most of these phases are achieved by the application of high pressures, which result in denser packings of molecules than in ice I_h . The first

high pressure phases were discovered almost a century ago by Tammann [145, 146] in a programme to study the pressure-volume-temperature relationships of various materials, and he named this phase ice III [147]. These phases of ice have been labelled with the Roman numerals in the approximate order in which they were produced experimentally. Each phase is stable over a certain range of temperature and pressure, but it is a feature of the ice system that many phases are metastable well outside their regions of stability and others have no region of absolute stability at all. Figure 6.1 shows the regions of stability of the crystalline phases of ice on the pressure and temperature p - T phase diagram. There are along the *conventional* phases of ice the deuterated phases with the same structure but deuterium in the place of protium. Neutrons are the suitable experimental probe to distinguish the protonated from the deuterated phases for their different neutron cross section [52, 59].

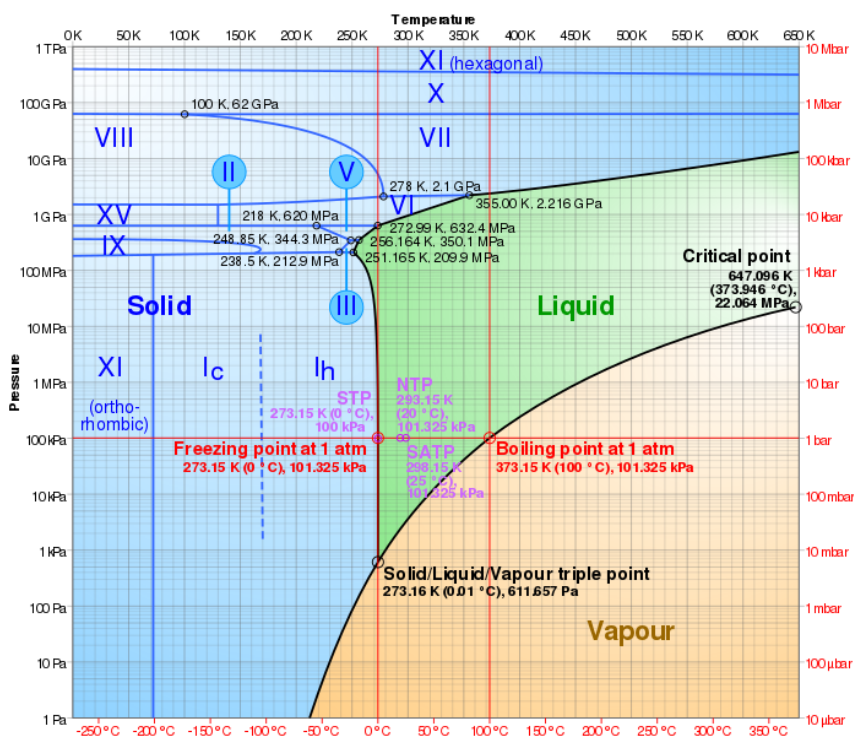


Figure 6.1: p - T phase diagram of ice. The colour divides solid, liquid and vapour phase. Picture taken from Ref. [31].

6.1.1 Order and ice rules

In the ice crystal structure each oxygen has four neighbours at the corners of a regular tetrahedron, two of them *accept* a H-bond while the other two *donate* an H-bond; the result is that the water molecule can have six possible orientations, showed in Fig. 6.2 in order to respect the ice rules. Some ice phases, as I_h , are unusual because, although the molecules lie on a regular crystal lattice, there is disorder in their orientations. In fact, the ice structures can be grouped as ordered or disordered crystal, in the first case both the oxygen and hydrogen atoms, and hence the molecule orientation, appear in a fixed crystal patterns so as that each unit cell is equivalent to another. In the disordered phase the orientation of the molecule is random but the tetrahedron structure and the ice rules

still holds; as a result there is a *limited* degree of disorder within the crystallographic order given by the oxygen atoms arrangement.

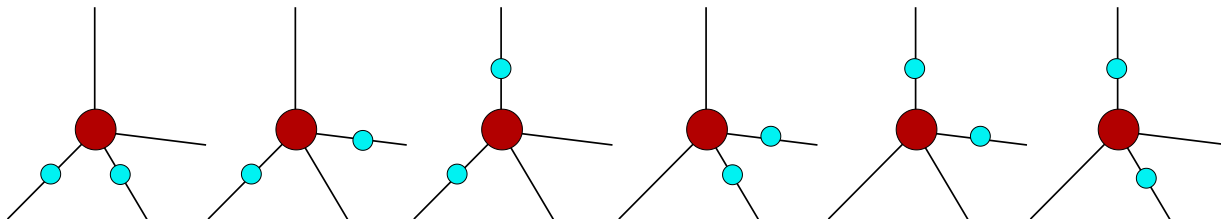


Figure 6.2: The six possible orientation of the water molecule in each crystal site.

In this second case every unit cell is different because of the molecule that can have six different orientation within the tetrahedron that give rise to the so called zero-point entropy given by the configurational disorder and calculated by Pauling [148]. Most of the hydrogen disordered crystal phases are present at high temperature and they transform to their ordered counterpart when the temperature is lowered in order to minimise the entropy that should be zero at zero temperature for the third law of thermodynamic [149]. This process is generally difficult to happen as involves the reorientation of the water molecules and considering that, in order to satisfy the ice rules, the molecule orientation is determined by the configuration of its neighbours the process requires defects that violate the ice rules; in fact, just ices III and VII have a spontaneous transition to hydrogen ordering when cooled, as opposed to the formation of ices XI, XIII, XIV, and XV that requires a doping percentage in the crystal structure [150, 151, 152]. The ordered and disordered phases are topologically related: in the ordered phase all the hydrogen bonds are oriented in one direction while in the disordered phase the bonds are oriented in more than one. The crystallographic experiments are generally performed with neutrons with deuterated samples for their greater coherent scattering cross section. In the ordered phase both hydrogen and oxygens are characterised by a fractional occupancy 0 to 1 depending on the nucleus presence while for the disordered phases the diffraction peak is weighted by all the possible orientation of the O-H bonding. Even if the ice phases are divided in these two groups, there is of course a shade of grey where the ices, considered originally as disordered, have a degree of partial order [153, 154]. The configurational zero-point entropy configurational is hence the reason why the disordered phases could not be thermal equilibrium structures at low temperatures. Entropy is a very important variable when the stability of a phase is studied with respect to another as nature minimise the Gibbs Free Energy, G , defined as

$$G = E + pV - TS, \quad (6.1)$$

where E is the internal energy, p the pressure, V the volume and S the entropy; our experiments will be performed at $p \sim 0$. Hence more stable the phase at each temperature lower the energy and higher the entropy.

6.1.2 Ice II, a unique phase

The experiments that will be described are thought to show the unusual stability of ice II. In fact, ice II is an ordered phase of crystalline water, thought to populate the core of icy moons like Jupiter's Ganymede, and it is unique because it does not have any disordered

counterpart as opposed to the other ordered phases of ice. It remains hydrogen-ordered at temperatures just below the melting point [154, 155], where there is a phase transition to other hydrogen-disordered ices rather than to its own hydrogen-disordered counterpart. Recent studies have shown that the phase transition from ice II to the hypothetical hydrogen-disordered ice II_d would take place only at temperatures well within the stability region of the liquid phase, for this reason ice II has shown a strong resilience towards hydrogen disordering [156]. The absence of a disordered counterpart and the constrained nature of the ice II hydrogen-bond network that remove itself from the water phase diagram when some impurities are added [157] has motivated the work reported in this chapter. The reason of the stability will be found, in our experiments, in the hydrogen dynamics of ice II compared with IX and VI phase and taking as a reference the ice I_h and I_{sd} where a large amount of data are available from literature [158, 92, 159]. Ice II is formed by compressing ice I_h at -80 °C; it is not easily formed on cooling ice III that remains metastable until the formation of the ordered phase ice IX. The comparison between ice II and IX is really interesting because they both are ordered and populate the same region of the phase diagram and have similar densities [31]. Ice VI is a disordered high pressure ice that will be used as a comparison for phases at higher densities. The QENS measurements on IRIS will be taken with ice I_{sd} as a reference as all the phases studied have a phase transition to ice I_{sd} , while ice I_h will be taken as DINS benchmark on VESUVIO using past measurements [160, 92, 158, 159, 44, 161, 162]. Ice I_{sd} is called stacking-disordered as it is composed by hexagonal (ice I_h) and cubic sequences (ice I_c) mixed, the percentage of the composition depends on the temperature and pressure condition where it is synthesised [24].

During the data analysis of these experiments I felt almost like *Mendeleev* who predicted with the periodic table that some places will be occupied by some, still undiscovered, elements; in my case I did the opposite thing on the phenomenology of the water phase diagram trying to motivate the non-existence of a disordered counterpart of ice II.

In the following sections the stability of ice II will be assessed by the measurement of the kinetic energy probed by DINS, by the dynamical entropy probed by QENS, INS spectra from literature and Ab-Initio simulations.

6.1.3 Sample Preparation

All the samples were synthesised by the Salzmann's team at University College London [163] being part of Zainab Sharif PhD project [164]. In all cases the ice samples were powder polycrystalline. The compression of ice was performed using a Zwick universal testing machine [165]. Ice was initially prepared by pipetting solutions of Millipore water into indium foils lining a pre-cooled hardened steel pressure die. To track the temperature of the sample, a thermocouple was attached to the pressure die with thermal paste and Teflon tape. Temperature data were recorded using a temperature controller which was linked to a LabView program. With the sample held at 77 K, it was compressed to set pressures before being left to heat up isobarically to set temperatures. For sample retrieval, the ice samples were quenched (cooled with liquid nitrogen to 77 K at a cooling rate $40 \text{ K } \frac{1}{\text{min}}$). Eventually the pressure was released from the samples and all further sample handling was performed under liquid nitrogen. The recovery of such phases under liquid nitrogen allows for their study as any potential reconstructive phase transitions occur with extremely slow kinetics due to the low temperature environment [22]. For ices II and IX, a 1.3 cm pressure die was

used to reach 0.3 GPa, and samples were quenched with liquid nitrogen from 244 K and 252 K respectively. For ice VI, a 1.0 cm die was used to reach 1.0 GPa, and samples were quenched at 250 K. The phase purity of each sample was confirmed by low temperature powder x-ray diffraction (PXRD) performed at UCL. This diffraction was carried out at using a standard diffractometer with Cu $K\alpha_1$ radiation at 40 kV, 30 mA and monochromated by a Ge 111 crystal. The low temperature of PXRD was achieved by performing the data collection in a stream of nitrogen gas; this ensured that the temperature of the samples was at least 95 K, well below the temperature of any phase transition to stacking disordered ice I_{sd} that would be expected for the ice phases investigated [166]. At the Rutherford Appleton Laboratory, respective samples of ice were prised from their indium foils in order to be ground. The ice samples were placed into a porcelain pestle and mortar in a polystyrene box which had been precooled with liquid nitrogen. Ice powder was then formed by crushing the ice samples with the pestle and mortar before being transferred to the precooled sample cells. The structure of the prepared ice phases (I_h , II, VI and IX) is represented in Fig. 6.3. The oxygen nuclei position should be taken as the crystal structure since there is more than one configuration in terms of water molecule orientation for ice I_h and VI being disordered phases; in fact, the oxygen position is the same for both the ordered and disordered counterpart. There are some characteristic features of the phases that one can observe such as the ice I_h hexagonal rings, the six-membered rings of the *ice nanotubes* in ice II, the spirals in ice III/IX and the second independent hydrogen-bonded networks in ice VI/XV.

6.2 Stability induced by Energy

In order to probe the nuclear kinetic energy of hydrogen and oxygen inside the ice structures, DINS experiment were performed on the VESUVIO spectrometer at the ISIS pulsed neutron and muon source [1, 167, 168]. In Table 6.1 the accumulated proton change in the ISIS synchrotron is indicated for each sample analysed.

Table 6.1: Proton current accumulated in the ISIS synchrotron for each ice phase and material used for the sample container

	Ice I_h	Ice II	Ice I_{sd}	Ice IX	Ice VI
Integrated current [μ Ah]	3240	6570	3150	4860	3600
Sample Container	NbAl	NbAl	NbAl	NbAl	Cu

The samples were transported to ISIS and loaded in liquid nitrogen, in order to avoid phase transitions caused by warming, and inserted in the VESUVIO sample position inside the CCR, whose temperature was set to 80 K for all the samples. At 80 K almost all the molecule vibrations are in their fundamental state, hence the zero point-motion of nuclei will be probed. The samples of ice II and IX were measured using a cell composed by niobium faces within an aluminum frame while, for the ice VI measurement, a Cu cell was used. The ice I_{sd} was obtained warming the ice II sample in steps of 20 K up to 180 K with thermocouples present on the VESUVIO stick keeping the CCR at 80 K. Then, the temperature was rapidly decreased to back to 80 K and started the measurement again. In order to have a reference sample measurement of ice I_h phase at 80 K, both for ice II

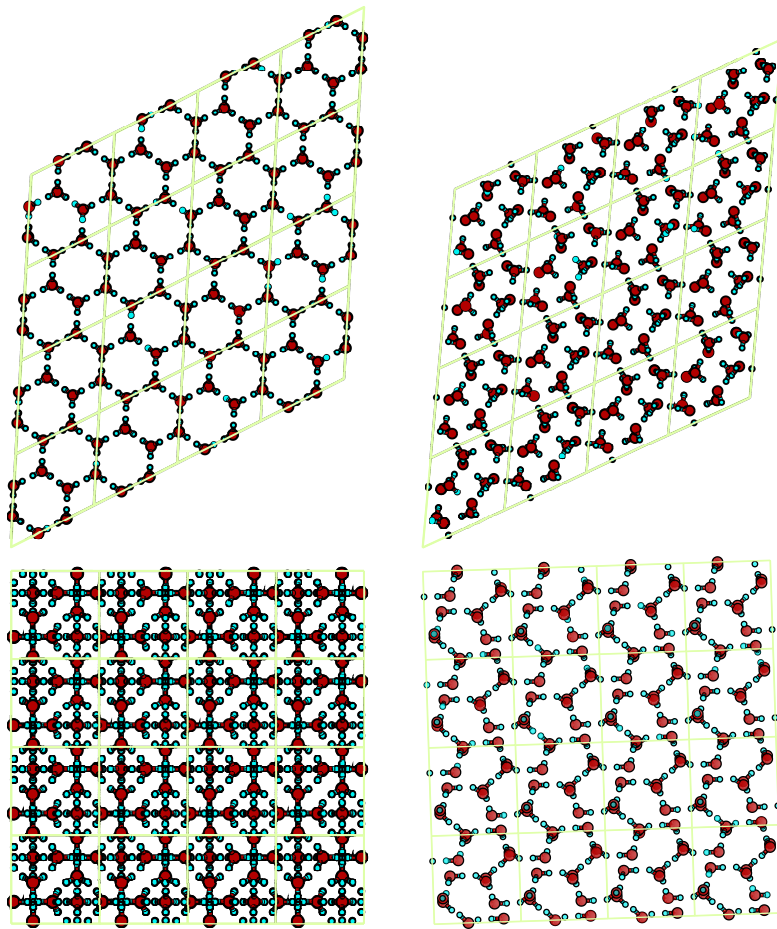


Figure 6.3: Crystal structure of ice I_h (top left), II (top right), VI (bottom left) and IX (bottom right).

(already ice I_{sd}) and ice IX, the samples were warmed up to 260 K, avoiding sublimation using a higher helium pressure. The ice phase changes were monitored using the diffraction capability of the VESUVIO backscattering detector banks [66]. In Fig. 6.4 the diffraction pattern of the same sample in the II, I_{sd} and I_h phase is shown. The experimental spectra on the top of the figure are compared with the expected diffraction pattern reported on the bottom obtained via the VESTA software [169] and the crystallography information file [170, 171]. A dotted line is used to show some *marker* peaks of the phases.

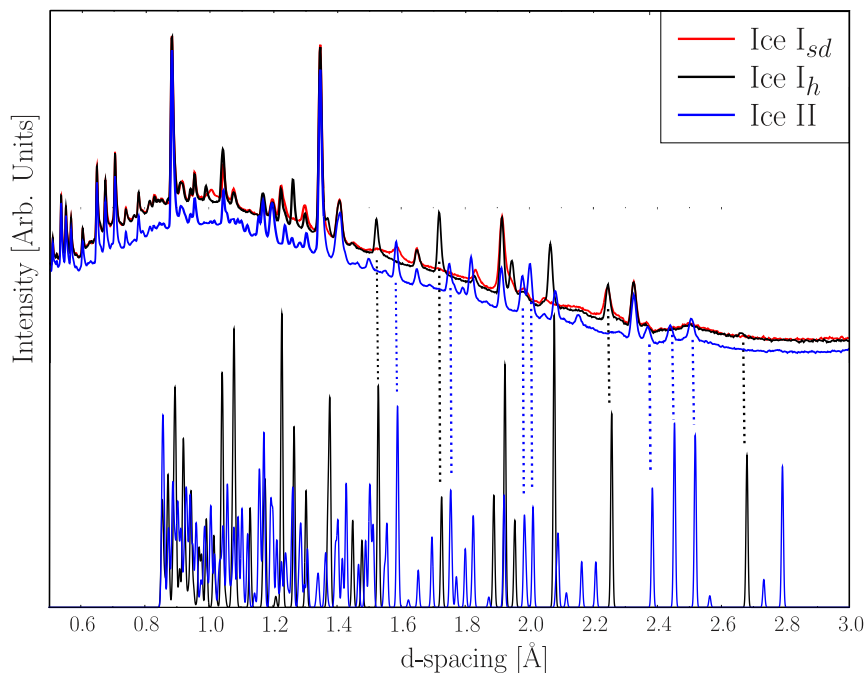


Figure 6.4: Experimental Diffraction pattern of ice II, I_{sd} and I_h on the VESUVIO spectrometer (top). The diffraction capability of the spectrometer was used to monitor the change from ice II to I_{sd} and finally to I_h . On the bottom of the figure the expected diffraction pattern of ice II and I_h are represented and, with some of the identification peaks, a comparison is made using a dotted line.

6.2.1 Sample Container Optimization

The present study aims to explore oxygen and hydrogen dynamics. The hydrogen is analysed in forward scattering as in backscattering the hydrogen peak is not present for kinematic constraints. For the oxygen, analysed in backscattering, the design of sample container deserves particular attention in order to separate contributions from the sample cell, thus enabling an efficient data reduction and line shape analysis. Figure 6.5 shows the experimental NCP, $\overline{F}(y, Q)$, averaged over all the detectors for the different ice phases, on the left the sample container contribution while on the right, at ca. $y=0$, the oxygen NCP peak. The experiment on ice VI was carried out using a copper container while the other phases were inserted in an innovative niobium cell within an aluminum frame. In fact, the atomic mass of niobium, larger than copper, allows an optimal separation of the oxygen Compton profile and the background from the sample container; moreover the niobium scattering cross-section is about 30% smaller than copper. Finally, the thickness of

the copper container was 0.5 mm for each face against the 0.2 mm of the niobium cell. All these optimizations are reflected in the experimental profiles as it is shown in Fig. 6.5 where $\bar{F}(y, Q)$ for ice VI is affected by a more intense and less-separated copper background peak.

6.2.2 Visual Evidence

Generally before a parametric analysis of the NCPs obtained by the fitting on VESUVIO data after the reduction [108] it is worth to compare the NCP one above the other and see the differences, if any, they will emerge even from the fitting procedure. After the gamma background [79] and multiple scattering correction [81], the reduced hydrogen experimental NCPs of all the ice phases measured are compared as shown in Fig. 6.6-6.7 in order to underline the low value of the hydrogen mean kinetic energy of ice II compared to the other phases with a preliminary visual inspection. In particular the NCPs are represented together with their difference, enlarged in the right panel. In every case the ice II lineshape is greater than the other compared with until $\pm\sigma$. This is a typical behaviour of two NCPs lineshapes with different associated mean kinetic energy, one greater than the other.

6.2.3 Fit on the NCPs

The reduced data were fitted using an isotropic and multivariate model (see Sec. 2.5 and 2.4). The results for both the approaches are listed in Table 6.2 and 6.3. The results for the ice I_h are in agreement with Ref. [160] used as a benchmark for our data analysis. As we can note from the results, the mean kinetic energy, and hence the standard deviation, of the oxygen NCP coincides within the error bar for all the samples. The results shows a decrease in the mean kinetic energy of hydrogen in ice II [156]. For what concerns the multivariate analysis, it is more difficult to comment considering the single vibrational modes because our fitting method orientates the energy \mathbf{K} ellipsoid in such a way to minimize the chi-square so it is orientated so as to be diagonal but not parallel to the libration, stretching or bending and, as in principle the vibration are different for the phases studied, the orientation of the ellipsoid is not fixed and it is different for different ice phases. For this reason, the α -direction for the ice I_h could be different from the α -direction of ice II obtaining for that direction different contributions from the vibrational modes for each direction. Anyway, we can confirm a difference in the position of the ellipsoid and so in the anisotropy.

Table 6.2

	I_h [meV]	I_{sd} [meV]	II [meV]	VI [meV]	IX [meV]
$\langle E_k \rangle$ H	150.9 ± 1.3	151.9 ± 1.3	145.78 ± 0.98	151.6 ± 1.9	149.4 ± 1.7
$\langle E_k \rangle$ O	22.7 ± 1.7	20.4 ± 1.6	23.4 ± 1.6	18.6 ± 3.4	22.2 ± 1.8

In Figure 6.8 on the right a graphical representation of the hydrogen and oxygen kinetic energy as a function of the density is reported; the total nuclear energy of the molecule is calculated with the virial theorem in the harmonic approximation ($E_k = U$ where U is the potential energy). On the top left the fit on the ice II NCP is reported together with the difference with the data, in Appendix D all the other fitted NCPs are reported. Finally on the bottom left the second momentum distribution is represented. It is pictorially

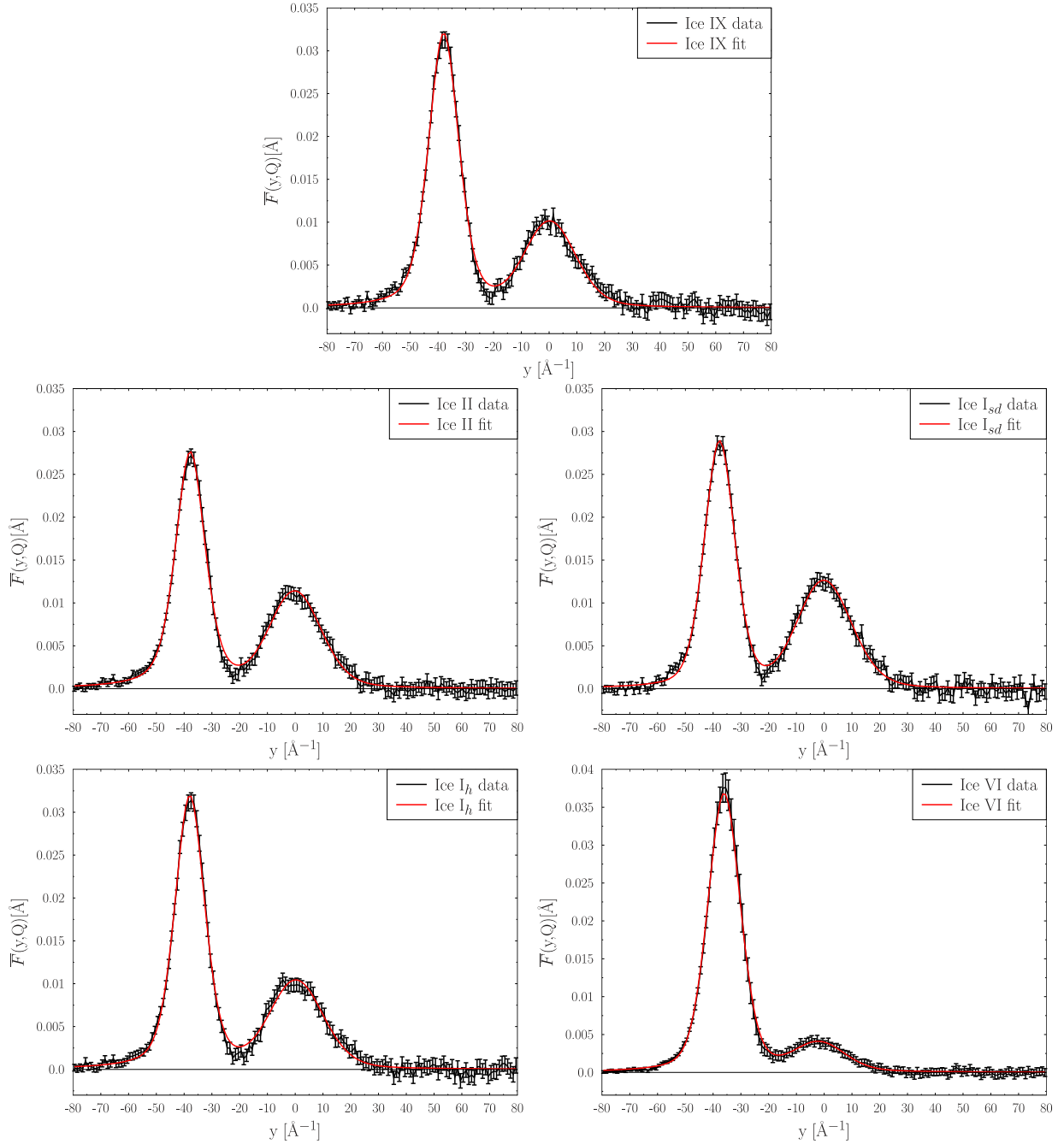


Figure 6.5: Experimental neutron Compton profile $\bar{F}(y, Q)$, with its fit, for the ice phases considered in the experiment. For ice VI a copper sample container was used while for the other phases an optimised niobium cell was adopted that allowed a better mass separation and background subtraction.

Table 6.3

	I_h [meV]	I_{sd} [meV]	II [meV]	VI [meV]	IX [meV]
$\langle E_k \rangle_x$ H	19.9 ± 1.9	16.0 ± 1.7	21.9 ± 4.1	11.1 ± 3.4	15.5 ± 2.2
$\langle E_k \rangle_y$ H	65.4 ± 9.5	66.9 ± 9.0	51.6 ± 9.4	67 ± 13	66 ± 10
$\langle E_k \rangle_z$ H	65.6 ± 9.4	69.1 ± 9	72.3 ± 9.7	73 ± 10	67 ± 10

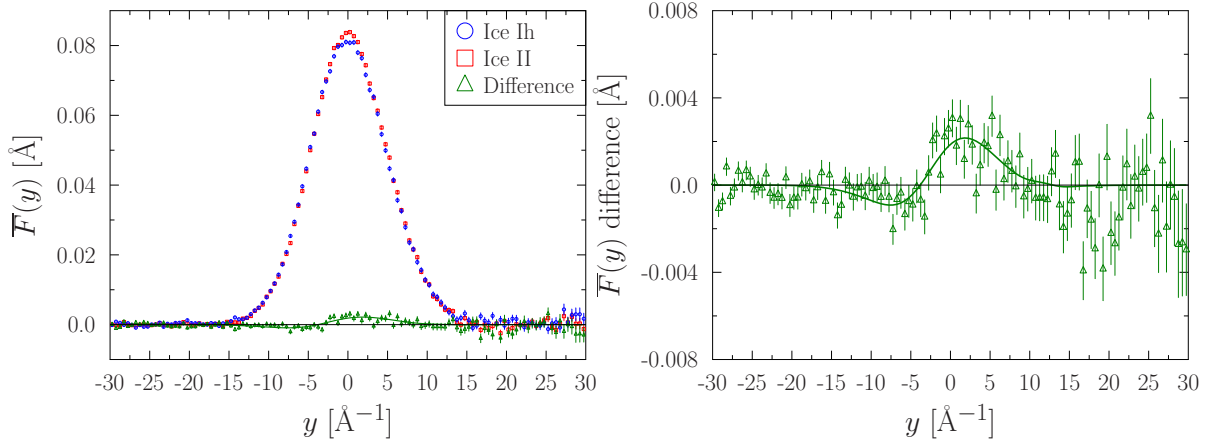


Figure 6.6: Experimental NCP of ice II compared with the other ice phases studied in this work. For $-\sigma < y < \sigma$ the ice II NCP is greater than the other as shown in the differences on the right side of the panel, this implies a lower mean kinetic energy.

represented here how the $n(p)$ of ice II is centred at lower values of p and how the total kinetic energy of ice II is lower with respect to the others.

6.2.4 Mean Force

The MF approach described in Sec. 2.4.1 was used for a further analysis on the corrected hydrogen NCPs. It is worth recalling here that a spherically-averaged anisotropic harmonic system returns a MF that departs from the linear trend, indeed shifting to a milder increase as a function of $x_{||}$ (with a slope that is always lower than the one of the corresponding isotropic reference). On the other hand, any exceeding of the linear slope is a clear sign of non-negligible anharmonicity of the atomic potential, possibly added to anisotropy smoothed by spherical averaging. After correction of the single-detector NCPs for FSEs, the NCPs have been averaged to recover, for each sample, the profile from which the MF was computed taking into account that the profile broadening due to instrumental resolution has been proven negligible. The results of the computation are shown in the Fig. 6.9 for the different ice phases.

It is interesting to look at the low value of $x_{||}$, Fig. 6.10, where the slope of the MF is dependent by the mean kinetic energy, lower the slope lower the mean kinetic energy as analysed in the $f(x_{||q})$ of Sec. 2.4.1. The slope of the ice II is slower than the other ice phases. It confirms the visual inspection and the fit results.

6.3 Stability induced by Entropy

The QENS [32, 27] measurements were performed at the IRIS [82] beam line on ice II, VI and IX. IRIS is an indirect geometry spectrometer where the energy of neutrons scattered by the sample is selected by means of the Bragg diffraction of a crystal-analyser array. There are two analyser banks, one made by pyrolytic graphite cooled at 10 K (higher efficiency and lower resolution) and the other by mica (lower efficiency and higher resolution). The range of the incident energy is defined by two choppers on the incident flight path located at 6.3 m and 10 m from the moderator. The incident energy-range defines the resolution

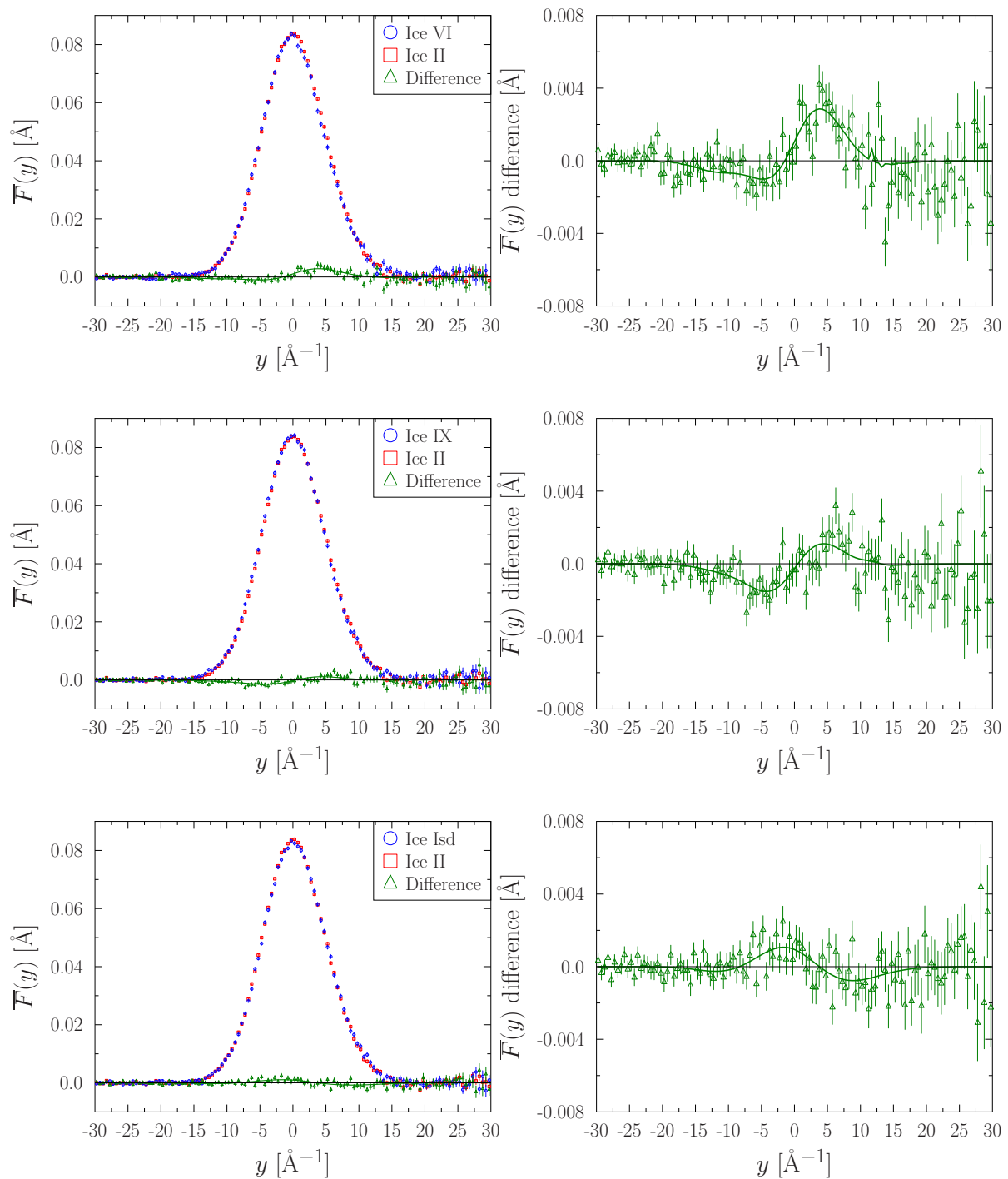


Figure 6.7: Experimental NCP of ice II compared with the other ice phases studied in this work. For $-\sigma < y < \sigma$ the ice II NCP is greater than the other as shown in the differences on the right side of the panel, this implies an mean kinetic energy.

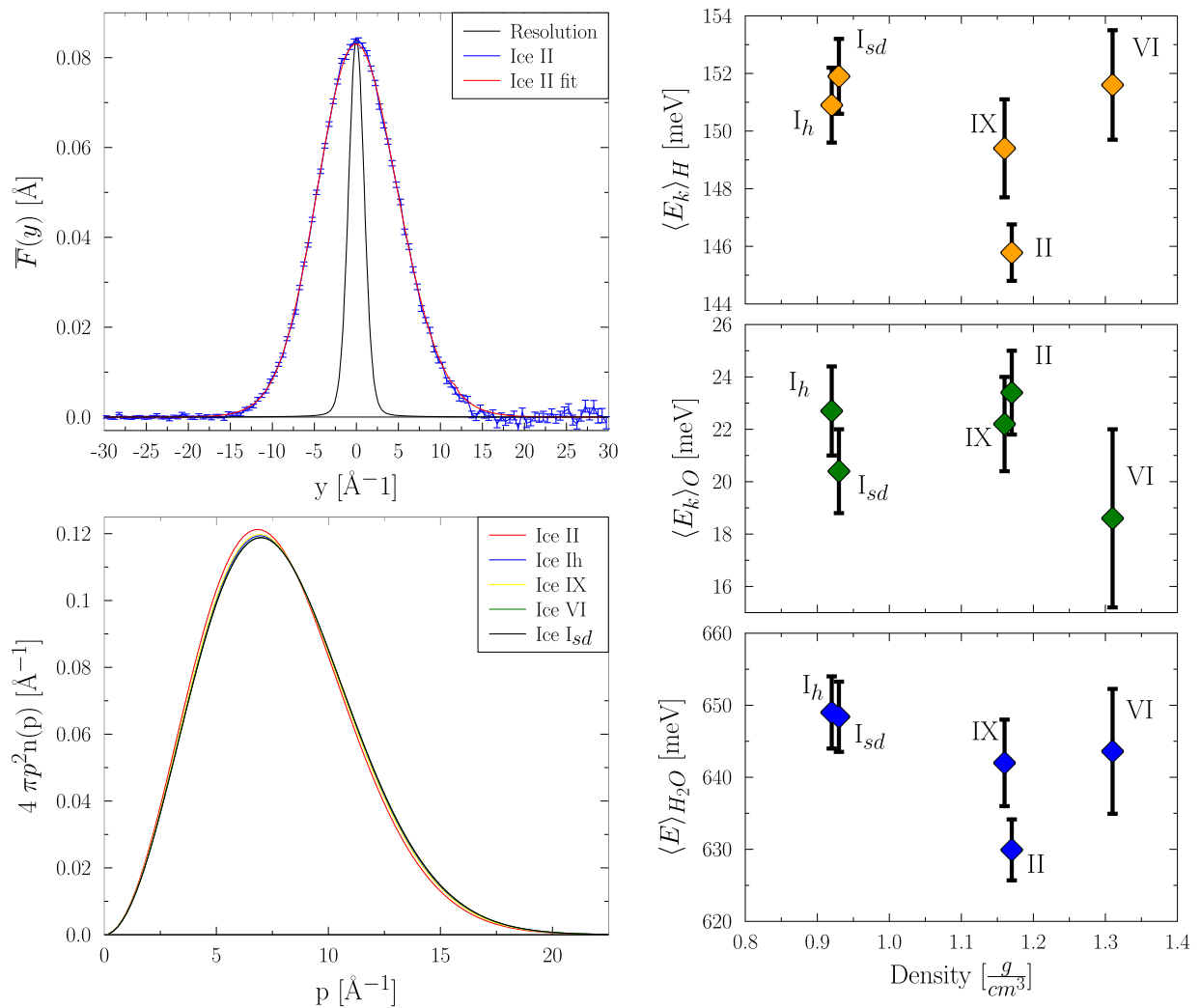


Figure 6.8: On the right panel the mean kinetic energy of hydrogen, oxygen and total molecule as a function of the phase density. On the top left the fit result of the hydrogen NCP in ice II while at the bottom the fitted second momentum for all the studied phases.

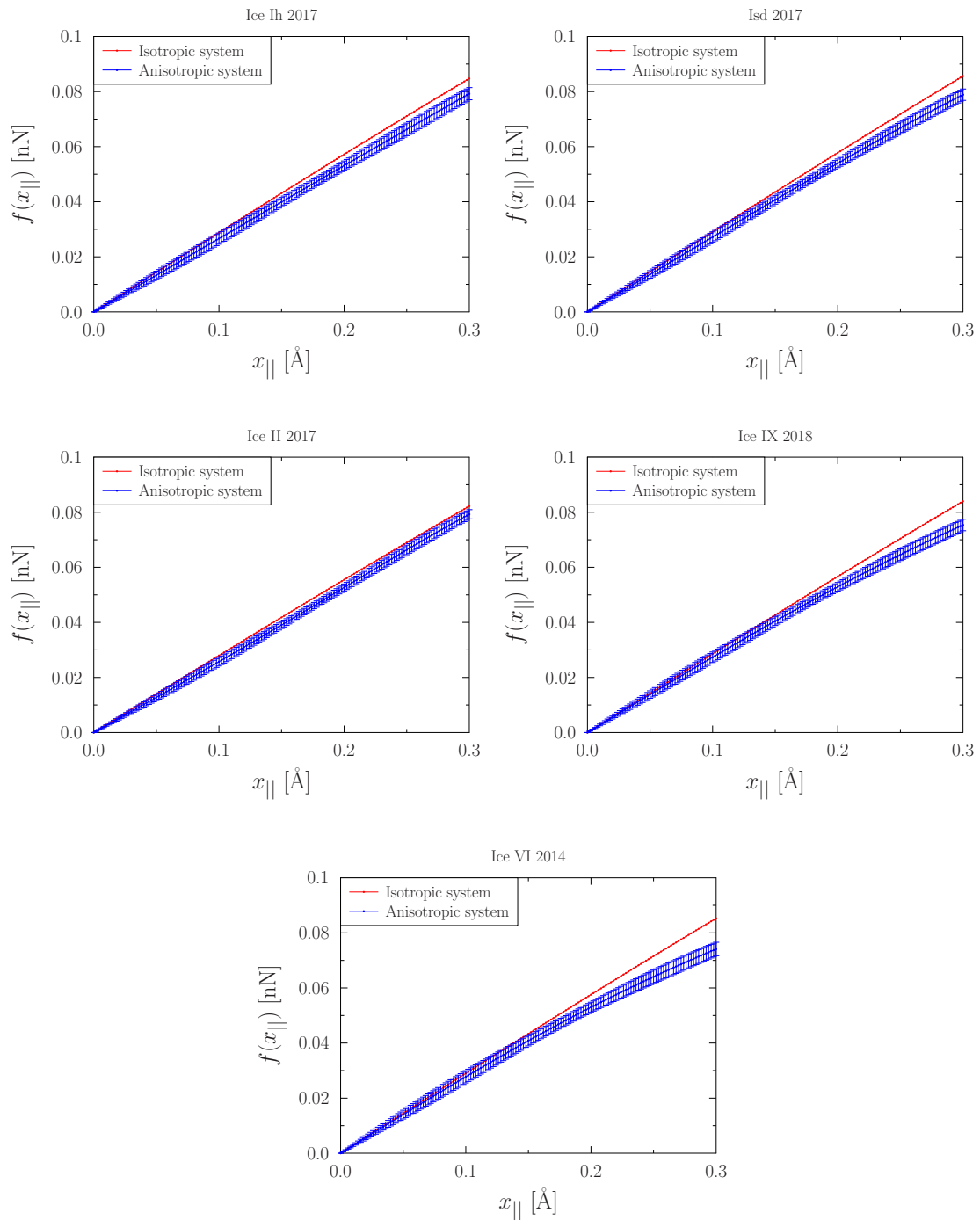


Figure 6.9: Mean force calculation for the experimental NCP in blue. The red line represents the isotropic limit of the distribution.

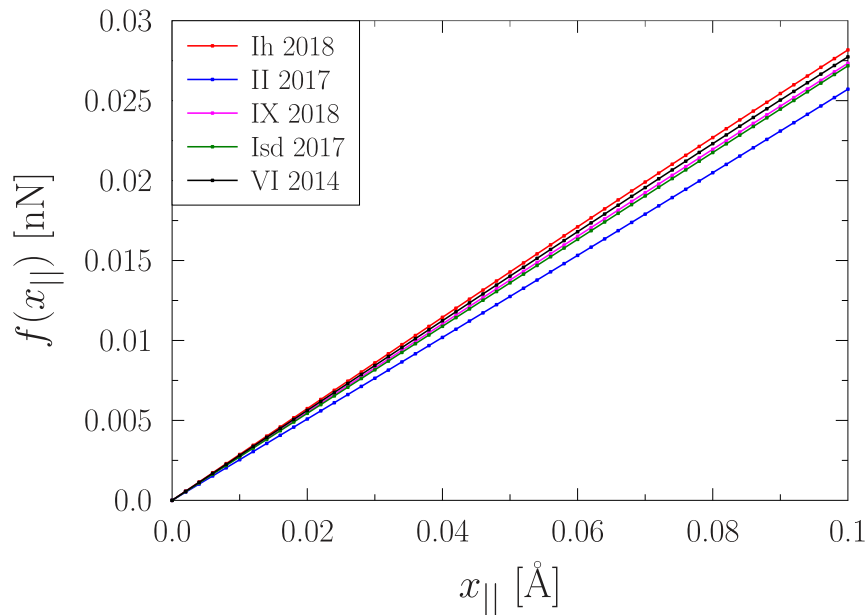


Figure 6.10: Mean Force calculation for the different ice phases. Ice II shows the lowest mean kinetic energy as it is associated with the lowest MF angular coefficient for low $x_{||}$.

and the energy transfer range of the experiment. Neutrons after the energy selection are detected by ZnS scintillator detector banks.

6.3.1 Experimental Detail

The powder samples with a packing fraction of about 50% were placed in aluminium flat-plate cans with dimension 40×40 mm² and thickness of about 0.3 mm to avoid multiple scattering effects. As it was decided to use primarily the low-Q graphite analyser, each sample was inserted in the IRIS Closed Circuit Refrigerator at an angle of about -45° with respect to the incident beam direction, Fig. 6.11, in the so called PG002 configuration [83] with ± 0.55 meV energy window around the elastic peak. In this configuration the blind spot, due to the flat can, is placed at high-Q scattering events of the graphite analyser. The reference sample used for the experiment is the stacking-disordered ice, I_{sd} . In fact, there is a phase transition to I_{sd} for ice VI and IX at ca. 150 K and at ca. 170 for ice II. The reference sample is used to eliminate the effect in the amount/density of the sample.

6.3.2 Data Reduction and Analysis

The detectors used for the data analysis were selected to eliminate the blind spot generated by the flat can as shown in Fig. 6.12, in particular detector 5-33 [0.5 - 1.5 Å⁻¹] were used.

During the experiment an elastic window scan [172, 83] was performed from 10 to 180 K every 10 K. For each temperature 10 minutes of data were acquired, about 33 μ Ah. For each temperature the elastic peak was integrated in the range $[-0.0175, 0.0175]$ meV and represented as a function of the temperature in Fig. 6.13.

The integrated elastic peak is proportional to the incoherent elastic cross section,

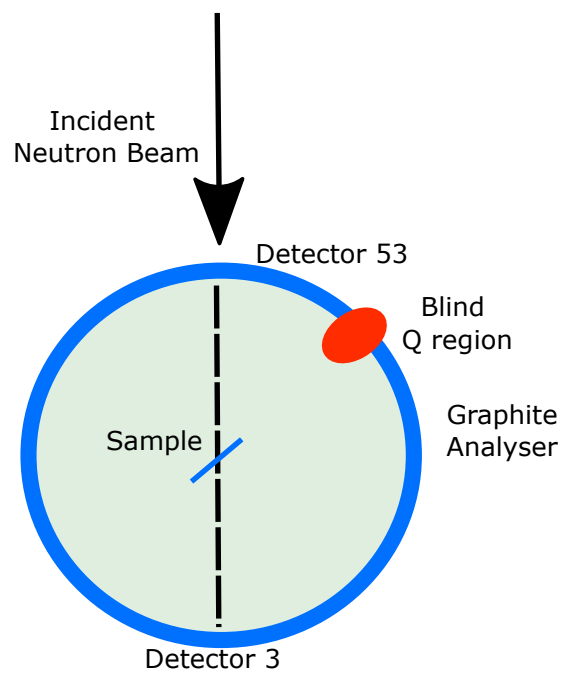


Figure 6.11: Geometry used for QENS-experiment.

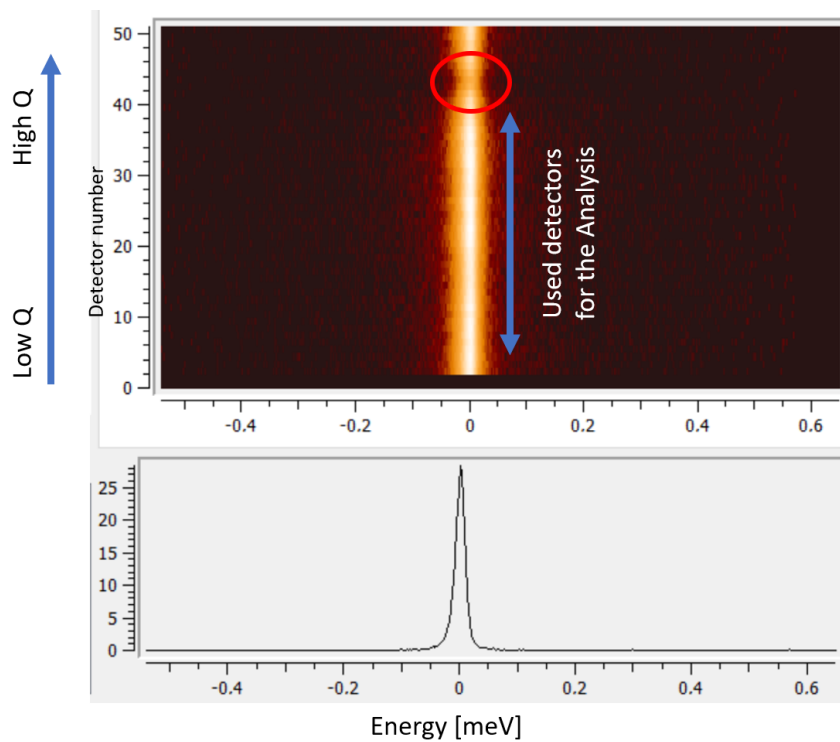


Figure 6.12: Spectrum viewer for the elastic peaks acquired on IRIS in the PG002 configuration. In red the blind-Q region and in blue the detector used for the analysis.

Sec. 2.2.1:

$$\left(\frac{d\sigma}{d\Omega}\right)_{inco-elast} \sim e^{(-2W)} = e^{-(\frac{1}{3}Q^2\langle u^2 \rangle)} = e^{\left(-\frac{\hbar Q^2}{6M} \int d\omega \frac{1}{\omega} g(\omega) \coth\left(\frac{\hbar\omega}{2k_B T}\right)\right)} \quad (6.2)$$

and

$$\langle u^2 \rangle = \frac{\hbar}{2M} \int d\omega \frac{1}{\omega} g(\omega) \coth\left(\frac{\hbar\omega}{2k_B T}\right) \quad (6.3)$$

where W is the Debye-Waller factor, Q is the scattering vector, $\langle u^2 \rangle$ the MSD around the equilibrium position, M the nucleus mass, ω the vibrational frequency and $g(\omega)$ the VDoS. In this picture higher is the MSD lower will the QENS signal be.

The integrated elastic peak is represented in Fig. 6.13 for each sample. It is evident the phase transition at ca. 150 K for VI and IX and at ca. 170 for ice II. Above those temperatures the three samples are in the same phase I_{sd} . In fact, the I_{sd} from the three samples is just slightly dependent upon the mother phase. By scaling all the ices I_{sd} coming from II, VI and IX to have the same integral from 90 to 170 K a comparison can be performed between ice II, VI and IX and shown in the bottom right of Fig. 6.13. In the

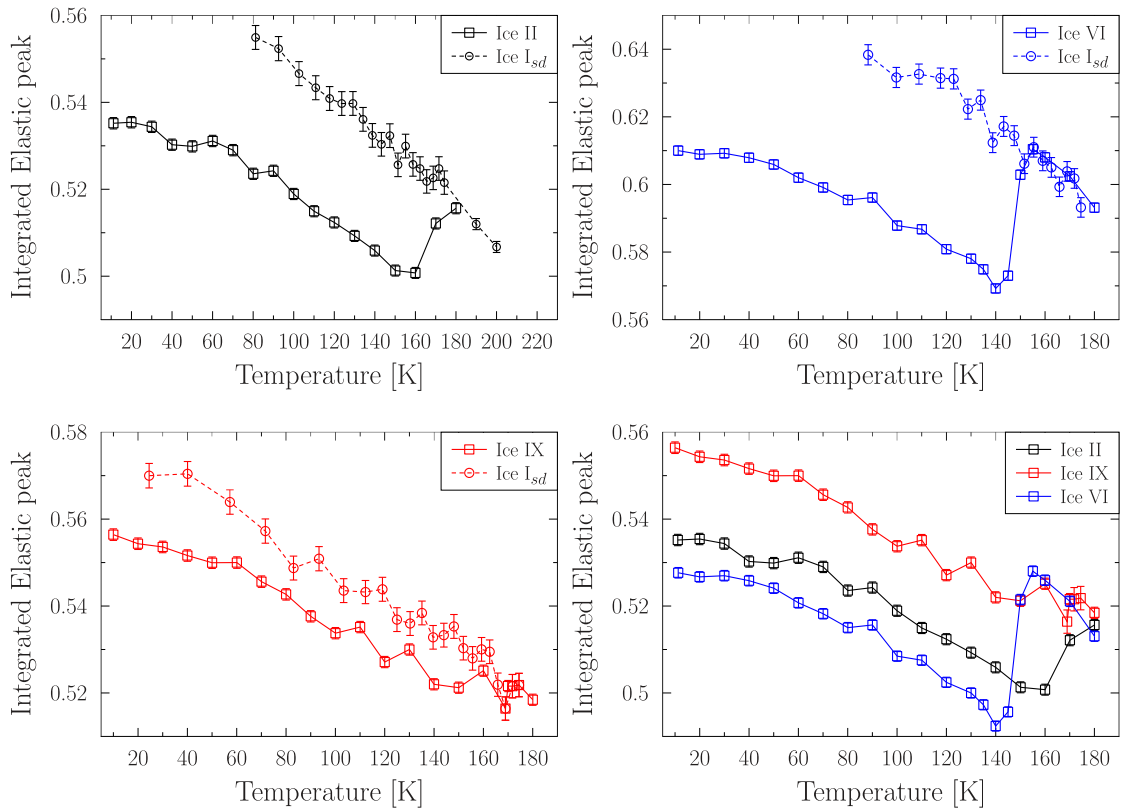


Figure 6.13: Elastic window scan for ice II, VI and IX.

spectra from different samples internally normalised to the common ice I_{sd} phase it is possible to appreciate how ice II has a higher MSD than ice IX, that is in turn higher than in ice I_{sd} . The result suggest that an additional term of entropy should be considered for the Gibbs potential to motivate the ice II stability. This term comes from the motion of the hydrogen that have low energy and high displacement around the equilibrium position. The *order* of the ice II phase and the absence of its disordered phase is then addressed to

the local hydrogen *disorder*. This disorder is not associated to the structure of ice like in the disordered phase but to the dynamics. In some extent the ice II molecule is dynamically stable.

The results from QENS and DINS are well correlated using INS data available in literature that will motivate qualitatively the evidences.

6.4 Inelastic scattering

INS data available in the literature [173, 135] were analysed in order to have a comparison between the VESUVIO and IRIS data. In fact, in Sec. 5.2.3 the mean kinetic energy and MSD were put in relation with the VDoS as the INS spectra are proportional to the VDoS as shown in Eq. 2.42.

The energy range of the vibrational spectra is from 0 to 140 meV for librations and translations and from 140 to 500 meV for bending and stretching as shown in Fig. 6.14.

For each INS spectrum the energy of the translation, libration, bending and stretching is calculated as the centroid of the band and reported in Table 6.4 for ice I_h, II, IX and VI. The kinetic energies and mean square displacements have been calculated using the contribution to the considered vibration, *i.e.*, the projected vibrational density of states $g_H(\omega)$. In the water molecule each hydrogen contributes for 0.5 of the energy in the libration, bending and stretching modes and 1/18 in the translations. In a single molecule model, the vibration contribution is then multiplied by the number of vibrations associated with each band, 3 for translation, 3 for libration, 1 for bending and 2 for stretching. Those coefficient are the $|\vec{e}_j|^2$ introduced in Chapter 5, in this case derived from physical consideration rather than Ab-Initio simulations. In fact, from a classical point of view we can define the j -nucleus contribution as the kinetic energy fraction:

$$|\vec{e}_j|^2 \sim \frac{\frac{1}{2}M_j\dot{\mathbf{x}}_j^2}{\sum_j \frac{1}{2}M_j\dot{\mathbf{x}}_j^2} \sim \frac{\frac{1}{2}M_j\mathbf{x}_j^2}{\sum_j \frac{1}{2}M_j\mathbf{x}_j^2} \quad (6.4)$$

where $\dot{\mathbf{x}}^2 \propto \mathbf{x}^2$ as in a classic harmonic oscillator when averaged on time. The translation is the motion of the centre of mass, hence all the \mathbf{x} are the same, and Eq. 6.4 is the ratio between the nuclear mass and the total molecule mass (1/18 for hydrogen and 16/18 for oxygen). In the rotation the oxygen is placed on the rotation axis so $\mathbf{x}_O = 0$ and $|\vec{e}_H|^2 = 1/2$ for each hydrogen. Finally for the stretching the hydrogen takes all the contribution for its lower mass $|\vec{e}_H|^2 = 1/2$.

Table 6.4: Energy of the vibration extrapolated from the INS spectra. The mean kinetic energy and MSD is also reported for each phase together with the shift with respect to ice I_h

Phase	Trasl. [meV]	Libr. [meV]	Bend. [meV]	Stretch. [meV]	$\langle E_k \rangle$ [meV]	$\langle u^2 \rangle$ [Å ²]	$\Delta \langle E_k \rangle$ [meV]	$\Delta \langle u^2 \rangle$ [Å ²]
Ih	14,75	69	200	411	154,24	0,0759	0	0
II	17,54	61	209	416	153,73	0,0778	-0,5087	0,0018
IX	16,11	65	209	414	154,67	0,0765	0,4317	0,0005
VI	17,14	59	204	425	154,59	0,0799	0,3496	0,004

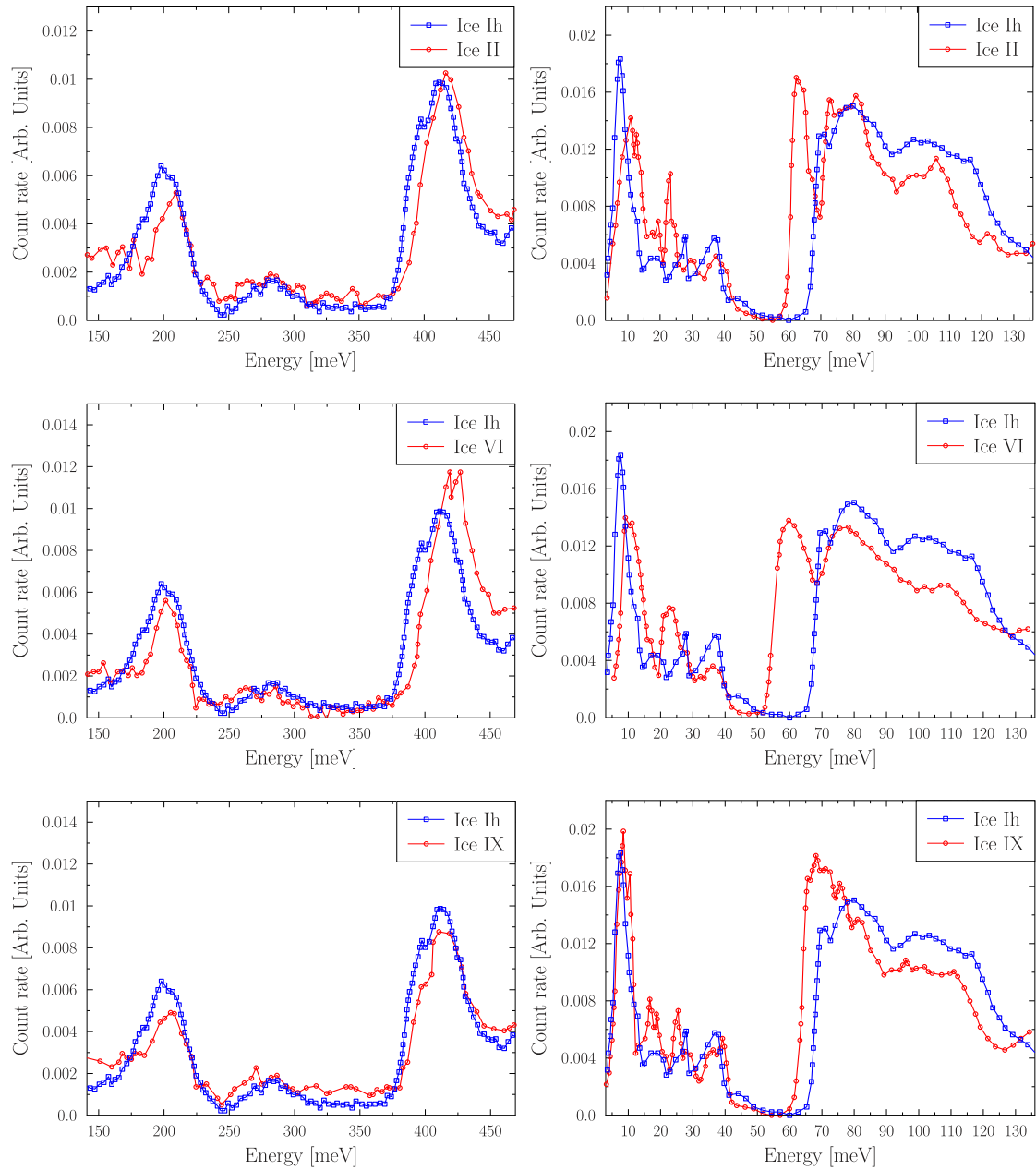


Figure 6.14: INS spectra reproduced from Ref. [173, 135].

As an example, the calculation of the zero-point total energy contribution for ice II is reported in the following both for the energy and mean square displacement shift with respect to ice I_h $\Delta\langle E_k \rangle$ and $\Delta\langle u^2 \rangle$:

$$\langle u^2 \rangle = \frac{\hbar^2}{2M} \int d\omega \frac{1}{\hbar\omega} g_H(\omega); \quad \Delta\langle u^2 \rangle_p = \langle u^2 \rangle_p - \langle u^2 \rangle_{Ih} \quad (6.5)$$

$$\langle E_k \rangle = \frac{\hbar}{4} \int d\omega \omega g_H(\omega); \quad \Delta\langle E_k \rangle_p = \langle E_k \rangle_p - \langle E_k \rangle_{Ih} \quad (6.6)$$

Where the p index stands for the ice II, IX and VI phase

$$\begin{aligned} \Delta\langle u^2 \rangle_{II} &= \\ &= \langle u^2 \rangle_{II} - \langle u^2 \rangle_{Ih} = \\ &= \left[\left(\frac{1}{17.5} - \frac{1}{14.7} \right) \cdot 3 \cdot \frac{1}{18} + \left(\frac{1}{61} - \frac{1}{69} \right) \cdot 3 \cdot 0.5 + \right. \\ &+ \left. \left(\frac{1}{209} - \frac{1}{200} \right) \cdot 1 \cdot 0.5 + \left(\frac{1}{416} - \frac{1}{411} \right) \cdot 2 \cdot 0.5 \right] \cdot \frac{\hbar^2}{2M} = \\ &= 0.0018 \text{\AA}^2 \end{aligned} \quad (6.7)$$

$$\begin{aligned} \Delta\langle E_k \rangle_{II} &= \\ &= \langle E_k \rangle_{II} - \langle E_k \rangle_{Ih} = \\ &= \left[(17.5 - 14.7) \cdot 3 \cdot \frac{1}{18} + (61 - 69) \cdot 3 \cdot 0.5 + \right. \\ &+ \left. (209 - 200) \cdot 1 \cdot 0.5 + (416 - 411) \cdot 2 \cdot 0.5 \right] \cdot \frac{1}{4} = \\ &= -0.51 \text{meV} \end{aligned} \quad (6.8)$$

The results for $\langle E_k \rangle$, $\langle u^2 \rangle$, $\Delta\langle E_k \rangle$ and $\Delta\langle u^2 \rangle$ for the other phases are reported in Table 6.4. The results calculated both for $\langle E_k \rangle$ and $\langle u^2 \rangle$ are of the same order of magnitude as found in literature [59, 58, 174]. Fig. 6.15 shows the results reported in the table for the MSD and mean kinetic energy as a function of the ice-phase density.

The general comment is that the analysis of the INS spectra is fully compatible with the DINS and QENS results. In fact, as for DINS, the ice II shows the lowest kinetic energy while, for the Mean Square Displacement, the highest value is for ice VI, the lowest for IX and ice II stands in the middle as in QENS results. The DINS and QENS trend would be exactly the opposite only in the case of an Einstein solid characterised by a single frequency, ω . In fact, in that case from Eq. 6.6 and 6.5:

$$\langle E_k \rangle \propto \omega; \quad \langle u^2 \rangle \propto 1/\omega. \quad (6.9)$$

Yet, in the general case of a vibrational density of states, the total zero-point energy is obtained from the sum over all vibrations:

$$\langle E_k \rangle \propto \sum \omega \quad \langle u^2 \rangle \propto \sum 1/\omega. \quad (6.10)$$

The dependence upon the frequency, or the inverse of the frequency, shows how the value of the mean square displacement is mainly driven by the low-energy frequencies, while the

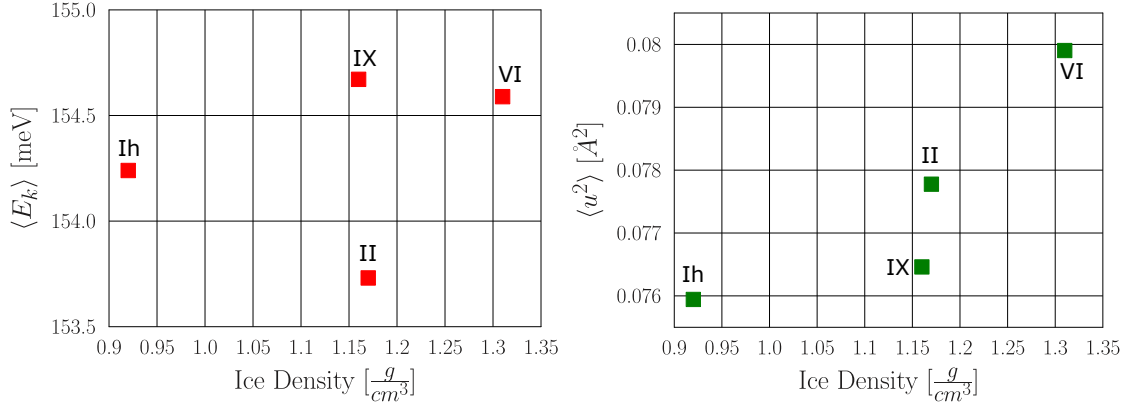


Figure 6.15: Values of $\langle E_k \rangle$ and $\langle u^2 \rangle$ calculated with INS frequencies as a function of the density.

value of the total (kinetic) zero-point energy is mainly driven by high-energy frequencies. Translations, despite the low energy, have little impact on the projected vibrational density of states (1/18 compared to 1/2 of the librations), for this reason librations are the main responsible for MSD trend. The INS spectra of ice II, IX and VI are reported in the same plot in Fig. 6.16 for a direct comparison.

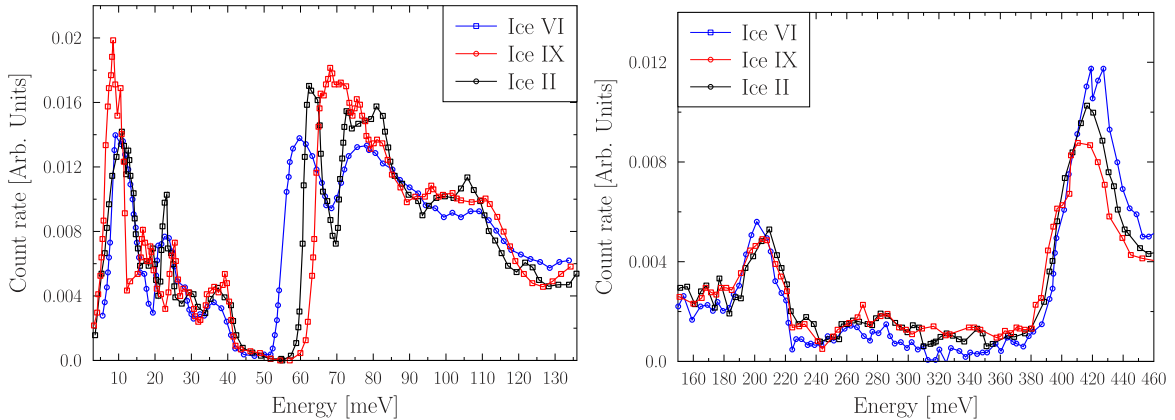


Figure 6.16: INS spectra for direct comparison of ice II, IX and VI.

Hence it is possible to use a quasiharmonic model [175, 41] that relates quantitatively and qualitatively INS, DINS and QENS results. Using the definitions of both MSDs and nuclear mean kinetic energies from an atom-projected vibrational density of states, *i.e.*, the measured INS data, we could reproduce the trend amongst ices II, IX and $I_s d$ that we obtained from the direct DINS and QENS measurements for the nuclear kinetic energy and MSD, respectively. One can interrogate the quasiharmonic model to assess the individual-mode contributions to MSDs and nuclear kinetic energy of hydrogen. We showed how the opposite shifts of stretching and librations in different phases of ice only partially cancel out, and that the trend of both QENS and DINS results is mainly driven by changes to the librational band frequency. In particular, this mode is the one most responsible for the high MSD and low mean kinetic energy in ice II, respectively. DINS and QENS results, as well as the quasiharmonic model, all suggest a picture whereby the hydrogen atom, experiencing a shallower potential along the librational mode, explores (and is delocalised)

over a larger volume of the direct space with respect to other ice forms. Such delocalisation can be interpreted as an orientational quantum disorder due to the quantum nature of hydrogen related to the nuclear wave function. The configurational disorder probed in diffraction experiments is static (assumes that the nuclei are not moving) and discrete (assumes that the molecule can move between a finite number of different configurations). On the other hand, the *orientational quantum disorder* we find is continuous and dynamical in nature, for the hydrogen wavefunction spans a continuous region around the hydrogen mean (classical) position and arises from the shallow librational mode. Generally when there is a phase transition between water and ice the stretching mode is translated towards lower energies because the hydrogen-oxygen distance of near molecule decreases and it is like another oxygen is stretching the spring in the other direction while the rotations become constrained and hence the energy increases. Hence rigid hydrogen bonding network would imply excess atomic kinetic energy due to localization induced by the network. The ice II structure instead combines a lowering of the hydrogen zero-point kinetic energy, and an increase of (zero-point) fluctuations in the hydrogen position, lifting geometrical frustration towards a hydrogen-ordered structure. The large displacement of hydrogen in ice II was already noticed by Kamb et al. in Ref. [176] where they measured a MSD of ca. 0.25 Å compared to 0.17 Å in ice I_h; they did not believe in their results in that moment but even if the changes in MSDs appear to be large for ice II relative to other phases there could be some truth behind the measurements as they correlate with our QENS results.

The beauty and the peculiarity of this stability, is that the *ordered* phase ice II is stable for its dynamical *disorder*.

6.4.1 Dynamics simulation

Driven by the curiosity to model the water molecule dynamics in ice I_h and II electronic Ab-Initio and phonon calculations were performed on the two phases. The structures were taken from Ref. [170] and [171] and the procedure followed in order to get the VDoS and the mean kinetic energy is the one reported in Chapter 5. In Fig. 6.17 the simulated $S(Q, \omega)$, once the VDoS was elaborated with AbINS, is represented and compared with the INS data taken from literature [173]. Even if the stretching mode is underestimated and the libration band overestimated, a known effect when PBE functional for the exchange-correlation term is used [44], the relative position of two ice phases is consistent with the experiment, hence lower libration and higher stretching for ice II that give rise to a competing quantum effect. Even the hydrogen simulated total kinetic energy correlates with DINS results as for ice II is 155.52 meV with respect to 156.03 meV for ice I_h, a summary of the kinetic energy simulated in the present study is reported in Table 6.5. Further studies will be addressed for simulation with the SCAN approximation and pseudopotentials that have been recently proved to be a good approximation for hydrogen bonds [177] and water systems.

Table 6.5: Simulated hydrogen and oxygen mean kinetic energy within the present study at 80 K.

	I _h (H)	II (H)	I _h (O)	II(O)
$\langle E_k \rangle$ [meV]	156.03	155.52	34.49	34.01

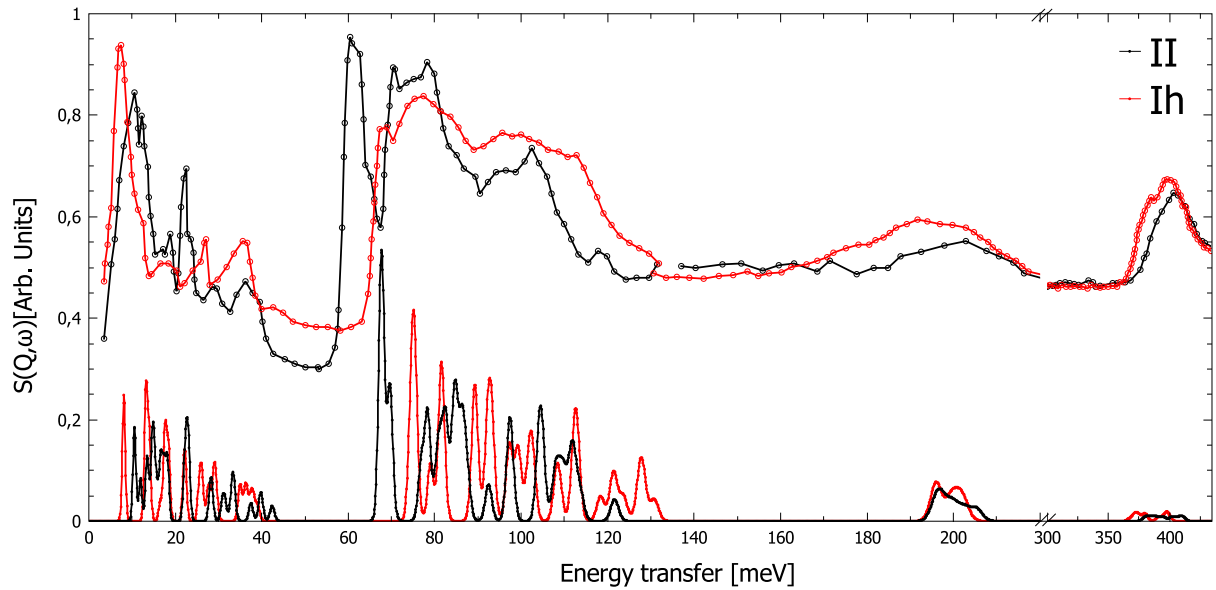


Figure 6.17: Experimental $S(Q, \omega)$ of ice II and I_h reproduced from Ref. [173] (top) and simulated (bottom).

As a final remark Ref. [178] by Ramirez et al. reports the molecular kinetic energy of ice I_h and II calculated using Path Integral Molecular Dynamics (PIMD-q-TIP4P/F) [179] (a sophisticated simulation method where even the nuclei are considered as quantum particles). They found that the total kinetic energy of ice II is lower than for ice I_h of about 4 meV, to be compared with the 5-10 meV from our DINS results. In Fig. 6.18 the results obtained within the PhD project and from Ramirez are represented.

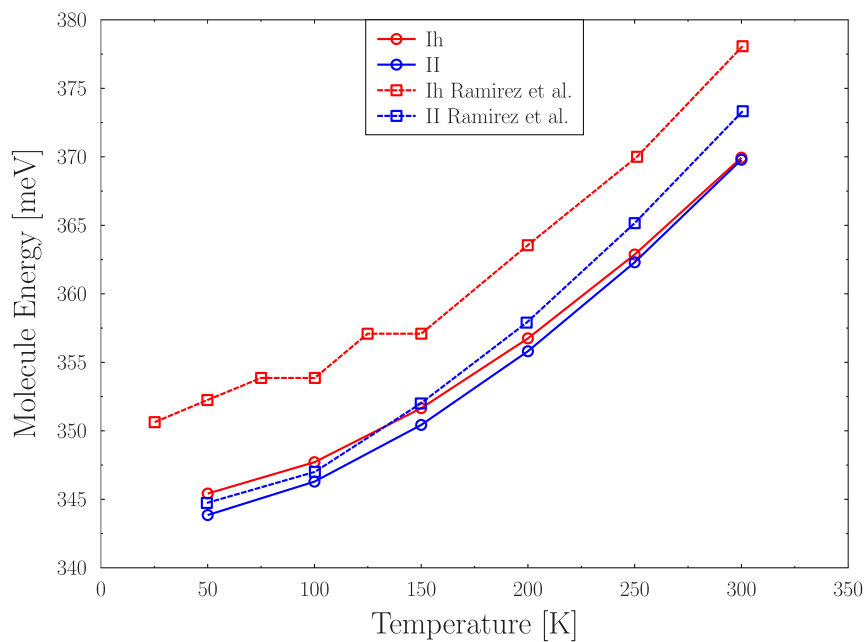


Figure 6.18: Mean kinetic energies reproduced from [178] (dotted line) and obtained in in the context of the PhD project (continuous line).

Chapter 7

Conclusion

The single-particle nuclear dynamics is a fundamental condensed-matter properties that is capable to answer to many open-question in Physics and Chemistry. In this work I have brought the eV neutron spectroscopy technique a step further, measured and simulated the biphenyl hydrogen dynamics and answered to an open topic regarding the phenomenology of the water phase diagram.

In Chapter 4 I have described an innovative device and an acquisition methodology, called γ DA that will be mounted and operate on VESUVIO and will broaden the capability of eV neutron spectroscopy; in fact, while DINS can provide such unique benchmarks for theory and computer simulations, it is a relatively slow experimental technique. VESUVIO at present makes use in forward scattering of a neutron energy selection based on a radiative resonance of two gold 12.5- μ m-thick foils; the photons produced by the reaction are detected just if they have an energy greater than a threshold of 600 keV. The choice was made when older uranium foils were used that were then substituted by gold foils for safety reasons. The characteristic of the gamma emission of gold, predominant at energy lower than 600 keV, brought the necessity of a new optimization of the detection method. Preliminary tests on a polyethylene sample where the threshold was lowered have shown how the change of the low-level discrimination threshold of the gamma-sensitive forward-scattering detectors on the VESUVIO spectrometer allows a substantial increase of the count rates, and a reduction of the experimental error bars and noise levels. In particular, by moving the threshold value from 600 keV to its minimum value, I have observed a threefold increase in count rate, and a reduction of ca. 40% and 35% of error bars and noise, respectively. Then I simulated the γ DA response with FLUKA simulations in terms of detection efficiency and resolution. I discovered that, at present, not only VESUVIO is working in a γ region where the emission of gold is not so intense but the detectors used are even more efficient in the low-energy region of about a factor 2. I have finally tested three γ DA set-ups with a biparametric acquisition chain, so as to boost the count rate at the VESUVIO spectrometer on a biphenyl sample. Biphenyl is a fundamental model compound to emulate the behaviour of lignin and the decomposition of the C-C linkage present between the two phenyl rings. I have found that a combination of thicker gold foils, and lower values of the acquisition threshold can bring gains in the count-rate of a factor of 5. When such changes are accompanied by additional shielding of the detectors with 0.5-mm-thick Pb foils, an improvement of the 50% in the signal-to-background ratio is obtained as well. The measurement of the biphenyl dynamics revealed a nuclear momentum distribution of hydrogen in biphenyl as a pure Gaussian function, both isotropic and

harmonic.

In Chapter 5 I used Ab-Initio simulations, performed within the QE and CASTEP environments, to reproduce the dynamics of hydrogen in biphenyl so as to be compared with the experiment. The experimental Gaussian momentum distribution proves that the harmonic approximation for the nuclear dynamics within the molecule, at the base of DFT-based phonon calculations, is valid. The kinetic energy simulated is in good agreement with the experiment, on the other hand, when such simulations are run on a single molecule or on single crystal, the theory predicts some anisotropy that is not found in the experimental data. I related the experimental result to the validity of the Central Limit Theorem, by simulating saturated hydrocarbons with increasing number of nuclei per molecule. The results give, on one hand, a decreasing value of the degree of anisotropy, as expected, that do not tend to zero as, on the other hand, happen experimentally. This is motivated by the fact that, for the real (disordered) system, the number of independent vibrations affecting the hydrogen dynamics is substantially higher than in a typical computer simulation and coupling effects of different normal modes are expected to reduce the level of anisotropy of the local potential. These are important pieces of information for the community studying molecular spectroscopy, *e.g.*, as for the modelling of chemical processes to convert lignin into monocyclic hydrocarbons. The step forward that could be made is to relate the energetic stability of biphenyl with the separated phenyl rings, with the opportunity to assess which is the best molecule to be combined to avoid the reformation of the C-C linkage between the two rings.

Finally in Chapter 6 I have discussed the unusual stability of ice II. In fact, the ice phases can be divided in ordered and disordered. Every ordered phase has a disordered counterpart but ice II. I studied the ice II stability with respect to ice IX, VI and I_h with Deep Inelastic and Quasi Elastic Neutron Scattering. The former technique gave an unusually low hydrogen zero-point kinetic energy as a consequence of the shallow potential where the hydrogen is seated. The low energy has a stabilising effect on the ice II molecule with a reduction of the system-internal energy. The Quasi Elastic experiment gave as result the vibrational Mean Square Displacement of hydrogen that was larger for Ice II, being, as a first approximation, the conjugate of the energy space. The larger displacement gives an additional contribution to the entropy of the system which is *ordered* by the nuclear *disorder*. Hence statically speaking ice II is ordered as the hydrogen-oxygen covalent bonds are oriented always in the same directions but the entropy, that generally stabilises the disordered phases, is recovered in ice II with the vibrational nuclear dynamics.

In conclusion this work has given a new detection device and methodology to perform a 5 times faster and 50% cleaner measurements of Deep Inelastic Neutron scattering with a consequent increase of the VESUVIO sensitivity towards a bulk hydrogen identification lower than $\mu\text{mol}/\text{cm}^{-2}$. The apparatus was used, in its final configuration, to have an insight on the hydrogen dynamics of biphenyl that was simulated with the most used Ab-Initio simulation tools. The instrumentation development was coupled in the PhD project with the characterization of the ice II phase and I succeed to answer to one of the unsolved problem of the water phase diagram: the unusual stability of ice II.

Chapter 8

Outlook and future perspectives

The simulation expertise learned will be addressed in the modelling of neutron cross sections of all the amino acids present in Nature that I measured on VESUVIO during the PhD period. Figure 8.1 shows a preliminary result of the experimental, as measured on VESUVIO with the standard GS20 transmission monitor and a novel GEM detector, and the simulated glutamic acid cross section normalised to the total free scattering cross section. The impact of this work will be devoted to the necessity of a cross-section database that can be used, as an example, for the boron neutron capture therapy [180], a radiation procedure for treating cancer, in order to reproduce the interaction between neutrons and human tissues.

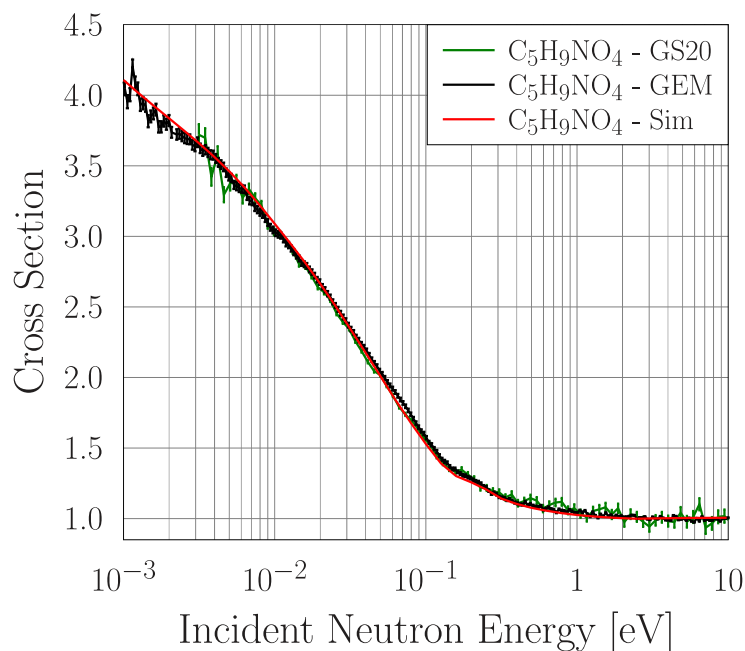


Figure 8.1: Simulated and Experimental glutamic acid scattering cross section as measured on VESUVIO with the standard GS20 and an innovative GEM detector.

Furthermore I am at present trying to reproduce, with the tools presented in this work, the hydrogen dynamics in the ice phases that populate the phase diagram as accurate as possible. As a first step, I found that the inclusion of van der Waals interactions, really important in molecular solids as ice or biphenyl or amino acids, increase the accuracy of the simulated INS spectrum showed in Fig. 8.2. In fact, the new approach brings the libration

band to a lower value and the stretching to higher energies with respect to the spectrum reported in Sec. 6.4.1. A comparison between the mean kinetic energy results from the two approximations is reported in Table 8.1 where the lower ice II energy, compared to ice I_h , is confirmed.

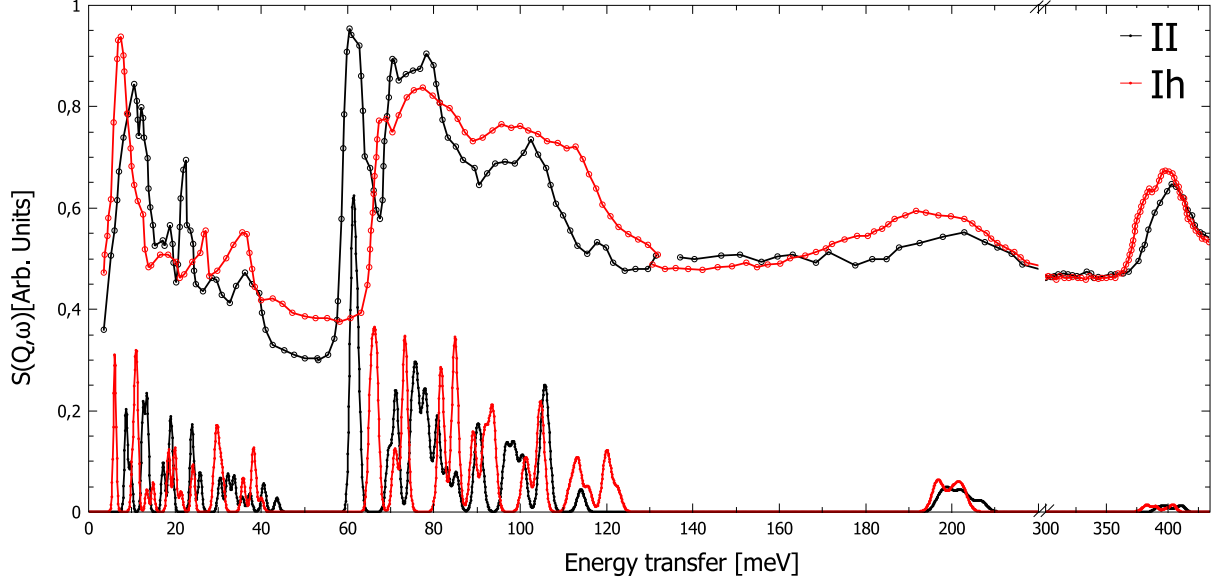


Figure 8.2: Experimental $S(Q, \omega)$ of ice II and I_h reproduced from Ref. [173] (top) and simulated using van der Waals functional [181, 182] (bottom).

Table 8.1: Simulated hydrogen and oxygen mean kinetic energy obtained within the present study at 80 K for PBE and van der Waals functionals.

	I_h (H)	II (H)	I_h (O)	II(O)
$\langle E_k \rangle$ [meV] PBE	156.03	155.52	34.49	34.01
$\langle E_k \rangle$ [meV] vdW	155.34	154.90	34.69	34.07

Chapter 9

Publications and Activities

9.1 Published papers

- Ulpiani, P., Romanelli, G., Onorati, D., Krzystyniak, M., Andreani, C. and Senesi, R. (2020). The effective isotropy of the hydrogen local potential in biphenyl and other hydrocarbons. *Journal of Chemical Physics*, 153(23), 234306.
- Onorati, D., Romanelli, G., Ulpiani, P., Cazzaniga, C., Preziosi, E., Arcidiacono, L., Festa, G., Andreani, C, Senesi, R. and Morone, M. C. (2020). FLUKA simulations and benchmark measurements of the YAP (Ce) scintillators installed on the VESUVIO spectrometer. *Nuclear Instruments and Methods A*, 969, 164012.
- Ulpiani, P., Romanelli, G., Onorati, D., Parmentier, A., Festa, G., Schooneveld, E., Cazzaniga C. Arcidiacono, L., Andreani, C. and Senesi, R. (2019). Optimization of detection strategies for epithermal neutron spectroscopy using photon-sensitive detectors. *Review of Scientific Instruments*, 90(7), 073901.
- Ulpiani, P., Romanelli, G., Arcidiacono, L., Onorati, D., Festa, G., Krzystyniak, M., Schooneveld, E., Fernandez-Alonso, F., Andreani, C and Senesi, R. (2018). Enhancement of counting statistics and noise reduction in the forward-scattering detectors on the VESUVIO spectrometer. *Journal of Physics: Conference Series*, 1055, 012008.
- Onorati, D., Andreani, C., Arcidiacono, L., Fernandez-Alonso, F., Festa, G., Krzystyniak, M., Romanelli, G., Ulpiani, P. and Senesi, R. (2018). Gamma background characterization on VESUVIO: before and after the moderator upgrade. *Journal of Physics: Conference Series*, 1055(1), 012009.
- Ulpiani, P., Romanelli, G., Onorati, D., Andreani, C. and Senesi, R. (2021). Central Limit Theorem applied to the nuclear hydrogen dynamics in biphenyl. *Nuovo Cimento C*. Submitted.
- Salzmann, C. et al. (2021). The origin of the ice II anomaly. In preparation.
- Romanelli, G., Onotati, D., Ulpiani, P., Cancelli, S., Perelli-Cippo, E., Márquez Damián, J. I., Capelli, S. C., Croci, G., Muraro, A., Trdocchi, M., Gorini, G., Andreani, C. and Senesi, R.(2021). Thermal neutron cross sections of amino acids from

average contributions of functional groups. Submitted to Journal of Physics: Condensed matter, already available on ArXiv at <https://arxiv.org/abs/2102.06147> .

- Romanelli, G., Festa, G., Onorati, D., Preziosi, E., Ulpiani, P., Andreani, C. and Senesi, R. (2021). Time-resolved Prompt-Gamma Activation Analysis at Spallation Neutron Sources and Applications to Cultural Heritage, Security, and Radiation Protection. Submitted to Physics Open.

9.2 Communications

- “The hydrogen dynamics in biphenyl probed by enhanced deep inelastic neutron scattering”, P. Ulpiani et al., 106° national congress of Società Italiana di Fisica, condensed matter section. 14-18/09/2020 (Talk).
- “The unusually low zero-point energy of ice II”, P. Ulpiani et al., 105 ° national congress of Società Italiana di Fisica, condensed matter section. 23-27/09/2019 (Talk).
- “New gamma detection strategies for epithermal neutron instrumentation”, P. Ulpiani et al., Molecular Spectroscopy Science Meeting 2018, UCL, London, UK. 6-8/11/2018 (Talk).
- “New detection strategies for highlighting anisotropy on the VESUVIO spectrometer”, P. Ulpiani et al., Molecular Spectroscopy Science Meeting 2018, UCL, London, UK. 6-8/11/2018 (Poster).
- “Enhancement of counting statistics and noise reduction in the forward-scattering detectors on the VESUVIO spectrometer”, 104° national congress of Società Italiana di Fisica, condensed matter section. 17-21/09/2018 (Talk).
- “Inelastic neutron scattering at eV energies with enhanced counting statistics and noise reduction at the VESUVIO spectrometer”, P. Ulpiani et al., VII International Workshop on eV Neutron Spectroscopy, Villa Wolkonsky e Museo Storico della Fisica e Centro Studi e Ricerche Enrico Fermi, Roma. 7-8/11/2018 (Poster).

9.3 Prizes

- SIF-SoNS Neutrons Matter prize, dedicated to a young researcher in neutron science with a master degree in Physics after January 2015, “Per le sue significative attività sperimentali nell’ottimizzazione dei metodi di rivelazione e analisi di energia dei neutroni agli elettronvolt, e le loro applicazioni alla misura dell’energia di punto zero nelle fasi cristalline nel ghiaccio”, 17/09/2018.
- Best communication in the 106° national congress of Società Italiana di Fisica, condensed matter section, entitled “The Hydrogen Dynamics in Biphenyl Probed by Enhanced Deep Inelastic Neutron Scattering”.

9.4 Experiments

- IRIS 24/02/20-01/03/20 Experiment RB1990327, QUENS experiment on Ice II, VI and IX. *Vibrational component of mean square displacement of ice phases.*
- VESUVIO 24/02/20-01/03/20 Experiment RB2010019, DOI: 10.5286/ISIS.E.RB2010019. *Measurement of the neutron cross section of α -alanine and other amino acids for dosimetry applications.*
- VESUVIO 31/05/2019-09/06/2019 Experiment RB1910165, DOI: 10.5286/ISIS.E.RB1910165. *Enhanced VESUVIO detection set-up for increased-accuracy DINS measurements of the hydrogen anisotropic local potential.*
- VESUVIO 07/10/2018-13/10/2018 Experiment RB1820056, DOI: 10.5286/ISIS.E.RB1820056. *Test of Neutron Effects On Commercial Off The Shelf FPGA.*
- ChipIR 07/10/2018-13/10/2018 Experiment RB1900005, DOI: 10.5286/ISIS.E.RB1900005. *Test of Neutron Effects On Commercial Off The Shelf FPGA.*
- VESUVIO 13/09/2018-17/09/2018 Experiment RB1900006, DOI: 10.5286/ISIS.E.RB1900006. *The unusually low zero-point energy of ice II: Critical benchmarking against ice IX.*
- VESUVIO 15/04/2018-20/05/2018 Experiment RB1810351, DOI: 10.5286/ISIS.E.RB1810351. *Improved detection limit of hydrogen in materials using VESUVIO.*
- CHipIR 20/04/2018-23/04/2018 Experiment RB1800062, DOI: 10.5286/ISIS.E.RB1800062. *Test of Neutron Effects On Low Power Devices.*
- VESUVIO 04/09/2018-16/09/2018 Experiment RB1710140, DOI: 10.5286/ISIS.E.RB1710140. *The zero-point energy of the unusual ice II phase.*
- VESUVIO Training on the VESUVIO analysis. Didcot, UK.

9.5 Other Activities

9.5.1 “Percorso Formativo 24 CFU”

- Pedagogia speciale e Bisogni speciali educativi, 3 CFU
- Tecnologie didattiche, 3 CFU
- Didattica generale, 3 CFU
- Fondamenti di pedagogia, 3 CFU
- Ricerca educativa, 3 CFU
- Pedagogia sperimentale, 3 CFU
- Psicologia generale, 6 CFU

9.5.2 Part-time Employment

- Tutor, Laboratorio di Fisica Sperimentale 1, Bachelor degree in Scienze dei Materiali, Università degli studi di Roma Tor Vergata. A.A. 2017/2018. Teacher: Prof. B. Bonanni.
- Tutor, Laboratorio di Fisica Sperimentale 2, Bachelor degree in Scienze dei Materiali, Università degli studi di Roma Tor Vergata. A.A. 2017/2018. Teacher: Prof. E. Placidi.

9.5.3 Seminars

- “DFT calculations applied to nuclear dynamics”, P. Ulpiani, 23/04/2020, course of *Laboratorio di Fisica della Materia* for the Master degree in Physics, University of Rome Tor Vergata.

Appendix A

Quantum Espresso Input

A.1 Structure and Nuclear Potential Calculation

```
&CONTROL
calculation = 'relax'
prefix = 'biph'
pseudo_dir = '../pseudo'
outdir= './out'
/
&SYSTEM
ecutwfc = 150
ibrav = 0
nat = 44
ntyp = 2
/
&ELECTRONS
conv_thr = 1.D-9
/
&IONS
/
&CELL
/
CELL_PARAMETERS (angstrom)
8.0878535 0.0000000 -0.7218217
0.0000000 5.6300000 0.0000000
0.0000000 0.0000000 9.5100000
ATOMIC_SPECIES
H 1.008 H_ONCV_PBE-1.0.upf
C 12.011 C_ONCV_PBE-1.0.upf
ATOMIC_POSITIONS (crystal)
H -0.083706 0.325677 0.135419
H 0.026497 0.315590 0.381466
H 0.212295 -0.014817 0.472760
H 0.286066 -0.333967 0.306158
```

```
H 0.172992 -0.329563 0.060836
H 0.583706 0.825677 -0.135419
H 0.473503 0.815590 -0.381466
H 0.287705 0.485183 -0.472760
H 0.213934 0.166033 -0.306158
H 0.327008 0.170437 -0.060836
H 0.083706 -0.325677 -0.135419
H -0.026497 -0.315590 -0.381466
H -0.212295 0.014817 -0.472760
H -0.286066 0.333967 -0.306158
H -0.172992 0.329563 -0.060836
H 0.416294 0.174323 0.135419
H 0.526497 0.184410 0.381466
H 0.712295 0.514817 0.472760
H 0.786066 0.833967 0.306158
H 0.672992 0.829563 0.060836
C 0.034362 -0.001589 0.075252
C -0.003203 0.178795 0.170183
C 0.059936 0.173982 0.311342
C 0.163786 -0.010397 0.362377
C 0.203884 -0.189541 0.269779
C 0.139568 -0.185585 0.128920
C 0.465638 0.498411 -0.075252
C 0.503203 0.678795 -0.170183
C 0.440064 0.673982 -0.311342
C 0.336214 0.489603 -0.362377
C 0.296116 0.310459 -0.269779
C 0.360432 0.314415 -0.128920
C -0.034362 0.001589 -0.075252
C 0.003203 -0.178795 -0.170183
C -0.059936 -0.173982 -0.311342
C -0.163786 0.010397 -0.362377
C -0.203884 0.189541 -0.269779
C -0.139568 0.185585 -0.128920
C 0.534362 0.501589 0.075252
C 0.496797 0.321205 0.170183
C 0.559936 0.326018 0.311342
C 0.663786 0.510397 0.362377
C 0.703884 0.689541 0.269779
C 0.639568 0.685585 0.128920

K_POINTS (automatic)
6 6 6 0 0 0
```

A.2 Vibrations and Eigenvectors

```
phonon calc
&inputph
outdir = './out'
prefix = 'biph'
ldisp = .true.
tr2_ph = 1.0d-16
amass(1) = 1.008
amass(2) = 12.011
nq1= 2, nq2 =2, nq3=2
fildyn = 'biph.dyn'
/
```

```
&input
fildyn = 'biph.dyn1',
fileig = 'biph.eig'
asr='simple',
/
```


Appendix B

Bi-parametric analysis script

```
"""
Python script to analyse binary Biparametric acquisitions.
The script write four txt files:
- three coloumn TOF ENERGY INTENSITY conyour map
- two coloumns TOF intensity spectrum
- two coloumns TOF intensity with Lower Level Discrimination Threshold (
  ↳ LLDT) selection
The script makes:
- inensity contour map for the foil in and out configuration after the
  ↳ cycling technique
- TOF spectrum in the foil in and out configuration
- TOF spectrum with LLDT selection
If the PGAA is selected in the script the cycling technique is not used
  ↳ and the VESUVIO
foils will be not considered
Authors:
G. Romanelli (giovanni.romanelli@stfc.ac.uk)
P. Ulpiani (pierfrancesco.ulpiani@uniroma2.it)
D. Onorati (dalila.onorati@uniroma2.it)
"""

import numpy as np
from os import path
import matplotlib.pyplot as plt
import csv
from struct import unpack
#set font size of figures
plt.rcParams.update({'font.size': 30})
# the caen module saves in units of 2 ns. The following factor converst to
  ↳ us.
unit_time_conversion = 2./1.e3
#Detector
det_name = "ls_7"
#energy conversion,converts channels into MeV
```

```
unit_energy_conversion = 0.660/7053
#if the calibration line does not pass through zero
unit_energy_conversion_intercept = 0.
#variable used for the cycling procedure
sign=1
#defining strings for end of line and tab space on outputs
endl= "\n"
tab = "\t"
# defining the parameters for the 1D tof, 1D en
n_tof = 600 # the number of bins for the TOF histogram
n_en = 500 # number of energy bins for the energy histogram
min_tof = 0 #in us minimum Time Of Flight (TOF)
max_tof = 600 #in us maximum time of flight
min_en = 0. #in MeV minimum energy (maximum long-gate value)
max_en = 3.5 #in MeV maximum energy (maximum long-gate value)
#energy for each bin
den=(max_en-min_en)/n_en
#TOF for each bin
dtof=(max_tof-min_tof)/n_tof
#TOF variable
tof=0.
#The CAEN digitizer caen works with C++ routines where 2147483647 is the
    ↪ max length of an integer
max_integer = 2147483647
#TOF Vector used for output and plot
x=np.arange(min_tof,max_tof,dtof)
#Energy Vector used for output and plot
energia=np.arange(min_en,max_en,den)
#2-D vector for bi-parametric contour maps
Y,X=np.meshgrid(energia,x)
#Intensity for bi-parametric contour maps
Matrix = [0. for i in range(len(x))]
#1=PGAA 0=DINS
technique=0
# number of foil in and out runs
#if PGAA insert number of total runs in the foil_in_runs
foil_in_runs = 1
foil_out_runs = 1
#Run name, if PGAA use foil_in
foil_in= ["001_"]
foil_out= ["002_"]
#root of the files, if PGAA use name_in
name_in = "bifenile_Au_Pb_1_"
name_out = "bifenile_Au_Pb_2_"
#Maximum Lower Level Discrimination Threshold (LLDT)
max_threshold = 0.6 # MeV
```

```

#number of range LLDT that will be tested dividinx 0-max_threshold
n_th = 3
#variable used to normalise spectra outside the kinematic domain (420 mus)
norm=0.
#histogram to be filled after foil-out/in subtraction
histo_cycl=[[0. for i in range(n_en)] for y in range(n_tof)]
histo_cycl=np.array(histo_cycl)
#variable used to account foil in and out
k_foil=0
#variable used to avoid the cycling tecnique when PGAA technique is
    ↪ selected
control=2
if technique==1:
    control=1
#output directory
odirectory='path'
#cycle over the in-out configurations if DINS
for k_foil in range(0,control):
#string for the root of the file name
    name=''
#number of runs for each configuration
    number_of_runs=0
#name and number of runs initialization
    if (k_foil==0):
        name = name_in
        number_of_runs = foil_in_runs
        #print("foil in: ",name,tab,number_of_runs,endl)
    if (k_foil==1):
        name = name_out
        number_of_runs = foil_out_runs
        #print("foil out: ",name,tab,number_of_runs,endl)
#open the output file for spectra projected in TOF, biparametric and TOF-
    ↪ LLDT selected
    out_tof_filtered= name + "output_tof_ths_"+det_name+".dat"
    out_tof_filtered=open(odirectory + out_tof_filtered,'w')
    out_bipa= name + "output_bip_"+det_name+".dat"
    out_bip=open(odirectory + out_bipa,'w')
    out=open(odirectory +name + det_name + '_out' + ".dat",'w')
#initialise TOF projected, biparametric and TOF LLST-filtered spectra
    histo_tof=np.zeros(n_tof)
    histo_tof_filtered=np.zeros(n_tof)
    histo_en=np.zeros(n_en);
    histo=[[0. for i in range(n_en)] for y in range(n_tof)]
    histo=np.array(histo)
#variable used to normalise the spectra to the acquisition time,
    ↪ considering the number of t0 pulses

```

```

    t0_lines = 0
#variable used to account the events correctly filled
    number_of_events = 0
#variable used to account the events recorded
    lines = 0
#index used for the name of the run number for each configuration
    ktittle = 0
#cycle over the runs for each onfiguration
    for ktittle in range (0,(number_of_runs)):
#string where the run name will be stored
    title=''
    if (k_foil == 0):
        foil='foil_in_'
        title = foil_in[ktittle]
    if (k_foil == 1):
        foil='foil_out_'
        title = foil_out[ktittle]
    if (technique==1):
        foil='LLDT_'
#name of the files to be opened, t0 and yap file
    filename_t0 = name + title+"ls_0.dat"
    filename_yap = name + title+ det_name + ".dat"
    fileinp_t0 = open(odirectory + filename_t0,'rb')
    fileinp_yap = open(odirectory + filename_yap,'rb')
#check if the files are opened
    if (str(path.exists(odirectory + filename_t0))==False'):
        print("Could not open specified file t0:",tab,filename_t0,endl)
    if (str(path.exists(odirectory + filename_t0))==True'):
        print("File opened successfully: ",tab,filename_t0,endl)
        tof_file=np.fromfile(odirectory + filename_t0, dtype=np.int32)
    if (str(path.exists(odirectory + filename_yap))==False'):
        print("Could not open specified file YAP:",tab,filename_yap,
            ↪ endl)
    if (str(path.exists(odirectory + filename_yap))==True'):
        print("File opened successfully: ",tab,filename_yap,endl)
        yap_file=np.fromfile(odirectory + filename_yap, dtype=np.int32)
#read the first six entries, the headers
    i=0
    while i<6:
        (a,)=unpack('I',fileinp_yap.read(4))
        #print("header YAP: ",a,endl)
        i=i+1
    i=0
    while i<6:
        (a,)=unpack('I',fileinp_t0.read(4))
        #print("header TOF: ",a,endl)

```

```

        i=i+1
#initialise the index for the cycle over the events
        i=2
#variable used to stop the reading of t0 line when the file is finished
        stamp=3
#read the first t0 frame
        (tstart,)= unpack('I',fileinp_t0.read(4))
        (tshort,)=unpack('I',fileinp_t0.read(4))
        (tlong,)=unpack('I',fileinp_t0.read(4))
        (tend,)=unpack('I',fileinp_t0.read(4))
#cycle over the yap file
        while i <(len(yap_file)/(3)):
#read YAP event
            (tyap,)=unpack('I',fileinp_yap.read(4))
            (longyap,)=unpack('I',fileinp_yap.read(4))
            (shortyap,)= unpack('I',fileinp_yap.read(4))
#Temporaly increase tend adding the max integer if tend is cleared with
    ↪ respect to tstart
            if (tstart > tend and tyap > tstart):
                tend = tend + max_integer
#Temporaly increase tend and tyap adding the max integer if tend and tyap
    ↪ is cleared with respect to tstart
            if (tstart >tend and tyap < tend):
                tend = tend + max_integer
                tyap = tyap + max_integer
#if tyap belongs to rhe next TOF frame read the next tend until the TOF
    ↪ file exists
            if ( tyap > tend and stamp<len(tof_file)/(3)-1):
                stamp=stamp+1
                tstart=tend
                fileinp_t0.read(4)
                fileinp_t0.read(4)
                (tend,)= unpack('I',fileinp_t0.read(4))
#convert channel to MeV and unit time in mus
            longyap = longyap * unit_energy_conversion +
    ↪ unit_energy_conversion_intercetta
            tof = (tyap - tstart)*unit_time_conversion
#if tyap is between tstart and tend and between min and max TOF fill the
    ↪ TOF histogram with the event
#if the energy is even between max and min energy fill the bipsrametric
    ↪ histogram
            if tyap >= tstart and tyap<tend:
                number_of_events=number_of_events+1

                if tof < max_tof and tof >min_tof :
                    j=int((tof-min_tof)/dtof)

```

```

        histo_tof[j] = histo_tof[j]+1
        if longyap<max_en and longyap>min_en :
            e=int((longyap-min_en)/den)
            histo[j][e] = histo[j][e]+1
#if tend was increased by the max integer
    if (tend > max_integer):
        tend = tend - max_integer
    i=i+1
#end of the yap file cycle
    if k_foil==1:
        sign=-1
#normalise histograms by length of the file over the t0 frame (3 number for
    ↪ each frame and 4 bit for each number)
    histo_tof=histo_tof/((len(tof_file)-6)/3*4)
    histo=histo/((len(tof_file)-6)/3*4)
    histo_cycl=histo_cycl+histo*sign
    norm=np.sum(histo_tof[int(420/dtof):])
    #print('normalizza',np.sum(histo_tof[int(420/dtof):]))
    lines=lines+((len(yap_file)-6)/3)
    t0_lines=t0_lines+((len(tof_file)-6)/3)
    #end the run cycle
#normalise outside the DINS kinematic domain
    histo_tof=histo_tof/norm
#write the output file with the TOF spectrum
    writer=csv.writer(out,delimiter=('\t'))
    writer.writerows(zip(x,histo_tof))
    out.close()
    print("Number of T0 lines read: ",t0_lines ,endl)
    print("Number of events correctly filed: ", number_of_events, " out of:
    ↪ ", lines ,endl)
    print("Number of events lost: " , lines - number_of_events, tab,round(
    ↪ number_of_events/lines,3),"%", endl)
#write biparametric output
    for l in range (0,len(histo)):
        t = [x[l] for y in range(0,len(energia))]
        writer=csv.writer(out_bip,delimiter=('\t'))
        writer.writerows(zip(t,energia,histo[l][:]))
        out_bip.write('\n')
    plt.figure()
#cycle for the TOF filtered histogram
    for k_th in range (1,n_th+1):
        energy_threshold=max_threshold / n_th * k_th
        print("threshold loop: ",k_th," out of: ",n_th,endl)
        print("Energy threshold fixed to (MeV): ",energy_threshold,endl)
        for ene in range (0,n_tof):

```

```

        histo_tof_filtered[ene]=np.sum(histo[ene][int((energy_threshold
        ↪ )/den):])
#plot the tof filtered spectra
    plt.plot(x, histo_tof_filtered,linestyle='-', color='C'+str(k_th),
        ↪ linewidth=2, label=foil+str(round(energy_threshold,2))+'MeV')
    plt.legend(loc='upper right',fontsize=10)
    plt.tick_params(labelsize=10)
#write the tof filtered spectra
    out_tof_filtered.write(endl)
    out_tof_filtered.write(str(k_th))
    out_tof_filtered.write(endl)
    writer=csv.writer(out_tof_filtered,delimiter=('\t'))
    writer.writerows(zip(x,histo_tof_filtered,np.sqrt(
        ↪ histo_tof_filtered)/np.sqrt(t0_lines)))
    plt.savefig(odirectory + name + "output_thr_" + det_name + '.png',
        ↪ format='png')
#plot the biparametric contour map foil in and out
    for j in range (0,len(x)):
        Matrix[j]=histo[j][:]
    plt.figure()
    plt.contourf(X, Y, Matrix,levels=np.linspace(0,np.max(Matrix),200))
    plt.title(foil+ 'biparametric',fontsize=20)
    plt.tick_params(labelsize=10)
    plt.ylim([0, 1.])
    print(odirectory + name + "output_bip_" + det_name + '.png')
    plt.savefig(odirectory + name + "output_bip_" + det_name + '.png',
        ↪ format='png')
    out_bip.close()
    out_tof_filtered.close()
    out.close()
    #end the foil cycle
#if DINS, plot and write biparametric contour map and the tof filtered
    ↪ spectra after the cycling technique
if technique!=1:
    out_thr_cycl=open(odirectory + "output_thr_cycl_" + det_name+'.dat', 'w
    ↪ ')
    out_cycl=open(odirectory + "output_bip_cycl_" + det_name+'.dat', 'w')
    for l in range (0,len(histo)):
        t = [x[l] for y in range(0,len(energia))]
        writer=csv.writer(out_cycl,delimiter=('\t'))
        writer.writerows(zip(t,energia,histo_cycl[l][:]))
        out_cycl.write('\n')
    for j in range (0,len(x)):
        Matrix[j]=histo_cycl[j][:]
    plt.figure()
    plt.contourf(X, Y, Matrix,levels=np.linspace(0,np.max(Matrix),200))

```

```
plt.title('foil in-out biparametric',fontSize=20)
plt.tick_params(labelsize=10)
plt.ylim([0, 1.])
plt.savefig(odirectory + name + "output_bip_cycling" + det_name + '.png'
           ↪ , format='png')
plt.figure()
for k_th in range (1,n_th+1):
    energy_threshold=max_threshold / n_th * k_th
    print("threshold loop: ",k_th," out of: ",n_th,endl)
    print("Energy threshold fixed to (MeV): ",energy_threshold,endl)
    for ene in range (0,n_tof):
        histo_tof_filtered[ene]=np.sum(histo_cycl[ene][int((
            ↪ energy_threshold)/den):])
    plt.plot(x[int((100)/dtof):], histo_tof_filtered[int((100)/dtof):],
           ↪ linestyle='-', color='C'+str(k_th),linewidth=2, label='foil
           ↪ in-out_'+str(round(energy_threshold,2))+'MeV')
    plt.legend(loc='upper right',fontSize=10)
    plt.tick_params(labelsize=10)
    out_thr_cycl.write(endl)
    out_thr_cycl.write(str(k_th))
    out_thr_cycl.write(endl)
    writer=csv.writer(out_thr_cycl,delimiter=('\t'))
    writer.writerows(zip(x,histo_tof_filtered))
plt.savefig(odirectory + "output_thr_cycl_" + det_name + '.png', format
           ↪ ='png')
plt.show()
out_thr_cycl.close()
out_cycl.close()
```

Appendix C

Mean Force calculation script

```
# Programm used to calculate numerically the Mean Force using as Input the
    ↪ experimental Nuclear Compton Profile
#Authors: Pierfrancesco Ulpiani, Giovanni Romanelli
import scipy.integrate as integrate
import scipy.interpolate as interp
import matplotlib.pyplot as plt
import numpy as np
file = open("mf_VI_iso.dat","w") # open the output file

#Constants definition
dt=0.002 # temperature error (Kelvin)
#KB = 0.08616733 # Boltzman constant (meV/Kelvin)
KB = 1.381*10**(-3)
T = 80. #Temperature value (Kelvin)
#m = 1. # mass of the stuck atom
m = 1.66*10**(-27)
beta = 1/(KB*T)
#hbq = 4.178; #Plank constant()
hbq = (6.626*10**(-14))**2
pend = m/((beta**2)*hbq)
print (1/beta)

#read the dataset file
data=np.loadtxt('iso_VI_reb.dat', dtype='float', comments='#', delimiter=
    ↪ ' ', converters=None, skiprows=0, usecols=None, unpack=False, ndmin
    ↪ =0)

#find the bin associated with y=0 for symmetrization
ie=0
while ie < len (data[:,0]) : #
    #print (ie)
```

```

    if (data[ie,0]==0.):
        #print("ciao")
        #print(ie)
        i=ie
        ie+= 1

er=(len (data[:,0]))/2.

#symmetrize the dataset respect to 0
ie=1
while ie < er :
    data[ie+i,1]=(data[ie+i,1]+data[i-ie,1])/2.
    data[ie+i,2]=(np.sqrt(data[ie+i,2]**2+data[i-ie,2]**2))/2.

    ie+= 1

# plot the dataset
plt.scatter(data[:,0],data[:,1])
plt.xlabel('y[A-1]')
plt.ylabel('J')

# interpolate the dataset: both the ordinate and the errorbars

interpolato= interp.interp1d(data[:,0],data[:,1])
interpolatoerr= interp.interp1d(data[:,0],data[:,2])
desiredRange = np.arange(0, 30, 0.05)
i=interpolato(desiredRange)
j=interpolatoerr(desiredRange)

#plt.plot(i) #plot the data interpolation
#plt.plot(j) #plot the errorbars interpolation
b=np.arange(0,0.702,0.002) #create the effective lenght range to calculate
    ↪ MF

a=0

cerr1=2.*KB*KB*m*T*dt/hbq
cerr2=KB*dt
print(2.*KB*KB*m*T*dt/hbq)
#calculation of the integrals
while a < len(b):
    free = -pend*b[a]
    free2 = cerr1*b[a]

```

```
A = integrate.quad(lambda x: x*interpolato(x)*np.sin(b[a]*x), 0, 20,
    ↪ limit=300)
B = integrate.quad(lambda x: interpolato(x)*np.cos(b[a]*x), 0, 20,
    ↪ limit=300)
C =integrate.quad(lambda x: (x*np.sin(b[a]*x)*interpolato(x))**2, 0,
    ↪ 20, limit=300)
D =integrate.quad(lambda x: (interpolato(x)*np.cos(b[a]*x))**2, 0, 20,
    ↪ limit=300)
E =integrate.quad(lambda x: (interpolato(x)*np.cos(b[a]*x))**4, 0, 20,
    ↪ limit=300)
F =integrate.quad(lambda x: (x*np.sin(b[a]*x)*interpolatoerr(x))**2, 0,
    ↪ 20, limit=300)
G =integrate.quad(lambda x: (interpolatoerr(x)*np.cos(b[a]*x))**2, 0,
    ↪ 20, limit=300)
mf =(free+np.multiply((1./beta),np.divide(A[0],B[0])))*0.1
errmf= (free2 + np.abs(np.multiply(cerr2,np.divide(A[0],B[0]))) +np.
    ↪ divide(np.sqrt(np.divide(F[0],D[0])+np.divide(np.multiply(C[0],G
    ↪ [0]),E[0])),beta))*0.1

#write on the output file

file.write(str(b[a]))
file.write(str(" "))
file.write(str(mf))
file.write(str(" "))
file.write(str(errmf))
file.write(str("\n"))

a += 1
```


Appendix D

Ice $\overline{F}(y, Q)$

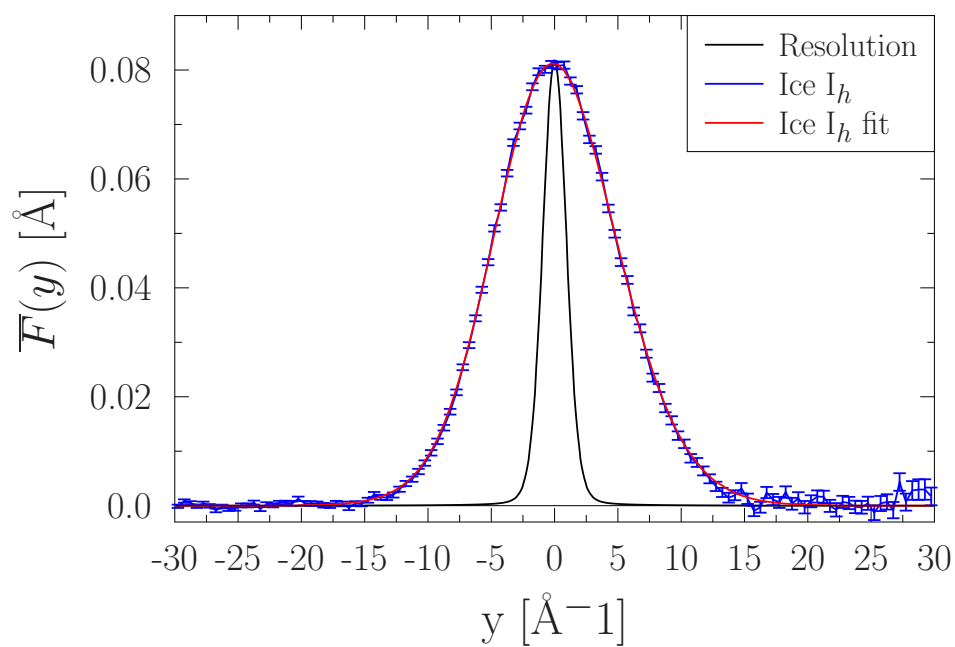


Figure D.1

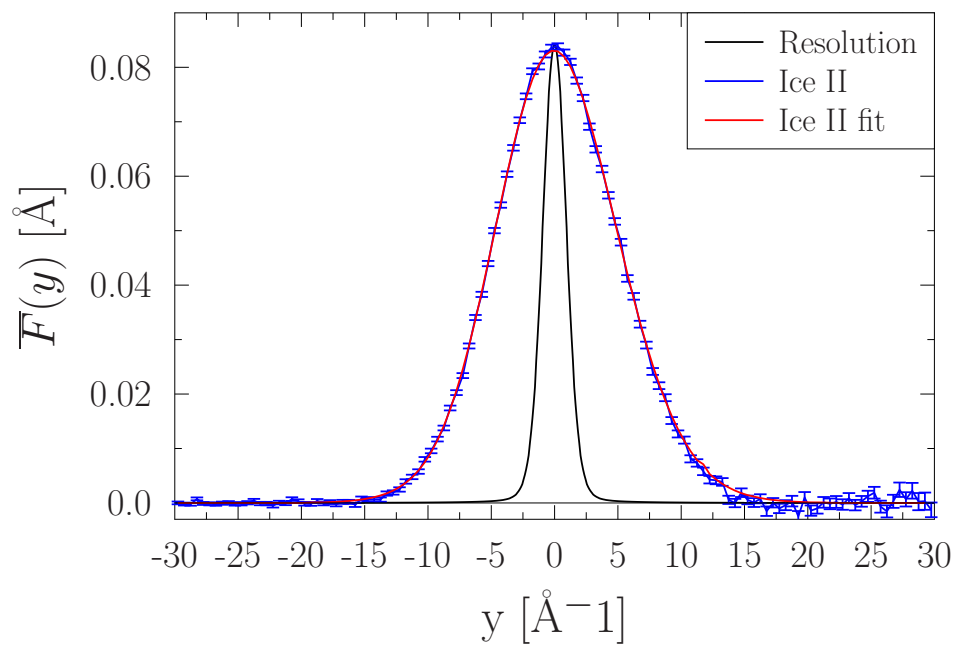


Figure D.2

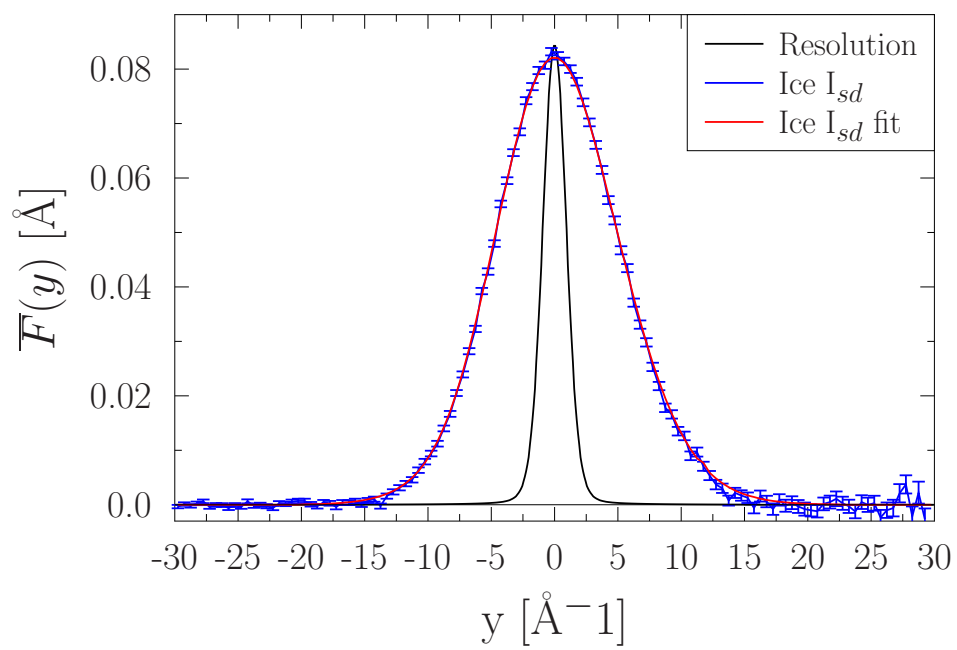


Figure D.3

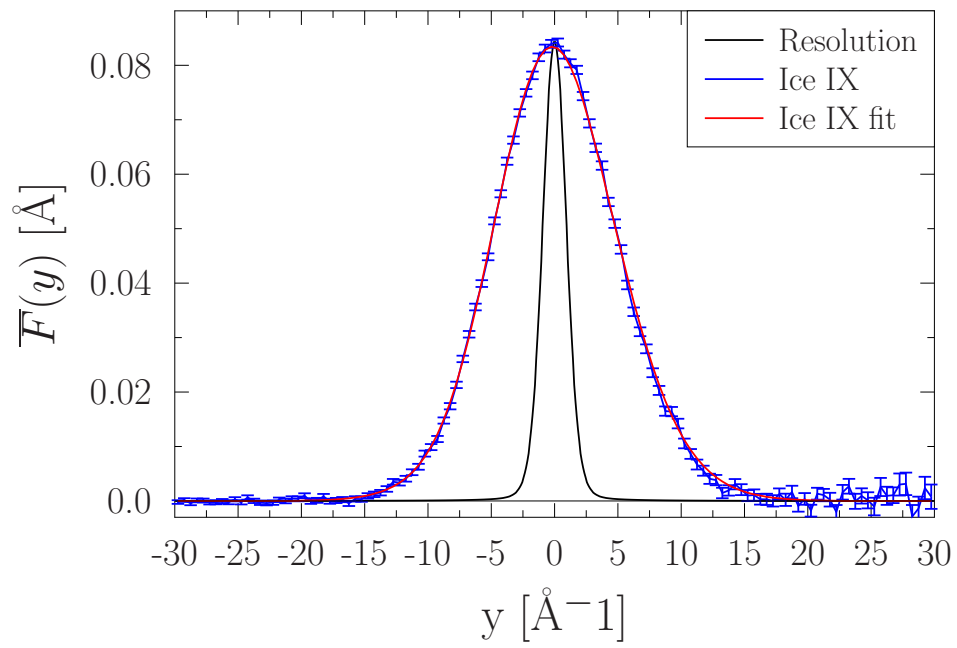


Figure D.4

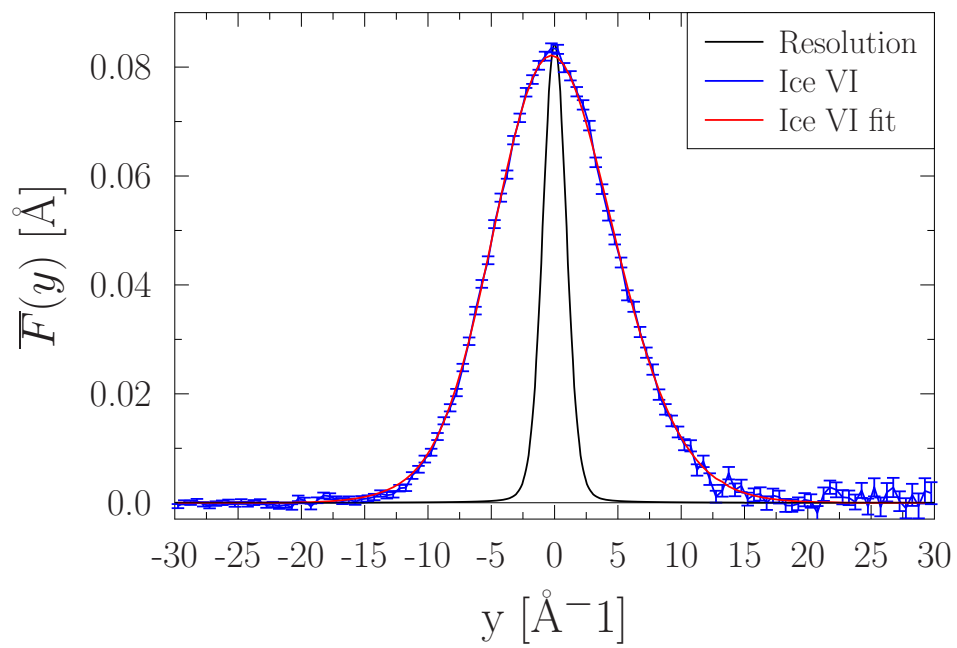


Figure D.5

Bibliography

- [1] C Andreani, D Colognesi, J Mayers, G F Reiter, and R Senesi. Measurement of momentum distribution of light atoms and molecules in condensed matter systems using inelastic neutron scattering. *Advances in Physics*, 54(5):377–469, 2005. [2](#), [15](#), [16](#), [46](#), [87](#)
- [2] Carla Andreani, Roberto Senesi, Matthew Krzystyniak, Giovanni Romanelli, and Felix Fernandez-Alonso. Chapter 7 - atomic quantum dynamics in materials research. In Felix Fernandez-Alonso and David L. Price, editors, *Neutron Scattering - Applications in Biology, Chemistry, and Materials Science*, volume 49 of *Experimental Methods in the Physical Sciences*, pages 403 – 457. Academic Press, 2017. [2](#), [15](#)
- [3] C Andreani, M Krzystyniak, G Romanelli, R Senesi, and F Fernandez-Alonso. Electron-volt neutron spectroscopy: beyond fundamental systems. *Advances in Physics*, 66(1):1–73, 2017. [2](#), [8](#), [15](#), [53](#)
- [4] Maciej Krzystyniak, Giovanni Romanelli, and Felix Fernandez-Alonso. Non-destructive quantitation of hydrogen via mass-resolved neutron spectroscopy. *Analyst*, 144:3936–3941, 2019. [2](#)
- [5] V Philipps, P Wienhold, A Kirschner, and M Rubel. Erosion and redeposition of wall material in controlled fusion devices. *Vacuum*, 67(3-4):399–408, 2002. [2](#)
- [6] Ian P. Silverwood, Stewart F. Parker, and C. Richard A. Catlow. Neutron scattering in catalysis and energy materials. *Phys. Chem. Chem. Phys.*, 18:17140–17140, 2016. [2](#)
- [7] EERO SJOSTROM. Chapter 4 - lignin. In EERO SJOSTROM, editor, *Wood Chemistry (Second Edition)*, pages 71 – 89. Academic Press, San Diego, second edition edition, 1993. [2](#), [52](#)
- [8] Pooya Azadi, Oliver R. Inderwildi, Ramin Farnood, and David A. King. Liquid fuels, hydrogen and chemicals from lignin: A critical review. *Renewable and Sustainable Energy Reviews*, 21(C):506–523, 2013. [2](#), [52](#)
- [9] Arthur J Ragauskas, Gregg T Beckham, Mary J Bidy, Richard Chandra, Fang Chen, Mark F Davis, Brian H Davison, Richard A Dixon, Paul Gilna, Martin Keller, et al. Lignin valorization: improving lignin processing in the biorefinery. *science*, 344(6185), 2014. [2](#), [52](#)
- [10] Seyed Hamidreza Ghaffar and Mizi Fan. Structural analysis for lignin characteristics in biomass straw. *Biomass and Bioenergy*, 57:264 – 279, 2013. [2](#), [52](#)

- [11] Jan Larsen, Mai Ostergaard Haven, and Laila Thirup. Inbicon makes lignocellulosic ethanol a commercial reality. *Biomass and Bioenergy*, 46:36 – 45, 2012. International Conference on Lignocellulosic ethanol. [2](#), [52](#)
- [12] Mads M. Jensen, Demi T. Djajadi, Cristian Torri, Helene B. Rasmussen, René B. Madsen, Elisa Venturini, Ivano Vassura, Jacob Becker, Bo B. Iversen, Anne S. Meyer, Henning Jørgensen, Daniele Fabbri, and Marianne Glasius. Hydrothermal liquefaction of enzymatic hydrolysis lignin: Biomass pretreatment severity affects lignin valorization. *ACS Sustainable Chemistry & Engineering*, 6(5):5940–5949, 2018. [2](#), [52](#)
- [13] Amandeep K. Sangha, Loukas Petridis, Jeremy C. Smith, Angela Ziebell, and Jerry M. Parks. Molecular simulation as a tool for studying lignin. *Environmental Progress & Sustainable Energy*, 31(1):47–54, 2012. [2](#), [52](#)
- [14] Seonah Kim, Stephen C. Chmely, Mark R. Nimlos, Yannick J. Bomble, Thomas D. Foust, Robert S. Paton, and Gregg T. Beckham. Computational study of bond dissociation enthalpies for a large range of native and modified lignins. *The Journal of Physical Chemistry Letters*, 2(22):2846–2852, 2011. [2](#), [52](#)
- [15] Jarod M. Younker, Ariana Beste, and A. C. Buchanan III. Computational study of bond dissociation enthalpies for substituted -o-4 lignin model compounds. *ChemPhysChem*, 12(18):3556–3565, 2011. [2](#), [52](#)
- [16] Hou-Min Chang and Xiao Jiang. Biphenyl structure and its impact on the macromolecular structure of lignin: A critical review. *Journal of Wood Chemistry and Technology*, 40(2):81–90, 2020. [2](#), [52](#)
- [17] Lin Dong, Longfei Lin, Xue Han, Xiaoqin Si, Xiaohui Liu, Yong Guo, Fang Lu, Svemir Rudić, Stewart F Parker, Sihai Yang, et al. Breaking the limit of lignin monomer production via cleavage of interunit carbon–carbon linkages. *Chem*, 5(6):1521–1536, 2019. [2](#), [52](#), [73](#), [74](#)
- [18] Aran Lamaire, Jelle Wieme, Sven MJ Rogge, Michel Waroquier, and Veronique Van Speybroeck. On the importance of anharmonicities and nuclear quantum effects in modelling the structural properties and thermal expansion of mof-5. *The Journal of chemical physics*, 150(9):094503, 2019. [3](#)
- [19] PD Haaland, R Pachter, and WW Adams. Stiffer under strain: mechanical properties of poly-p-phenylene. *Polymer*, 35(2):300–305, 1994. [3](#), [72](#)
- [20] Ekaterina A Zheligovskaya and Georgii G Malenkov. Crystalline water ices. *Russian Chemical Reviews*, 75(1):57, 2006. [3](#), [83](#)
- [21] John L Finney. Water? what’s so special about it? *Philosophical Transactions of the Royal Society of London. Series B: Biological Sciences*, 359(1448):1145–1165, 2004. [3](#), [83](#)
- [22] Christoph G. Salzmann, Paolo G. Radaelli, Ben Slater, and John L. Finney. The polymorphism of ice: five unresolved questions. *Phys. Chem. Chem. Phys.*, 13:18468–18480, 2011. [3](#), [83](#), [86](#)

- [23] Victor F Petrenko and Robert W Whitworth. *Physics of ice*. OUP Oxford, 1999. 3, 83
- [24] Tamsin L Malkin, Benjamin J Murray, Christoph G Salzmann, Valeria Molinero, Steven J Pickering, and Thomas F Whale. Stacking disorder in ice I. *Physical Chemistry Chemical Physics*, 17(1):60–76, 2015. 3, 83, 86
- [25] Christoph G Salzmann, Benjamin J Murray, and Jacob J Shephard. Extent of stacking disorder in diamond. *Diamond and Related Materials*, 59:69–72, 2015. 3, 83
- [26] Giulia Festa, Giovanni Romanelli, Roberto Senesi, Laura Arcidiacono, Claudia Scatigno, Stewart F Parker, MPM Marques, and Carla Andreani. Neutrons for cultural heritage techniques, sensors, and detection. *Sensors*, 20(2):502, 2020. 5
- [27] Marc Bée. Quasielastic neutron scattering. 1988. 8, 92
- [28] Philip CH Mitchell, Stewart F Parker, Timmy AJ Ramirez-cuesta, and John Tomkinson. *Vibrational Spectroscopy With Neutrons-With Applications In Chemistry, Biology, Materials Science And Catalysis*, volume 3. World Scientific, 2005. 8
- [29] Molecular Quantum Mechanics. Pw atkins and rs friedman, 1997. 9
- [30] Donald E Parks, JR Beyster, MS Nelkin, and NF Wikner. Slow neutron scattering and thermalization with reactor applications. 1970. 12
- [31] Martin Chaplin. Water structure and science. <http://www1.lsbu.ac.uk/water/>, 2014. 12, 84, 86
- [32] Gordon Leslie Squires. Introduction to the theory of thermal neutron scattering. *PhT*, 32(10):69, 1979. 13, 92
- [33] CJ Carlile and Mark A Adams. The design of the iris inelastic neutron spectrometer and improvements to its analysers. *PhyB*, 182(4):431–440, 1992. 14
- [34] D Colognesi, M Celli, F Cilloco, RJ Newport, SR Parker, V Rossi-Albertini, F Sacchetti, J Tomkinson, and M Zoppi. TOSCA neutron spectrometer: The final configuration. *APPLIED PHYSICS A-MATERIALS SCIENCE & PROCESSING*, 74(Part 1 Suppl. S):S64–S66, DEC 2002. 14
- [35] J M F Gunn, C Andreani, and J Mayers. A new approach to impulsive neutron scattering. *Journal of Physics C: Solid State Physics*, 19(36):L835, 1986. 15
- [36] G. I. Watson. REVIEW ARTICLE: Neutron Compton scattering. *Journal of Physics Condensed Matter*, 8:5955–5975, August 1996. 15
- [37] Lin Lin, Joseph A. Morrone, Roberto Car, and Michele Parrinello. Displaced path integral formulation for the momentum distribution of quantum particles. *Phys Rev Lett*, 105(11):110602, Sep 2010. 15
- [38] R. Ramirez and C. P. Herrero. Kinetic energy of protons in ice Ih and water: A path integral study. *Physical Review B*, 84:064130, Aug 2011. 15

- [39] Michele Ceriotti, Wei Fang, Peter G. Kusalik, Ross H. McKenzie, Angelos Michaelides, Miguel A. Morales, and Thomas E. Markland. Nuclear quantum effects in water and aqueous systems: Experiment, theory, and current challenges. *Chemical Reviews*, 116(13):7529–7550, 2016. [15](#), [47](#)
- [40] R. Moreh and D. Nemirovsky. On the proton kinetic energy in H₂O and in nanotube water. *The Journal of Chemical Physics*, 133(8):084506, August 2010. [15](#)
- [41] Y. Finkelstein and R. Moreh. Temperature dependence of the proton kinetic energy in water between 5 and 673 K. *Chemical Physics*, 431:58–63, March 2014. [15](#), [102](#)
- [42] G. B. West. Electron scattering from atoms, nuclei and nucleons. *Physics Reports*, 18:263–323, June 1975. [15](#), [59](#)
- [43] V. F. Sears. Scaling and final-state interactions in deep-inelastic neutron scattering. *Physical Review B*, 30:44–51, July 1984. [16](#), [18](#)
- [44] D. Flammini, A. Pietropaolo, R. Senesi, C. Andreani, F. McBride, A. Hodgson, M. A. Adams, L. Lin, and R. Car. Spherical momentum distribution of the protons in hexagonal ice from modeling of inelastic neutron scattering data. *The Journal of Chemical Physics*, 136:024504, 2012. [17](#), [86](#), [103](#)
- [45] A. Parmentier, C. Andreani, G. Romanelli, J. J. Shephard, C. G. Salzmann, and R. Senesi. Hydrogen mean force and anharmonicity in polycrystalline and amorphous ice. *Frontiers of Physics*, 13(1):136101, Oct 2017. [17](#), [43](#), [49](#)
- [46] L. Lin, J. A. Morrone, R. Car, and M. Parrinello. Momentum distribution, vibrational dynamics, and the potential of mean force in ice. *Physical Review B*, 83(22):220302, June 2011. [17](#), [49](#)
- [47] A Parmentier, J J Shephard, G Romanelli, R Senesi, C G Salzmann, and C Andreani. Evolution of hydrogen dynamics in amorphous ice with density. *The Journal of Physical Chemistry Letters*, 6(11):2038–2042, 2015. [17](#), [49](#)
- [48] Alexander I. Kolesnikov, George F. Reiter, Narayani Choudhury, Timothy R. Prisk, Eugene Mamontov, Andrey Podlesnyak, George Ehlers, Andrew G. Seel, David J. Wesolowski, and Lawrence M. Anovitz. Quantum tunneling of water in beryl: A new state of the water molecule. *Phys. Rev. Lett.*, 116:167802, Apr 2016. [17](#)
- [49] C Andreani, G Romanelli, and R Senesi. Direct measurements of quantum kinetic energy tensor in stable and metastable water near the triple point: An experimental benchmark. *The Journal of Physical Chemistry Letters*, 7(12):2216–2220, 2016. [17](#), [47](#), [73](#), [75](#)
- [50] M Krzystyniak, K Druzbecki, G Romanelli, M J Gutmann, S Rudic, S Imberti, and F Fernandez-Alonso. Nuclear dynamics and phase polymorphism in solid formic acid. *Physical Chemistry Chemical Physics*, 19:9064–9074, 2017. [17](#)
- [51] Timothy R. Prisk, Alexander I. Kolesnikov, Garrett E. Granroth, Jun-Li Lin, and Brent J. Heuser. Vibrational modes and quantum zero-point energy of hydrogen in zrh0.0155 and zrh2. *Journal of Alloys and Compounds*, 818:152832, 2020. [17](#)

- [52] G Romanelli, M Ceriotti, D E. Manolopoulos, C Pantalei, R Senesi, and C Andreani. Direct measurement of competing quantum effects on the kinetic energy of heavy water upon melting. *The Journal of Physical Chemistry Letters*, 4(19):3251–3256, 2013. [17](#), [84](#)
- [53] G. F. Syrykh, A. A. Stolyarov, M. Krzystyniak, G. Romanelli, and R. A. Sadykov. Temperature dependence of the kinetic energy in the zr40be60 amorphous alloy. *JETP Letters*, 105(9):591–594, May 2017. [17](#)
- [54] Vincenzo De Michele, Giovanni Romanelli, and Antonio Cupane. Kinetic energy and radial momentum distribution of hydrogen and oxygen atoms of water confined in silica hydrogel in the temperature interval 170–325 k. *SCIENCE CHINA Physics, Mechanics & Astronomy*, 62(10):107012, 2019. [17](#), [75](#)
- [55] Adrien Perrichon, Erik Jedvik Granhed, Giovanni Romanelli, Andrea Piovano, Anders Lindman, Per Hyldgaard, Göran Wahnström, and Maths Karlsson. Unraveling the ground-state structure of bazo3 by neutron scattering experiments and first-principles calculations. *Chemistry of Materials*, 32(7):2824–2835, 2020. [17](#)
- [56] R. Moreh, W. C. Sellyey, D. Sutton, and R. Vodhanel. Widths of the 6.92 and 7.12 MeV levels in ^{16}O and the influence of the effective temperature. *Physical Review C*, 31:2314–2316, June 1985. [17](#), [69](#)
- [57] C. Andreani, E. Degiorgi, R. Senesi, F. Cillico, D. Colognesi, J. Mayers, M. Nardone, and E. Pace. Single particle dynamics in fluid and solid hydrogen sulphide: An inelastic neutron scattering study. *The Journal of Chemical Physics*, 114:387–398, January 2001. [17](#), [69](#)
- [58] C. Andreani, G. Romanelli, and R. Senesi. A combined INS and DINS study of proton quantum dynamics of ice and water across the triple point and in the supercritical phase. *Chemical Physics*, 427:106–110, December 2013. [17](#), [69](#), [101](#)
- [59] G Romanelli, F Fernandez-Alonso, and C Andreani. The harmonic picture of nuclear mean kinetic energies in heavy water. In *Journal of Physics: Conference Series*, volume 571, page 012003, 2014. [17](#), [46](#), [47](#), [69](#), [84](#), [101](#)
- [60] G Romanelli and M Krzystyniak. On the line-shape analysis of compton profiles and its application to neutron scattering. *Nuclear Instruments and Methods in Physics Research Section A*, 819:84 – 88, 2016. [18](#), [46](#), [71](#)
- [61] JANIS WebSite. <https://www.oecd-neo.org/janis/>. [19](#), [20](#), [31](#)
- [62] Kenneth S Krane, David Halliday, et al. *Introductory nuclear physics*. 1987. [19](#)
- [63] C. Andreani, A. Pietropaolo, R. Senesi, G. Gorini, E. Perelli-Cippo, M. Tardocchi, N. Rhodes, and E. M. Schooneveld. A resonant detector for high-energy inelastic neutron scattering experiments. *Appl Phys Lett*, 85:5454, November 2004. [23](#)
- [64] C Andreani, A Pietropaolo, R Senesi, G Gorini, M Tardocchi, A Bracco, N Rhodes, and E Schooneveld. Electron-volt spectroscopy at a pulsed neutron source using a

- resonance detector technique. *Nuclear Instruments and Methods in Physics Research Section A*, 481:509–520, April 2002. 23
- [65] ISIS website. <http://www.isis.stfc.ac.uk>. 23, 26
- [66] G Romanelli, M Krzystyniak, R Senesi, D Raspino, J Boxall, D Pooley, S Moorby, E Schooneveld, N J Rhodes, C Andreani, and F Fernandez-Alonso. Characterisation of the incident beam and current diffraction capabilities on the VESUVIO spectrometer. *Measurement Science and Technology*, 28(9):095501, 2017. 27, 52, 89
- [67] Marvin J Weber. Inorganic scintillators: today and tomorrow. *Journal of Luminescence*, 100(1-4):35–45, 2002. 29
- [68] Christian Massimi, César Domingo-Pardo, Gianni Vannini, Laurent Audouin, C Guerrero, U Abbondanno, G Aerts, H Alvarez, F Alvarez-Velarde, S Andriamonje, et al. Au 197 (n, γ) cross section in the resonance region. *Physical Review C*, 81(4):044616, 2010. 31
- [69] Gabor Molnar. *Handbook of prompt gamma activation analysis: with neutron beams*, volume 1. Springer Science & Business Media, 2004. 32, 34
- [70] A. Pietropaolo, C. Andreani, A. Filabozzi, E. Pace, and R. Senesi. Resolution function in deep inelastic neutron scattering using the Foil Cycling Technique. *Nuclear Instruments and Methods in Physics Research Section A*, 570:498–510, 2007. 33
- [71] E M Schooneveld, J Mayers, N J Rhodes, A Pietropaolo, C Andreani, R Senesi, G Gorini, E Perelli-Cippo, and M Tardocchi. Foil cycling technique for the VESUVIO spectrometer operating in the resonance detector configuration. *Review Scientific Instruments*, 77:5103, September 2006. 33, 44, 53
- [72] J. Mayers, J. Tomkinson, T. Abdul-Redah, W. G. Stirling, C. Andreani, R. Senesi, M. Nardone, D. Colognesi, and E. Degiorgi. VESUVIO-the double difference inverse geometry spectrometer at ISIS. *Physica B Condensed Matter*, 350:E659–E662, July 2004. 33
- [73] J. M. Carpenter, N. Watanabe, S. Ikeda, Y. Masuda, and S. Sato. Tests of A Resonance Detector Spectrometer for Electron-Volt Spectroscopy. In *Proceedings of the Sixth International Collaboration on Advanced Neutron Sources*, pages 266–278, 1982. 33
- [74] A. Pietropaolo, C. Andreani, A. D’Angelo, R. Senesi, G. Gorini, S. Imberti, M. Tardocchi, N. Rhodes, and E. S. Schooneveld. γ detectors for Deep Inelastic Neutron Scattering in the 1-100 eV energy region. *Applied Physics A: Materials Science & Processing*, 74:189–190, 2002. 33
- [75] G. Gorini, E. Perelli-Cippo, M. Tardocchi, C. Andreani, A. D’Angelo, A. Pietropaolo, R. Senesi, S. Imberti, A. Bracco, E. Previtali, G. Pessina, N. J. Rhodes, and E. M. Schooneveld. The resonant detector and its application to epithermal neutron spectroscopy. *Nuclear Instruments and Methods in Physics Research Section A*, 529:293–300, August 2004. 33

- [76] C. Andreani, A. D'Angelo, G. Gorini, S. Imberti, A. Pietropaolo, N. J. Rhodes, E. M. Schooneveld, R. Senesi, and M. Tardocchi. CdZnTe γ detector for deep inelastic neutron scattering on the VESUVIO spectrometer. *Applied Physics A: Materials Science & Processing*, 78:903–913, 2004. [33](#), [34](#)
- [77] M. Tardocchi, A. Pietropaolo, C. Andreani, A. Bracco, A. D'Angelo, G. Gorini, S. Imberti, R. Senesi, N. J. Rhodes, and E. M. Schooneveld. Cadmium-Zinc-Telluride photon detector for epithermal neutron spectroscopy-pulse height response characterisation. *Nuclear Instruments and Methods in Physics Research Section A*, 526:477–492, July 2004. [33](#), [39](#), [52](#)
- [78] C. Andreani, A. Pietropaolo, R. Senesi, G. Gorini, E. Perelli-Cippo, M. Tardocchi, N. Rhodes, and E. M. Schooneveld. A resonant detector for high-energy inelastic neutron scattering experiments. *Appl Phys Lett*, 85:5454, November 2004. [34](#)
- [79] J. Mayers. Calculation of background effects on the VESUVIO eV neutron spectrometer. *Measurement Science and Technology*, 22(1):015903, January 2011. [35](#), [90](#)
- [80] V.F. Sears. Slow-neutron multiple scattering. *Advances in Physics*, 24(1):1–45, 1975. [35](#)
- [81] J Mayers, AL Fielding, and R Senesi. Multiple scattering in deep inelastic neutron scattering: Monte carlo simulations and experiments at the ISIS evs inverse geometry spectrometer. *Nuclear Instruments and Methods in Physics Research Section A*, 481(1-3):454–463, 2002. [36](#), [59](#), [60](#), [90](#)
- [82] Iris website. <http://www.isis.stfc.ac.uk/Pages/IRIS.aspx>. [36](#), [92](#)
- [83] Iris manual. <https://www.isis.stfc.ac.uk/Pages/irisman.pdf>. [37](#), [96](#)
- [84] D Onorati, C Andreani, L Arcidiacono, F Fernandez-Alonso, G Festa, M Krzystyniak, G Romanelli, P Ulpiani, and R Senesi. Gamma background characterization on VESUVIO: Before and after the moderator upgrade. *Journal of Physics: Conference Series*, 1055(1):012009, 2018. [39](#), [57](#)
- [85] Dalila Onorati, Giovanni Romanelli, Pierfrancesco Ulpiani, Carlo Cazzaniga, Enrico Preziosi, Laura Arcidiacono, Giulia Festa, Carla Andreani, Roberto Senesi, and Maria Cristina Morone. Fluka simulations and benchmark measurements of the yap (ce) scintillators installed on the VESUVIO spectrometer. *Nuclear Instruments and Methods in Physics Research Section A: Accelerators, Spectrometers, Detectors and Associated Equipment*, page 164012, 2020. [39](#), [41](#), [42](#), [43](#), [57](#)
- [86] I. S. Anderson, R. McGreevy, and H. Z. Biliheux. *Neutron Imaging and Applications*. Springer, New York, 2009. [39](#), [46](#), [51](#), [52](#)
- [87] P Ulpiani, G Romanelli, L Arcidiacono, D Onorati, G Festa, M Krzystyniak, E Schooneveld, F Fernandez-Alonso, C Andreani, and R Senesi. Enhancement of counting statistics and noise reduction in the forward-scattering detectors on the VESUVIO spectrometer. *Journal of Physics: Conference Series*, 1055(1):012008, 2018. [39](#), [44](#), [57](#)

- [88] TT Böhlen, F Cerutti, MPW Chin, Alberto Fassò, Alfredo Ferrari, P Garcia Ortega, Andrea Mairani, Paola R Sala, G Smirnov, and V Vlachoudis. The fluka code: developments and challenges for high energy and medical applications. *Nuclear data sheets*, 120:211–214, 2014. [39](#)
- [89] Zhang Su-Ya-La-Tu, Chen Zhi-Qiang, Han Rui, Liu Xing-Quan, R Wada, Lin Wei-Ping, Jin Zeng-Xue, Xi Yin-Yin, Liu Jian-Li, and Shi Fu-Dong. Study on gamma response function of ej301 organic liquid scintillator with geant4 and fluka. *Chinese Physics C*, 37(12):126003, 2013. [40](#)
- [90] G. F. Knoll. *Radiation detection and measurement*. 1979. [40](#)
- [91] S Baccaro, K Blaek, F De Notaristefani, P Maly, JA Mares, R Pani, R Pellegrini, and A Soluri. Scintillation properties of yap: Ce. *Nuclear Instruments and Methods in Physics Research Section A: Accelerators, Spectrometers, Detectors and Associated Equipment*, 361(1-2):209–215, 1995. [43](#)
- [92] R. Senesi, G. Romanelli, M.A. Adams, and C. Andreani. Temperature dependence of the zero point kinetic energy in ice and water above room temperature. *Chemical Physics*, 427:111–116, 2013. [46](#), [47](#), [86](#)
- [93] Rene Brun and Fons Rademakers. Rootan object oriented data analysis framework. *Nuclear Instruments and Methods in Physics Research Section A: Accelerators, Spectrometers, Detectors and Associated Equipment*, 389(1-2):81–86, 1997. [47](#)
- [94] H Postma, M Blaauw, P Bode, P Mutti, F Corvi, and P Siegler. Neutron-resonance capture analysis of materials. *Journal of radioanalytical and nuclear chemistry*, 248(1):115–120, 2001. [50](#)
- [95] RL Paul and RM Lindstrom. Prompt gamma-ray activation analysis: fundamentals and applications. *Journal of Radioanalytical and Nuclear Chemistry*, 243(1):181–189, 2000. [50](#)
- [96] G Festa, L Arcidiacono, A Pappalardo, T Minniti, C Cazzaniga, A Scherillo, C Andreani, and R Senesi. Isotope identification capabilities using time resolved prompt gamma emission from epithermal neutrons. *Journal of Instrumentation*, 11(03):C03060, 2016. [50](#)
- [97] Owen Arnold, Jean-Christophe Bilheux, JM Borreguero, Alex Buts, Stuart I Campbell, L Chapon, Mathieu Doucet, N Draper, R Ferraz Leal, MA Gigg, et al. Mantiddata analysis and visualization package for neutron scattering and μ sr experiments. *Nuclear Instruments and Methods in Physics Research Section A: Accelerators, Spectrometers, Detectors and Associated Equipment*, 764:156–166, 2014. [51](#), [57](#)
- [98] S Jackson, M Krzystyniak, A G Seel, M Gigg, S E Richards, and F Fernandez-Alonso. VESUVIO data analysis goes mantid. *Journal of Physics: Conference Series*, 571(1):012009, 2014. [51](#)

- [99] D Monserrat, A Vispa, L C Pardo, R Tolchenov, S Mukhopadhyay, and F Fernandez-Alonso. Fabada goes mantid to answer an old question: How many lines are there? *Journal of Physics: Conference Series*, 663(1):012009, 2015. [51](#)
- [100] Mantid website. <http://download.mantidproject.org/>. [51](#)
- [101] E Oram. An overview of the development of indirect inelastic data reduction and analysis in mantid between july 2015-july 2016. *RAL Technical Reports*, 11, 2016. [51](#)
- [102] E Oram and L McCann. Simulation support and further indirect inelastic specific improvements within mantid. *RAL Technical Reports*, 19, 2016. [51](#)
- [103] J Mayers and G Reiter. The VESUVIO electron volt neutron spectrometer. *Measurement Science and Technology*, 23:045902, 2012. [52](#), [55](#), [57](#)
- [104] Sigma-Aldrich website. <https://www.sigmaaldrich.com/>. [52](#)
- [105] C. Andreani, G. Baciocco, R. S. Holt, and J. Mayers. Resolution in deep inelastic neutron scattering using pulsed neutron sources. *Nuclear Instruments and Methods in Physics Research Section A*, 276:297–305, March 1989. [53](#)
- [106] S. Imberti, C. Andreani, V. Garbuio, G. Gorini, A. Pietropaolo, R. Senesi, and M. Tardocchi. Resolution of the VESUVIO spectrometer for High-energy Inelastic Neutron Scattering experiments. *Nuclear Instruments and Methods in Physics Research Section A*, 522:463, 2005. [53](#)
- [107] J Mayers and M A Adams. Calibration of an electron volt neutron spectrometer. *Nuclear Instruments and Methods in Physics Research Section A*, 625:47–56, January 2011. [53](#)
- [108] G Romanelli, B Hewer, M Krzystyniak, M Gigg, R Tolchenov, S Mukhopadhyay, and F Fernandez-Alonso. Data analysis of neutron compton scattering experiments using MANTID. *Journal of Physics: Conference Series*, 1055:012016, jul 2018. [55](#), [59](#), [60](#), [76](#), [90](#)
- [109] Pierfrancesco Ulpiani, Giovanni Romanelli, Dalila Onorati, Alexandra Parmentier, Giulia Festa, Erik Schooneveld, Carlo Cazzaniga, Laura Arcidiacono, Carla Andreani, and Roberto Senesi. Optimization of detection strategies for epithermal neutron spectroscopy using photon-sensitive detectors. *Review of Scientific Instruments*, 90(7):073901, 2019. [57](#), [60](#), [76](#)
- [110] E. Pace, G. Salmè, and G.B. West. Final state interaction in quasi-elastic electron scattering by nuclei and γ scaling. *Physics Letters B*, 273(3):205 – 210, 1991. [59](#)
- [111] J.I. Robledo, J. Dawidowski, J.I. Márquez Damián, G. Škoro, C. Bovo, and G. Romanelli. Measurement of neutron total cross sections at the VESUVIO spectrometer. *Nuclear Instruments and Methods in Physics Research Section A: Accelerators, Spectrometers, Detectors and Associated Equipment*, 971:164096, 2020. [59](#)

- [112] Varley F. Sears. Neutron scattering lengths and cross sections. *Neutron News*, 3(3):26–37, 1992. [60](#)
- [113] VF Sears. Atomic momentum distributions in condensed matter. *Canadian Journal of physics*, 63(1):68–75, 1985. [60](#), [75](#)
- [114] Maurice G Kendall and Alan Stuart. The advanced theory of statistics, vol. 1 (charles griffin and company, ltd., london). 1958. [60](#)
- [115] P. Hohenberg and W. Kohn. Inhomogeneous electron gas. *Phys. Rev.*, 136:B864–B871, Nov 1964. [66](#)
- [116] W. Kohn and L. J. Sham. Self-consistent equations including exchange and correlation effects. *Phys. Rev.*, 140:A1133–A1138, Nov 1965. [66](#)
- [117] Feliciano Giustino. *Materials modelling using density functional theory: properties and predictions*. Oxford University Press, 2014. [66](#), [73](#), [75](#)
- [118] Marvin L Cohen. Application of the pseudopotential model to solids. *Annual Review of Materials Science*, 14(1):119–144, 1984. [67](#)
- [119] Paolo Giannozzi, Stefano Baroni, Nicola Bonini, Matteo Calandra, Roberto Car, Carlo Cavazzoni, Davide Ceresoli, Guido L Chiarotti, Matteo Cococcioni, Ismaila Dabo, et al. Quantum espresso: a modular and open-source software project for quantum simulations of materials. *Journal of physics: Condensed matter*, 21(39):395502, 2009. [68](#), [72](#)
- [120] Stewart J Clark, Matthew D Segall, Chris J Pickard, Phil J Hasnip, Matt IJ Probert, Keith Refson, and Mike C Payne. First principles methods using CASTEP. *Zeitschrift für Kristallographie-Crystalline Materials*, 220(5/6):567–570, 2005. [68](#), [72](#)
- [121] Neil W Ashcroft, N David Mermin, et al. Solid state physics by neil w. ashcroft and n. david mermin., 1976. [68](#)
- [122] Atsushi Togo and Isao Tanaka. First principles phonon calculations in materials science. *Scripta Materialia*, 108:1–5, 2015. [69](#)
- [123] Anna A Hoser and Anders Østergaard Madsen. Dynamic quantum crystallography: lattice-dynamical models refined against diffraction data. i. theory. *Acta Crystallographica Section A: Foundations and Advances*, 72(2):206–214, 2016. [71](#)
- [124] Louis J Farrugia. Wingx and ortep for windows: an update. *Journal of Applied Crystallography*, 45(4):849–854, 2012. [72](#)
- [125] Paul LA Popelier, Peter I Maxwell, Joseph CR Thacker, and Ibon Alkorta. A relative energy gradient (reg) study of the planar and perpendicular torsional energy barriers in biphenyl. *Theoretical chemistry accounts*, 138(1):12, 2019. [72](#)
- [126] Jesús Hernández-Trujillo and Chérif F Matta. Hydrogen–hydrogen bonding in biphenyl revisited. *Structural Chemistry*, 18(6):849–857, 2007. [72](#)

- [127] Colin R Groom, Ian J Bruno, Matthew P Lightfoot, and Suzanna C Ward. The cambridge structural database. *Acta Crystallographica Section B: Structural Science, Crystal Engineering and Materials*, 72(2):171–179, 2016. 72, 73
- [128] G-P Charbonneau and Y_ Delugeard. Structural transition in polyphenyls. iii. crystal structure of biphenyl at 110 k. *Acta Crystallographica Section B: Structural Crystallography and Crystal Chemistry*, 32(5):1420–1423, 1976. 72, 73
- [129] Riccardo Sabatini, Tommaso Gorni, and Stefano De Gironcoli. Nonlocal van der waals density functional made simple and efficient. *Physical Review B*, 87(4):041108, 2013. 72
- [130] Massimo Nespolo. International tables for crystallography, volume a, space-group symmetry. *Acta Crystallographica Section A Foundations and Advances*, 73(3):274–276, 2017. 72
- [131] Chris J Pickard. On-the-fly pseudopotential generation in CASTEP. *School of Physics and Astronomy, University of St Andrews St Andrews, KY16 9SS, United Kingdom*, 2006. 72
- [132] DR Hamann. Optimized norm-conserving vanderbilt pseudopotentials. *Physical Review B*, 88(8):085117, 2013. 72
- [133] S.F Parker, C.J Carlile, T Pike, J Tomkinson, R.J Newport, C Andreani, F.P Ricci, F Sacchetti, and M Zoppi. Tosca: a world class inelastic neutron spectrometer. *Physica B: Condensed Matter*, 241-243:154 – 156, 1997. Proceedings of the International Conference on Neutron Scattering. 73
- [134] Krzysztof Dymkowski, Stewart F Parker, Felix Fernandez-Alonso, and Sanghamitra Mukhopadhyay. AbINS: The modern software for INS interpretation. *Physica B: Condensed Matter*, 551:443–448, 2018. 73
- [135] INS-database website. <https://www.isis.stfc.ac.uk/Pages/INS-database.aspx>. 74, 99, 100
- [136] Bingqing Cheng, Jörg Behler, and Michele Ceriotti. Nuclear quantum effects in water at the triple point: Using theory as a link between experiments. *The Journal of Physical Chemistry Letters*, 7(12):2210–2215, 2016. 73
- [137] Carla Andreani, Roberto Senesi, Matthew Krzystyniak, Giovanni Romanelli, and Felix Fernandez-Alonso. Experimental studies of nuclear quantum effects in condensed matter: The case of water. *La Rivista del Nuovo Cimento*, 41:291–340, 05 2018. 73
- [138] Carla Andreani, Carmelo Corsaro, Domenico Mallamace, Giovanni Romanelli, Roberto Senesi, and Francesco Mallamace. The onset of the tetrabonded structure in liquid water. *Sci. China Phys. Mech. Astron.*, 62:107008, 2019. 73
- [139] H t Bonadeo and E Burgos. Lattice dynamical calculations of the mean square amplitudes of crystalline biphenyl. *Acta Crystallographica Section A: Crystal Physics, Diffraction, Theoretical and General Crystallography*, 38(1):29–33, 1982. 76

- [140] G Romanelli, R Senesi, X Zhang, K P Loh, and C Andreani. Probing the effects of 2d confinement on hydrogen dynamics in water and ice adsorbed in graphene oxide sponges. *Physical Chemistry Chemical Physics*, 17(47):31680–31684, 2015. [75](#)
- [141] G Romanelli, A Liscio, R Senesi, R Zamboni, E Treossi, F Liscio, G Giambastiani, V Palermo, F Fernandez-Alonso, and C Andreani. Soft confinement of water in graphene-oxide membranes. *Carbon*, 108:199–203, 2016. [75](#)
- [142] Srinivasan Damodaran, Kirk L Parkin, and Owen R Fennema. *Fennema's food chemistry*. CRC press, 2007. [83](#)
- [143] George A Jeffrey and Wolfram Saenger. *Hydrogen bonding in biological structures*. Springer Science & Business Media, 2012. [83](#)
- [144] Christoph G Salzmann. Advances in the experimental exploration of waters phase diagram. *The Journal of chemical physics*, 150(6):060901, 2019. [83](#)
- [145] Gustav Tammann. Ueber die grenzen des festen zustandes iv. *Annalen der Physik*, 307(5):1–31, 1900. [84](#)
- [146] PW Bridgman. Effect of pressure on freezing point of water. In *Proc. Am. Acad*, volume 47, pages 441–558, 1912. [84](#)
- [147] W Barclay Kamb and Sankar K Datta. Crystal structures of the high-pressure forms of ice: ice III. *Nature*, 187(4732):140–141, 1960. [84](#)
- [148] Linus Pauling. The structure and entropy of ice and of other crystals with some randomness of atomic arrangement. *Journal of the American Chemical Society*, 57(12):2680–2684, 1935. [85](#)
- [149] Jacob J Shephard and Christoph G Salzmann. The complex kinetics of the ice vi to ice xv hydrogen ordering phase transition. *Chemical Physics Letters*, 637:63–66, 2015. [85](#)
- [150] Christoph G Salzmann, Paolo G Radaelli, Andreas Hallbrucker, Erwin Mayer, and John L Finney. The preparation and structures of hydrogen ordered phases of ice. *Science*, 311(5768):1758–1761, 2006. [85](#)
- [151] Y Tajima, T Matsuo, and H Suga. Phase transition in koh-doped hexagonal ice. *Nature*, 299(5886):810–812, 1982. [85](#)
- [152] Christoph G Salzmann, Paolo G Radaelli, Erwin Mayer, and John L Finney. Ice xv: A new thermodynamically stable phase of ice. *Physical review letters*, 103(10):105701, 2009. [85](#)
- [153] Luis G MacDowell, Eduardo Sanz, Carlos Vega, and José Luis F Abascal. Combinatorial entropy and phase diagram of partially ordered ice phases. *The Journal of chemical physics*, 121(20):10145–10158, 2004. [85](#)
- [154] E Whalley and DW Davidson. Entropy changes at the phase transitions in ice. *The Journal of Chemical Physics*, 43(6):2148–2149, 1965. [85](#), [86](#)

- [155] Colin Lobban, John L Finney, and Werner F Kuhs. The p–t dependency of the ice ii crystal structure and the effect of helium inclusion. *The Journal of chemical physics*, 117(8):3928–3934, 2002. 86
- [156] Tatsuya Nakamura, Masakazu Matsumoto, Takuma Yagasaki, and Hideki Tanaka. Thermodynamic stability of ice II and its hydrogen-disordered counterpart: role of zero-point energy. *The Journal of Physical Chemistry B*, 120(8):1843–1848, 2016. 86, 90
- [157] Jacob J Shephard, Ben Slater, Peter Harvey, Martin Hart, Craig L Bull, Steven T Bramwell, and Christoph G Salzmänn. Doping-induced disappearance of ice ii from waters phase diagram. *Nature Physics*, 14(6):569–572, 2018. 86
- [158] C. Andreani, P. Bosi, F. Sacchetti, and C. K. Loong. Absolute measurements of the stretching mode density of states in polycrystalline ice Ih. *The Journal of Chemical Physics*, 83:750–753, July 1985. 86
- [159] C. Andreani, D. Colognesi, A. Pietropaolo, and R. Senesi. Ground state proton dynamics in stable phases of water. *Chemical Physics Letters*, 518(0):1 – 6, 2011. 86
- [160] R. Senesi, D. Flammini, A. I. Kolesnikov, E. D. Murray, G. Galli, and C. Andreani. The quantum nature of the oh stretching mode in ice and water probed by neutron scattering experiments. *The Journal of Chemical Physics*, 139(7):074504, 2013. 86, 90
- [161] R Senesi, A I Kolesnikov, and C Andreani. Measurement of proton momentum distributions using a direct geometry instrument. *Journal of Physics: Conference Series*, 571(1):012007, 2014. 86
- [162] C. Pantalei, A. Pietropaolo, R. Senesi, S. Imberti, C. Andreani, J. Mayers, C. Burnham, and G. Reiter. Proton Momentum Distribution of Liquid Water from Room Temperature to the Supercritical Phase. *Physical Review Letters*, 100(17):177801, May 2008. 86
- [163] UCL Salzmänn Research Lab. <https://www.ucl.ac.uk/uccacgs/>. 86
- [164] Zainab Sharif. *New insights into Water’s Phase Diagram Using Ammonium Fluoride*. PhD thesis, University College London, 2020. 86
- [165] Zwick universal machine site. <https://www.zwickroell.com/it-it/macchine-di-prova-universali>. 86
- [166] Y Paul Handa, DD Klug, and Edward Whalley. Energies of the phases of ice at low temperature and pressure relative to ice Ih. *Canadian journal of chemistry*, 66(4):919–924, 1988. 87
- [167] A G Seel, M Krzystyniak, and F Fernandez-Alonso. The VESUVIO spectrometer now and when? *Journal of Physics: Conference Series*, 571(1):012006, 2014. 87
- [168] J. Mayers. Measurement of the proton wave function in molecular hydrogen by neutron Compton scattering. *Phys Rev Lett*, 71:1553–1556, September 1993. 87

- [169] Koichi Momma and Fujio Izumi. An integrated three-dimensional visualization system vesta using wxwidgets. *Commission on Crystallogr. Comput., IUCr Newslett*, 7:106–119, 2006. [89](#)
- [170] John D Bernal and Ralph H Fowler. A theory of water and ionic solution, with particular reference to hydrogen and hydroxyl ions. *The Journal of Chemical Physics*, 1(8):515–548, 1933. [89](#), [103](#)
- [171] Barclay Kamb. Ice II a proton-ordered form of ice. *Acta crystallographica*, 17(11):1437–1449, 1964. [89](#), [103](#)
- [172] Sanghamitra Mukhopadhyay. How to use mantid for low energy inelastic neutron scattering data analysis on indirect geometry instruments. Technical report, Technical Report RAL-TR-2014-005, Rutherford Appleton Laboratory, 2014. [96](#)
- [173] Jichen Li. Inelastic neutron scattering studies of hydrogen bonding in ices. *The Journal of Chemical Physics*, 105(16):6733–6755, 1996. [99](#), [100](#), [103](#), [104](#), [110](#)
- [174] C. P. Herrero and R. Ramirez. Isotope effects in ice Ih: A path-integral simulation. *The Journal of Chemical Physics*, 134(9):094510, March 2011. [101](#)
- [175] Philip B Allen. Anharmonic phonon quasiparticle theory of zero-point and thermal shifts in insulators: Heat capacity, bulk modulus, and thermal expansion. *Physical Review B*, 92(6):064106, 2015. [102](#)
- [176] Barclay Kamb, Walter C Hamilton, Sam J LaPlaca, and Anand Prakash. Ordered proton configuration in ice ii, from single-crystal neutron diffraction. *The Journal of Chemical Physics*, 55(4):1934–1945, 1971. [103](#)
- [177] Mohan Chen, Hsin-Yu Ko, Richard C Remsing, Marcos F Calegari Andrade, Biswajit Santra, Zhaoru Sun, Annabella Selloni, Roberto Car, Michael L Klein, John P Perdew, et al. Ab initio theory and modeling of water. *Proceedings of the National Academy of Sciences*, 114(41):10846–10851, 2017. [103](#)
- [178] R Ramírez, N Neuerburg, M-V Fernández-Serra, and CP Herrero. Quasi-harmonic approximation of thermodynamic properties of ice Ih, II, and III. *The Journal of chemical physics*, 137(4):044502, 2012. [104](#), [105](#)
- [179] Joseph A. Morrone and Roberto Car. Nuclear quantum effects in water. *Phys Rev Lett*, 101(1):017801, Jul 2008. [104](#)
- [180] Jeffrey A Coderre and Gerard M Morris. The radiation biology of boron neutron capture therapy. *Radiation research*, 151(1):1–18, 1999. [109](#)
- [181] T Thonhauser, S Zuluaga, CA Arter, K Berland, E Schröder, and P Hyldgaard. Spin signature of nonlocal correlation binding in metal-organic frameworks. *Physical review letters*, 115(13):136402, 2015. [110](#)
- [182] Kristian Berland, Valentino R Cooper, Kyuho Lee, Elsebeth Schröder, T Thonhauser, Per Hyldgaard, and Bengt I Lundqvist. van der waals forces in density functional theory: a review of the vdW-DF method. *Reports on Progress in Physics*, 78(6):066501, 2015. [110](#)

Acknowledgements

La più importante delle sezioni l'ho tenuta da parte per quelli che hanno condiviso, sofferto e combattuto con me per il raggiungimento di questo obiettivo. Non è stato facile, ma credo che il felice epilogo di questo lavoro sia dovuto in buona parte a loro.

Un sentito ringraziamento va alla Prof.ssa Andreani per avermi offerto la possibilità di mettermi alla prova facendomi muovere i primi frizzanti passi nel mondo della ricerca. E' stato un onore e un piacere essere guidati dal Prof. Roberto Senesi e dal Dott. Giovanni Romanelli. Caro Roberto, nonostante le difficoltà mi hai sempre teso una mano e nei momenti di sconforto mi hai sempre rimesso in carreggiata; non potevo far scelta più azzeccata, ho avuto l'occhio lungo...forse perchè avevo già sentito la sensazione di casa. Caro Giovanni, vorrei dedicarti molto di più di poche parole su un pezzo di carta, abbiamo spinto insieme questo progetto a suon di videochat e risate; anche se non dovessimo parlare di Fisica (spero non ci passi mai la voglia) non scordarti mai l'appuntamento settimanale. Un ringraziamento speciale va agli amici di sempre che non serve nominare, alle chiacchierate spensierate, alle pescate della domenica all'alba e alle mie radici che mi hanno portato fin qui.

Alla Mia Dalila infine voglio dedicare questo lavoro, mi hai sempre spinto oltre le mie paure, da qui tutto è iniziato e chissà quale avventura il futuro avrà in serbo per noi.

Per tutti quanti: abbiamo tanto da festeggiare, questo è un motivo di più, aspettiamo forti sulla riva del fiume che tutto passi... io sono pronto a dar fuoco alle polveri.

Non vedo l'ora di riabbracciarvi